NIST-GCR-94-661

FUNDAMENTAL MECHANISMS FOR CO AND SOOT FORMATION

Robert J. Santoro

NIST

NIST-GCR-94-661

FUNDAMENTAL MECHANISMS FOR CO AND SOOT FORMATION

Robert J. Santoro
Department of Mechanical Engineering
Pennsylvania State University
University Park, PA 16802-2320

June 1994
Issued November 1994

Final Report

for

Fundamental Mechanisms for CO and Soot Formation

Grant 60NANBOD1035

Robert J. Santoro
Department of Mechanical Engineering
The Pennsylvania State University
University Park, PA 16802-2320

June, 1994

Table of Contents

Abstract

Studies investigating the oxidation of soot and carbon monoxide (CO) have been conducted in a series of laminar diffusion flames. Both overventilated and underventilated conditions have been examined. For the overventilated studies, the production and destruction of CO has been found to be influenced by the amount of soot present in the flame. Measurements of the hydroxyl radical (OH·) have demonstrated that soot can compete for OH· when undergoing oxidation and, thus, impede the oxidation of CO to CO_2. Absolute concentration measurements for OH· have shown that superequilibrium values of OH· are achieved in the upper region of these diffusion flames. In these situations, equilibrium estimates for OH· are in error, underestimating the OH· concentration significantly. However, as soot concentration increases to a point where soot is emitted from the flame, rapid reactions between soot particle and OH· result in concentration levels close to equilibrium values. These results clearly demonstrate that soot particles are far from passive species in flames and can directly affect the chemical pathways involved in the oxidation process through radiative effects on temperature and soot particle reactivity effects on radical concentrations.

The CO and smoke yields were observed for underventilated laminar diffusion flames burning methane and ethene for global equivalence ratio Φ over the range 0.5 to 4.0. A Burke-Schumann type burner with fuel in the center tube and air in the annular region was used. The peak CO yields for methane and ethene, 0.37 and 0.47 respectively, are at least a factor of 100 greater than for overventilated burning. The ratio of CO/CO_2 versus Φ for the methane flame is compared with local measurements of this ratio for both overventilated and underventilated laminar diffusion flames and with the results for turbulent natural gas flames quenched in an upper layer. The peak smoke yields for methane at a flow rate of 10 cm^3/s and for ethene at a fuel flow rate of 6.4 cm^3/s are 0.01 and 0.05, respectively, compared to yields of 0. and 0.028 for the overventilated case. The proportionality between smoke yield and CO yield observed for overventilated burning for a wide range of fuels is found not to be valid for the underventilated case. The chemical makeup and structure of the smoke produced at high equivalence ratio is qualitatively different from smoke produced under overventilated conditions; the smoke is mainly organic rather than graphitic and it has an agglutinated structure rather than an agglomerate structure with distinct primary spheres usually observed in overventilated burning.

1.0 Introduction

The occurrence and growth of a fire is characterized by a complex set of phenomena involving the interaction between combustion and fluid mechanical processes. Over the past decade an extensive effort has been undertaken to understand these basic processes and their relationship to the practical world of fire protection. With the major objective to limit the loss of life and property, an emphasis has been given to developing a better understanding of the manner in which fires propagate and the impact of the species produced in a fire. Through the incorporation of this understanding into suitable fire modeling efforts, systematic design and assessment tools have been developed and continue to evolve. Clearly improved performance of these modelling approaches relies on continued development of our understanding of the basic phenomena involved in fire situations. Although considerable progress has been made over the last decade, important questions remain to be addressed and resolved.

Recently, a major interest has emerged regarding the production of carbon monoxide in fires. Carbon monoxide is recognized as the most serious combustion product resulting from a fire. An understanding of its production and transport can greatly aid in improving victim survivability in fire situations. One focus of the present research effort was to understand the conditions and processes which control the emission of carbon monoxide from a fires. In particular, consideration was given to the effects that the presence of soot particles have on CO emission. Soot has long been recognized as a major hazardous product of fires because of its contribution to visual obscuration and post fire respiratory difficulties. The former effect impedes victim escape while the latter influences long term victim survival rates. Furthermore, soot particles through their radiative properties aid in energy transport, thus, enhancing fire spread rates. Through this active role in the fire process, soot particles affect the temperature and species concentration conditions present in fires and, consequently, can directly influence and formation and destruction of CO.

The present research program emphasized the study of the combustion processes that directly affect the emission of combustion products from fires. Consequently, the studies concentrated on the upper regions of diffusion flames where extensive fuel decomposition and soot growth have already occurred. A major objective of the work was to systematically

1

investigate the effects introduced by the presence of soot particles in varying concentrations on gas phase species produced in the flame. Of particular interest are the effects that soot particles exert on carbon monoxide emission from the flame.

The studies were conducted in a coannular laminar diffusion flame environment and combine both intrusive probe and laser diagnostic techniques. Conditions typical of both overventilated and underventilated flames were examined. Building on recent work in which well controlled amounts of soot are formed in diffusion flames, the present studies provide information on the sensitivity of CO formation to local temperature and equivalence ratio conditions. A novel feature of the research is the integrated and comprehensive nature of the studies regarding the evolution of the combustion processes.

Both stable products such as CO_2, CO and O_2 were measured using sampling probe techniques while an important radical species, OH·, was determined using laser induced fluorescence. These measurements provide a suitable basis from which to evaluate the dominant oxidation routes for CO and soot particles. Thus, the effects of soot particle concentrations on the mechanism controlling CO formation and destruction can be directly examined. Taken as a whole, these studies provide a comprehensive examination of the evolution of the soot particle and its effects on other property and species fields in fires.

2

2.0   The Oxidation of Soot and Carbon Monoxide in Hydrocarbon Flames for Over-ventilated Conditions.

A series of studies were conducted to examine the oxidation of soot and CO in coannular laminar diffusion flames. In particular, the importance of hydroxyl radicals in the oxidation of soot particles was examined as a function of soot particle volume fraction. Laser-induced fluorescence (LIF) was used to determine the OH radical concentrations for flames burning methane and ethene as well as fuel mixtures of methane/butane and methane/butene. The result of the studies will be briefly summarized here. More extensive descriptions are contained in references 1 and 2 which are included as appendices A and B.

Quantitative $OH \cdot$ concentrations have been measured in four coannular diffusion flames, burning methane at a single fuel flow rate and ethene at fuel flow rates which produce non-smoking, incipient smoking, and smoking conditions. Laser-induced fluorescence has been used to make point profile, line image, and two-dimensional image measurements. These data have been placed on an absolute basis by reference to earlier absorption results [3]. Particular emphasis has been placed on the investigation of the soot oxidation region in these laminar flames, since current soot models must utilize either assumed or estimated $OH \cdot$ concentrations. As the soot concentration increases, both the $OH \cdot$ concentrations and the flame temperature are found to decrease. Estimates of the superequilibrium levels of $OH \cdot$ increase as the measured concentration decrease, which makes accurate *a priori* prediction of $OH \cdot$ concentrations problematic in diffusion flames containing significant soot concentrations.

The total uncertainty in these measurements is estimated to be $\pm 50\%$, based upon errors associated with our calibration procedure, corrections for the laser beam intensity, and quenching rate considerations. These experimental results should both test and guide the development of soot production models which include oxidation processes. It is especially noteworthy in this regard that an equilibrium approach is not a reasonable starting point for estimating $OH \cdot$ concentrations in the region where soot oxidation rates are expected to be largest. Departures from equilibrium estimates increase with increasing soot concentrations, decreasing temperatures, and decreasing $OH \cdot$ concentrations.

Quantitative $OH \cdot$ concentrations and primary soot particle sizes have also been

determined in the soot oxidation regions of axisymmetric diffusion flames burning methane, methane/butane, and methane/1-butene in air at atmospheric pressure. The total carbon flow rate was held constant in these flames while the maximum amount of soot varied by a factor of seven along the centerline. Laser-induced fluorescence measurements of OH· were placed on an absolute basis by calibration against earlier absorption results [3]. The primary size measurements of the soot particles were made using thermophoretic sampling and transmission electron microscopy. OH· concentrations approach equilibrium values when the soot loading is high. The diminished OH· concentrations are found to arise from reactions with the soot particles and only to a minor degree from lower temperatures due to soot radiation losses. Analysis of the soot oxidation rates computed from the primary particle size profiles as a function of time along the flame centerlines shows that OH· is the dominant oxidizer of soot. Higher collision efficiencies of OH· reaction with soot particles are found for the flames containing larger soot concentrations at lower temperatures. A comparison of the soot and CO oxidation rates shows that although CO is inherently more reactive than soot, the soot successfully competes with CO for OH· and hence suppresses CO oxidation for large soot concentrations.

Measurements of the hydroxyl radical concentration and the size of the primary soot particles have also been made in a series of hydrocarbon/air diffusion flames containing varying amounts of soot. The observes OH· concentrations are suppressed in the presence of soot particles. A comparison of the fuel lean OH· concentrations in the presence and absence of soot particles reveals that the OH· concentration is reduced primarily due to reactions with soot rather than as a consequence of the lower flame temperatures measured for the higher soot loadings. The effect of lower temperatures on the OH· concentration is comparatively small, accounting for only 7% ± 4% of the measured decrease in the OH· concentration.

The soot oxidation rates computed from the primary particle size profiles as a function of time reveal interesting trends for the soot particle reactivity. Higher collision efficiencies are deduced for the flames containing larger soot concentrations at lower temperatures. The variation of the collision efficiency with temperature suggests that fewer active sites per unit surface area exist at higher temperatures.

A comparison of the soot and CO oxidation rates shows that although CO is inherently

more reactive than soot on a per carbon basis, for large soot concentrations the soot successfully competes with CO for OH· and hence suppresses CO oxidation.

3.0 Generation of CO and Smoke During Underventilated Combustion

While there has been extensive research on overventilated laminar diffusion flames in terms of smoking height, yield of smoke and combustion gases, and species concentrations in the flame itself, there has been relatively little research on underventilated laminar diffusion flames beyond the work of Burke and Schumann [4]. Studies recently have been conducted of inverse laminar diffusion flames [5,6] which represent a closely related flame configuration. In these studies the oxidizer flow is surrounded by the fuel flow; the reverse of the normal laminar diffusion flame arrangement. There have been several studies of the species produced by underventilated turbulent flames [7-14]. These include small scale studies of CO yield for slightly underventilated burning for solid fuels [7] and for propane and propylene [8]. In larger scale tests [9-14] with turbulent flames the overall ventilation is controlled by adjusting the height of the collection hood relative to the burner. The fuels studied include methane by Toner et al.[9,11], methane, ethene, and propylene by Morehart et al. [10,12] and a variety of hydrocarbons, alcohols, as well as several polymers by Beyler [13,14]. In these studies there is an abrupt increase in the CO concentration as the global equivalence ratio, Φ, defined as the fuel-to-air ratio normalized by the stoichiometric fuel-to-air ratio approaches a value of 1.0. This large increase in CO is of concern in regards to safety implications for fires in structures and continuing research is underway to characterize the CO production during underventilated burning in enclosures [15,16].

The focus of the present study was to provide a quantitative data base on the production of CO and smoke particulates from laminar underventilated diffusion flames à la Burke Schumann [4]. Advantages of the underventilated laminar diffusion flame system over previous studies [7-16] include a wider range of Φ up to at least 4, the ease in measuring Φ and the yields of CO and smoke, and the potential for theoretical analysis of the generation rates of the combustion products. We have chosen to study methane, which is the simplest hydrocarbon and ethene, which has a moderate tendency to smoke. Methane [17-20] and ethene [21-24] are among the most carefully studied fuels for laminar overventilated flames. There are also data [9-12] for CO concentration on turbulent underventilated flames for these gases. We are not aware of any quantitative study of smoke production during underventilated burning.

6

In the present study emphasis was given to the general trends observed for both CO and soot production in terms of the global equivalence ratio. The trends in the CO and soot yields in these underventilated laminar flame studies differ distinctively from results observed in overventilated diffusion flames. Additionally the very nature of the soot formed in these flames is different from that observed in the more widely studied overventilated conditions. Care is also taken to describe the conditions under which stable underventilated flames can be established and the procedure for systematically observing the effects of the equivalence ratio variations. Below the results of the underventilated flame studies are summarized. A detailed description of these studies is given in Appendix C, which contains a copy of Mr. S. Léonard's Master of Science Thesis.

The CO and smoke yields observed for underventilated laminar diffusion flames were studied for methane and ethene for global equivalence ratio Φ over the range 0.5 to 4.0. A Burke-Schumann type burner with fuel in the center tube and air in the annular region was used. The peak CO yields for methane and ethene, 0.37 and 0.47 respectively, are at least a factor of 100 greater than for overventilated burning. The ratio of CO/CO_2 versus Φ for the methane flame is compared with local measurements of this ratio for both overventilated and underventilated laminar diffusion flames and with the results for turbulent natural gas flames quenched in an upper layer. The peak smoke yields for methane at a flow rate of 10 cm^3/s and for ethene at a fuel flow rate of 6.4 cm^3/s are 0.01 and 0.05, respectively, compared to yields of 0. and 0.028 for the overventilated case. The proportionality between smoke yield and CO yield observed for overventilated burning for a wide range of fuels is found not to be valid for the underventilated case. The chemical makeup and structure of the smoke produced at high equivalence ratio is qualitatively different from smoke produced under overventilated conditions; the smoke is mainly organic rather than graphitic and it has an agglutinated structure rather than an agglomerate structure with distinct primary spheres usually observed in overventilated burning.

An investigation of the generation of CO and smoke for underventilated laminar diffusion flames, burning methane and ethene, has revealed both strong similarities and differences with studies considering turbulent overventilated conditions. In particular, the proportionality between smoke yield and CO yield observed for the post-flame (overfire) region of turbulent

7

overventilated flames for a wide range of fuels is not found to be valid for the underventilated laminar diffusion flame case. In fact, the soot observed in the underventilated flames is observed to vary considerably in terms of the chemical structure from that typically observed in overventilated flames. The highly organic nature of the soot implies that the structure of the soot may be more similar to early agglutinated soot particles recently observed in diffusion flames than to the more aged aggregates typical of the post-flame region for overventilated flames. Comparisons in terms of the ratio of CO and CO_2 as a function of global equivalence ratio in the post-flame region of the underventilated flames show a similar behavior to that previously observed for in-flame measurements for both overventilated and underventilated diffusion flames which examined the dependence of this ratio on local equivalence ratio conditions. This suggests that for the in-flame fuel-rich region, the chemical environment excluding soot is correlated with equivalence ratio in a similar way for both an overventilated flame and an underventilated flame. The low production of CO in the post-flame region of overventilated flames is simply a result of the oxidation of CO to CO_2 in the upper region of these flames. Finally, the present studies illustrate the utility of the study of underventilated flame environments where product yields and trends can be quite different from overventilated conditions. These studies should have significance for combustion phenomena in which underventilated conditions are typical, such as in fires.

References

1. Puri, R., Moser, M., Santoro, R.J. and Smyth, K.C., *Twenty-Fourth Symposium (International) on Combustion, The Combustion Institute*, 1992, Pittsburgh, PA, pp. 10015-1022.

2. Puri, R., Santoro, R.J. and Smyth, K.C., *Combustion and Flame*, 97:125-144 (1944).

3. Smyth, K.C., Tjossem, P.J.H., Hamins, A. and Miller, J.H., *Combustion and Flame*, 79:366-380 (1990).

4. Burke, S.P. and Schumann, T.E.W., *Industrial and Engineering Chemistry*, 20:998-1004 (1928).

5   Wu, K-T. and Essenhigh, R.H., *The Twentieth Symposium (International) on Combustion*, The Combustion Institute, Pittsburgh, 1984, pp. 1925-1932.

6. Sidebotham, G.W. and Glassman, I., *Combustion and Flame*, 90, pp. 269-283 (1992).

7. Tewarson, A. and Steciak, J., *Combustion and Flame*, 53: 123-134 (1983).

8. Tewarson, A., in *Society for Fire Protection Engineering Handbook*, pub. by National Fire Protection Assoc., Quincy, Mass., 1-179 to 1-199 (1988).

9. Toner, S.J., Zukoski E.E., and Kubota, T., National Bureau of Standards - Grant Contract Research Report 87-528, Gaithersburg, MD (1987)

10. Morehart, J.H., Zukoski, E.E., and Kubota, T., National Institute of Standards and Technology - Grants Contract Research Report 90-585, Gaithersburg, MD (1990).

11. Zukoski, E.E., Morehart, J.H., Kubota, T. and Toner, S.J., *Combustion and Flame*, 83:325-332 (1991).

12. Zukoski, E.E., Toner, S.J., Morehart, J.H., and Kubota, T., in *Proceedings of the Second Fire Safety Science International Symposium*, (T. Wakamatsu, Y. Hasemi, A. Sekizawa, P.G. Seeger, P.J. Pagni and C.E. Grant, Eds.), 1989, pp. 295-304.

13. Beyler, C.L., *Fire Safety Journal*, 10:47-56 (1986).

14. Beyler, C.L., in *Proceedings of the First Fire Safety Science International Symposium* (C. Gra . and P. Pagni, Eds.), Hemisphere, New York, 1986, pp.431-440.

15. Gottuk, D.T., Roby, R.J., Peatross, M.J. and Beyler, C.L., *J. of Fire Prot. Engr.*, 4:133-150 (1992).

16. Bryner, N. P., Johnsson, R.L., and Pitts, W.M., "Carbon Monoxide Production in Compartment Fires - Reduced Scale Test Facility," National Institute of Standards and Technology -Internal Report, Gaithersburg, MD, to appear.

17. Mitchell, R.E., Sarofim, A.F. and Clomburg, L.A., *Combustion and Flame*, 37:227-244 (1980).

18. Smyth, K.C., Miller, J.H., Dorfman, R.C., Mallard, W.G., and Santoro, R.J., *Combustion and Flame*, 62:157-181 (1985).

19. Garo, A., Lahaye, J., and Prado, G., *Twenty-First Symposium (International) on Combustion*, Combustion Institute, Pittsburgh, 1986, pp. 1023-1031.

20. Garo, A., Prado, G., and Lahaye, J., *Combustion and Flame*, 79:226-233 (1990).

21. Kent, J.H. and Wagner, H. Gg., *Combustion Science and Technology*, 41:245-269 (1984).

22. Santoro, R.J., Semerjian, H.G., and Dobbins, R.A., *Combustion and Flame*, 51:203-218 (1983).

23. Honnery, D.R. and Kent, J.H., *Combustion and Flame*, 82:426-434 (1990).

24. Santoro, R.J., Yeh, T.T., Horvath, J.J., and Semerjian, H.G., *Combustion Science and Technology*, 53:89-115 (1987).

Appendix A.   **Laser-Induced Fluorescence Measurements of OH·Concentrations in the Oxidation Region of Laminar, Hydrocarbon Flames**

by

R. Puri, M. Moser, R. J. Santoro and K. C. Smyth,
Twenty-Fourth Symposium (International) on Combustion,
1992, pp. 1015-1022.

LASER-INDUCED FLUORESCENCE MEASUREMENTS OF OH· CONCENTRATIONS IN THE OXIDATION REGION OF LAMINAR, HYDROCARBON DIFFUSION FLAMES

RAHUL PURI, MARLOW MOSER AND ROBERT J. SANTORO

Department of Mechanical Engineering
Pennsylvania State University
University Park, PA 16802 USA

AND

KERMIT C. SMYTH

Building and Fire Research Laboratory
National Institute of Standards and Technology
Gaithersburg, MD 20899 USA

Quantitative OH· concentrations have been measured in four coannular diffusion flames, burning methane at a single fuel flow rate and ethene at fuel flow rates which produce non-smoking, incipient smoking, and smoking conditions. Laser-induced fluorescence has been used to make point profile, line image, and two-dimensional image measurements. These data have been placed on an absolute basis by reference to earlier absorption results. Particular emphasis has been placed on the investigation of the soot oxidation region in these laminar flames, since current soot models must utilize either assumed or estimated OH· concentrations. As the soot concentration increases, both the OH· concentration and the flame temperature are found to decrease. Estimates of the superequilibrium levels of OH· increase as the measured concentrations decrease, which makes accurate *a priori* prediction of OH· concentrations problematic in diffusion flames containing significant soot concentrations.

Introduction

Recent laboratory studies of soot formation have focussed on a wide variety of important processes, including particle inception, surface growth, fuel concentration and temperature effects, and the properties and morphology of the soot particles. In parallel with these experimental efforts several groups have independently developed models of the formation and evolution of soot in hydrocarbon diffusion flames, in both laminar and turbulent environments.[1-7] However, relatively little attention has been paid to the soot oxidation step,[8-11] which is the key link between the soot produced within the flame and the smoke yield. Previous work has also shown that the emission of CO from diffusion flames is closely related to the observed soot concentrations,[12,13] with larger CO concentrations surviving as the soot concentration increases. Higher soot loadings can affect the level of CO survival by two distinct mechanisms: (1) The increased radiation of heat lowers the temperature, which can enhance CO emission by reducing the OH· concentration and thus the oxidation rate of CO; and (2) there exists a competition between CO and soot for OH·, since the hydroxyl radical is the key oxidizer for both CO[14] and soot[8,9] under many flame conditions.

Flame structure calculations of OH· concentrations in soot free regions of methane/air diffusion flames[15] are in excellent agreement with experimental measurements. However, when radiation losses from soot particles are included, predictions of the temperature field and the degree of radical superequilibrium are difficult to make. In a recent study of an atmospheric pressure laminar methane/air diffusion flame, Smyth *et al.*[16] found that their measured maximum OH· concentrations were greater than full equilibrium values and smaller than a partial equilibrium estimate (by more than a factor of two in each case). These findings are consistent with investigations of premixed flames.[17,18] In addition, the superequilibrium ratio of the experimental OH· concentration to full equilibrium estimates increased rapidly for both lean and rich flame conditions. In general, one expects that the superequilibrium OH· ratio will increase as the OH· concentration decreases.[19] This behavior has also been observed in turbulent hydrogen/air diffusion flames.[20]

The present work is intended to specifically establish how the OH· concentration varies as the soot volume fraction is changed, with particular emphasis on the soot oxidation region. These data are essential input for integrated soot formation models, since thus far the oxidation step for all of the proposed models rests upon calculated or assumed quantities. Quantitative measurements of the OH· concentration in sooting regions are also needed in order to understand the competition between soot particles and CO for OH·, which controls CO emissions.

In the current study, laser-induced fluorescence (LIF) measurements of OH· have been calibrated against earlier absorption data in order to obtain quantitative concentration profiles in laminar diffusion flames containing soot particles. Most of the earlier LIF measurements on OH· in hydrocarbon diffusion flames have been confined to regions where significant amounts of soot have not formed,[16,21,22] with only Garo et al.[10] reporting OH· concentrations in the presence of soot particles for a methane/air flame. Lucht et al.[23] have also made OH· concentration measurements in sooting premixed $CH_4/O_2/N_2$ flames.

Experimental Approach

Burner and Detection Configuration:

Laminar diffusion flames were established on a coannular burner,[24] which consists of a 1.11 cm diameter fuel tube surrounded by a 10.2 cm diameter air annulus. Methane and ethene fuels were studied at volumetric flow rates of 7.7 cm^3/s for methane and 3.85, 4.6 and 4.9 cm^3/s for ethene. The air flow rate for the methane flame and the 3.85 cm^3/s ethene flame was 1060 cm^3/s and was 1300 cm^3/s for the higher ethene flow rate flames. In the ethene flame having the lowest fuel flow rate, no soot is observed to survive the flame tip, while for the largest fuel flow rate soot emission from the flame is easily detected. For the intermediate ethene flow rate, the flame is quite close to the smoke point condition.[25] These flames are designated as non-smoking (NS), incipient smoking (IS), and smoking (S).

Figure 1 shows a schematic diagram of the experimental setup for the laser-induced fluorescence measurements. The output from a Nd:YAG pumped dye laser was frequency doubled to produce the UV beam, which was focussed into the flame. A pyroelectric joulemeter was used to monitor the beam intensity, and the fluorescence signal was collected at 90° with a cooled CCD camera. This camera incorporated a 18 mm microchannel plate image intensifier to provide gating and signal amplification before detection by the cooled CCD chip, which
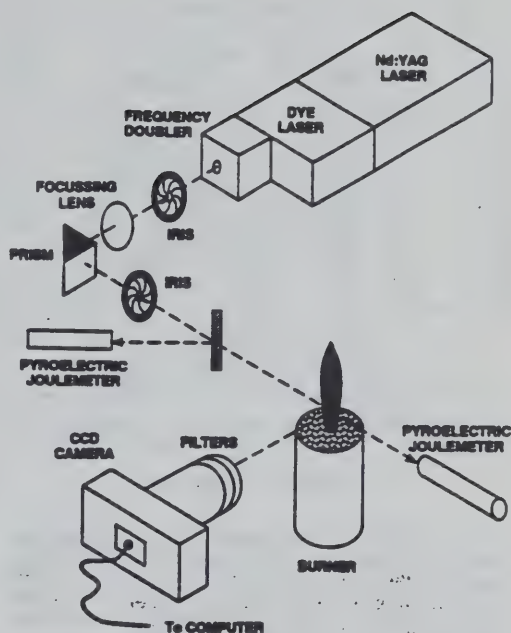

FIG. 1. Schematic diagram of the laser-induced fluorescence experimental setup.

had a 576 (row) × 384 (column) pixel format. The laser wavelength was tuned to either 278.83 nm or 283.55 nm, corresponding to the excitation of the $S_{21}(8)$ and $Q_1(8)$ lines of the $A^2\Sigma^+ \leftarrow X^2\Pi_i$ (1,0) band of OH·, respectively. Excitation from the $N'' = 8$ level was selected in order to minimize the Boltzmann population correction with temperature (less than 5% over the range 1400 to 2100 K). At elevated temperatures the variation of the quenching rate upon the initially excited rotational level ($N' = 8$ and $N' = 10$ for the transitions studied here) is expected to be less than 10%.[26] Low laser energies were utilized, and checks were made to ensure that the laser-induced fluorescence signals varied linearly with the laser intensity. Glass filters were placed in front of the CCD camera with 50% transmission cutoffs at 305 nm and 385 nm. These filters attenuated elastically scattered light from the soot particles and transmitted the (0,0) and (1,1) emission bands of OH·, as well as broadband laser-induced fluorescence attributed to polycyclic aromatic hydrocarbons (PAH).[27]

The experimental arrangement depicted in Fig. 1 was used to obtain 1D images with the laser tuned to the $S_{21}(8)$ line. The beam was focussed with a long focal length (1000 mm) lens to minimize the variation of the beam diameter (full width = 0.9 mm), and hence intensity, across the flame. For the 2D images this lens was replaced with a combination of three cylindrical lenses, giving a sheet 25 mm high with an estimated total thickness of 0.2
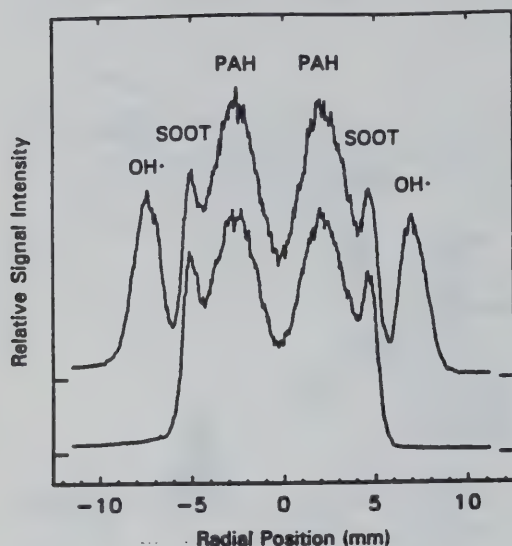
FIG. 2 (Top). On-resonance signal profile obtained by binning 22 pixel rows from a 1D image obtained in the axisymmetric ethene non-smoking flame at an axial location 7 mm from the exit of the fuel tube. The profile displays the signals due to three processes: OH· fluorescence (furthest from the centerline), light scattered by soot particles, and PAH fluorescence (closest to the centerline). The direction of laser beam propagation is left to right, and the laser wavelength is 278.83 nm, corresponding to the excitation of the weak S_{21} (8) line of OH· (see text).

(Bottom). Signal profile obtained from a 1D image with the laser wavelength tuned off the OH· excitation line.

mm. Since the light intensity was greatly reduced in the sheet, the 2D fluorescence images were obtained with the laser tuned to the much stronger Q_1(8) line of the (1,0) band of OH· (52 times larger stimulated Einstein coefficient than the S_{21}(8) line)[29]. The Q_1(8) line also provided improved OH· signals in regions where scattering from the soot particles was large. Corrections due to absorption of the incoming beam for the Q_1(8) transition (<1%) and trapping of the laser-induced fluorescence photons (<3%) were negligible.

Image Analysis:

The 1D and 2D images have been analyzed by binning the signals over a number of pixel rows (typically 22), corresponding to the region of interest. Figure 2 (Top) shows an example of a profile thus obtained from a 1D image of the ethene non-smoking flame. This profile exhibits the expected symmetry about the burner centerline and shows

three distinct features arising from OH· fluorescence in the primary reaction zone (furthest from the centerline), the attenuated light scattering from soot particles, and PAH fluorescence in rich flame regions (closest to the centerline). With the laser tuned off the OH· excitation line, the signal due to OH· fluorescence disappears (Fig. 2 Bottom). Since this off-resonance profile was obtained by changing the laser wavelength by only 0.03 nm, the difference in signals due to light scattering from soot particles (which has λ^{-4} dependence) and PAH fluorescence (which is broadband in nature) is undetectable for identical laser energies. Thus, subtraction of the off-resonance profile from the on-resonance profile gives the signal due to OH· fluorescence, even in the presence of soot particles.

Calibration of the Absolute OH· Concentration:

In addition to the 1D and 2D measurements, point profile data were obtained in the coannular burner as well as in a Wolfhard-Parker burner using methane as the fuel. These data provide the comparative basis from which to determine the absolute OH· concentrations in the coannular flames. The peak OH· concentration has been established in the Wolfhard-Parker methane flame from absorption measurements (1.76×10^{16}/cm³ for a temperature of 2032 K at a height of 7 mm above the burner surface[16]). Comparison of the OH· laser-induced fluorescence signals for the methane/air flames on the two burners gave agreement within 13%. The point and line profiles at various heights agreed within 7%.

In order to determine the OH· concentration in the ethene flames, information on the local quenching rate must be combined with the measured fluorescence signal. Smyth *et al.*[16] reported the contributions of the major stable species to the collisional quenching of excited state OH· in their CH_4/air diffusion flame. They found that H_2O and CO_2 were the main OH· quenchers at the location of the maximum OH· concentration and also established that the total quenching rate varied slowly (± 18%) over the entire region where OH· was detected. No detailed species profile data are available for the coannular flames studied here. If we assume that the quenching environment in the two flame geometries is identical (however, see below), then absolute OH· concentration profiles in the coannular flames are given by:

$$[OH·]_C = \frac{S_C \, [OH·]_{WP} \, T_{WP}^{0.5}}{S_{WP} \, T_C^{0.5}}.$$

Here the subscripts C and WP refer to the coannular and the Wolfhard-Parker burners, respectively, and S is the fluorescence signal normalized

by the incident laser intensity. An approximate correction to the overall quenching rate ($T^{-0.5}$) has been included in order to account for large temperature variations (1300 to 2100 K). Based upon the earlier study of methane/air flames on the Wolfhard-Parker burner,[16] this temperature correction may underestimate the OH· quenching rate in rich flame regions by as much as 20%. Radiation corrected temperatures were measured using a rapid insertion technique to minimize errors due to soot deposition;[29] the Pt/Pt-10% Rh thermocouple had an uncoated junction diameter of 0.32 mm. Since the quenching rate is proportional to $T^{-0.5}$, even a 100 K temperature error gives only a 3% error in the OH· concentration.

One additional correction has been included, since in fact the ethene flames have significantly different H_2O and CO_2 concentrations than the methane flame. Due to the lower H/C ratio of ethene, less H_2O and more CO_2 is present. The overall effect is an estimated 13% lower quenching rate in the ethene flame as compared to the methane flame, based on equilibrium predictions of H_2O, CO_2, CO, O_2 and N_2 concentrations over a local equivalence ratio range of $\phi = 0.6$ to 1.2 and $T = 1400$ to 2100 K. This lower quenching rate implies a $\approx 13\%$ higher LIF signal in the ethene flame than the methane flame for identical OH· concentrations.

Results and Discussion

OH· Profiles:

A series of OH· concentration profiles is presented in Fig. 3a for several axial positions in the 3.85 cm^3/s fuel flow rate ethene/air flame. At each position the off-resonance signal has been subtracted from the on-resonance signal in order to eliminate the soot and PAH contributions. The resulting relative intensity profile was then used in conjunction with the temperature measurements and the peak OH· concentration calibration to obtain the profiles shown. The shape of the OH· concentration profile, after the temperature correction for quenching, closely resembles that of the raw OH· fluorescence signal.

Figure 3a shows that the peak OH· concentration sharply decreases while the spatial extent of the profile increases with height in the flame. The peak OH· concentration occurs on the lean side of the temperature maximum. Data for the two lower heights were obtained from 1D images with the laser tuned to the $S_{21}(8)$ line. The central regions of these two profiles, which display larger noise contributions, are not presented. At higher axial locations the OH· concentrations were determined from the 2D images using the much stronger $Q_1(8)$ line due to the presence of the larger soot concentrations.

(a)

(b)
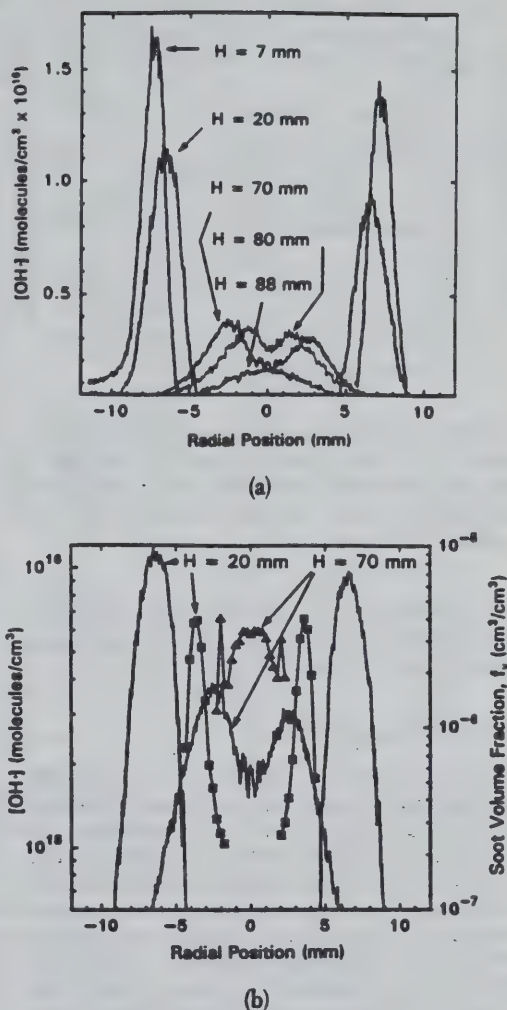
FIG. 3. (a) OH· concentration profiles in the axisymmetric non-smoking ethene/air flame at axial positions H = 7, 20, 70, 80 and 88 mm from the fuel tube exit. The asymmetry in the OH· concentration profiles is due to the attenuation of the laser light (propagating from left to right) by soot particles.

(b) OH· concentration and soot volume fraction, f_v, profiles (shown as lines and filled symbols, respectively) in the axisymmetric non-smoking ethene/air flame at axial positions of H = 20 and 70 mm from the fuel tube exit.

Figure 3b compares the soot volume fraction, f_v, and the OH· concentration measurements for the 20 mm and 70 mm axial locations. This figure shows the evolution of the OH· profiles with increasing height with respect to the soot particle field and demonstrates that OH· concentration
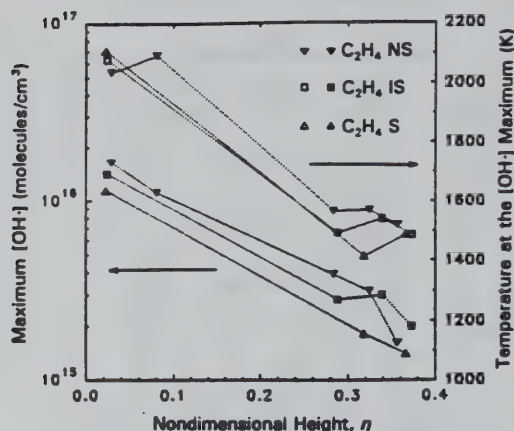
FIG. 4. Peak OH· concentration and the temperature, at the same spatial location, as a function of the nondimensional height (see text) in the ethene non-smoking (NS), incipient smoking (IS) and smoking (S) flames.

FIG. 5. OH· concentration and the temperature at the soot layer as a function of the nondimensional height (see text) in the ethene non-smoking (NS), incipient smoking (IS) and smoking (S) flames.

measurements can be obtained under similar soot volume fraction conditions in both the soot particle formation and oxidation regions.

Peak OH· Concentrations:

Figure 4 shows the variation in the peak OH· concentration at various nondimensional heights, η = H * D_{fuel, N_2}/Q, in the three ethene flames, as well as the measured temperature at the location of the maximum OH· concentration. Each axial location, H, was normalized using the diffusion coefficient of ethene in N_2 (0.156 cm^2/s), evaluated at 300 K, and the volumetric flow rate of ethene, Q. This variable is suitable for the spatial comparison of flames with different overall heights[24] (the visible flame heights were 88 mm for ethene non-smoking, and 110 mm for ethene incipient smoking). The dotted lines in Fig. 4 simply connect the data points for each flame.

Previous studies have established that the soot concentration in these ethene/air flames increases as the fuel flow rate is increased.[24,30] As the soot concentration increases, the maximum OH· concentration and the temperature decrease. The ethene smoking flame has lower peak OH· concentrations than the ethene non-smoking flame by up to a factor of 1.7. The peak OH· concentration in all of these flames drops by an order of magnitude over the flame height.

OH· Concentration at the Soot Layer:

For testing model predictions of soot oxidation rates it is important to examine the OH· concen-

trations at the high temperature, lean edge of the soot layer, where oxidation rates are expected to be highest. Figure 5 plots the OH· concentration and the temperature at the location where the signal due to light scattered by soot particles sharply increases (see Fig. 2 Bottom) in the three ethene flames. Both the OH· concentrations and the temperatures at the soot layer decrease with increasing soot concentration. The ethene smoking flame exhibits a lower OH· concentration at the soot layer than the ethene non-smoking flame by a factor of 1.5 to 2.0.

For the methane/air flame the peak OH· concentration and the results at the edge of the soot layer have not been included in Figs. 4 and 5 for the sake of clarity. The data are tabulated in Table I and show a much smaller variation with axial location. The OH· concentration at the soot layer in the methane flame actually increases slightly with flame height in the soot oxidation region.

Comparison with Equilibrium Predictions:

The present experimental results can be compared to equilibrium[31] predictions by combining our temperature data with an estimate of the local flame stoichiometry. At the location of the peak OH· concentration, analysis of the Wolfhard-Parker results for the methane/air flame gives a value of ϕ = 0.85 at a height of 9 mm. For the OH· concentration at the soot layer a value of ϕ = 0.925 was taken, based on observations in the oxidation regions of axisymmetric flames burning mixtures of methane/butane and methane/1-butene.[12,32] Table I compares the equilibrium concentrations of OH·, calculated at the

TABLE I

Comparison of the peak OH· concentration (molecules/cm^3 × 10^{15}) and the OH· concentration at the soot layer with equilibrium predictions as a function of the height (H) above the burner in the Methane/Air, Non-Smoking Ethene/Air (NS), Incipient Smoking Ethene/Air (IS), and the Smoking Ethene/Air (S) flames.

| Flame | H (mm) | η | Peak [OH·] | | | | Soot Layer [OH·] | | | |
			Temp (K)	[OH·] Expt	[OH·] Equil	Ex/Eq	Temp (K)	[OH·] Expt	[OH·] Equil	Ex/Eq
Methane	7	0.017	2011	15.9	6.16	2.58	1982	13.20	4.73	2.79
	30	0.073	2048	13.5	7.19	1.88	1943	2.81	3.93	0.72
	50	0.122	1955	6.67	4.80	1.39	1981	3.24	4.73	0.68
	70	0.171	1848	6.18	2.86	2.16	1926	4.71	3.66	1.29
Ethene NS	7	0.028	2037	16.4	5.73	2.86	2024	4.49	4.76	0.94
	20	0.081	2093	11.0	7.20	1.53	2031	3.13	4.90	0.64
	70	0.284	1563	3.84	0.41	9.37	1571	3.76	0.38	9.89
	80	0.324	1568	3.12	0.43	7.26	1566	3.07	0.37	8.30
	88	0.357	1510	1.61	0.28	5.75	—	—	—	—
Ethene IS	7	0.024	2079	14.1	6.81	2.07	2010	4.35	4.48	0.97
	85	0.288	1490	2.79	0.23	12.1	1499	2.52	0.22	11.5
	100	0.339	1540	2.98	0.35	8.51	1462	2.29	0.16	14.3
	110	0.373	1485	2.00	0.23	8.70	—	—	—	—
Ethene S	7	0.022	2109	11.4	7.66	1.49	2015	3.63	4.58	0.79
	100	0.318	1413	1.81	0.12	15.1	1413	1.81	0.11	16.5
	115	0.366	1486	1.40	0.23	6.09	1382	1.26	0.08	15.8

measured temperatures and these stoichiometries, with the experimental peak concentrations and the OH· concentrations at the soot layer for the four flames studied. The equilibrium predictions are much lower than the measurements for the ethene flames and show a greater variation over the flame height.

Table I also presents the ratio of the experimental values to the equilibrium concentrations of OH·. In the methane flame the OH· superequilibrium ratio is close to a factor of two, which is in good agreement with the observations made in the Wolfhard-Parker burner.[16] The ethene flames, which have much more soot than the methane flame, show a greater departure from equilibrium. As the soot concentration increases, the overshoot of the measured OH· concentration above equilibrium values increases. These results show that equilibrium estimates of OH· concentration are not accurate in hydrocarbon diffusion flames containing significant soot concentrations, even with a knowledge of the local flame temperature and the stoichiometry.

In the absence of detailed species profiles for the coannular flames the degree of superequilibrium OH· levels is difficult to quantify, since [OH·]$_{Equil}$ is a strong function of the local stoichiometry and the temperature. Equilibrium calculations were run at various temperatures and values of ϕ to examine this sensitivity. For a given temperature, the peak [OH·]$_{Equil}$ occurs close to $\phi = 0.65$ for both methane and ethene flames. At $\phi = 0.85$, a 100 K temperature error at 1450 K changes [OH·]$_{Equil}$ by a factor of 2.4 and at 2050 K by 1.6. This sensitivity to temperature increases monotonically with increasing ϕ. The functional dependence of [OH·]$_{Equil}$ on ϕ is more complex. While a ±0.05 error in ϕ at $\phi = 0.85$ and $T = 2050$ K changes [OH·]$_{Equil}$ by only ±7%, a similar uncertainty at $\phi = 1.00$ results in a 2.6 fold range in [OH·]$_{Equil}$. However, the sensitivity to ϕ quickly decreases to ±25% for $\phi = 1.15$.

The upshot of these considerations is that the largest uncertainty in the degree of superequilibrium at the location of the peak OH· concentration is due to possible errors in the temperature measurements, which are judged to be accurate to better than ±10%. The superequilibrium ratios at the peak OH· concentrations are estimated to be accurate to a factor of about two. However, the degree of superequilibrium for the OH· concentration at the edge of the soot layer is far more difficult to establish. Soot formation is confined to a narrow fuel rich region at the lower heights of hydrocarbon diffusion flames. As the soot particles are convected upward, diffusion continually changes the local stoichiometry at the soot layer. In the oxidation region the soot particles must pass from rich to lean flame

conditions. If the stoichiometry at the soot layer in the ethene flames is richer than the estimated value of $\phi = 0.925$, considerably larger superequilibrium values than given in Table I can be expected.

Concluding Remarks

Quantitative OH· concentrations have been made in a series of methane and ethene diffusion flames, with particular emphasis upon the soot oxidation regions. The total uncertainty in these measurements is estimated to be ±50%, based upon errors associated with our calibration procedure, corrections for the laser beam intensity, and quenching rate considerations. These experimental results should both test and guide the development of soot production models which include oxidation processes. It is especially noteworthy in this regard that an equilibrium approach is not a reasonable starting point for estimating OH· concentrations in the region where soot oxidation rates are expected to be largest. Departures from equilibrium estimates increase with increasing soot concentrations, decreasing temperatures, and decreasing OH· concentrations.

Future work will evaluate the competition between CO and soot particles for OH·, by combining the present results on OH· concentrations with measurements of the disappearance rates for CO and soot. In addition, measurements of O_2 concentrations will allow us to quantify the relative contribution to soot oxidation by OH· and O_2.

Acknowledgement

REFERENCES

1. Moss, J. B., Stewart, C. D. and Syed, K. J.: Twenty-Second Symposium (International) on Combustion, p. 413, The Combustion Institute, 1989.
2. Kennedy, I. M., Kollmann, W. and Chen, J.-Y.: Combust. Flame 81, 73 (1990).
3. Kennedy, I., Kollmann, W. and Chen, Y.: AIAA Paper #90-0459 (1990).
4. Syed, K. J., Stewart, C. D. and Moss, J. B.: Twenty-Third Symposium (International). on Combustion, p. 1533, The Combustion Institute, 1991.
5. Stewart, C. D., Syed, K. J. and Moss, J. B.: Combust. Sci. Tech. 75, 211 (1991).
6. Leung, K. M., Lindstedt, R. P. and Jones, W. P.: Combust. Flame 87, 289 (1991).
7. Metternich, M., Kollmann, W. and Kennedy, I. M.: Pdf Prediction of Sooting Turbulent Flames, submitted to AIAA Aerospace Sciences Meeting in Reno, 1991.
8. Neoh, K. G., Howard, J. B. and Sarofim, A. F.: in, *Particulate Carbon Formation During Combustion*, Siegla, D. C., and Smith, G. W. (editors) Plenum, New York, p. 261, 1981.
9. Neoh, K. G., Howard, J. B. and Sarofim, A. F.: Twentieth Symposium (International) on Combustion, p. 951, The Combustion Institute, 1985.
10. Garo, A., Prado, G. and Lahaye, J.: Combust. Flame 79, 226 (1990).
11. Dixon-Lewis, G., Bradley, D. and El-Din Habik, S.: Combust. Flame 86, 12 (1991).
12. Puri, R. and Santoro, R. J.: Fire Safety Science— Proc. of the Third International Symposium, p. 595 (1991).
13. Köylü, Ü. Ö., Sivathanu, Y. R. and Faeth, G. M.: Fire Safety Science—Proc. of the Third International Symposium, p. 625 (1991).
14. Fristrom, R. M. and Westenberg, A. A.: *Flame Structure*, McGraw Hill, New York, 1965.
15. Norton, T. S., Smyth, K. C., Miller, J. H. and Smooke, M. D.: Comparison of Experimental and Computed Species Concentration and Temperature Profiles in Laminar, Two-Dimensional Methane/Air Diffusion Flames, submitted to Combust. Sci. Tech.
16. Smyth, K. C., Tjossem, P. J. H., Hamins, A. and Miller, J. H.: Combust. Flame 79, 366 (1990).
17. Biordi, J. C., Lazzara, C. P. and Papp, J. F.: Sixteenth Symposium (International) on Combustion, p. 1097, The Combustion Institute, 1977.
18. Bittner, J. D.: A Molecular Beam Mass Spectrometer Study of Fuel-Rich and Sooting Benzene-Oxygen Flames, D. Sc. Dissertation, Massachusetts Institute of Technology, 1981.
19. Kaskan, W. E.: Combust. Flame 2, 229 (1958).
20. Barlow, R. S., Dibble, R. W., Chen, J.-Y. and Lucht, R. P.: Combust. Flame 82, 235 (1990).
21. Wolfhard, H. G. and Parker, W. G.: Proc. Phys. Soc. (London) A 65, 2 (1952).
22. Stepowski, D. and Garo, A.: Applied Optics 24, 2478 (1985).
23. Lucht, R. P., Sweeney, D. W. and Laurendeau, N. M.: Combust. Sci. and Tech. 42, 259 (1985).

24. SANTORO, R. J., SEMERJIAN, H. G. AND DOBBINS, R. A.: Combust. Flame, 51, 203 (1983).

25. SCHUG, P., MANHEIMER-TIMNAT, Y., YACCARINO, P. AND GLASSMAN, I.: Combust. Sci. Tech., 22, 235 (1980).

26. KOHSE-HÖINGHAUS, K., JEFFRIES, J. B., COPELAND, R. A., SMITH, G. P. AND CROSLEY, D. R.: Twenty-Second Symposium (International) on Combustion, p. 1857, The Combustion Institute, 1989.

27. SMYTH, K. C., MILLER, J. H., DORFMAN, R. C., MALLARD, W. G. AND SANTORO, R. J.: Combust. Flame 62, 157 (1985).

28. DIMPFL, W. L. AND KINSEY, J. L.: J. Quant. Spectrosc. Radiat. Transfer 21, 233 (1979).

29. KENT, J. H. AND WAGNER, H. Gg.: Combust. Sci. Tech., 41, 245 (1984).

30. SANTORO, R. J., YEH, T. T., HORVATH, J. J. AND SEMERJIAN, H. G.: Combust. Sci. Tech. 53, 89 (1987).

31. GORDON, S. AND McBRIDE, B. J.: Computer Program for Calculation of Complex Chemical Equilibrium Compositions, Rocket Performance, Incident and Reflected Shocks, and Chapman-Jouguet Detonations, NASA SP-273 Interim Revision N78-17724, March 1976.

32. PURI, R. AND SANTORO, R. J.: Unpublished data.

COMMENTS

Marcus Alden, Lund Institute of Technology, Sweden. Are the asymmetric OH density profiles shown caused by laser absorption by OH? If yes, can this be used for in-situ calibration?

Author's Reply. The profiles shown in Figs. 2 and 3 reveal attenuation of the laser beam, which propagates from left to right. This attenuation is caused primarily by scattering and absorption due to soot particles and not by OH· absorption, which is estimated to be < 1.5% across the entire flame for the optical transitions used in our experiments. Therefore, an in-situ calibration of the OH· concentration cannot be made from these measurements.

Appendix B.   The Oxidation of Soot and Carbon Monoxide in Hydrocarbon Diffusion Flames

by

R. Puri, R. J. Santoro, and K. C. Smyth, Combustion and Flame, 97:125-144 (1994).

The Oxidation of Soot and Carbon Monoxide in Hydrocarbon Diffusion Flames

RAHUL PURI* and **ROBERT J. SANTORO**

Department of Mechanical Engineering, The Pennsylvania State University, University Park, PA 16802

and

KERMIT C. SMYTH

Building and Fire Research Laboratory, National Institute of Standards and Technology, Gaithersburg, MD 20899

Quantitative OH · concentrations and primary soot particle sizes have been determined in the soot oxidation regions of axisymmetric diffusion flames burning methane, methane/butane, and methane/1-butene in air at atmospheric pressure. The total carbon flow rate was held constant in these flames while the maximum amount of soot varied by a factor of seven along the centerline. Laser-induced fluorescence measurements of OH · were placed on an absolute basis by calibration against earlier absorption results. The primary size measurements of the soot particles were made using thermophoretic sampling and transmission electron microscopy. OH · concentrations are greatly reduced in the presence of soot particles. Whereas large super-equilibrium ratios are observed in the high-temperature reaction zones in the absence of soot, the OH · concentrations approach equilibrium values when the soot loading is high. The diminished OH · concentrations are found to arise from reactions with the soot particles and only to a minor degree from lower temperatures due to soot radiation losses. Analysis of the soot oxidation rates computed from the primary particle size profiles as a function of time along the flame centerlines shows that OH · is the dominant oxidizer of soot, with O_2 making only a small contribution. Higher collision efficiencies of OH · reactions with soot particles are found for the flames containing larger soot concentrations at lower temperatures. A comparison of the soot and CO oxidation rates shows that although CO is inherently more reactive than soot, the soot successfully competes with CO for OH · and hence suppresses CO oxidation for large soot concentrations.

I. INTRODUCTION

In recent years increasing attention has been devoted to oxidation processes in hydrocarbon diffusion flames due to their key role in the production of combustion-generated pollutants. Not only does the soot oxidation step determine the amount of smoke that will be emitted from a flame, but it also strongly influences the quantity of carbon monoxide (CO) that will survive a given combustion process [1]. Emissions of both CO and soot particles present significant fire hazards, indicate poor combustion efficiency, and are objectionable from an environmental standpoint.

Prior to the work of Fenimore and Jones [2] that elucidated the importance of OH · radi-cals, soot oxidation rates were calculated using the expression determined by Nagle and Strickland-Constable (NSC) for pyrographite oxidation [3] by assuming that molecular oxygen alone was responsible. Neoh et al. [4] also showed that OH · is the primary oxidant of soot in the main reaction zone of premixed flames and that the contribution of molecular oxygen is significant only when the oxygen mole fraction is greater than 5%. The recent study of Dixon-Lewis et al. [5] has reopened the question of whether OH · or O_2 is the primary oxidant of soot in premixed flames. They proposed a catalytic mechanism in which H atoms react with O_2 at or close to the soot surface to produce either OH · radicals or O atoms, which then more efficiently attack soot.

Soot oxidation studies have often assumed that soot particles are spherical and have used laser light scattering and extinction measurements to obtain information on their size [6].

---

* Current address: Allison Engine Company, P. O. Box 420, Speed Code T-14, Indianapolis, IN 46206-0420.

In reality, the soot particles are agglomerates of a variable number of smaller, uniformly sized, approximately spherical "primary" particles [7]. Therefore, the assumption of spherical particles can result in a significant error in the estimation of the particle surface area and thus the oxidation rate. With the incorporation of fractal concepts, it is now possible to obtain a reasonable estimate of the surface area of agglomerated soot particles [8].

Despite these advances in characterizing the soot particle surface area, complexities exist in determining the fraction of the surface area that participates in reactions, that is, the number of active sites. Although the concept of reactions at active sites is relatively new in the area of soot surface growth, it was proposed over 30 years ago to explain the heterogeneous reactions of various gases with carbon [9]. In fact the NSC expression is based on a concept similar to the active sites approach. Howard [10] has recently suggested an active site description involving radicals for soot oxidation by $OH \cdot$. His reevaluation of previous data [4] shows an interesting correlation between the H/C ratio in the soot and the measured collision efficiency of soot with $OH \cdot$.

Not much is known about the nature and origin of active sites for either soot growth or oxidation processes. Tesner [11] argues that active sites are formed when reactive species collide with the incipient particle surface. Once formed, these sites are thought to be self-renewing [12] and are not affected by coagulation, surface growth, or gas-phase chemistry [13]. It is not known whether the same active sites that participate in the surface growth reactions following soot inception also play a role in oxidation processes. Recent x-ray photoelectron spectroscopy investigations [14, 15] have shown adsorbed as well as chemically bound oxygen to be present on soot particles.. It has been suggested that the active sites include surface-adsorbed oxygenated complexes that are responsible for the catalytic reactivity of the carbon particles [15].

Our understanding of soot oxidation in terms of both the reactive area as well as the primary oxidant is still not complete. In the present investigation concentration profiles of the hydroxyl radical have been obtained in the soot oxidation regions of laminar, hydrocarbon diffusion flames using laser-induced fluorescence. The data have been placed on a quantitative basis by calibrating [16] against an earlier absorption measurement. Soot primary particle size measurements have also been made using a thermophoretic sampling procedure [7] followed by transmission electron microscopy (TEM). The time evolution of the primary particle profiles is used in conjunction with results of a fractal aggregate analysis to calculate soot oxidation rates. Specific attention is devoted here to the factors that control the $OH \cdot$ concentrations in the soot oxidation region.

II. EXPERIMENTAL APPROACH

A coannular burner consisting of a 1.1-cm-diameter fuel tube and a concentric 10.2-cm-diameter air annulus [17] was used to establish the laminar diffusion flames. CP grade purity (99%) fuels were used in these studies, while an in-house compressor was employed to supply the air. The air and fuel flows to the burners were metered with rotameters, which were arranged to allow mixing of two fuels. A fuel mixture approach was adopted in order to vary the soot concentration while keeping the total carbon flow rate constant, which ensured similar flame sizes and shapes. Flames burning methane (9.8 cm^3/s) and methane (5.6 cm^3/s) doped with either butane (1.05 cm^3/s) or 1-butene (1.05 cm^3/s) were studied. The air flow rate was maintained at 1300 cm^3/s for all flames.

A. OH · Concentration Measurement

Figure 1 presents a schematic diagram of the laser-induced fluorescence measurement setup. The UV beam was produced by frequency doubling the output of a Nd:YAG pumped dye laser. The wavelength was tuned to 283.55 nm, which corresponds to the excitation of the $Q_1(8)$ line of the $A^2\Sigma^+ \leftarrow X^2\Pi_i$ (1, 0) band of $OH \cdot$. Excitation from the $N'' = 8$ level minimizes the Boltzmann population correction with temperature (less than 5% over the temperature range 1400–2100 K). Since the pulse energy was high enough (~ 1 mJ/pulse) to easily saturate this strong transition. only the reflected
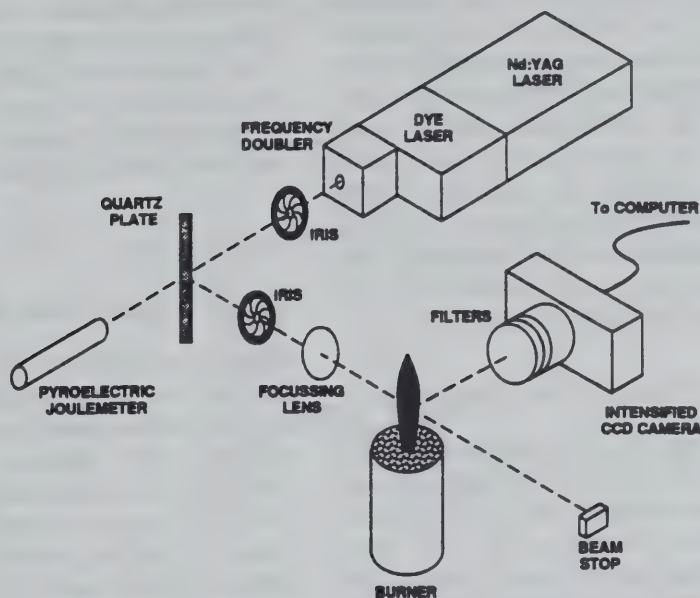
Fig. 1. Schematic diagram of the laser-induced fluorescence experimental setup.

beam from the first surface of a thick piece of quartz (~ 0.03 mJ/pulse) was passed through the flame. This procedure ensured that the laser-induced fluorescence signals were linear with the laser energy. A pyroelectric joulemeter was placed behind the quartz plate to monitor the laser energy for each pulse. The fluorescence signal was collected at 90° with a cooled CCD (charge coupled device) camera equipped with a microchannel plate image intensifier. Glass filters placed in front of the camera attenuated elastically scattered light from the soot particles and transmitted the (0, 0) and (1, 1) emission bands of OH·, as well as the broadband fluorescence which has been attributed to polycyclic aromatic hydrocarbons [18].

The details of the experimental procedure have been described elsewhere [16] and are only briefly outlined here. At each measurement location two one-dimensional images were obtained with the laser wavelength tuned on and off the $Q_1(8)$ excitation line of OH·. Relative intensity radial profiles were obtained from these images by binning data over several pixel rows in the region of interest. While the on-resonance profiles show signals due to OH· fluorescence, light scattered by soot particles, and PAH fluorescence. the off-resonance profiles exhibit only the latter two contributions.

Since the off-resonance images were obtained by tuning the laser wavelength by only 0.03 nm, the signals due to light scattered by soot particles and broadband PAH fluorescence were unchanged. Thus, subtracting the off-resonance profile from the on-resonance profile gives the raw OH· signal even in regions where there are significant amounts of soot.

The relative intensity of the OH· signal was calibrated using an earlier absorption measurement in a methane/air diffusion flame on a Wolfhard-Parker burner [19]. Detailed measurements of the major species have been obtained along the centerline for the axisymmetric flames studied here [1], and these allow a complete quenching correction to be made [19–21]. For the radial OH· profiles only an approximate correction for the overall quenching rate (proportional to $1/\sqrt{T}$) was applied [16], since radial species profile data are not available in these flames. An additional correction must be made for determining the OH· concentrations along the centerline in order to account for the attenuation of the laser beam intensity by soot particles (absorption by OH· is less than 1% [16]). This attenuation leads to asymmetric fluorescence profiles. with the asymmetry being greatest for the methane/1-butene flame which contains the largest soot concentrations. The OH· signal profiles have

23

been corrected using local extinction measurements of the soot particle field in identical flames [22]. Extinction values depend upon the wavelength of light being used and the refractive index of the soot particles at that wavelength. Since the latter quantity has not be obtained with certainty, the extinction profile measurements [22] were scaled such that symmetric OH · fluorescence profiles resulted. The intensity of the laser beam could then be derived at each radial flame location.

B. Soot Primary Particle Size Measurements

A thermophoretic sampling technique similar to that used by Dobbins and Megaridis [7] was employed to measure the size of the primary soot particles. The thermophoretic probe consisted of a carbon-coated 200-mesh copper grid held in place between two strips of sheet metal, machined to expose the grid to the flame. The probe was rapidly inserted into the flame environment (~ 3.3 m/s) for a brief exposure duration of 50 ms before being quickly withdrawn. This exposure time is short enough to provide a cold surface to collect soot particles by thermophoresis as well as to quench any heterogeneous reactions on the captured particles [7]. The rapid insertion and retraction motion was made possible by mounting the probe on the displacement rod of a double acting pneumatic cylinder. The direction reversal of this cylinder was achieved by supplying the driving air (at 40 psi) through a three-way solenoid valve controlled with a variable time-delay relay circuit.

Transmission electron microscopy (TEM) was used to examine the grids, and micrographs were obtained at a magnification of 60,000. These micrographs were then imaged with a CID (charge injection device) camera that provided an additional, approximately tenfold magnification. The CID camera software was utilized to measure the primary particle size, d_p, by locating the measurement cursor at diametrically opposite sides of each spherical primary particle and noting the coordinates. A minimum of 75 d_p measurements were made at each flame location. An image of engineering graph paper was also obtained to provide an absolute length calibration for the CID camera magnification. Finally, the primary particle sizes were obtained by accounting for the TEM magnification. The camera images had a pixel resolution varying from 0.6 nm for the methane flame images to 1.0 nm for the methane/1-butene flame images.

III. RESULTS

A. OH · Concentration Measurements

Figure 2 presents the OH · concentration profiles in the 9.8-cm^3/s methane/air diffusion flame at several axial locations above the fuel tube exit. The methane flame has a visible height of 10.7 cm, corresponding to the location where soot particles are completely oxidized. Therefore, the OH · concentration profiles at 10.2 and 11.4 cm correspond to locations immediately below and above the visible flame tip, respectively. It is interesting that the profile at 10.2 cm shows two OH · maxima and a valley in the region where the soot particles are being oxidized. In contrast, diffusion processes at this height result in maxima along the centerline for all fuel-derived major species (such as CO_2, CO, and H_2O) as well as for the temperature. Once the soot particles are completely oxidized, the OH · concentration profile shows a single peak along the flame centerline at an axial position of 11.4 cm.

Figure 3 presents the OH · concentration results in the methane/butane flame. As in the methane flame, the OH · profiles show evidence of OH · consumption close to the flame tip. In the methane/butane flame the profiles at 11.4 and 12.7 cm correspond to locations immediately below and above the visible flame tip at 11.7 cm. Although diffusion processes result in a single maximum at the centerline for the temperature and the fuel-derived major species, the OH · concentration profile again exhibits two maxima at the axial location of 11.4 cm. Above the visible flame tip where there are no soot particles, the OH · profile shows a single peak along the centerline.

Figure 4 presents the OH · concentration results in the methane/1-butene flame. The methane/1-butene flame does not have a visi-

Fig. 2. OH· concentration profiles in the pure methane diffusion flame at axial positions of 7.6, 8.9, 10.2, 11.4, and 12.7 cm from the fuel tube exit.

ble flame tip, since it emits smoke. In this respect the lack of buildup of OH· along the centerline of this flame suggests that reactions between OH· and soot particles strongly reduce the OH· concentrations.

B. Soot Primary Particle Size Measurements

Figure 5 presents the volume mean diameter, d_{p30}, as a function of time along the centerline of the methane, methane/butane, and methane/1-butene flames. The values of d_{p30} were determined from the d_p measurements by taking the cube root of the averaged value of d_p^3. Also shown in Fig. 5 are the soot volume fraction measurements, f_v [22]. Velocity data obtained from laser velocimetry measurements in identical flames [22] were used to convert the axial positions to time. The primary particle size in the methane and the methane/butane flames decreases rapidly and shows a convex upwards shape, consistent with particle burnout. In contrast, the methane/1-

butene flame shows a concave upward shape, and the particle sizes approach a constant value. This behavior is consistent with smoking conditions.

The soot volume fraction measurements shown in Fig. 5 are related to the volume mean diameter through the number concentration of the primary particles N_p:

$$f_v = \frac{\pi}{6} d_{p30}^3 N_p. \tag{1}$$

In the present analysis N_p is assumed to be constant along the flame centerline. This assumption is based on (1) the results of a fractal aggregate analysis [8] applied to a laminar ethene/air diffusion flame along a nearly isothermal streamline passing through the location of the maximum soot volume fraction [23], (2) the small temperature variation (less than 250 K) observed in the soot oxidation region of the flames studied here, and (3) the narrow size distribution of the primary particle size at each measurement location.
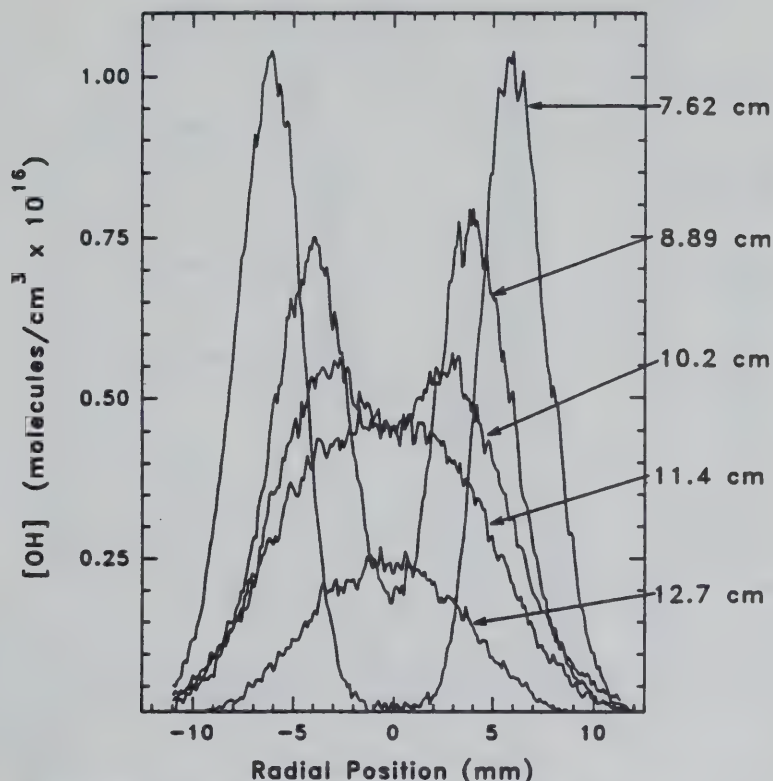
25

Fig. 3. OH · concentration profiles in the methane/butane diffusion flame at axial positions of 7.6, 8.9, 10.2, 11.4, and 12.7 cm from the fuel tube exit.

Assuming that there is no slip between the particles and the hot combustion gases, a ±125 K temperature variation at 1500 K will cause the number concentration of primary particles to change by less than ±10% (as determined from the temperatures and the ideal gas law). The radial temperature profiles in the oxidation region of the flames studied exhibit temperature gradients less than 66 K/mm near the centerline. An effective upper limit of the lateral thermophoretic displacement of soot particles, as they traverse the region studied, is estimated to be only 0.08 mm. Due to their large mass, transport of soot particles by diffusion is negligible.

The size distribution of the primary particles at each measurement location in this study is narrow (±18%), suggesting that each primary particle at a given location in the flame grows and oxidizes at roughly the same rate. Therefore, the assumption of a constant primary particle number concentration N_p should hold for our conditions.

Data in the methane/butane flame support the relative constancy of N_p, which has also been reported by others along convective streamlines in premixed propane/oxygen [24] and ethene/air laminar diffusion [25] flames. In the methane flame there are insufficient soot volume fraction data for a similar check. For this flame the soot volume fraction, f_v, and the d_{p30} results overlap in time only near 0.115 s (Fig. 5). Here the shape of the profiles, i.e., the small rate of change with respect to time, suggests that both f_v and d_{p30} are close to their maximum values along the centerline. For the methane/1-butene flame the measurements indicate a significant increase in N_p, particularly at earlier times where the soot volume fraction increases. whereas the primary particle size decreases. However, this may be an artifact of the thermophoretic sampling procedure because the annular soot volume fraction in the methane/1-butene flame is more than a factor of two higher than the centerline values at the earlier times examined
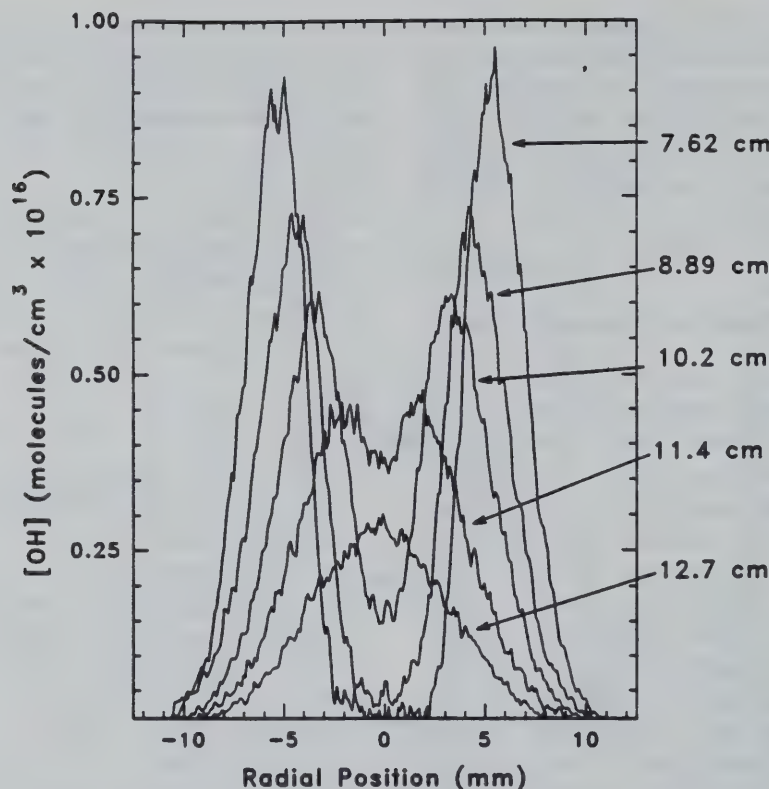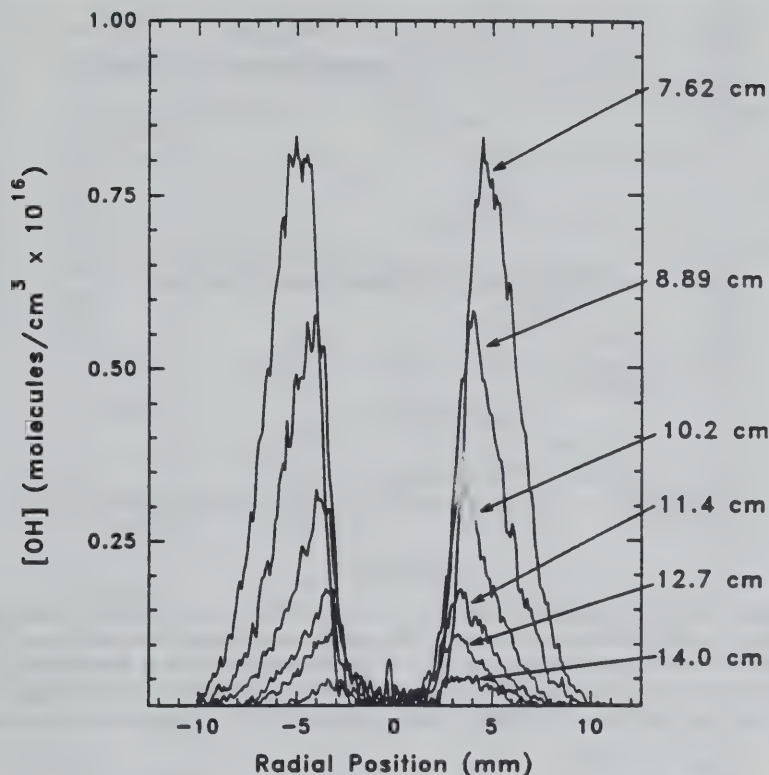
Fig. 4. OH · concentration profiles in the methane/1-butene diffusion flame at axial positions of 7.6, 8.9, 10.2, 11.4, 12.7, and 14.0 cm from the fuel tube exit.

in the soot oxidation region. Thus, the centerline TEM samples may have been contaminated with soot particles from the annular region which contains larger primary particles. Of the flames studied here such a situation occurs in the oxidation region only for the methane/1-butene flame. In the methane and methane/butane flames, the soot volume fraction peaks at the centerline for the axial positions examined in the oxidation region. At radial locations corresponding to the rapidly oxidizing annular soot region, the soot volume fraction is lower than the centerline values by up to a factor of seven. This discussion is relevant when considering the collision efficiency of OH · with soot (see section IV.D).

IV. DISCUSSION

The OH · measurements in the methane, methane/butane, and methane/1-butene flames show that the OH · concentration is suppressed in the presence of soot particles.

The larger the soot concentration, the greater the effect upon the OH · levels due to its apparent consumption in the soot oxidation region. Thus, soot particles are likely to reduce the amount of OH · available for CO oxidation. Prior investigations have also shown that the yield of CO from hydrocarbon diffusion flames is closely related to the measured soot concentrations within the flame, with larger CO concentrations surviving at the higher soot loadings [1, 26]. For the flames of the present study the CO concentration measurements have been made primarily along the centerline [1]. Thus, attention will be focused on centerline measurements in the oxidation region.

A. Superequilibrium OH · Concentrations

Figure 6 shows the OH · concentration results along the centerline as a function of the axial position above the fuel tube exit. The error bars represent the standard error of the 22 pixel measurements that constitute the approx-
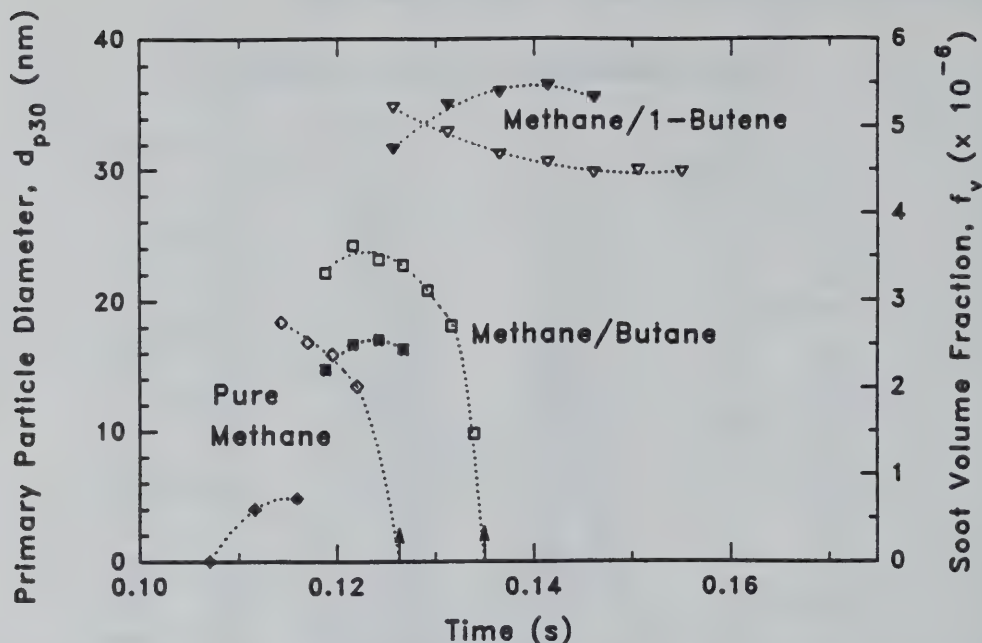
Fig. 5. Comparison of the soot volume fraction, f_v (solid symbols), and the primary particle volume mean diameter, $d_{p_{30}}$ (open symbols), as a function of time along the centerline in the three flames. The data for $d_{p_{30}}$ correspond to axial centerline positions of 7.6–9.5 cm in the pure methane flame ($\diamond$, $\blacklozenge$); 7.6–11.4 cm in the methane/butane flame ($\square$, $\blacksquare$); and 7.6–15.2 cm in the methane/1-butene flame ($\triangledown$, $\blacktriangledown$). The arrows on the time axis denote the visible flame tip locations of the methane and the methane/butane flames.

imately constant signal about the centerline (± 1 mm). These statistical uncertainties are smaller than the symbol size for the methane and methane/butane flames where the OH · concentrations are high and the signal-to-noise ratios are large. Also presented in Fig. 6 are the centerline measurements of temperature, soot volume fraction, and CO for the three flames of this study.

Figures 2–4 and 6 clearly show that as the soot concentration increases (going from the methane to the methane/butane to the methane/1-butene flame), the centerline OH · concentration decreases. The peak centerline soot volume fractions are 0.76, 2.6, and 5.5 ppm in the methane, the methane/butane, and the methane/1-butene flames, respectively [22]. A noteworthy feature of Fig. 6 is that the OH · concentrations in the methane and the methane/butane flames reach approximately the same value along the centerline once the soot particles are completely oxidized. At an axial location of 12.7 cm the centerline temperatures (1610 K and 1549 K) and the

local stoichiometries (0.84 and 0.86) are also closely similar in these two flames (see also Table 1).

The centerline and peak OH · concentration data have also been compared with equilibrium predictions [27]. These results are of particular interest to investigators modeling the soot oxidaton process [28–31] since radical concentrations thus far have been either estimated from equilibrium considerations or assumed. Here, the equilibrium OH · values were calculated using the measured temperatures and the local equivalence ratio obtained from the species concentration measurements [1]. Table 1 presents the results along with the local flame conditions (T and ϕ) at each measurement location. With increasing height and decreasing ϕ, the superequilibrium OH · levels decrease along the centerline for all flames. It is interesting to note in the methane/1-butene flame that emits smoke the OH · concentration along the centerline quickly approaches the equilibrium prediction at the higher measurement locations where $\phi < 1$. For axial loca-
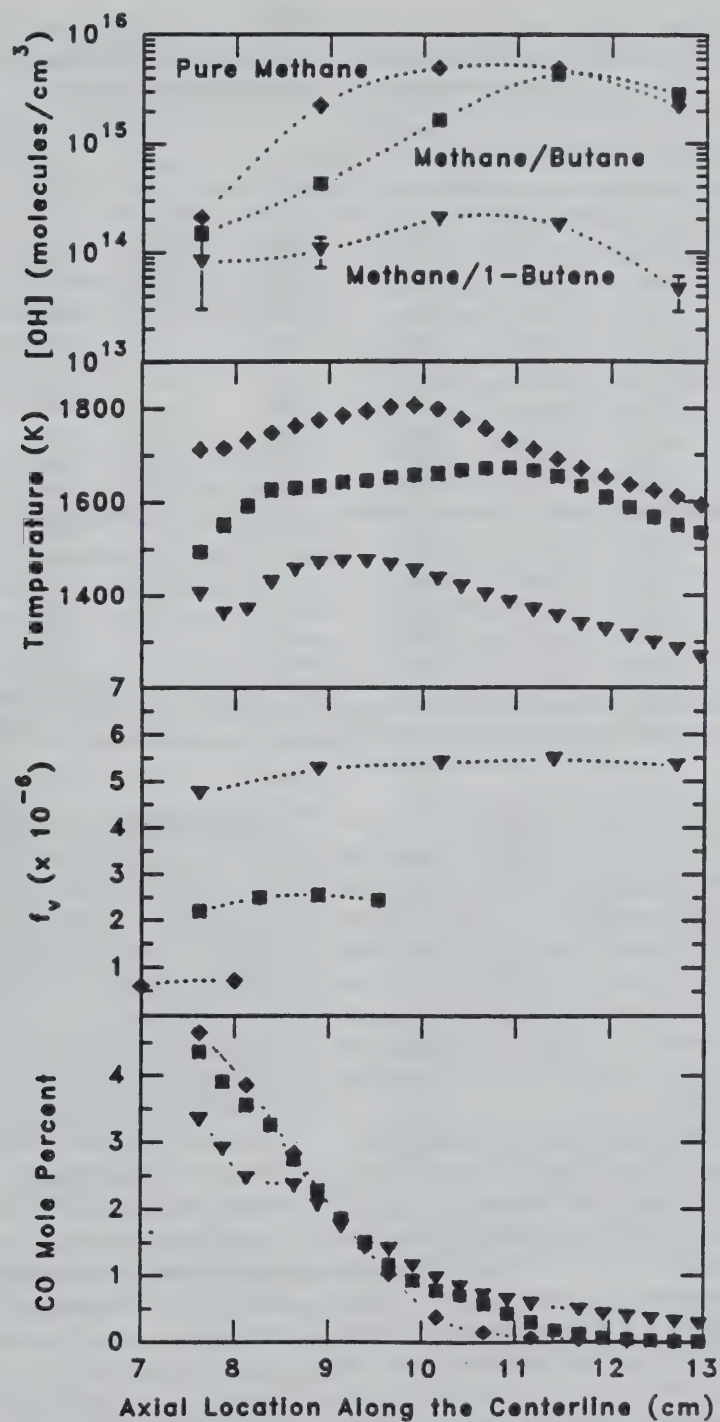
Fig. 6. Centerline OH · concentration profiles in the three flames; the error bars denote statistical uncertainties only (see text). Also shown are the radiation corrected thermocouple temperature, soot volume fraction, and CO measurements. The symbols for the methane (◆), methane/butane (■), and methane/1-butene (▼) flames are the same for each panel.

29

TABLE 1

Summary of Flame Measurements Obtained Along the Centerline and at the Location of the Peak OH · Concentration
for Various Heights H (cm) Above the Fuel Tube Exit[a]

| Flame	Centerline					Location of Peak OH ·		
	H	ϕ	T	$[OH \cdot]_{Ex}$	SR	T	$[OH \cdot]_{Ex}$	SR
CH_4	7.62	1.21	1712	2.1E14	5.5	1748	1.0E16	6.2
	8.89	1.06	1774	2.2E15	14	1799	7.9E15	3.6
	10.2	0.99	1798	5.0E15	4.1	1742	5.7E15	3.6
	11.4	0.92	1690	4.9E15	4.8	1690	4.9E15	4.7
	12.7	0.84	1610	2.3E15	3.3	1610	2.3E15	3.3
CH_4/C_4H_{10}	7.62	1.19	1494	1.5E14	69	1718	9.3E15	6.9
	8.89	1.06	1634	4.3E14	15	1658	7.4E15	8.0
	10.2	1.01	1660	1.6E15	16	1611	6.1E15	9.1
	11.4	0.96	1653	4.4E15	6.6	1610	4.7E15	7.1
	12.7	0.86	1549	2.8E15	6.6	1549	2.8E15	6.7
$CH_4/1-C_4H_8$	7.62	1.16	1403	8.2E13	154	1560	8.0E15	17.4
	8.89	1.06	1469	1.0E14	37	1444	5.8E15	32.2
	10.2	0.99	1435	2.0E14	2.2	1377	3.2E15	32.2
	11.4	0.93	1352	1.8E14	2.7	1293	1.8E15	43.0
	12.7	0.85	1283	4.6E13	1.2	1242	1.1E15	48.9
	14.0	0.77	1236	2.7E12	0.1	1192	5.3E14	42.2

[a] The OH · number densities (molecules/cm^3), local stoichiometries ϕ, temperatures T (K), and superequilibrium OH · concentration ratios (SR) are shown. For the peak OH · results, a local stoichiometry of $\phi = 0.85$ has been assumed [16].

tions where the peak OH · concentrations occur in the annular region, greater departures from the equilibrium predictions, calculated at an assumed stoichiometry of $\phi = 0.85$ [16], are observed as the soot concentration increases (see Table 1). The same qualitative result has been observed for the maximum OH · concentrations measured in a series of ethene/air diffusion flames in which the soot volume fraction was varied [16].

Table 1 shows that while the peak OH · concentration in the methane/1-butene flame exhibits larger superequilibrium values, the centerline OH · concentrations are closer to equilibrium values for $\phi < 1$ than in the other flames of this study. This result can be rationalized as follows. As the soot concentration increases in a hydrocarbon diffusion flame, the temperatures decrease due to heat loss by radiation. Apparently, the concentrations of the major radicals (OH ·, O:, and H ·), which are controlled by fast, bimolecular shuffle reactions and three-body recombination reactions, do not adjust quickly to the lower temperatures. Thus, with increasing soot concentrations and lower flame temperatures, larger

superequilibrium OH · concentrations are observed at the location of peak OH · concentration. Note that there are no soot particles in this region. Within the envelope of the visible flame the lower superequilibrium ratios can be ascribed to the presence of soot particles. The large soot surface area can serve as a sink for the radical pool in two ways: as a reactive partner and/or as a chaperon, M, for the three-body recombination reactions.

Carbon has been reported by Mulcahy and Young [32] to efficiently catalyze the recombination reaction of OH · with H atom at 298 K. These workers report a lower limit of 0.04 for the collision efficiency between OH · and soot, $\eta_{OH,c}$, for the catalyzed recombination reaction:

$$H \cdot + OH \cdot + C \rightarrow H_2O + C.$$

This reaction was assumed to be first order in the OH · concentration and zero order in the H-atom concentration [32]. If we assume the same value of the collision efficiency for our conditions, the normalized reaction rate of OH · (determined from $\omega_{OH}/[OH \cdot]$) is 17,510 s^{-1} in the methane/1-butene flame at

the centerline for an axial position of 8.89 cm; the temperature is 1469 K. At the same location $\omega_{OH}/[OH \cdot]$ for the termolecular recombination reaction in the gas phase

$$H \cdot + OH \cdot + M \rightarrow H_2O + M$$

is calculated to be only 9 s^{-1}. Here the H-atom concentration was obtained from the OH $\cdot$, H_2, and H_2O concentration measurements by assuming equilibration of:

$$H \cdot + H_2O \leftrightarrows OH \cdot + H_2.$$

Appropriate rate constants were obtained from the work of Baulch et al. [33]. This analysis indicates that the presence of soot particles reduces the local OH $\cdot$ concentration and can cause a more rapid adjustment of superequilibrium OH $\cdot$ levels toward equilibrium values.

B. Thermal versus Chemical Effects on the OH $\cdot$ Concentration

Consideration will now be given to the factors that affect the OH $\cdot$ concentrations in these flames. Figures 2–4 and 6 show a strong dependence of the OH $\cdot$ concentration upon the local soot concentration. From equilibrium calculations one finds that the OH $\cdot$ concentration depends on both the temperature and on the local stoichiometry, ϕ. It is also possible that the amount of CO, which is not uniquely related to ϕ [1], will affect the OH $\cdot$ concentration. Therefore, the OH $\cdot$ concentration can be functionally represented as follows:

$$[OH \cdot] = f(\phi, T, [Soot], [CO]). \qquad (2)$$

The relative contributions of thermal versus chemical effects on the OH $\cdot$ concentration are difficult to establish in flames, where the controlling parameters are highly coupled. For example, as the soot concentration increases, the temperature decreases due to radiative heat transfer. Hydrocarbon diffusion flames, therefore, do not offer the opportunity of holding one parameter fixed and varying the others. However, estimates of thermal versus chemical effects can still be made. Equilibrium predictions of the OH $\cdot$ concentration show a weak dependence on ϕ in the fuel lean region ($\phi \leq$

0.95). Therefore, Eq. 2 can be rewritten as

$$[OH \cdot] = f(T, [Soot], [CO]) \qquad (3)$$

for $\phi \leq 0.95$. The OH $\cdot$ concentration as a function of the temperature alone can be established at the locations of the maximum OH $\cdot$ concentration and at greater radial locations where $\phi \leq 0.85$. Here there are no soot particles present, and the CO concentration is either very low or undetectable (< 100 ppm). Figure 7 plots the temperature dependence of the OH $\cdot$ concentration in the methane/butane and the methane/1-butene flames. The steep gradients in both the OH $\cdot$ concentration and the temperature measurements require careful alignment of their respective profiles for this analysis. The values of the OH $\cdot$ concentrations presented in Fig. 7 are averages of up to five measurements at the same temperature but for different radial profiles. The uncertainties in the OH $\cdot$ concentrations are estimated to be as much as $\pm 50\%$ from the scatter of the values about their mean.

There are two major mechanisms which control OH $\cdot$ concentrations in the oxidation region of hydrocarbon diffusion flames, namely thermal quenching due to radiation losses (thermal effect) and reactions of OH $\cdot$ with soot particles and CO (chemical effect). These can be examined by comparing the $[OH \cdot] = f(T)$ data from Fig. 7 with $[OH \cdot] = f(T, [Soot], [CO])$ for $\phi \leq 0.95$ obtained from the centerline profiles shown in Fig. 6. The methane/butane and the methane/1-butene flames have been selected for this analysis since the measured values of the local stoichiometry as a function of the axial location are closely similar in these flames. If

$$F_1 = \frac{f_1(T)}{f_2(T)} \quad \text{and} \quad F_2 = \frac{f_1(T, [Soot], [CO])}{f_2(T, [Soot], [CO])},$$
$$(4)$$

where the subscripts 1 and 2 represent the flames methane/butane and methane/1-butene, respectively, then the relative contribution of thermal quenching to the observed decrease of the OH $\cdot$ concentration in the methane/1-butene flame is the ratio F_1/F_2.
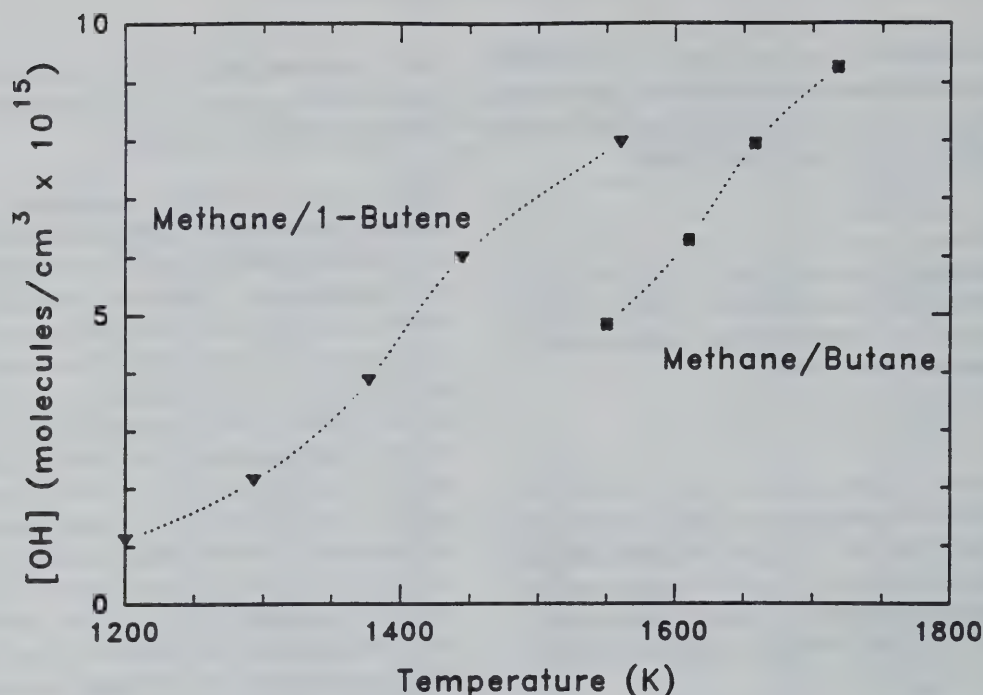
Fig. 7. The dependence of the OH · concentration on the temperature in the methane/butane and the methane/1-butene flames for $\phi \leq 0.85$ obtained at the location of the maximum OH · concentrations and in leaner flame regions.

Table 2 summarizes the values of F_1, F_2, F_1/F_2 for three temperature ratios T_1/T_2 at $\phi \leq 0.95$ in these two flames. Since a common temperature regime was not available for $\phi \leq 0.95$ along the centerline, a temperature ratio approach has been used. As this temperature ratio increases, both F_1 and F_2 increase. However, the ratio F_1/F_2 does not show any systematic change and is approximately 0.07, which indicates that the contribution of thermal quenching to the observed decrease of the centerline OH · concentration is only 7% in the methane/1-butene flame. In light of the

uncertainty in establishing $[OH \cdot] = f(T)$, this value could be in error by $\pm 50\%$. Nevertheless, this analysis indicates that the consumption of OH · by soot and/or CO is mainly responsible for the low OH · concentration in the central region of the methane/1-butene flame (see Fig. 4).

C. Soot Oxidation Rates by OH · and O$_2$

An evaluation of the competition between soot and CO for oxidizing species requires knowledge of their individual oxidation rates, particularly due to OH · . The reaction rate for soot particles can be expressed in terms of the temporal evolution of the soot volume fraction:

$$R_{Soot} = \rho \frac{df_v}{dt}, \tag{5}$$

where ρ is the density of the soot particles. This rate can also be characterized from the time dependence of the $d_{p_{30}}$ profiles by substituting f_v from Eq. 1 into the above expression. Treating N_p as constant along a streamline

TABLE 2

Evaluation of the Relative Contribution of Thermal Quenching to the Observed Decrease in the OH · Concentration Along the Centerline of the Methane/1-Butene Flame[a]

T_1/T_2	F_1	F_2	F_1/F_2
1.19	1.86	22.9	0.08
1.22	2.25	24.2	0.09
1.28	3.72	93.6	0.04

[a] 1, methane/butane flame; 2, methane/1-butene flame.

and assuming $\rho = 1.8$ g/cm^3 (150 kmol/m^3 for an atomic weight of 12) gives

$$R_{\text{Soot}} = 235.6 N_p d_{p_{30}}^2 \frac{d(d_{p30})}{dt}, \qquad (6)$$

where the units of R_{soot}, N_p, $d_{p_{30}}$, and $d(d_{p_{30}})/dt$ are kmol/m^3-s, cm^{-3}, cm, and cm/s, respectively. The assumption of a constant soot particle density is based upon the observation that no internal cavities are detected in soot particles collected from the oxidation region of diffusion flames [25]. Furthermore, there exist no experimental data to indicate a change in density of soot particles in this region.

The number concentration of primary particles, N_p, calculated from consistent f_v and $d_{p_{30}}$ measurements, is almost a factor of two lower in the methane flame (2.1×10^{11} cm^{-3}) than that in the methane/butane and the methane/1-butene flames (3.7×10^{11} cm^{-3}). The slope of the $d_{p_{30}}$ profile as a function of time is evaluated from a combination of second-, third-, and fourth-order polynomial fits. For the methane and methane/butane flames the fits also include the fact that the diameter of the primary particles must approach zero at the location of the visible flame tip (see Fig. 5). This procedure ensures a more accurate slope at the last temporal measurement locations. For the earliest time in the methane flame, however, the slope of the $d_{p_{30}}$ profile is quite uncertain since the primary particle size is expected to be close to its maximum value (see section III. B). Employing the fitting procedure just described in conjunction with Eq. 6 gives the net reaction rate (growth as well as oxidation) due to all species. Note that the use of d_p measurements in conjunction with Eq. 6 is a more direct way of determining the soot oxidation rate than Eq. 5 and the soot volume fraction measurements. The d_p results are preferred since the local soot volume fraction is obtained from tomographic inversion of laser light extinction data, which can result in significant uncertainties at the centerline.

The soot oxidation rate can be obtained from the temporal evolution of the $d_{p_{30}}$ profiles only at locations where soot growth species (i.e., hydrocarbons) are absent. In this region, which is typically fuel lean, the soot oxidation rate due to OH $\cdot$ can be determined by subtracting contributions due to other oxidizing species. For the conditions of this study the equilibrium O-atom concentration is calculated to be 2–3 orders of magnitude lower than the equilibrium OH $\cdot$ concentration. Therefore, the relative contribution of O atoms to the total soot oxidation rate is expected to be small, even though superequilibrium O-atom concentrations are likely [19] and the collision efficiency for the oxidation of soot by O atoms is high [34]. In the present analysis the only oxidizing species are assumed to be OH $\cdot$ and O$_2$.

Based upon these considerations, the soot oxidation rate due to OH $\cdot$ alone is given by:

$$\frac{d[\text{Soot}]}{dt}\bigg|_{\text{OH}\cdot} = \frac{d[\text{Soot}]}{dt}\bigg|_{\text{meas}} - \frac{d[\text{Soot}]}{dt}\bigg|_{\text{O}_2}, \qquad (7)$$

where the oxidation rate due to O$_2$ is estimated from the Nagle and Strickland-Constable (NSC) expression [3]. These OH $\cdot$ and O$_2$ contributions to the observed soot oxidation rate are presented in Fig. 8 and show that the contribution of O$_2$ to the observed soot oxidation rate is small throughout the oxidaton region in all three flames studied.

Use of the NSC expression to estimate the O$_2$ contribution to the soot oxidation rate is subject to some uncertainty. Numerous investigators [35–39] have compared experimental oxidation rates of various carbons with the NSC expression and report rates that range between a factor of 20 lower to a factor of 6 higher than that given by NSC values. However, the trend in the reported comparisons suggests that the NSC expression overpredicts the O$_2$ contribution to soot oxidation at lower temperatures and possibly underpredicts O$_2$ contributions at higher temperatures (see below). Of particular interest is recent work on the oxidation of soot [35] and synthetic chars [36] by O$_2$ that indicates the use of the NSC rate expression overestimates the O$_2$ oxidation rate at temperatures below 1800 K. Note that the centerline temperatures in the methane, methane / butane, and methane/butene flames range be-
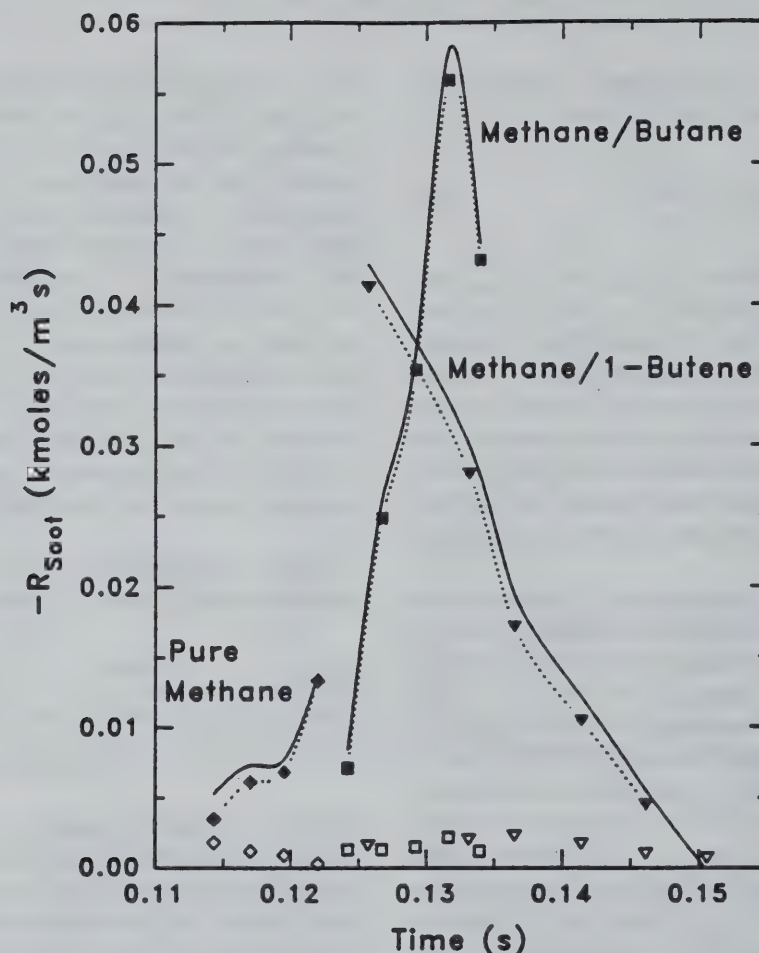
Fig. 8. Plots of the observed centerline soot oxidation rate, shown as a solid line. The contribution of O_2 as determined by the NSC expression (open symbols) and the derived soot oxidation rate due to OH · (from Eq. 7; solid symbols connected by dotted curve) are shown for the pure methane ($\Diamond$, $\blacklozenge$), the methane/butane ($\Box$, $\blacksquare$) and the methane/1-butene ($\triangledown$, $\blacktriangledown$) flames.

tween 1610–1798 K, 1494–1660 K, and 1236–1469 K, respectively (see Table 1).

Chan et al. [35] studied the low-temperature oxidation of soot in a propane diffusion flame and the oxidation of collected soot in an O_2/N_2 environment using an isothermal thermogravimetric technique. The oxidation rate of soot in the thermogravimetric study was an order of magnitude lower than that predicted by the NSC rate for a temperature of ~ 1100 K. At the same temperature these workers [35] report good agreement wth the NSC rate for the diffusion flame study in which the soot oxidation rate was attributed completely to O_2 reactions. However, using an estimated equilibrium

concentration of OH · for the conditions of their diffusion flame yields a soot oxidation rate (assuming a collision efficiency of 0.1 [4]) that is 3 times faster than the NSC rate. Thus, it is likely that OH · reactions were important in their propane diffusion flame and the soot oxidation rate due to O_2 was overestimated by Chan et al. [35].

The work of Levendis et al. [36] on synthetic chars reports good agreement with the NSC rate only at higher temperatures (1800–2300 K). These workers observed oxidation rates to be 20 times lower than the NSC rate in the temperature range 800–1600 K. They ascribed the increase in reactivity of the chars above

1600 K to graphitization, which increased the total surface area. Felder et al. [37] also find the NSC expression to overpredict the oxidation kinetics of carbon blacks in the 1300–1700 K temperature range. In the upper temperature regime (i.e., above the apparent graphitization temperature of 1600 K reported by Levendis et al. [36], Cadman et al. [38] report a factor of 6 higher soot oxidation rates compared with the NSC rate. In addition, Park and Appleton [39] justified the use of the NSC expression for soot oxidation based on shock tube experiments at higher temperatures (1700–4000 K).

In light of the studies cited above, the use of the NSC rate probably overestimates the soot oxidation rate due to O_2 in the oxidation region of the flames investigated here. This would give a larger contribution of OH · to the observed soot oxidation rate, but the increase would be slight since the O_2 contribution is already small (Fig. 8).

D. Collision Efficiencies of OH · with Soot Particles

The soot oxidation rate due to OH · is often discussed from a fundamental kinetic theory viewpoint, which incorporates a collision efficiency parameter. This parameter is defined as the fraction of collisions that result in a carbon atom being removed from soot. Thus, the collision efficiency η is simply a means of matching the observed soot oxidation rates with the following expression obtained by considering OH · to be an ideal gas colliding with a soot surface:

$$R_{Soot} = \eta\left(4.6 \times 10^{-18} d_p^{\ 2} N_p [\text{OH} \cdot]\sqrt{T}\right). \quad (8)$$

Here R_{soot} is expressed in kmol/m³-s and the units of d_p, N_p, [OH ·], and T are cm, cm⁻³, molecules/cm³, and degrees Kelvin, respectively. Estimates of the collision efficiency can be obtained by equating Eqs. 7 and 8.

Table 3 summarizes the values of η determined in the three flames at the various measurement locations. The asterisks denote either regions where soot particle growth is taking place (for example, in the methane/butane flame) or regions where the estimated contribution due to O_2 is greater than the total soot reaction rate (in the methane/1-butene flame).

TABLE 3

Summary of the Collision Efficiency, η, Between Soot and OH · Obtained in the Three Flames as a Function of Time Along the Centerline Streamline[a]

Methane		Methane/Butane		Methane/1-Butene	
Time (s)	$\eta_{OH\cdot}$	Time (s)	$\eta_{OH\cdot}$	Time (s)	$\eta_{OH\cdot}$
0.114	0.120	0.119	*	0.126	0.65
0.117	0.043	0.122	*	0.131	0.37
0.120	0.030	0.124	0.044	0.137	0.13
0.122	0.050	0.127	0.065	0.141	0.10
—	—	0.129	0.070	0.146	0.18
—	—	0.132	0.079	0.151	*
—	—	0.134	0.140	—	—

[a] —, no measurements; *, η for OH · cannot be determined.

The first data point in the methane flame yields a higher value for η than at later times. As mentioned earlier (section III.B), here the value of $d_{p_{30}}$ should be close to its maximum along the centerline, and thus the net soot reaction rate should be close to zero. The other calculated values of η are roughly constant for the methane flame, with the average value being 0.04.

In the methane/butane flame the collision efficiency shows an increase with time. The average of all the determinations is 0.08. For the methane/1-butene flame the collision efficiencies are found to be the highest. However, the first two values are unrealistically large and are likely to be in error due to the uncertainty in collecting samples across the high soot volume fraction annular region (see section III.B). Omitting these two values, the average collision efficiency between OH · and soot is 0.14.

The collision efficiencies determined for these flames fall within the range of values reported in prior investigations. Neoh et al. [4] measured an average value of 0.13 based on the primary particle size. The data of Roth et al. [40] exhibit large scatter for η, ranging from 0.1 to more than 0.3. Note that in both of these studies the OH · concentration was not measured directly. Neoh et al. obtained the OH · concentration from a partial equilibrium estimate, and Roth et al. utilized the H_2/air mechanism given by Warnatz [41]. Mulcahy and Young [32] determined an effective upper limit of η for the gasification of carbon to be

0.08. These workers generated OH · by the following reaction:

$$H \cdot + NO_2 \rightarrow OH \cdot + NO$$

and obtained the OH · concentration by measuring the equimolar concentration of NO with a mass spectrometer.

The collision efficiency results described above reveal some interesting features. Not only do the derived collision efficiencies generally increase with time as soot oxidation proceeds, they also are larger in the flames with more soot. Figure 9 presents a striking correlation of the selected values of η with residence time; the collision efficiency increases at a rate of $4.8 \pm 0.8 \times 10^{-3}$/ms. This result suggests that either (a) the soot particle reactivity changes with time, and/or (b) other oxidizing species are important. The inclusion of additional species in Eq. 7 would reduce both the soot oxidation rate due to OH · and its collision efficiency η.

The soot particle reactivity is known to change in the growth region of hydrocarbon flames [42–44]. This observation has been interpreted in terms of the concept of active sites. The growth of soot particles is argued [11] to accelerate after the inception region

due to collisions of reactive species with the particle surface which produce active sites. At later times the reactivity of the soot particles changes due to thermal annealing or radical site stabilization processes [12, 13]. The modeling results of Frenklach and Wang [45] indicate that the fraction of surface sites available for reaction (α) is lower at higher temperatures. They conclude that α is determined by steric effects, with the mobile soot particle crystallites aligning themselves to limit access to gaseous species at higher temperatures. The collision efficiencies determined here are plotted as a function of temperature in Fig. 10 and reveal a slow decrease at a rate of $-2.2 \pm 0.6 \times 10^{-2}$/100 K. In terms of active sites, the collision efficiency should reflect the fraction of surface sites that are active (α). The variation of η with temperature shown in Fig. 10 is consistent with fewer active sites being present at higher temperatures.

A second possible explanation for the apparent change in soot particle reactivity involves the presence of oxidizing species other than O_2 and OH · considered here. Dixon-Lewis et al. [5] have proposed a mechanism in which radicals catalyze attack by molecular oxygen. In their scheme the OH · radicals or O atoms,
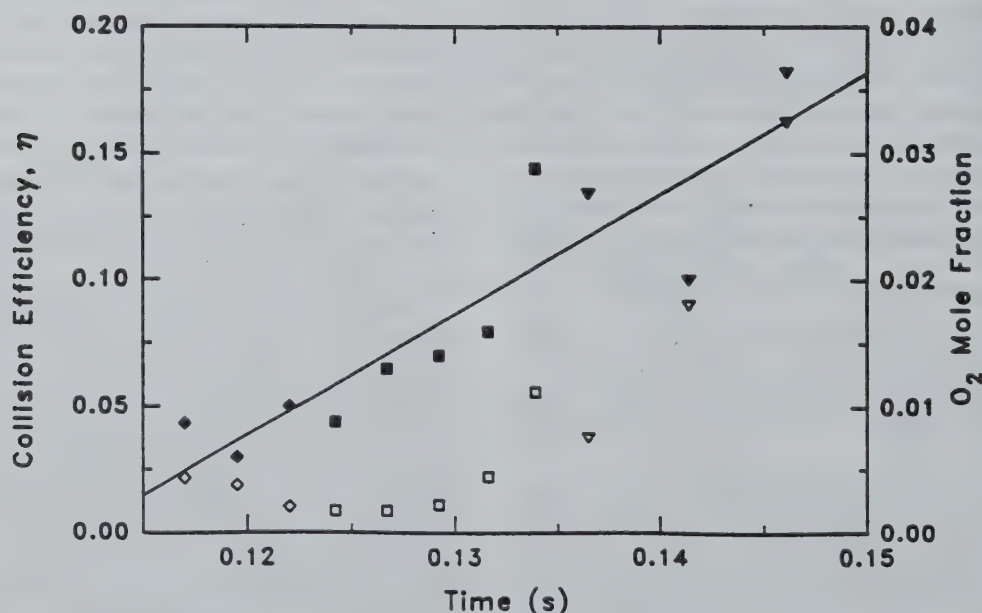
Fig. 9. Plots of the collision efficiency, η (solid symbols), and the O_2 mole fraction (open symbols) as a function of residence time along the centerline of the methane ($\diamond$, $\blacklozenge$), methane/butane ($\square$, $\blacksquare$), and methane/1-butene flames ($\triangledown$, $\blacktriangledown$). The line is a linear least squares fit to the collision efficiency data.
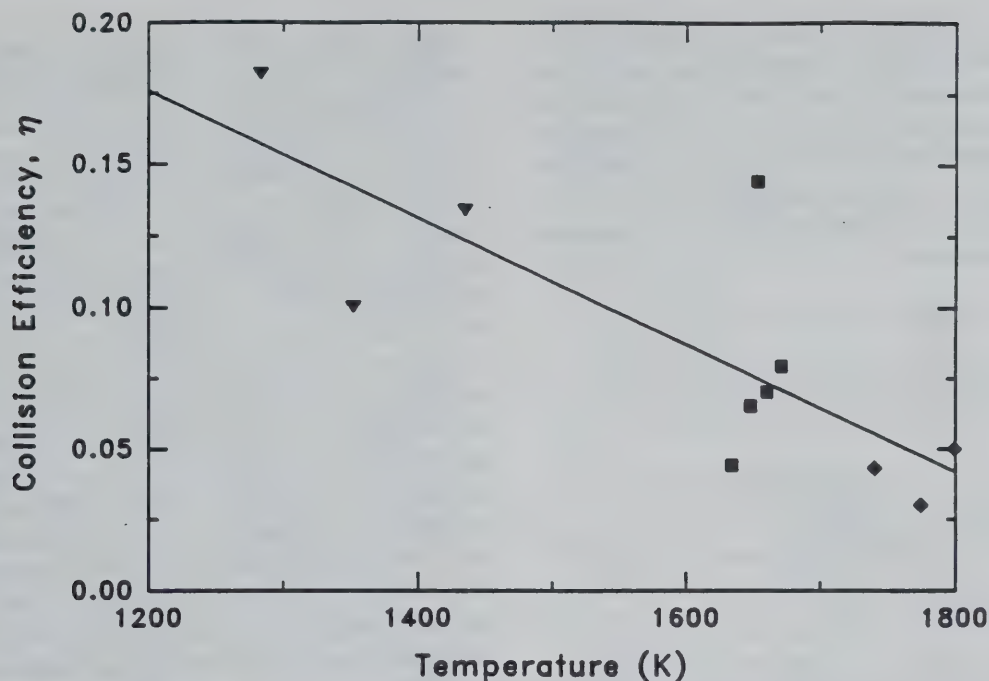
Fig. 10. Plot of the collision efficiency, η, estimated from the soot oxidation rates and the OH·
concentrations as a function of temperature in the methane (♦), methane/butane (■), and methane/1-
butene (▼) flames. The line is a linear least squares fit to the data.

formed from the reaction of molecular O_2 with
H atoms, attack carbon more effectively than
O_2. This explains the observed increased oxi-
dation rate of graphite introduced into the
main reaction zone of premixed flames. Figure
9 includes O_2 concentration data along with
the calculated values of η as a function of
time. The O_2 concentrations do not change
substantially at early times (and at the higher
temperatures). The H-atom concentration is
expected to exhibit a maximum value near
$\phi = 1.0$ [19]. Thus, the H-atom concentration
should be decreasing for the last two points in
the methane/butane flame and the three
points in the methane/1-butene flame (see
Table 1). Although the data for the methane/
1-butene flame show larger O_2 concentrations,
the temperatures are much lower and so is the
expected H-atom concentration. Thus, the cat-
alytic mechanism does not account for the
observed increased reactivity over the whole
range of our experimental conditions.

In summary, the observed increase in the
collision efficiency of soot oxidation by OH·
with time most likely arises from an increasing
reactivity of the soot particles. It is interesting

to note that the flames that form more soot
(possibly due to a larger fraction of active sites,
α) also exhibit larger collision efficiencies with
OH·. At this point one cannot determine
whether the increased reactivity is a result of
(1) the lower temperatures in more highly soot-
ing flames and hence an increase fraction of
surface sites available for reaction due to
greater access to gaseous species, as proposed
by Frenklach and Wang [45], or (2) the fact
that a greater number of active sites, which
originate in the inception zone and produce a
larger soot concentration, are still available in
the soot oxidation region and are involved in
oxidation reactions.

E. Competition for OH · between CO and Soot

The competition between CO and soot for
OH· can be evaluated by comparing the soot
oxidation rate computed from Eq. 8 with the
forward rate of the CO + OH· reaction [46]:

$$\frac{d[CO]}{dt} = 1.5 \times 10^4 T^{1.3} e^{386/T} [CO][OH\cdot],$$

$$(9)$$

where $d[CO]/dt$ is given in kmol/m^3-s. The collision efficiency values for this analysis have been obtained from the linear least squares fit shown in Fig. 9. Since both the CO and soot oxidation rates have a first-order dependence on their respective concentrations, it is also appropriate to compare their normalized rates. If we consider

$$F_3 = \frac{\dfrac{d[CO]}{dt}}{\dfrac{d[Soot]}{dt}} \quad \text{and}$$

$$F_4 = \frac{\dfrac{1}{[CO]} \times \dfrac{d[CO]}{dt}}{\dfrac{1}{[Soot]} \times \dfrac{d[Soot]}{dt}}, \quad (10)$$

then the ratio F_3 is an indication of the amount of competition between CO and soot for OH $\cdot$. For example, a value of $F_3 = 1$ implies an equal probability that an OH $\cdot$ molecule will react with CO or soot. The ratio F_4 reflects the intrinsic reactivity of OH $\cdot$ with CO vs. soot and is a function of the collision efficiency η, the primary particle size $d_{p_{30}}$, and the temperature T (see Eqs. 1, 8, and 9):

$$F_4 \propto \frac{d_p T^{0.8} e^{386/T}}{\eta}. \quad (11)$$

The direct dependence of F_4 on the primary particle size is intuitively understandable, since for the same soot volume fraction a larger d_p will result in a smaller soot oxidation rate due to the decreased surface area. With increasing temperature the ratio F_4 increases due to a higher inherent reactivity of CO and a lower inherent reactivity of soot (smaller η).

Table 4 summarizes the ratios F_3 and F_4 determined for the three flames at various values of the residence time. The methane flame shows the least competition between CO and soot for OH $\cdot$, as reflected by the high values for F_3 and F_4. The OH $\cdot$ + CO rate is far larger than that for OH $\cdot$ + soot. This is due both to a low soot reactivity (Table 3) and to the low soot concentration. As the soot concentration increases in the methane/butane and methane/1-butene flames, the competition between CO and soot for OH $\cdot$ increases. In the methane/1-butene flame, the soot oxidizes faster than CO at all but the two earliest residence times shown in Table 4. With increasing time in all of the flames, an increasing value of η increases the OH $\cdot$ + soot oxidation rate relative to the OH $\cdot$ + CO rate. This is reflected by the decreasing values of F_4 with time. Although CO is intrinsically more reactive with OH $\cdot$ than with soot in all of the flames of this study (i.e., the F_4 values are all greater than 1), its oxidation is suppressed in the presence of large soot concentrations. This is most evident in the methane/1-butene flame.

V. CONCLUSIONS

Measurements of the hydroxyl radical concentration and the size of the primary soot particles have been made in a series of hydrocarbon/air diffusion flames containing varying

TABLE 4

Summary of the Ratio of the CO Oxidation Rate to the Soot Oxidation Rate (F_3) and the Ratio of the Normalized CO Reaction Rate to the Normalized Soot Oxidation Rate (F_4) in the Three Flames

Methane			Methane/Butane			Methane/1-Butene		
Time (s)	F_3	F_4	Time (s)	F_3	F_4	Time (s)	F_3	F_4
0.114	82.7	25.3	0.119	13.6	12.2	0.126	2.31	10.0
0.117	42.6	13.1	0.122	6.3	10.3	0.131	1.13	7.1
0.120	21.9	8.9	0.124	3.7	8.0	0.137	0.47	5.2
0.122	12.3	5.9	0.127	1.9	6.7	0.141	0.23	4.2
—	—	—	0.129	1.1	5.3	0.146	0.13	3.4
—	—	—	0.132	0.9	4.1	0.151	0.07	3.0
—	—	—	0.134	0.9	2.0	—	—	—

amounts of soot. The observed OH · concentrations are suppressed in the presence of soot particles. A comparison of the fuel lean OH · concentrations in the presence and absence of soot particles reveals that the OH · concentraton is reduced primarily due to reactions with soot rather than as a consequence of the lower flame temperatures measured for the higher soot loadings. The effect of lower temperatures on the OH · concentration is comparatively small, accounting for only 7% ± 4% of the measured decrease in the OH · concentration.

The soot oxidation rates computed from the primary particle size profiles as a function of time reveal interesting trends for the soot particle reactivity. Higher collision efficiencies are deduced for the flames containing larger soot concentrations at lower temperatures. The variation of the collision efficiency with temperature suggests that fewer active sites per unit surface area exist at higher temperatures.

A comparison of the soot and CO oxidation rates shows that although CO is inherently more reactive than soot on a per carbon basis, for large soot concentrations the soot successfully competes with CO for OH · and hence suppresses CO oxidation. The soot oxidation rates due to OH · were obtained by subtracting the contribution due to O_2 (determined from the Nagle Strickland-Constable expression [3]) from the observed rates. Although the NSC expression is likely to overestimate the soot oxidation rate due to O_2 under the conditions of this study, the contribution of O_2 to the soot oxidation rate is found to be small compared with that due to OH · .

REFERENCES

1. Puri, R., and Santoro, R. J., *Fire Safety Science—Proceedings of the Third International Symposium*, 1991, pp. 595–604.
2. Fenimore. C. P., and Jones. G. W., *J. Phys. Chem.* 71:593–597 (1967).
3. Nagle, J., and Strickland-Constable, R. F., *Proceedings of the Fifth Carbon Conference*, Pergamon, Oxford, 1962, Vol. 1, pp. 154–164.
4. Neoh, K. G., Howard, J. B., and Sarofim, A. F., *Particulate Carbon Formation During Combustion*, (D. C. Siegla and G. W. Smith, Eds.), Plenum, New York, 1981, pp. 261–282.
5. Dixon-Lewis, G., Bradley, D., and El-Din Habik, S., *Combust. Flame* 86:12–20 (1991).
6. Garo, A., Prado, G., and Lahaye, J., *Combust. Flame* 79:226–233 (1990).
7. Dobbins, R. A., and Megaridis, C. M., *Langmuir* 3:254–259 (1987).
8. Dobbins, R. A., Santoro, R. J., and Semerjian, H. G., *Twenty-Third Symposium (International) on Combustion*, The Combustion Institute, Pittsburgh, 1990, p. 1525.
9. Walker, P. L. Jr., Rusinko, F. Jr., and Austin, L. G., *Adv. Catal.* 11:133–221 (1959).
10. Howard, J. B., *Twenty-Third Symposium (International) on Combustion*, The Combustion Institute, Pittsburgh, 1990, p. 1107.
11. Tesner, P. A., *Combust. Flame* 86:187–188 (1991).
12. Woods, I. T., and Haynes, B. S., *Combust. Flame* 85:523–525 (1991).
13. Harris, S. J., *Combust. Sci. Technol.* 72:67–77 (1990).
14. Saito, K., Gordon, A. S., Williams, F. A., and Stickle, W. F., *Combust. Sci. Technol.* 80:103–119 (1991).
15. Toossi, R., *Combust. Flame* 90:1–10 (1992).
16. Puri, R., Moser, M., Santoro, R. J., and Smyth, K. C., *Twenty-Fourth Symposium (International) on Combustion*, The Combustion Institute, Pittsburgh, 1992, p. 1015.
17. Santoro, R. J., Semerjian, H. G., and Dobbins, R. A., *Combust. Flame* 51:203–218 (1983).
18. Smyth, K. C., Miller, J. H., Dorfman, R. C., Mallard, W. G., and Santoro, R. J., *Combust. Flame* 62:157–181 (1985).
19. Smyth, K. C., Tjossem, P. J. H., Hamins, A., and Miller, J. H., *Combust. Flame* 79:366–380 (1990).
20. Fairchild. P. W., Smith, G. P., and Crosley, D. R., *J. Chem. Phys.* 79:1795–1807 (1983).
21. Smith, G. P., and Crosley, D. R., *J. Chem. Phys.* 85:3896–3901 (1986).
22. Richardson, T. F., Ph.D. dissertation, Department of Mechanical Engineering, The Pennsylvania State University, 1993.
23. Puri, R., Richardson, T. F., Santoro, R. J., and Dobbins. R. A., *Combust. Flame* 92:320–333 (1993).
24. Prado, G., Jagoda. J., Neoh, K., and Lahaye, J., *Eighteenth Symposium (International) on Combustion*, The Combustion Institute, Pittsburgh, 1981, p. 1127.
25. Megaridis. C. M., and Dobbins, R. A., *Combust. Sci. Technol.* 66:1–16 (1989).
26. Köylü. Ü. Ö., Sivathanu, Y. R., and Faeth, G. M., *Fire Safety Science—Proceedings of the Third International Symposium*, 1991, pp. 625–634.
27. Gordon. S., and McBride. B. J., NASA SP-273 Interim Revision N78-17724, March 1976.
28. Kennedy. I. M., Kollmann, W., and Chen. J.-Y., *Combust. Flame* 81:73–85 (1990).

29. Kennedy, I. M., Kollmann, W., and Chen, J.-Y., *AIAA J.* 29:1452–1457 (1991).

30. Moss, J. B., Stewart, C. D., and Syed, K. J., *Twenty-Second Symposium (International) on Combustion*, The Combustion Institute, Pittsburgh, 1988, p. 413.

31. Leung, K. M., Lindstedt, R. P., and Jones, W. P., *Combust. Flame* 87:289–305 (1991).

32. Mulcahy, M. F. R., and Young, B. C., *Carbon* 13:115–124 (1975).

33. Baulch, D. L., Cobos, C. J., Cox, R. A., Esser, C., Frank, P., Just, Th., Kerr, J. A., Pilling, M. J., Troe, J., Walker, R. W., and Warnatz, J., *J. Phys. Chem. Ref. Data* 21:411–734 (1992).

34. Gersum, S. von, and Roth, P. *Twenty-Fourth Symposium (International) on Combustion*, The Combustion Institute, Pittsburgh, 1992, p. 999.

35. Chan, M.-L., Moody, K. N., Mullins, J. R., and Williams, A., *Fuel* 66:1694–1698 (1987).

36. Levendis, Y. A., Flagan, R. C., and Gavalas, G. R., *Combust. Flame* 76:221–241 (1989).

37. Felder, W., Madronich, S., and Olson, D. B., *Ener. Fuels* 2:743–750 (1988).

38. Cadman, P., Cornish, R., and Denning, R. J., *Seventeenth International Shock Tube Symposium*, 1990, pp. 751–755.

39. Park, C., and Appleton, J. P., *Combust. Flame* 20:369–379 (1973).

40. Roth, P., Brandt, O., and Gersum, S. von, *Twenty-Third Symposium (International) on Combustion*, The Combustion Institute, Pittsburgh, 1990, p. 1485.

41. Warnatz, J., *Ber. Bunsenges. Phys. Chem.* 87:1008–1022 (1983).

42. Harris, S. J., and Weiner, A. M., *Combust. Sci. Technol.* 31:155–167 (1983); 32:267–275 (1983); 38:75–87 (1984).

43. Bockhorn, H., Fetting, F., Heddrich, A., and Wannemacher, G., *Twentieth Symposium (International) on Combustion*, The Combustion Institute, Pittsburgh, 1984, p. 979.

44. Baumgärtner, L., Hesse, D., Jander, H., and Wagner, H. Gg., *Twentieth Symposium (International) on Combustion*, The Combustion Institute, Pittsburgh, 1984, p. 959.

45. Frenklach, M., and Wang, H., *Twenty-Third Symposium (International) on Combustion*, The Combustion Institute, Pittsburgh, 1990, p. 1559.

46. Wilk, R. D., Cernansky, N. P., Pitz, W. J., and Westbrook, C. K., *Combust. Flame* 77:145–170 (1989).

Appendix C. **Carbon Monoxide and Soot Formation in Underventilated Laminar Diffusion Flames**

by

S. Léonard

ABSTRACT

An investigation of the generation of CO and smoke for under-ventilated laminar diffusion flames has revealed both strong similarities and differences with studies considering over-ventilated conditions. In particular, the proportionality between smoke yield and CO yield observed for the post-flame (over-fire) region of over-ventilated flames for a wide range of fuels is not found to be valid for the under-ventilated case. In fact, the soot observed in the under-ventilated flames is observed to vary considerably in terms of the chemical structure from that typically observed in over-ventilated flames. The highly organic nature of the soot implies that the structure of the soot may be more similar to early agglutinated soot particles recently observed in diffusion flames than to the more aged aggregates typical of the post-flame region for over-ventilated flames. Comparisons in terms of the ratio of CO and CO_2 as a function of global equivalence ratio in the post-flame region of the under-ventilated flames show a similar behavior to that previously observed for in-flame measurements for both over-ventilated and under-ventilated diffusion flames which examined the dependence of this ratio on local equivalence ratio conditions. This suggests that for the in-flame fuel-rich region, the chemical environment excluding soot is correlated with equivalence ratio in a similar way for both an over-ventilated flame and an under-ventilated flame. The low production of CO in the post-flame region of over-ventilated flames is simply a result of the oxidation of CO to CO_2 in the upper region of these flames. Finally, the present studies illustrate the utility of the study of under-ventilated flame environments where product yields and trends can be quite different from over-ventilated conditions. These studies should have significance for combustion phenomena in which under-ventilated conditions are typical, such as in fires.

TABLE OF CONTENTS

LIST OF FIGURES

47

LIST OF TABLES

CHAPTER 1
INTRODUCTION

1.1. Importance of Carbon Monoxide and Soot in Unwanted Fires

On the morning of September 26 1987, firefighters in Sharon, Pennsylvania found three unconscious women on the second floor of a three bedroom duplex. Two of the victims were found dead from carbon monoxide (CO) poisoning and the third succumb later the same day to burns resulting from her incapacitation due to the CO levels present in the room. Although the fire was confined to the first floor kitchen, the three victims were on the second floor. The kitchen walls were made of wood panels and represented, along with the ceiling, a large supply of fuel for the fire. This incident highlights the significant hazard to life of fires beyond direct contact, resulting from the combustion products of the fire.

This is an example of the tragic properties of incomplete products of combustion. As the fire progressed and its air supply expended, the conditions went from an over-ventilated to an under-ventilated fire. The toxic gases produced by incomplete combustion then spread to other parts of the house especially the second floor. Among these gases, although it is not the most toxic, CO causes the greatest number of fatalities (Friedman 1988). Not only does it cause death but it also incapacitates victims and prevents them from escaping the fire when they become aware of the threat (Purser 1988).

A second important product of incomplete combustion is emitted soot or smoke. Low concentrations of smoke can result in eye and lung irritation. Smoke can also reduce visibility, preventing victims from seeing emergency exit signs or firefighters from finding their way inside a burning building. Soot is also suspected to be a potential carcinogen. Soot particles are also an important part of the flame energy transfer process since soot radiates an important quantity of heat to the surroundings. In fact, soot radiation is "the primary mode of heat transfer in any reasonably sized fire" (McCaffrey and Harkleroad 1988, pp. 1252) and thus aids in the spread of the fire. Therefore a good understanding of how soot is formed and then oxidized is important in order to predict the smokiness of a fire.

The accident in Sharon shows that a better understanding of how CO and soot are formed is necessary to increase the chances of victims to escape from a fire quickly and safely. It is also important to predict the formation of CO in fires with limited oxygen if construction materials are to become safer or less susceptible to form CO. Because large fires are complicated and difficult to study, simpler experiments which isolate the important phenomena are desirable. In the present study, laminar diffusion flames offer a simple way to study under-ventilated flames. Although small scale laminar diffusion flames appear to be quite different from turbulent fires, in terms of CO and soot formation they allow the study of the important phenomena under conditions involving a limited number of well controlled parameters.

The objective of this work is to study laminar diffusion flames and their products when the air supply to the flame is reduced below what is required for complete combustion (under-ventilated). Specific information on the CO and soot formation processes has been obtained by measuring the concentration of products of combustion (gaseous

49

and particulate) and temperatures and by comparing these results with data obtained from over-ventilated flames (actual air to fuel ratio greater than the stoichiometric air to fuel ratio). Some general information on the flame structure of under-ventilated flames has also been investigated using flame height predictions. Different fuels have been studied to determine their effect on soot and CO formation. The physical aspects of particles formed in the flame have been observed using a transmission electron microscope (TEM) and their content analyzed using a thermal-optical method in hope of learning more about their formation process. Studies of CO formation have been conducted using gas sampling involving intrusive probes followed by appropriate analysis procedures.

Since the present study focuses on the formation of CO and soot in under-ventilated laminar diffusion flames, it is appropriate to briefly review previous work done on laminar diffusion flames. In the following sections a concise review of laminar diffusion flames, soot particle formation and CO production is given. This review is intended to present key elements in our current understanding of these phenomena. Additionally, this material will lay the foundations for the discussion of the results of the current study.

1.2. Laminar Diffusion Flames

The first extensive study of laminar diffusion flames was published by Burke and Schumann in 1928. Before Burke and Schumann (1928) published their work, only descriptive papers on diffusion flames were available. In their work, Burke and Schumann (1928) were successful at predicting flame height and contour, and species concentrations of over- and under-ventilated flames involving co-annular burners. In their work two concentric circular tubes were used with fuel issuing from the inner tube and air from the outer tube. Burke and Schumann (1928) varied the tubes diameters such that the fuel and oxidizer always had equal exit velocities. Their model of this flame was based on the diffusion equation and required four basic assumptions for solution: 1) the velocities in the flame are constant, 2) the coefficient of interdiffusion for both gases is constant, 3) there is only radial diffusion and 4) mixing is only due to diffusion. These assumptions have been discussed in many other subsequent papers (Barr 1949, Savage 1962, Roper 1977, Roper et al. 1977) and are considered valid for the case of the concentric circular burner. Roper (1977) gave a more complete solution for burners of different geometries and this work will be described in more detail later in this section.

Before proceeding further, a more detailed definition of the terms over-ventilated and under-ventilated is required. If the amount of oxidizer available for reaction with the fuel exceeds that required to completely convert the fuel to carbon dioxide (CO_2) and water (H_2O), i.e. complete combustion, the flame is referred to as over-ventilated. For the case where the available oxidizer is less than that required for complete combustion, the flame is under-ventilated. These conditions can also be represented in terms of the equivalence ratio, Φ, which is defined as the stoichiometric air to fuel ratio divided by the air to fuel ratio actually supplied for burning,

$$\Phi = \frac{[A/F]_{Stoi}}{[A/F]_{Actual}}$$

If Φ is greater than one (fuel rich), the flame is under-ventilated while for Φ less than one (fuel lean) the flame is over-ventilated. To determine the flame equivalence ratio the total air and fuel flow rates are used and thus represent a "global or overall" equivalence ratio (Φ). This global equivalence ratio differs from the "local" equivalence ratio (ϕ) observed in the flame itself which is a function of the local species concentration and the extent of reaction at a

particular location. Each diffusion flame has a single global equivalen ratio while the local equivalence ratio will vary throughout the flame. Results related to each of these definitions of equivalence ratio will be described in subsequent sections and care will be taken to differentiate between global and local conditions.

Since Burke and Schumann (1928) were studying steady flames resulting from the reaction of interdiffused oxygen and a combustible gas, they considered combustion limited to a surface referred to as the flame front. Burke and Schumann (1928, pp. 999) defined the flame front as "the locus of those points where the rate of diffusion of combu ible gas outward and the rate of diffusion of oxygen inward have the ratio required by the stoichiometric equat or complete combustion of the combustible gas". They also noted that the "central bright part" of the flame due to incandescent particles has nothing to do with the actual flame front. The flame height would be the vertical position of the flame front either along the central axis ($\Phi < 1$) or at the edge of the air stream ($\Phi > 1$). They found a relationship to determine the height of a diffusion flame by solving the diffusion equation in radial coordinates,

$$\frac{\partial C}{\partial t} = k\left(\frac{\partial^2 C}{\partial r^2} + \frac{\partial C}{r \partial r}\right)$$

where C is the concentration of the combustible, t is time, r is the radial coordinate and k is the coefficient of interdiffusion of the combustible and oxidizer gases.

Assuming that the velocities are constant in the flame and by using boundary conditions imposed by the geometry of the burner, the solution of the ordinary differential equation yields the concentration for steady conditions as

$$C(y,r) = \frac{C_0 L^2}{R^2} - \frac{C_2}{i} + \frac{2LC_0}{R^2}\sum \frac{J_1(\mu L)J_0(\mu r)}{\mu(J_0(\mu R))^2} e^{-\frac{k\mu^2 y}{v}},$$

where L is the radius of the inner tube, R the radius of the outer tube, v the velocity of the gas (keeping in mind that the air and fuel velocities are assumed equal), y the vertical distance corresponding to the radial location r, J_1 and J_0 are Bessel functions of the first kind, μ are all the positive roots of the equation $J_1(\mu R) = 0$, i is the stoichiometric number of oxygen molecules, C_2 is the initial concentration of oxygen and C_0 is the sum of the initial concentration of fuel and C_2/i. The flame front can be found from the locus of points corresponding to the solution with C=0 and the flame height is given when r=R for an under-ventilated flame and r=0 for an over-ventilated flame. This relationship shows one of the most important conclusion of the Burke and Schumann (1928) study; that for a constant geometry burner, the flame height is propor onal to the fuel flow rate. The authors also inferred that the size of the fuel and oxidizer tubes did not affect the flame height if the flow of fuel and air were kept constant. Their conclusion was supported by experimental comparisons. They were also able to predict concentration of CO, CO_2 and N_2 along the centerline of a CO/air diffusion flame.

At the end of their paper, Burke and Schumann (1928) also briefly mention two experiments done with an inverted flame. For an inverted flame the air flows through the inner tube with the fuel on the outside. The flame heights of the predicted and measured inverted flames were almost the same (less that 1% difference). The theoretical treatment of the inverted flame therefore did not seem to be any different from the normal laminar diffusion flame.

One important reason why the predicted and experimental flame he ts agreed so well in the Burke and Schumann (1928) work was due to their use of a "mean" diffusion coeffici This coefficient was calculated from a

single experiment and applied to all other calculations with the same gaseous composition. Barr (1949) pointed out that by obtaining the diffusion coefficient from one experiment and then applying it to other calculations, the coefficient acts as a correction factor and makes up for errors in the assumptions used in the solution of the diffusion equation. He also argued that this coefficient is not constant and is expected to vary with the composition of the gas mixture. Burke and Schumann (1928) also recognized the limitations of their analysis and discussed some of the reasons for the relatively good agreement between experiment and theory.

Following Burke and Schumann (1928) numerous authors studied confined and unconfined diffusion flames. One of the more important paper on laminar diffusion flames was published by Roper in 1977. Roper (1977) suggested modifying the Burke and Schumann theory to account for mass continuity everywhere in the flame and considered other burner geometries. Roper's model was based on seven assumptions: 1) temperature and diffusivity are constant in regions controlling diffusion, 2) combustion doesn't change the number of molecules, 3) axial diffusion can be neglected, 4) Schmidt and Lewis number are equal to one (the Schmidt number is the ratio of the rate of momentum transport over the rate of mass transport and the Lewis number is the rate of energy transport over the rate of mass transport), 5) the gas velocity is uniform across the regions controlling diffusion, 6) in the reaction zone the gas velocity is equal to the flame velocity, 7) when buoyancy is important the flame gases start at an initial value and accelerate due to buoyancy. The major difference between these assumptions and those used by Burke and Schumann (1928) is that Roper (1977) does not consider the gas velocity to be constant in the flame but rather satisfies continuity. Roper (1977) also pointed out that no assumption was made concerning the thickness of the flame front since the boundary of the reaction zone was defined as the location where oxidant and fuel are in stoichiometric ratio.

Based on these assumptions and continuity, Roper (1977) found a general relationship for the flame height. For circular and square burners, the relationship predicts that the flame height is proportional to the volumetric flow rate and a second term which is constant for a particular fuel. Roper (1977) therefore concluded that the flame height in circular and square burners is unaffected by buoyancy forces or the velocity of the air flow surrounding the fuel flow in agreement with the results of Burke and Schumann (1928). Roper (1977, pp. 225) stated that this observation was due to the fact that "any factors which change the flame gas velocity (such as buoyancy) cause an opposing change in the time required for diffusion. So the flame height remains constant". On the other hand, flame heights from long slot burner can be affected by momentum, buoyancy or both simultaneously and a more complicated behavior is observed for the flame height dependence on fuel flow and burner dimensions.

Roper's model also allowed calculation of the concentration profile within the flame by assuming that the gas products are in thermodynamic equilibrium. A constant diffusion coefficient was also assumed and, as in the Burke and Schumann theory, was assumed to be a mean coefficient representing the fuel and oxidant interdiffusion.

In a second paper by Roper et al. (1977), Roper's model is compared to experimental values. The flame heights were separately measured using the CO and soot concentration. As described above, Roper's model allowed Roper et al. (1977) to predict the concentration profile of different species assumed in thermodynamic equilibrium and was used to compute the amount of CO at the end of the flame front of the diffusion flame. With this concentration known, a series of CO concentration measurements at different axial locations in the flame allowed Roper et al. (1977) to determine the flame height. Another method of determining the flame height was based on

soot concent...tion measurements. The maximum soot concentration was assumed t... be where net soot formation stops and oxidation starts. At this point hydrocarbons are replaced by oxygen and must correspond to the flame front. Soot concentrations were then measured using a densitometer at different axial locations and the height at which maximum soot concentration occurred was considered to be the flame height. Roper and Smith (1979, pp. 132) noted the importance of distinguishing the "visible flame height (end of reaction such as soot oxidation) and diffusion flame height (stoichiometric conditions on the flame axis)". The visible flame height would be determined by the oxidation of soot particles by OH and not by O_2 according to Fenimore and Jones (1967).

One important note about Roper's work (1977) concerns one of his assumptions used in solving the continuity equation. Roper (1977) assumed that as the distance from the burner lip approaches infinity, the "dimensionless oxygen defect" goes to zero. This assumes in other words that there is plenty of oxygen available away from the burner. In the case of an under-ventilated flame this is not true. When $\Phi > 1$ all the oxygen in principle is expended in the post flame zone. The derived equations in Roper's work (1977) are therefore not valid for under-ventilated flames and the conclusions summarized here are thus limited to over-ventilated flames.

The works of Roper (1977), Roper et al. (1977) and Burke and Schumann (1928), essentially contains what is generally known and accepted about laminar diffusion flames. Several other papers have been published concerning specific details regarding laminar diffusion flames and mostly concern over-ventilated conditions. These studies will be briefly reviewed next.

Other papers published since the Burke and Schumann (1928) work have investigated diffusion flame structure (Barr 1949; Savage 1962; Jones and Rosenfeld 1972; Roper and Smith 1979; Mitchell et al. 1980; Lomax and Simmons 1986), flame stability (Barr 1953) of over- and under-ventilated flames, and inverted diffusion flames (Walker 1979; Wu and Essenhigh 1984; Sidebotham and Glassman 1992). These papers will be discussed in this section.

Barr in his 1949 paper studied diffusion flames in vitiated atmospheres. In this paper Barr (1949, pp. 200) considered under-ventilated flames to be "of academic interest only" and studied the flame elongation as the amount of air is reduced towards stoichiometric air flow. In a second paper Barr studied instability in over- and under-ventilated flames. Some of these instabilities were observed during the present work and are described in Chapter 2. Barr's paper is one of the few papers describing normal under-ventilated diffusion flames, however the results are mainly descriptive.

Savage (1962) examined the flame structure of over-ventilated butane/air laminar diffusion flames. He studied flame shape and height using photographs of laminar diffusion flames and noted two distinct boundaries: 1) a blue radiation in the lower portion of the flame and 2) an intense radiation appears higher in the flame "considered to be due to hot carbon particles" (Savage 1962 pp. 82). Jones and Rosenfeld (1972) also studied enclosed diffusion flames. In their paper the authors considered the fact that soot oxidation in the reaction zone may not be infinitely fast. Before this paper, authors appeared to consider the flame height to be the visual flame height determined by the oxidation process of soot in the upper leaner portion of the flame rather than the location below, corresponding to the stoichiometric surface. In both the Savage (1962) and Jones and Rosenfeld (1972) studies, no mention of under-ventilated flames is made. Savage (1962) reduced the air/fuel ratio to the point where the butane diffusion flame

became smoking. At this point, however, the flame is still over-ventilated and the air/fuel ratio was not reduced any further.

Roper and Smith (1979) also study the effect of air starvation although here again only over-ventilated flames were considered. Their conclusion was that air starvation did not increase soot formation but reduced the flame temperature in the second half of the diffusion flame and allowed soot to escape. Kent and Wagner (1984) confirmed this conclusion by locally heating the tip of a sooting flame which clearly reduced soot emission. The authors concluded that "burnout cessation and consequent smoke emission are determined by the temperature in the downstream region" (Kent and Wagner 1984 pp. 257).

Mitchell et al. (1980) gave a good description of the flame reaction zone and its composition. This work also described where the important combustion products for fire safety considerations are produced, e.g. CO. In the Mitchell et al. (1980) work, concentration measurements are given at points spanning a wide range of local equivalence ratio including where the equivalence ratio is greater than one. In the over-ventilated flame study by Mitchell et al. (1980), those results come from point measurements inside the flame where fuel is abundant.

In the work by Lomax and Simmons (1986) in which they studied propane diffusion flames, CO and CO_2 concentration are given for different global equivalence ratios. According to their results the ratio of CO and CO_2 concentration increases considerably when the global equivalence ratio is greater than 1. In their study, Lomax and Simmons (1986) took care to avoid soot formation in their flames through the addition of diluents. Lomax and Simmons (1986) also measured concentration profiles in a propane diffusion flame using a mass spectrometer. Instead of using air for oxidizer they used a mixture of oxygen and argon to avoid the problem of identifying CO in the presence of nitrogen. Lomax and Simmons (1986) noted from the measured profiles that the concentration of CO and other intermediate hydrocarbons decreased as the global equivalence ratio decreased.

Even though over- and under-ventilated flames are physically different, local measurements obtained in over-ventilated flames provide a starting point for the study of under-ventilated flames. Another approach to compare over- and under-ventilated diffusion flames is to consider inverted laminar diffusion flames. These flames can have the overall composition of an under-ventilated flame but the shape of a normal over-ventilated laminar diffusion flame.

Inverted laminar diffusion flames are theoretically the same as normal diffusion flames but in practice the air flows though the inner tube and the fuel through the outer tube of the co-annular burner. The resulting flames tend to produce less soot (Sidebotham and Glassman 1992) and have been reported to produce more CO and H_2 at the tip of the flame (Wu and Essenhigh 1984). The study of these flames could shed some light on the relationship between CO and soot formation.

Burke and Schumann (1928) reported two experiments on inverted flame at the end of their paper. The agreement between the predicted and experimental values of the flame height seems to imply that there is no difference in the physical mechanisms which control the flame contour and height between the normal and inverted flame. On the other hand visual observation of inverted flames shows that they seem to produce less soot than normal flames. This was reported by Walker (1979 pp. 198), "a reverse flame is entirely blue until a large amount of air is forced into the flame". Unfortunately Walker's paper (1979) is mainly descriptive and little absolute values of flow rates are reported.

Wu and Essenhigh (1984) offered a more rigorous study of inverse diffusion flames. Their typical methane flame at a global equivalence ratio of 6.56 was about 2cm high. Their theoretical analysis and predicted species concentrations were compared with measurements of CH_4, CO_2, CO, H_2 and N_2. Reported results show that at the tip of the flame, CO_2 concentration are over predicted and a "substantial pool" of CO and H_2 exists there. Radial concentration profiles also showed an over-prediction of CO_2 on the centerline at a height of 1.84cm. These concentration values as a function of local equivalence ratio were compared to those reported by Mitchell et al. (1980) in his study of normal over-ventilated flames. Wu and Essenhigh (1984) reported that for each species a single curve could be obtained describing its dependence on equivalence ratio regardless of where in the flame the measurements were obtained. This result is similar to the results of Mitchell et al. (1980). Wu and Essenhigh (1984) though, found no counterpart to the high CO and H_2 concentrations observed in inverted flames when compared to normal diffusion flames.

Sidebotham and Glassman (1992) recently studied soot formation in inverse diffusion flames. According to the authors, inverse diffusion flames offer the advantage of separating pyrolysis processes from oxidation processes. Since soot is formed on the rich side of a diffusion flame which is always away from the reaction zone of an inverse diffusion flame, the formed soot is not oxidized in the principal reaction zone. They also offer the advantage of having a much lower soot loading than normal diffusion flames and more easily allow the investigation transition from smoking to nonsmoking conditions. Lastly, since the fuel region of interest is on the outside of the flame front, probe disturbances are limited since the probe does not have to cross the reaction zone.

In the work by Sidebotham and Glassman (1992) flame temperature and fuel structure effects on flame structure and soot formation were observed. The fuels tested were methane, ethene, propene and 1-butene. All the flames studied had a global equivalence ratio of 0.667. An inverted laminar diffusion flame with a global equivalence ratio less than one would normally look fan-shaped but Sidebotham and Glassman (1992) obtained a closed round flame by adding a diluent to the fuel. Furthermore, since the authors were concerned with soot formation, the only species reported are potential hydrocarbon precursors to soot particles and no values of CO or CO_2 were reported.

It is interesting to observe that the theoretical treatment for normal and inverted flames are the same. Yet inverted flames produce less visible soot and more CO at the tip of the flame than normal diffusion flames. Thus inverted laminar diffusion flames could provide further information on CO and soot formation relationships since these quite different combustion products have common chemical and physical formation mechanisms in both normal and inverted flames, but quite different soot production levels.

1.3. Soot Formation

Soot formation has been extensively studied during the past years and several extensive reviews exist (Glassman 1988; Haynes and Wagner 1981; Palmer and Cullis 1965; Wagner 1978). In laminar diffusion flames soot formation is first observed low in the flame on the fuel side. The first soot particles form from condensed phase materials and are sometimes referred as soot nuclei although current theories do not necessarily view this first formation step as nucleation. The process is likely to follow from the growth of the hydrocarbon precursors to form large particle-like "clusters" which is often called particle inception. After particle inception, surface growth increases the mass of soot present, but the number of particles stays the same. During surface growth, gas phase

species react on the surface of the particles and are incorporated into the particles. The particular shape of soot particles is explained by the third step; agglomeration, which occurs when soot particles stick to each other and become chains of spherical particles. If surface growth is rapid these agglomerate surfaces may be smoothed over to produce a more spherical-like particle morphology. In the case of over-ventilated flames, soot particles cross the reaction zone at the top of the flame were they are attacked and oxidized by OH radicals under fuel rich conditions and by O_2 under fuel lean conditions (Fenimore and Jones 1967; Neoh et al. 1981). The oxidation rate of soot and its initial quantity as it enters the oxidation zone will determine if the flame actually emits soot (smoking). In under-ventilated flames, soot particles do not cross the flame reaction zone and are emitted directly into the flame plume.

Megaridis and Dobbins (1990) and Puri et al. (1993) have modified this description and expressed it from a cluster aspect. The inception region of soot extends over a limited region near the bottom of the flame. In the inception region, chemical reactions create a high concentration of primary particles which collide and form "young aggregates" whose number through out the flame remains constant. These primary particles will grow and coagulate to form clusters. These particles progress upward in the flame to the reaction zone in over-ventilated flames where the size of the clusters is reduced by oxidation. Although the size of the cluster can change, the number of primary particles and there size at a particular height are relatively constant. The uniform size and constant number of the primary particles was confirmed by TEM measurements (Megaridis and Dobbins 1990). The agglomerate structure of soot particles was accounted for based on a "fractal-like" structure for the particles rather than assuming them to be spherical. This approach allowed for a more accurate measurements of the soot volume fraction, particle diameter and number concentration properties.

In several studies of soot formation in diffusion flames, critical temperature regions have been identified for both the formation and oxidation processes. In terms of formation, soot particles do not form in laminar diffusion flames if the temperature lies below 1300K (Santoro et al. 1987; Gomez et al. 1984, 1987; Sidebotham and Glassman 1992) while most of the formation occurs in the temperature range 1300-1700K (Kent and Honnery 1991). Oxidation on the other hand as been observed to cease at temperatures below 1300K (Kent and Wagner 1984). Species measurements made in inverted flames by Sidebotham and Glassman (1992) concerning the formation of soot particles are consistent with the hypothesis that the formation of aromatic rings is a controlling factor in soot formation and that acetylene is the principal species once soot inception has begun. These results are consistent with experimental (Harris and Weiner 1983, 1984) and theoretical (Frenklach et al. 1984) premixed flame studies

In the present work the major emphasis involves post flame measurements of soot production and consequently reflect the net results of the soot formation mechanism described above. In addition in-flame probe sampling of gas phase species has been obtained for some limited flame conditions which can be compared to similar measurements obtained in inverted flames.

1.4. CO Formation

Carbon monoxide (CO) is formed from the oxidation of hydrocarbons. According to Glassman (1987 pp. 67), "It is apparent that in any hydrocarbon oxidation process, that CO is the primary product and forms in substantial amounts". CO itself is oxidized primarily through the reactions

$$CO + OH \quad \rightarrow \quad CO_2 + H$$
$$H + O_2 \quad \rightarrow \quad OH + O$$

for temperature condition typical of laminar diffusion flames.

The oxidation of CO to CO_2 usually comes late in the reaction sequence observed in laminar diffusion flames, that is CO_2 formation does not start before the fuel has been converted to CO. It is only when the hydrocarbon species have disappeared that the hydroxyl (OH) concentration increases sufficiently to convert CO to CO_2. This oxidation process takes place at temperature above 1100K. In any practical system where the temperature is below 1100 K or not enough O_2 is present to supply OH radicals, the conversion of CO to CO_2 may not occur. Lomax and Simmons (1986) have shown that CO concentration increases rapidly in oxygen depleted atmospheres. According to this mechanism, most of the CO formed in a diffusion flame during the fuel oxidation process would be oxidized to CO_2 as it progresses to fuel lean regions at high temperatures. Some CO would typically be formed later in the flame as well, when soot particles are oxidized. Although an extensive literature exists on CO oxidation (Yetter et al. 1985), for the purposes of the present study, research studies related primarily to fire situations are more relevant and will be presented.

Zukoski et al. (1991) and Beyler (1986) studied products of incomplete combustion in compartment fires. These studies focused primarily on CO formation. A hood which could extend into the plume region of the fire was used and prevented products of combustion from escaping in the atmosphere. This maintained a layer of gases over the flame similar to the ceiling layer which occurs in room fires. Results of these studies show similar trends involving a progressive increase in CO when the equivalence ratio becomes greater than 0.5 ($\Phi > 0.5$). Beyler (1986) repeated the same experiment with different fuels and noticed a fuel composition influence on the CO yield. Oxygen containing species especially acetone (C_3H_6O), ethanol (C_2H_5OH) and methanol (CH_3OH) show a higher normalized CO yield than propane, propene or hexane. On the other hand, toluene (C_7H_8), which is an aromatic fuel shows the lowest normalized CO yield. No soot measurements were done in Beyler's experiment (1986) but visual observation of alcohol flames show that they produced little soot (i.e. a methanol flame is almost invisible) and that toluene had a very low sooting point (i.e. produces a lot of smoke).

Previous work done by Fisher and Grosshandler (1988) and McCaffrey and Harkleroad (1988) in pool fires has established a simple relationship between the formation of CO and smoke in diffusion flames. McCaffrey and Harkleroad (1988) were careful in the comments section of their paper to note that pool fires are not laminar diffusion flames. Pool fires might exhibit similar regions to laminar diffusion flames, but the oxidation process inside pool fires is more complex because of the buoyancy induced turbulent nature of these flames. According to the authors, reactive species can be expelled through turbulent mixing achieving colder regions where quenching may occur.

Puri and Santoro (1991) studied the influence of soot formation on CO in over-ventilated laminar diffusion flames. Two possible process could influence CO production; 1) quenching because of lower temperatures achieved due to radiation from soot particles and 2) competition for oxidizing radical species, particularly OH, both of which would reduce the conversion of CO to CO_2. Puri and Santoro (1991) observed that a smoking flame produced more CO at higher locations (fuel lean) in an over-ventilated diffusion flame than a nonsmoking one. In fuel rich regions though, they note that "more heavily soot forming flames contain less CO at similar equivalence ratio" (Puri and

Santoro 1991 pp. 599). This is similar to the observation of Beyler (1986) in his study of pool fires. So even though less CO is formed within a smoking flame, the final amount emitted is greater than in a nonsmoking flame. After comparing the reaction rates for the oxidation of CO and soot by OH radicals Puri and Santoro (1991 pp. 602) concluded that competition between soot and CO for OH "is a plausible mechanism that can be responsible for the high CO emissions from fires". However, in these studies the CO and soot production were predominantly studied under fuel lean conditions typical of the oxidation region of over-ventilated laminar diffusion flames. Less information was available on the relationship between soot and CO formation for fuel rich condition.

Recent work on soot and CO emissions from the over-fire (post-flame) regions of turbulent diffusions has also been pursued (Köylü et al. 1991). These studies indicate that for long resident times CO and soot are emitted in direct proportion regardless of the fuel burned. Although these results were obtained over a range of fuel and flow conditions, they correspond to over-ventilated conditions. Thus, information related to fuel rich conditions is still lacking.

The above brief review places in perspective our current understanding of the relationship between soot and CO production in fire situations. Clearly little fundamental information is available for fuel rich conditions regarding the relationship between the formation of these two key combustion products for fires. Based on this assessment a series of under-ventilated diffusion flames studies have been undertaken to characterize the relationship between soot and CO produced in these flames. Measurements have emphasized post flame conditions although some in-flame measurements have also been obtained. The relationship between CO an soot concentrations has been determined for a range of global equivalence ratios extending from 0.5 to 4.0. Studies have mainly focused on methane and ethene as the fuels under consideration. Limited studies involving toluene and methanol have been done to examine the effects of a heavily sooting fuel (toluene) and the influence of oxygen bound to the fuel (methanol).

In the next section the experimental procedure, apparatus and conditions are described. This section is followed by a presentation of the results of the study. These results are then discussed and finally the conclusions of the study are presented.

CHAPTER 2
EXPERIMENTAL TECHNIQUE

The present study of CO and soot production for under-ventilated conditions was conducted using laminar diffusion flames established on a co-annular burner. The experimental apparatus required several distinct components which included: 1)the burner and chimney, 2) flow control system, 3) a dilution assembly for the post-flame analysis, 4) sampling systems for both the in-flame and post-flame measurements and 5) a series of diagnostic techniques to measure the flame products (CO, CO_2, soot, fuel, etc.) and flame conditions (shape and temperature) important in these studies. Measurements techniques included photography for determining the relationship between flame shape and equivalence ratio, non-dispersive infrared (NDIR) analyzers for post-flame CO and CO_2 measurements, gas chromatography for in-flame species measurements, filter collection for soot determination (TEM, mass and composition analysis) and platinum/platinum-rhodium thermocouples for temperature measurements. Application specific sampling probes were utilized for the in-flame and post-flame measurements.

2.1. The Burner Assembly and Dilution System

In order to study under-ventilated laminar diffusion flames, a concentric annular brass burner was used in which fuel flowed through the inner tube and air on the outside. A quartz tube was employed as a chimney to prevent ambient air from interfering with the flame or changing the global equivalence ratio of the flame. The burner assembly and dilution system are shown in Figure 2.1. The design of the burner allowed different combinations of fuel and air tubes to be utilized. Based on observations for several combinations of tubes, three configurations were found to produce sufficiently stable flames over the desired range of global equivalence ratios. These three configurations were subsequently studied and used as a basis to asses burner effects on the flame structure and products (CO, CO_2).

2.1.1. The Burner Assembly

The burner housings were machined from 50.8mm and 25.4mm diameter brass rods. These two burner housings allowed using different quartz tube chimneys to vary the diameter of the air passage. Selection of a particular burner housing was based on providing a leak tight fit between the burner and the quartz tube used for the chimney. Table 2.1 lists the combinations and dimensions of the fuel and air tubes used in the present study. Brass tubes of 9.6mm and 12.7mm O.D. were used for the fuel tubes. The height of the fuel tube with respect to the burner housing could be adjusted by loosening a compression fitting at the bottom of the burner. The fittings were chosen so that the fuel tubes could be interchanged from one housing to the other. The fuel tubes were chosen to be long enough, about 20cm, to ensure laminar flow at the outlet of the tube.

Inside the burner a total of seven 70 gauge screens and 3mm diameter glass beads spread the air flow uniformly around the fuel tube. Flow conditioning with beads and screens aided in obtaining stable flames. Two different diameter fuel tubes and three quartz tubes allowed different velocities for the fuel and air flow. However for a particular burner configuration the air and fuel velocities were not matched when different values of the equivalence ratio, Φ, were studied. The quartz tubes were sealed to the brass housing using Teflon tape or O-rings depending on

BURNER ASSEMBLY

SMOKE COLLECTING
FILTER

PROBE
ASSEMBLY

NITROGEN

O-RING

TRIPPER
PLATE

SCREENS

GLASS BEADS
(DIA=3mm)

AIR

AIR

FUEL
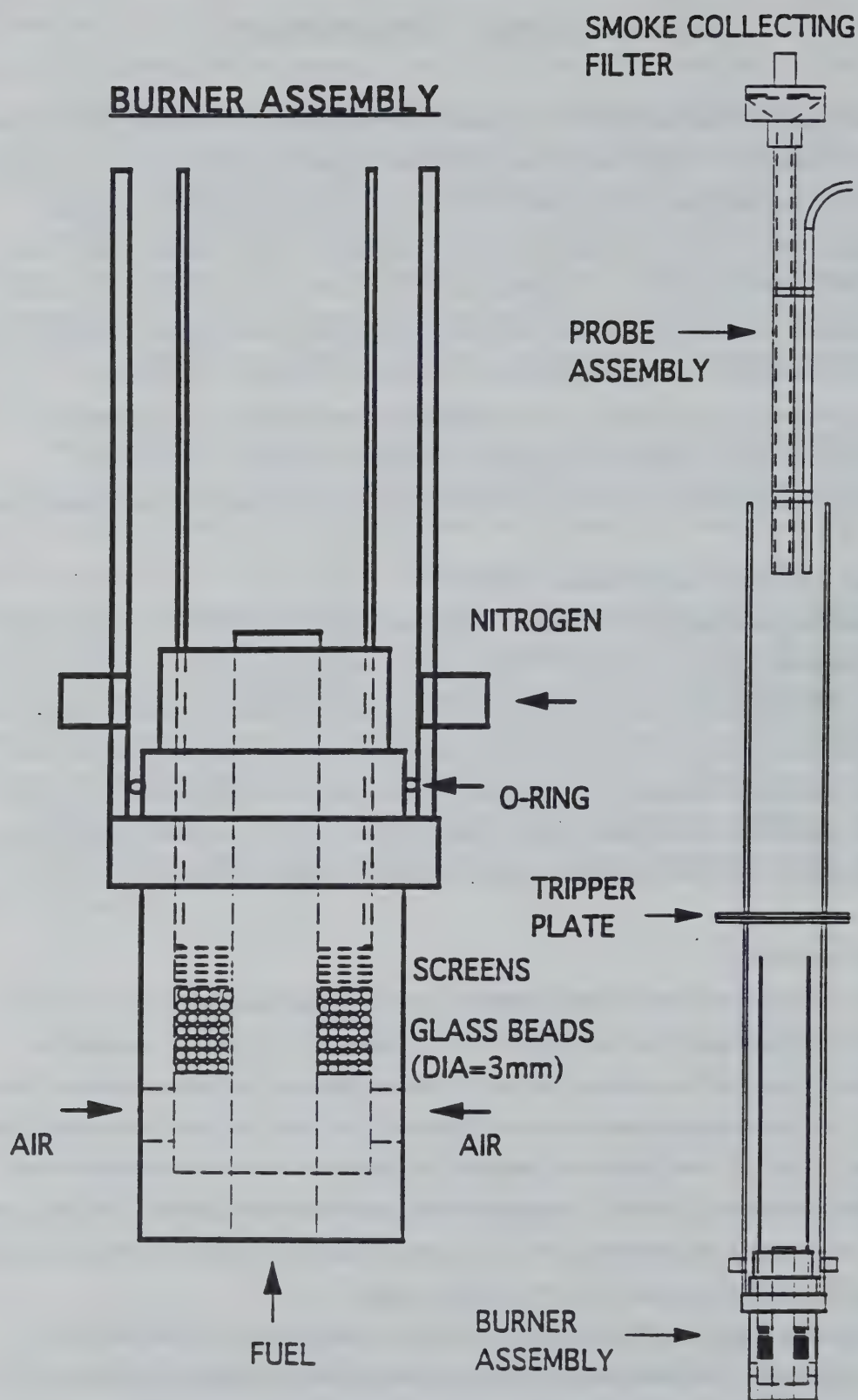
BURNER
ASSEMBLY

Figure 2.1. Burner assembly and dilution system

60

	Inner Fuel Tube (mm) [1]	Outer Air Tube (mm) [2]
Burner Configuration 1	9.6 O.D. (⅜")	29 I.D. 32 O.D.
(50.8mm burner housing)	7.3 I.D.	
Burner Configuration 2	9.6 O.D. (⅜")	22 I.D. 25 O.D.
(25.4mm burner housing)	7.3 I.D.	
Burner Configuration 3	12.7 O.D. (½")	22 I.D. 25 O.D.
(25.4mm burner housing)	11.2 I.D.	

Table 2.1. Tube Dimensions for Co-flow Burners

[1] Brass
[2] Quartz

their diameter. Quartz tubes could resist temperatures high enough to allow soot deposits to be burned off the quartz surface using a propane torch. Another method using employing solvents was tried to clean soot deposits off the quartz tubes, but were not as effective and rapid as burning deposits with a torch. The burner was mounted on a milling machine to allow accurate positioning in three dimensions (± 0.025mm).

2.1.2. The Dilution Assembly

In order to provide a uniformed well mixed region for post-flame sampling, a dilution section followed the quartz chimney (see Figure 2.1). In this dilution section, nitrogen (N_2) was introduced near the bottom of the burner housing through a concentric outer tube. Zero grade nitrogen was provided from a compressed gas bottle. The flow rate was controlled with a needle valve and measured by a rotameter calibrated with a dry test meter (Singer American Meter Division model 802). The nominal flow rate of $590 cm^3/s$ diluted combustion products by a factor of 2 to 30 depending on the global equivalence ratio. The nitrogen was mixed with the product gases 2.5cm below a tripper plate which forced uniform mixing. Two gaskets and a clamp maintained the tripper plate tightly between two Pyrex tubes forming the chimney. The second part of the chimney extended from the tripper plate to the outlet where the exhaust gases were sampled. The chimney extended a total of 55cm from the outlet of the fuel tube to the sampling probe at the outlet of the chimney. The chimney was sealed to the housing using a rubber stopper for the smaller burner and an O-ring was used for the larger burner. Gas sampling at seven radial positions indicated less than a 2% variation in the CO and CO_2 concentration across the chimney exit area and confirmed appropriate mixing. When samples were taken for the gas chromatograph, helium would replace nitrogen to prevent interference with the nitrogen contained in air. The same valve and rotameter used with the nitrogen diluent were retained for the helium case but with, of course, a different calibration curve.

2.1.3. Flow System and Gases

The air supplied to the burner was from a filtered air line at 137.9kPa (20psig). The methane and ethene of CP grade were provided from compressed gas bottles. Figure 2.2 shows a schematic of the flow control system. Needle valves were used to control the flow rates while rotameters provided flow measurement capability. The rotameters were calibrated using bubble flow meters of different sizes and a dry meter for larger air and nitrogen flow rates. During calibration a pressure gauge at the outlet of the rotameter assured that no back pressure was influencing the reading. The position of the ball in rotameters is known to depend on the back pressure (through its effect on gas density) and must be maintained at the same value through out calibration and experimentation. Two rotameters were used to monitor the air flow accurately over the span of values required in the present study. Table 2.2 lists the model number of the rotameter and flow range used for each gas. The tubing between the flow meter and the burner was chosen to be 9.6mm O.D. (3/8") to minimize any pressure drop.

The equivalence ratios were chosen such that they would be equally spaced on a logarithmic scale. By definition the equivalence ratio is

$$\Phi = \frac{[A/F]_{Stoi}}{[A/F]_{Actual}},$$

where $[A/F]_{Stoi}$ is the stoichiometric air to fuel ratio given by $4.76(a + b/4 - c/2)$ where a, b and c, for a specific fuel burning at its stoichiometric condition to form CO_2 and H_2O as products, are defined by

$$C_aH_bO_c + (a + b/4 - c/2)(O_2 + 3.76N_2) \rightarrow aCO_2 + b/2H_2O + 3.76(a + b/4 - c/2)N_2 .$$
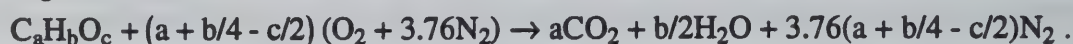
For methane and ethene this expression becomes

$$CH_4 + 2(O_2 + 3.76N_2) \rightarrow CO_2 + 2H_2O + 7.52N_2 \text{ and}$$
$$C_2H_4 + 3(O_2 + 3.76N_2) \rightarrow 2CO_2 + 2H_2O + 11.28N_2 .$$
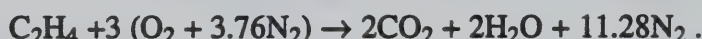
For methane A/F_{Stoi} is therefore 9.52 and 14.28 for ethene. The air flow rates for different equivalence ratios are shown in Table 2.3 for the methane and ethene flames studied.

2.2. Vaporizer System for Liquid Fuel Components

One of the objectives of the present study was to investigate some of the effects of fuel structure on the CO and sooting characteristics of under-ventilated laminar diffusion flames. In particular, the effects of oxygen containing and aromatics fuels were of interest. Consequently a limited number of studies were conducted in which methanol or toluene was added to a methane or ethene flame. To be able to mix methanol or toluene with methane or ethene, a vaporizer was required. Once the liquid fuel vaporized and mixed with the gas carrier fuel flow, the mixture would be injected into the burner through the inner fuel tube. Heating wire was used to prevent condensation in the line from the vaporizer to the burner.

2.2.1. Fuel Supply

A diagram of the fuel supply system for the vaporizer is shown in Figure 2.3. The liquid fuel was supplied to the rotameter through Teflon tubing using a gravity fed approach. Teflon is compatible with toluene and methanol. A 30 micron 304 stainless steel filter prevented the valve from clogging due to any particulates contained in the liquid fuel. A 316 stainless steel needle valve with Kalrez O-ring monitored the flow. A glass and Teflon

Table 2.2. Flow Range and Tube Number of Matheson Rotameters

Gas	Tube Number	Flow Range (cm^3/s)
Nitrogen	605	472 - 708
Air	603	10 - 80
Air	604	80 - 200
Ethene	602	3.2 - 6.4
Methane	602	10 - 21
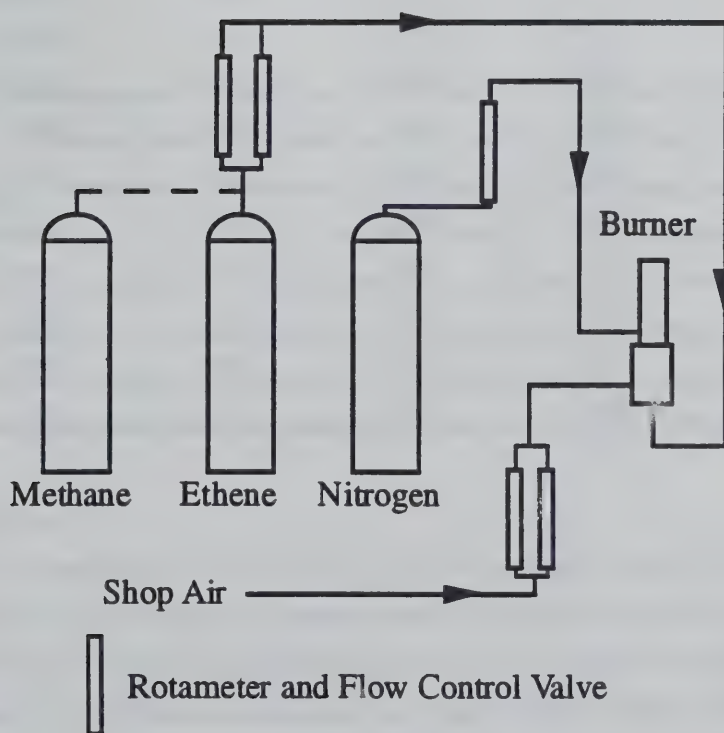
Figure 2.2. Flow Control System for the Burner Assembly and Dilution System

Table 2.3. Air Flows (in cm^3/s) for Different Fuels, Flow Rates and Equivalence ratios

	Methane (CH$_4$)			Ethene (C$_2$H$_4$)	
Φ	10cm^3/s	12.8cm^3/s	20cm^3/s	3.2cm^3/s	6.4cm^3/s
0.50	190.4	243.7	380.8	91.4	182.8
0.57	167.0	213.8	334.0	80.2	160.3
0.66	144.2	184.6	288.5	69.2	138.5
0.76	125.3	160.3	250.5	60.1	120.3
0.87	109.4	140.1	218.9	52.5	105.0
1.00	95.2	121.9	190.4	45.7	91.4
1.15	82.8	106.0	165.6	39.7	79.5
1.32	72.1	92.3	144.2	34.6	69.2
1.52	62.6	80.2	125.3	30.1	60.1
1.74	54.7	70.0	109.4	26.3	52.5
2.00	47.6	60.9	95.2	22.8	45.7
2.52	37.8	48.4	75.6	18.1	36.3
3.18	29.9	38.3	59.8	14.4	28.7
4.00	23.8	30.5	47.6	11.4	22.8

rotameter FL-1 was calibrated using the barrel of a 1 cm^3 syringe and a stopwatch. During operation the liquid fuel was fed from the rotameter to the vaporizer through a 1.59mm O.D. (1/16") stainless steel tube. Before injection in the carrier gas, the liquid fuel was heated to slightly below its boiling temperature to prevent vapor lock and consequently flame pulsation. For reference, Table 2.4 lists the boiling point and heat of vaporization of the two liquids used in this study.To be able to compare the flames with the fuel additives to the pure methane or ethene flames a constant carbon flow rate of 12.8cm^3/s (carbon mass flow rate of 153.6g/s) was maintained. In this study 80% of the carbon was provided by the gaseous fuel (methane or ethene) and the rest is vaporized liquid fuel. The calculation for the stoichiometric air flow rate is a little different than in the pure gaseous fuel case. For methane flames the stoichiometric air to fuel ratios are given for methanol addition by

$$0.8CH_4 + 0.2CH_3OH + 1.9 (O_2 + 3.76N_2) \rightarrow CO_2 + 2H_2O + 7.14N_2$$

and for toluene addition by

$$0.8CH_4 + \frac{0.2}{7}C_7H_8 + 1.86 (O_2 + 3.76N_2) \rightarrow CO_2 + 1.71H_2O + 6.98N_2 .$$
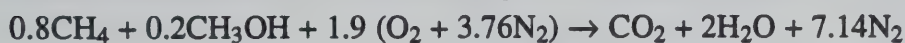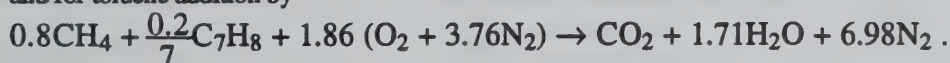
For the ethene flame these ratios are given for methanol addition by

$$0.4C_2H_4 + 0.2CH_3OH + 1.5 (O_2 + 3.76N_2) \rightarrow CO_2 + 1.2H_2O + 5.64N_2$$

and for toluene addition by

$$\frac{0.8}{2}C_2H_4 + \frac{0.2}{7}C_7H_8 + 1.46 (O_2 + 3.76N_2) \rightarrow CO_2 + 0.91H_2O + 5.48N_2 .$$
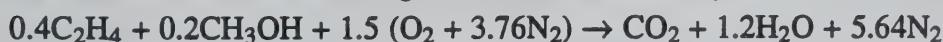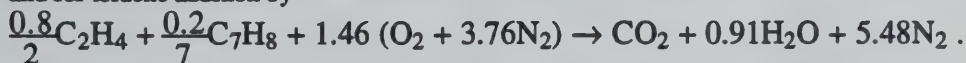
The air flow rates for the different liquid and gaseous fuel flow rates as a function of equivalence ratio, Φ are shown in Table 2.5.

2.2.2. The Vaporizer

A sketch of the vaporizer is shown in Figure 2.4. The vaporizer itself is essentially a 12.7mm O.D. (1/2") brass tube filled with 3mm diameter glass beads in which the open end of the liquid fuel tube was inserted. The brass tube was heated to supply enough energy to completely vaporize the liquid fuel passing through the inner tube. If the energy had only been supplied by the carrier gas, the temperature drop of the gas mixture would have been to large to maintain completely vaporized liquid. The outlet temperature of the mixture was monitored to assure that the temperature of the mixture never dropped below the condensation temperature. Heating wire was also placed around the tubing up to the burner to prevent condensation. Transparent Teflon PFE tubing capable of withstanding temperatures up to 260°C, was used to allow visual verification that no liquid was condensing in the tubing.

2.2.3. The Carrier Gas

The heated carrier gas was introduced through a cross connector and initially flowed in a concentric tube surrounding the liquid fuel supply line (see Figure 2.4). Methane or ethene was used for the carrier gas depending on the flame desired. The carrier gas was heated to a specified temperature below the boiling temperature of the liquid fuel. This carrier gas provided additional heat to the preheated liquid fuel through the stainless steel tube before mixing with the vaporized liquid. The pressure of the carrier gas at the inlet of the vaporizer was measured to assure that the calibration of the flow meters was still valid.
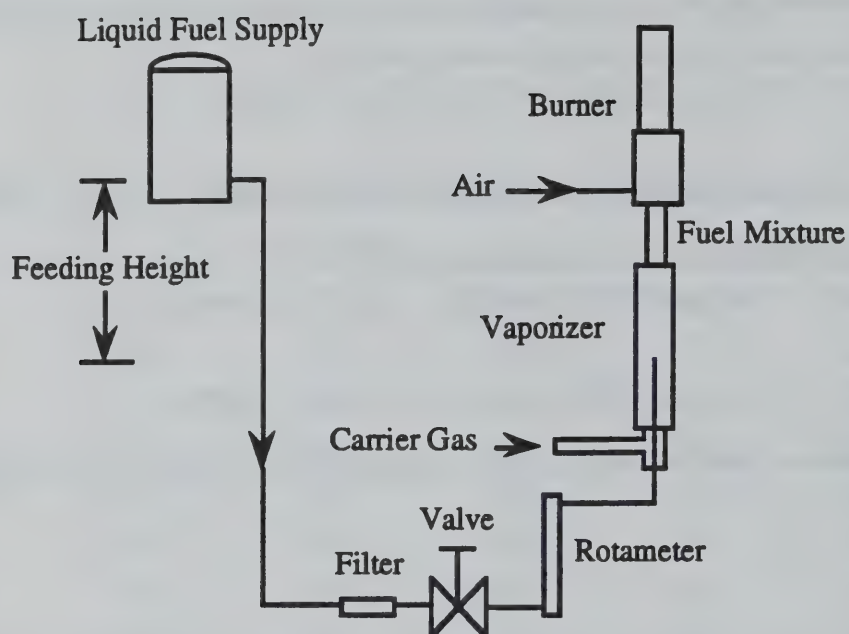
Figure 2.3. Fuel Supply System for the Vaporizer

Table 2.4. Properties of liquid fuels used in the present study

Fuel	Chemical Formula	Boiling Point (K)	Heat of vaporization (kJ/mol)
Methanol	CH_3OH	337.7	36
Toluene	$C_6H_5CH_3$	383.8	34

Table 2.5. Air flow rates (in cm^3/s) for methane and ethene mixture flames with methanol and toluene as a function of equivalence ratio.

Φ	Methane 12.8cm^3/s		Ethene 6.4cm^3/s	
	20% Methanol	20% Toluene	20% Methanol	20% Toluene
0.50	231.4	226.3	182.8	177.5
0.57	203.0	198.5	160.3	155.7
0.66	175.3	171.5	138.5	134.5
0.76	152.3	148.9	120.3	116.8
0.87	133.0	130.1	105.0	102.0
1.00	115.7	113.2	91.4	88.8
1.15	100.6	98.4	79.5	77.2
1.32	87.7	85.7	69.2	67.2
1.52	76.1	74.5	60.1	58.4
1.74	66.5	65.0	52.5	51.0
2.00	57.9	56.6	45.7	44.4
2.52	45.9	44.9	36.3	35.2
3.18	36.4	35.6	28.7	27.9
4.00	28.9	28.3	22.8	22.2

Figure 2.4. Schematic representation of the liquid fuel vaporizer

2.3. Flame Pictures

The pictures of the flames shown in this work were taken using a Nikon 8008 camera and a Nikkor micro lens with a minimum f_{stop} of 3.5 and a focal length of 5.5cm. The camera was set on a tripod and adjusted to be located at the same height as the burner. The film used was Kodak Gold *Plus* with a sensitivity of 400 ASA. Because of the difficult lighting conditions, exposures were bracketed and pictures were chosen from among those judged to reproduce the flame colors most accurately.

2.4. Gas Sampling

Gas sampling probes were used to provide gas species concentration measurements both in the flame and at the chimney exit. For the in-flame measurements, one of two types of quartz microprobes were utilized depending on the soot loading and flame location conditions as will be described below. For the carbon monoxide (CO) and carbon dioxide (CO_2) measurements obtained as part of the global equivalence ratio studies, a simple stainless steel tube probe was located at the chimney exit. The sample gas would then be directed through non dispersive infrared (NDIR) analyzers or stored in sample loops before being analyzed by the gas chromatograph.

2.4.1. Post-Flame Measurements as a Function of Global Equivalence Ratio

2.4.1.1. Sampling System

Figure 2.5 shows the gas sampling and the soot collection system used in the global equivalence ratio studies. The soot collection system will be described in section 2.5. A 6.35mm O.D. (1/4") stainless tube sampled product gases from the top of the chimney. The gas was then filtered using a Whatmann Hepa-Cap 36 filter and passed through a wet ice and a dry ice bath. The system could be run for three to four hours before requiring thawing of the line which passed through the dry ice bath. Once filtered and dried, the sample gas was pumped through a bellows pump to a rotameter to assure the operator that the sample flow rate was within recommended flow specifications of the analyzers. The bellows pump was used in order to eliminate contamination of the sample gas with oil or ambient gases. The CO and CO_2 concentrations in the sample gas were then measured by NDIR analyzers before the gas was expelled through a hood.

2.4.1.2. NDIR and Gas Chromatographic Analyzers

Data on the CO and CO_2 concentrations achieved at the chimney exit were obtained using two different sets of NDIR analyzers. The first set of data was measured using two Horiba NDIR analyzers using a separate valve and flow meter to assure that the sample flow rate was within the proper operational range. When comparison runs were made with the gas chromatograph, the sample loops were placed between the bellows pump and the rotameter. A discrepancy between the NDIR analyzers and the gas chromatograph results of 10% to 15% was noted during the study and a second set of data was taken using two different NDIR analyzers as will be described later in this section.
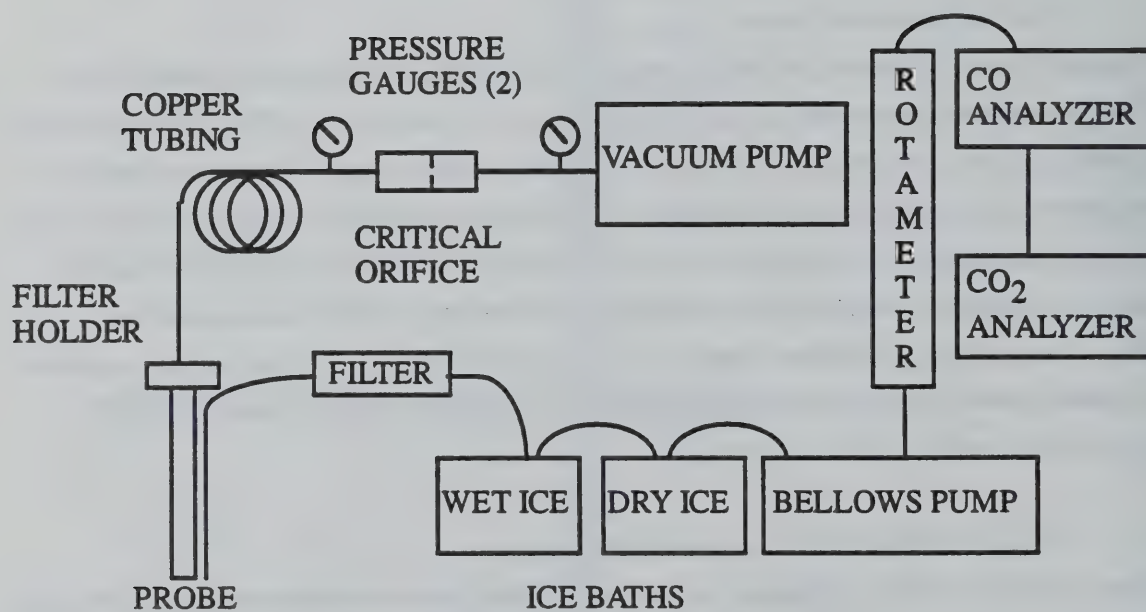
Figure 2.5. Gas and soot sampling system used in global equivalence ratio studies.

In a typical me surement sequence, readings from the CO and CO_2 NDIR gas analyze would be recorded, Φ would then be changed by varying the air flow rate and after about sixty seconds to allow equilibration in the sample volume, the gas analyzer readings for the new condition would be recorded.

The first set of data obtained used two linearized Horiba NDIR analyzers (model PIR-2000). They were calibrated using a 0.105% CO in N_2 and a 5.03% CO_2 in N_2 certified mixtures. These values were verified with the gas chromatograph to be within ±5%. These analyzers required the sample gas to be filtered and free of water vapor. As mentioned above, part way through the study a 10% to 15% difference was noted between the NDIR and gas chromatograph analyzers for CO and CO_2. Since the NDIR analyzers provided for more rapid measurement capability and ease of operation, it was deemed necessary to resolve these differences. Thus a second set of data was taken using a CO analyzer model VIA-510 from Horiba that compensated for CO_2 and water vapor interference and a CO_2 analyzer model 864 from Beckman. They were calibrated using 0.920% CO in nitrogen and 4.59% CO_2 in nitrogen mixtures. The Horiba CO analyzer had an output linearizing board which provided a linear voltage response for this instrument as a function of the CO concentration. The Beckman CO_2 analyzer was not linearized and the voltage output of the CO_2 analyzer had to be converted to a concentration using the calibrations curve sent with the instrument from the company. Both sets of NDIR analyzers were also tested using Standard Reference Material Gas Mixtures (NIST SRM 2619a, 5066±5ppm CO_2 in N_2 and NIST SRM 2637a, 2400±24ppm CO in N_2). These calibration with the Standard Reference Material Gas Mixtures indicated that the first set of analyzers were in error by a small amount, but that the second set of analyzers were quite accurate. Based on the results of Standard Reference Material Gas calibration, data taken with the first set of analyzers were corrected as described in Appendix A. The drift in the zero for the NDIR instruments was on the order of the instruments sensitivity. A slight cross sensitivity of the CO meter to ethene was observed. These uncertainties combined with uncertainty of the calibration gas are estimated to be ±2% for the CO and ±3% for the CO_2 gas analyzer.

2.4.2. In-Flame Concentration Measurements

2.4.2.1. Sampling Probes for In-Flame Measurements

Detailed in-flame measurements for fuel and combustion products where obtained for two under-ventilated flames in order to more fully characterize the structure of these flames. Concentration profiles of a methane/air diffusion flame with a fuel flow rate of $10 cm^3/s$ and an ethene/air diffusion flame with a fuel flow rate of $6.4 cm^3/s$ at a $\Phi = 4$ were measured. During these tests the outer Pyrex tube part of the dilution system was not used. For the concentration profiles two types of probe were used. The simplest one was a quartz microprobe with an orifice diameter of 0.094mm. This probe was limited to the non-sooting area of the flame due to its small orifice which was easily clogged by soot particles. The small orifice diameter had the advantage of offering better sampling resolution and had no visible effect on the flame. Schoenung and Hanson (1981) examined the measurement capabilities of uncooled quartz probes for CO and concluded that lower pressures (approximately 6.67kPa) minimized post sampling reactions. Since the concentration measurements using the quartz probe were taken at a pressure below 1.33kPa, CO to CO_2 conversion in the probe were assumed to be negligible.

71

The second probe utilized was the Electromechanical Sonic Probe developed at The Pennsylvania State University (Puri 1992) which employs a larger orifice of an equivalent diameter of 0.184mm. The principle behind this probe is to place a small metal fiber through the orifice and oscillate it to maintain the orifice free of soot particles. A function generator produces a voltage at a fixed frequency that is applied to a solenoid which acts on the iron core of the fiber inside the probe. The resulting motion of the fiber prevents soot from building up and obstructing the orifice. This probe could sample gas in sooting areas of the flame, but would disrupt the flame if used at too low a height. Fortunately it was possible to find suitable locations where either the quartz microprobes or the Electromechanical Sonic Probe could be applied. Measurements of the radial profile of the species concentration were obtained at several heights above the burner. In general the probe was traversed across the burner in steps of 1.5mm. Samples were stored and subsequently analyzed on the gas chromatograph.

The different locations at which concentration profiles were measured were selected based on the local equivalence ratio at the center line of the flame. In an over-ventilated laminar diffusion flame it is possible to relate measurement position to the flame height. In under-ventilated flames this is much more difficult since the flame height varies for different burner geometries. Thus it would be difficult to relate flames from different burners. The height at which profiles were obtained was therefore based on achieving similar local equivalence ratios at the flame centerline. For under-ventilated flames with a global equivalence ratio (Φ) of 4, the span of local equivalence ratio (ϕ) varies theoretically from 0 at the air exit to infinity at the exit of the fuel. The maximum value observed was actually in the thousands due to the diffusion of certain species and the precision of the gas chromatograph.

2.4.2.2. Sampling System

To quench the species reactions in the microprobe, a sonic sampling approach was used in which a vacuum pump was used to provide the low pressure region behind the orifice. The sample loops were located between the probe and the vacuum pump which eliminated any possible contamination from the pump. The sampling system used for in-flame measurements is shown in Figure 2.6. A dry ice bath was used to condense water vapor before the samples were stored through a multi-position valve in sample loops whose volume was $10cm^3$. A maximum of fifteen samples could be stored before analysis with the gas chromatograph. Once dried the gas would fill a large cylinder which was then pressurized to approximately 100kPa using a piston compression arrangement. A pressure of 100kPa was verified to be high enough to assure the sample to fill the gas chromatograph sample loop which had a volume of 250µl. The piston inside the cylinder was activated by helium which was also used as a carrier gas in the gas chromatograph. The operation of the gas chromatograph will be described in the next section. Following the acquisition of a sample, the entire system was purged as illustrated in Figure 2.6 and another sample could be obtained. The piston and the cylinder were made of brass and Buna-N O-rings prevented leaks around the piston. In case leaks did occur, concentrations were computed to adjust for dilution by helium based on a mass balance for the measured species.

Leaks in the sampling system were checked before each series of tests by lowering the pressure using the vacuum pump and then monitoring the pressure increase over some fixed time. A minimum absolute pressure would typically be 26.7Pa (0.2torr). A pressure increase of 13Pa at an absolute pressure of 100Pa after at least 10min was judged acceptable. The sampling system and valve sequence during leak testing is shown in Figure 2.7.

Valves Condition	1	2	3	4	5	Cyl
Return Cyl. to A	C	C	C			B → A
Pre Sampling	O	C	O			A
Sampling (1 min)	O	O	O			A
Post Sampling	C[2]	O	C[1]			A
Filling Loop	C	C	C			A → B

When Sample Loop Pressure Reaches 15 psi ➔ Switch Sample Loop

[1] First Step

[2] Second Step (after another minute)

O Open
C Close
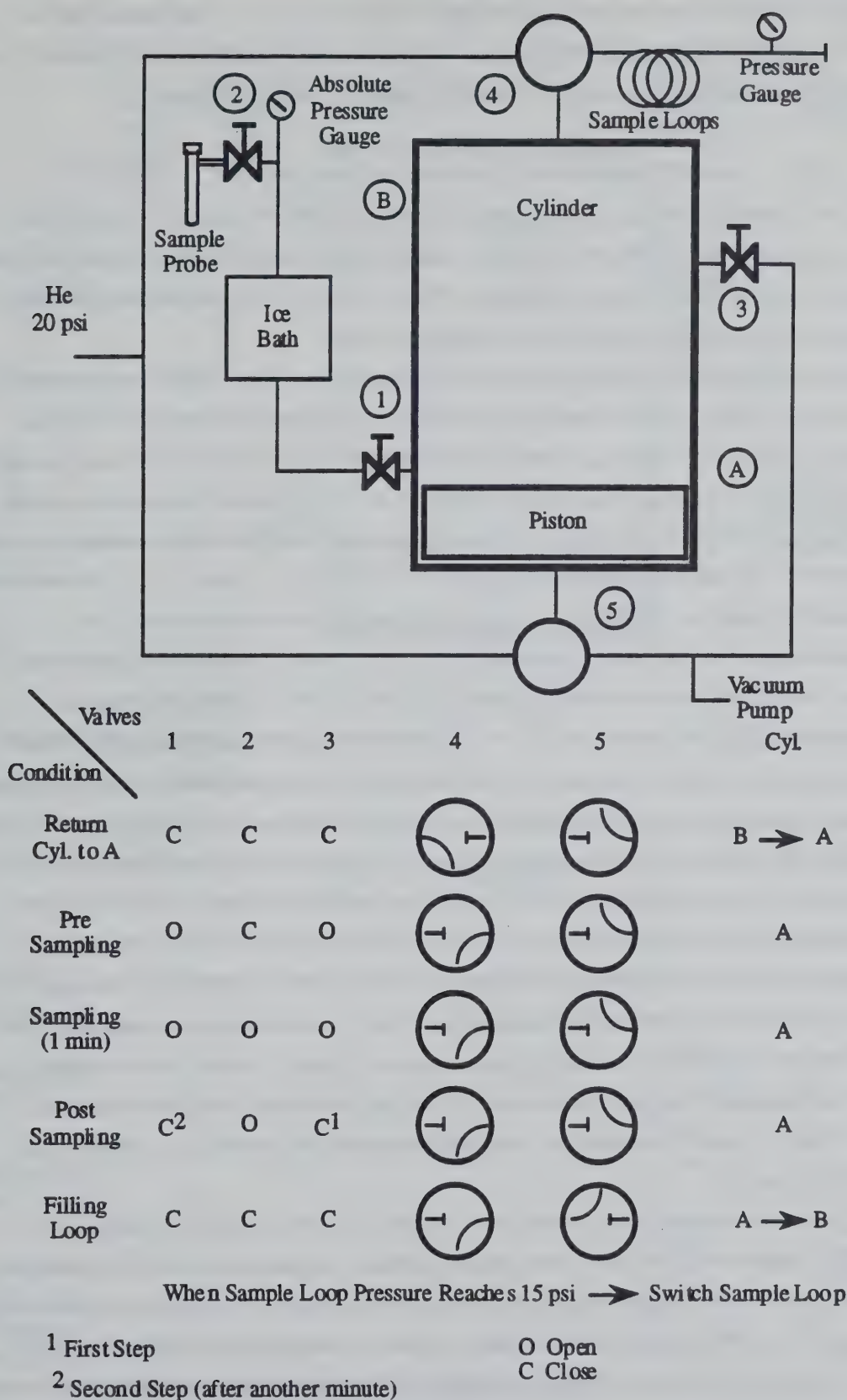
Figure 2.6. Cylinder system and valve sequence during sampling

73

2.4.3. Gas Chromatography

Although the NDIR analyzers provided rapid measurements of the CO and CO_2 concentration they were limited to those two species. The gas chromatograph on the other hand provided concentration measurements of any species separable by the columns and measurable by the analyzers inside the gas chromatograph.

2.4.3.1. Species Separation and Concentration Measurements

Samples were injected into the gas chromatograph (GC) using a valve. The sample valve is shown in Figure 2.8. This is by far the most reliable way of injecting samples. The sample first flows through valve 1 and onto the sample loop contained inside the gas chromatograph. When valve 1 is switch ON the sample is injected into the helium gas flow (carrier gas) and carried onto the separation columns.

Three columns were used to separate the different components of the sample gas. These columns were connected in series but the order of the columns could be altered via a valve switching arrangement contained in the GC (see Figure 2.9). The three columns, a Porapak Q, a Porapak S and a molecular sieve 5A, each 1.83m long, were used in the GC to separate the species contained in each sample. Figure 2.10 shows schematically the separation process and the column switching of the gas chromatograph. The analysis procedure using the columns switching approach will be briefly described. The sample containing H_2, O_2, Ar, N_2, CO, CH_4, CO_2, C_2H_4, C_2H_2, C_2H_6 and other hydrocarbons is initially injected onto the Porapak Q column. The Porapak Q column separates CO_2 and hydrocarbons from each other but is incapable of separating H_2, O_2, Ar, N_2 and CO which elude together onto the Porapak S column. The Porapak S column can not separate H_2, O_2, Ar, N_2 and CO either, but separates hydrocarbons especially C_2H_n. The gases H_2, O_2, Ar, N_2, CO finally elude onto the molecular sieve 5A which offers the separation capability necessary to measure their concentration. The molecular sieve 5A could not separate oxygen from argon so a constant ratio was assumed between argon and nitrogen based on the composition of air, in order to correct the oxygen measurements for the presence of argon. The order of the molecular sieve 5A and the two Porapak Q and S columns is reversed before CH_4 and CO_2 elude onto the molecular sieve column. If CH_4 was allowed onto the molecular sieve, the species retention time would be much longer and the CH_4 concentration measurement could interfere with other hydrocarbons eluding from the two Porapak columns at a later time. CO_2 on the other hand can not be allowed to elude onto the molecular sieve where it would be trapped permanently. Once valve 2 is switched and the column order reversed, species elude from the Porapak S column onto the analyzers. Species inside the molecular sieve when the columns order is altered have to elude once more through the two Porapak columns. Table 2.6 shows all the separable species, their retention time and the type of analyzer which measures their concentration.

Once the gases were separated by the columns they were measured by two analyzers or detectors. The present GC (Hewlett-Packard model 3890) contains two detectors, a Flame Ionization Detector (FID) and a Thermal Conductivity Detector (TCD). The former measures the change in the ion current in the analysis flame used in the FID as a sample eludes from the GC column, while the latter responds to a change in thermal conductivity. The major problem with helium as a carrier gas in this GC configuration is the measurement of hydrogen. Hydrogen can not be detected with the FID since hydrogen does not affect the flame ions and its thermal conductivity is similar to helium and therefore is barely detectable by the TCD. When hydrogen was present, it often eluded at two

Absolute Pressure Gauge

②

Sample Probe

Ice Bath

①

Cylinder

Ⓑ

④

Sample Loops

Pressure Gauge

③

Ⓐ

Vacuum Pump

Piston

⑤
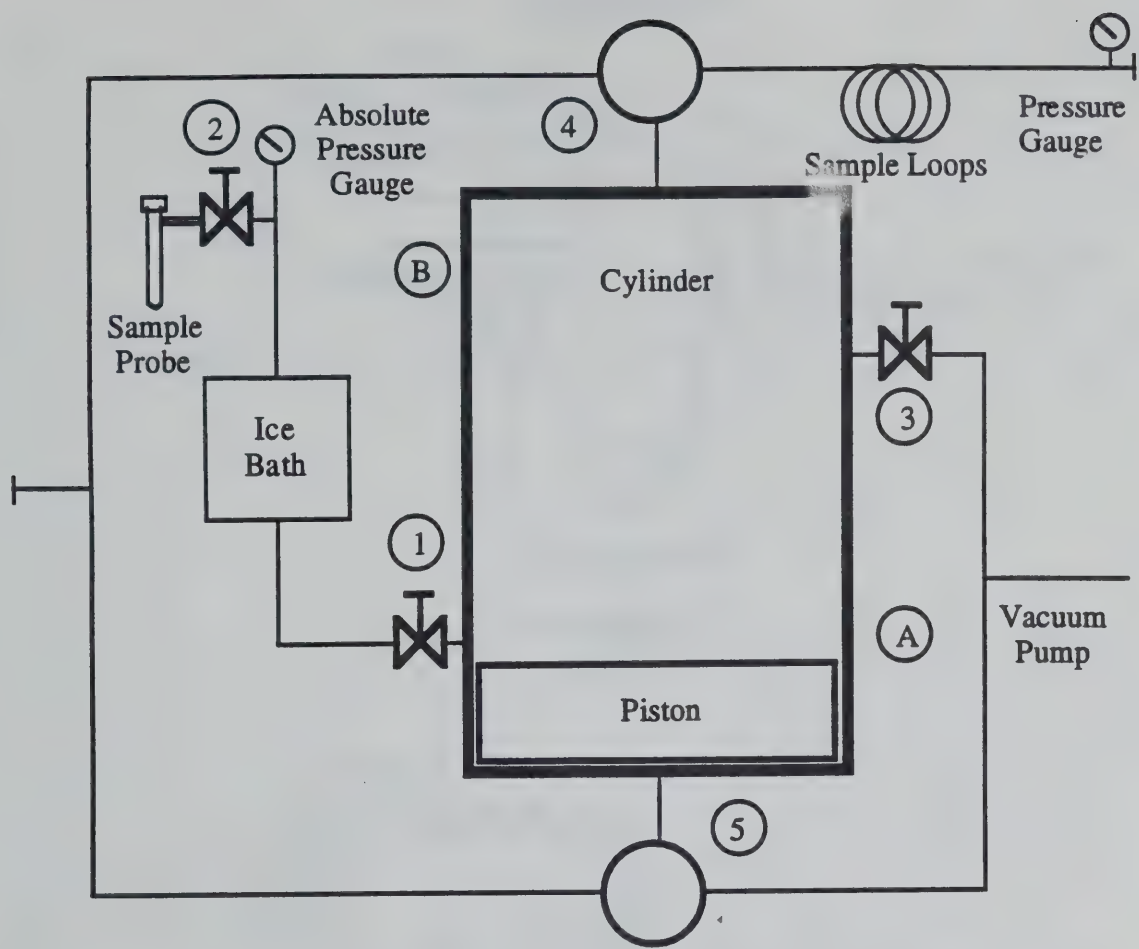
O Open
C Close

Leak Testing

Condition \ Valves	1	2	3	4	5
Evacuating He Line	O	C	O		
Evacuating Loop Line	O	C	O		
Pressure Monitoring (Vacuum Pump Off)	O	C	C		

Figure 2.7. Cylinder system and valve sequence during purge and leak test

VALVE 1

Valve 2

Sample In

Carrier Gas

Sample Out

Sample Loop

OFF

Valve 2

Carrier
Gas

Sample Loop
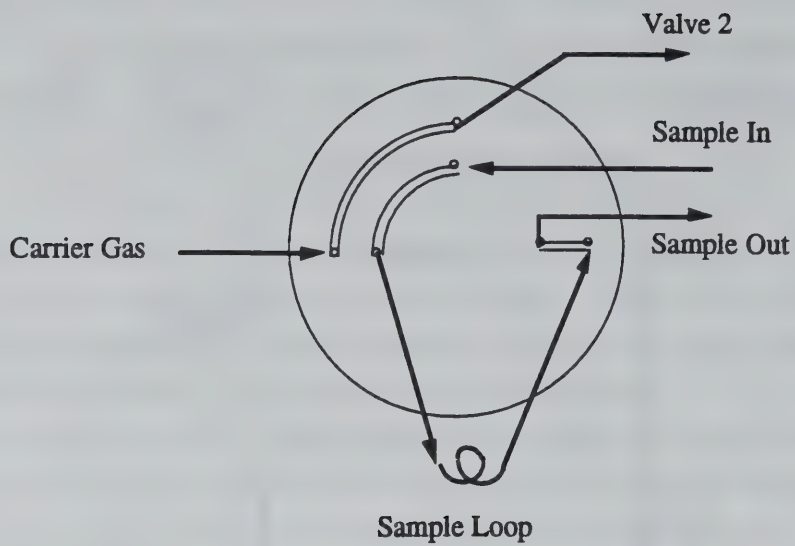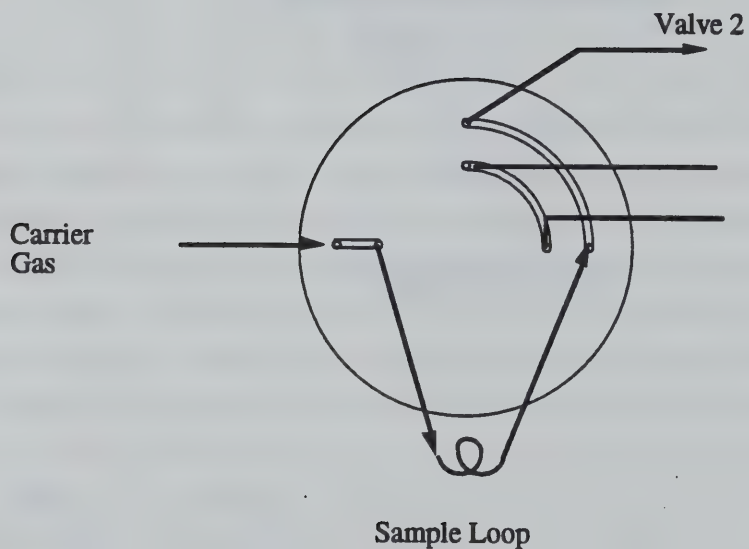
ON

Figure 2.8. Sample valve in the gas chromatograph

VALVE 2

Porapak S   Porapak Q

Sample

Detectors

Molecular Sieve 5A

OFF

Porapak S   Porapak Q

Sample

Detectors

Molecular Sieve 5A
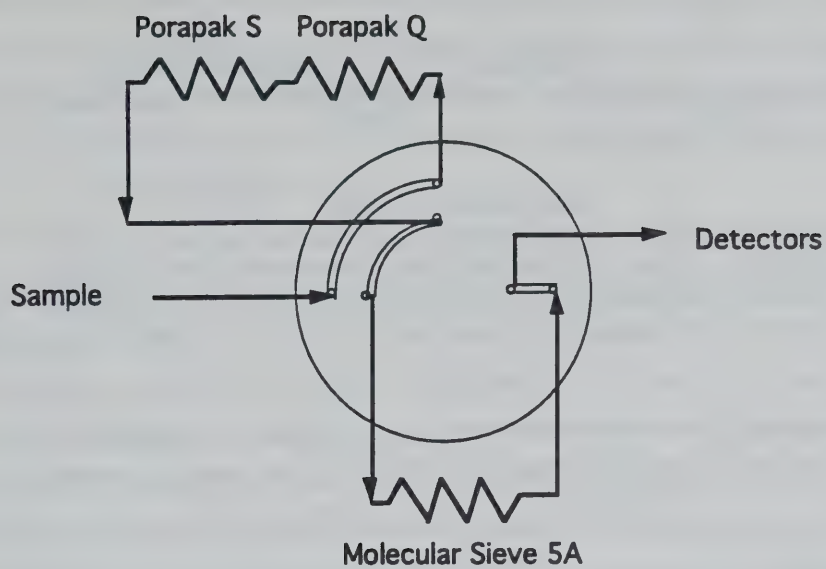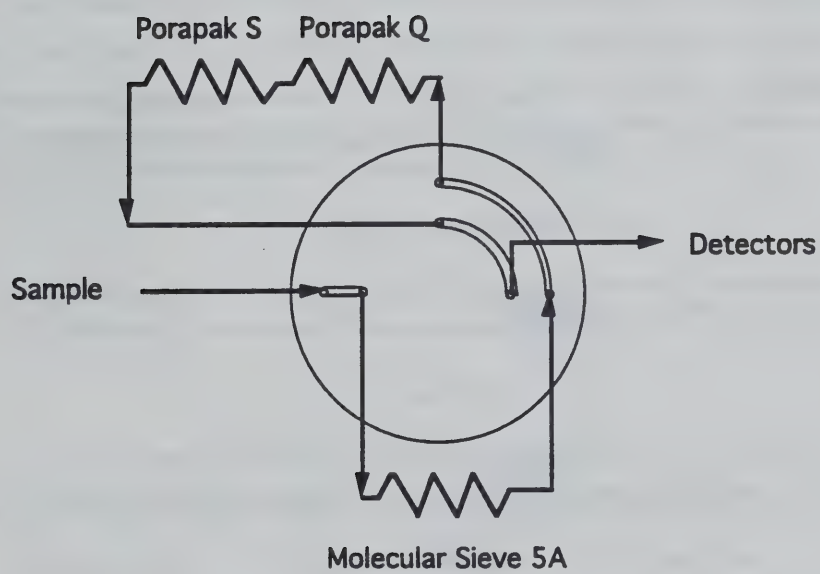
ON

Figure 2.9. Column switching valve in the gas chromatograph

77
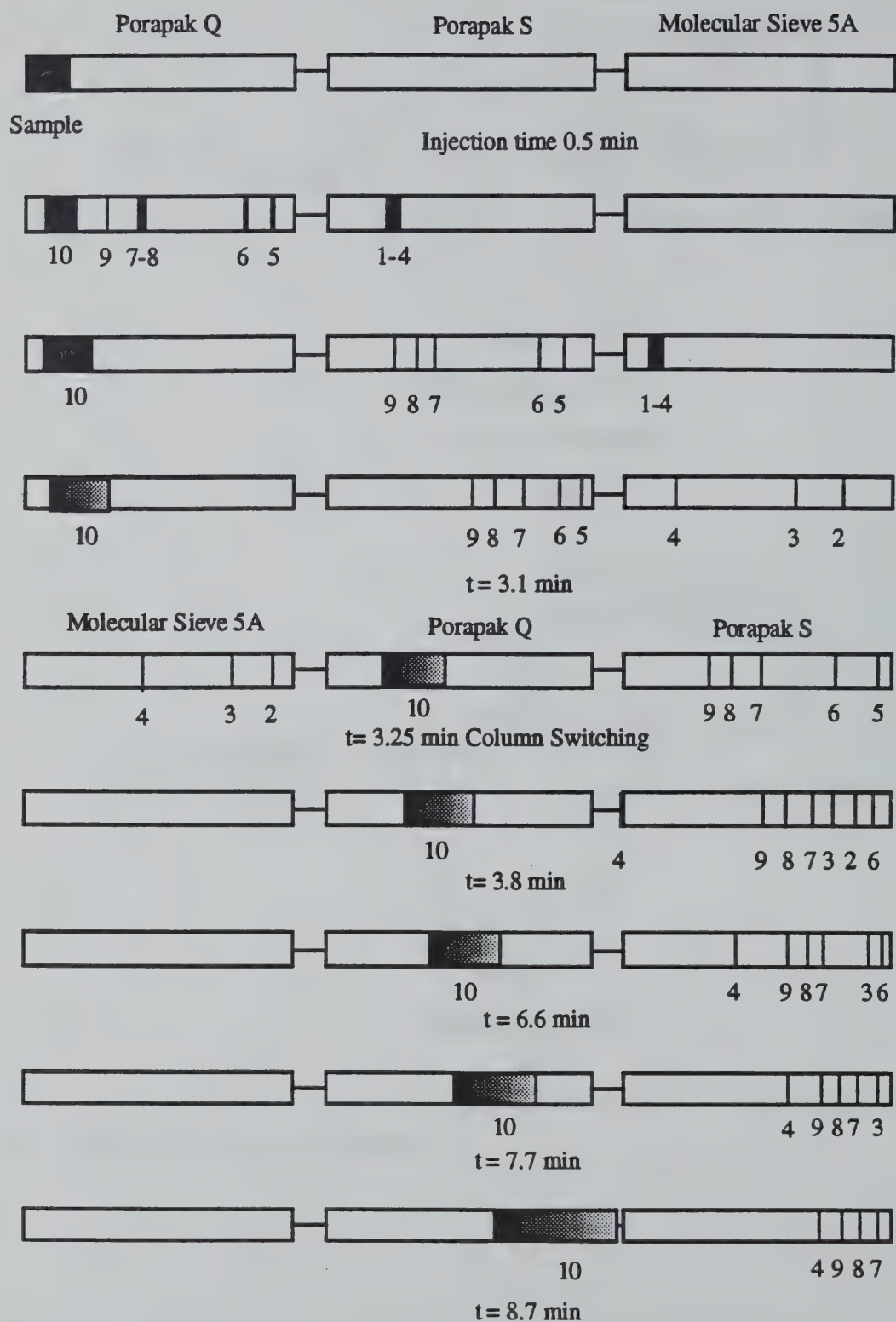
Figure 2.10. Schematic diagram of column separation and column switching where the numbers correspond to: 1 - H_2, 2 - O_2, 3 - N_2, 4 - CO, 5 - CH_4, 6 - CO_2, 7 - C_2H_4, 8 - C_2H_2, 9 - C_2H_6 and 10 - other hydrocarbons.

separate times and calibration for hydrogen was impossible. The TCD measured methane (CH_4), oxygen (O_2), carbon dioxide (CO_2), nitrogen (N_2), carbon monoxide (CO) and high concentrations of ethene (C_2H_4). The FID measured the hydrocarbons. The signals from the analyzers were sent to two integrators (model HP3396A) which plotted the detectors response and determined each gas concentration from previous calibrations.

2.4.3.3. Calibration

The calibration of the gas chromatograph was done using Scott's calibration mixtures. The content of the different calibration mixtures used for calibration is shown in Table 2.7. Multi-level calibration was necessary for most of the species since the TCD and FID were not linear throughout the span of concentration values found in the samples. To calibrate for methane and ethene concentrations above 5%, mixtures had to be custom made. The FID can not be damaged by higher concentration of hydrocarbons, but tends to saturate so the TCD was also calibrated for high concentrations of methane and ethene. The concentrations of the calibration gases were based on the partial pressure of each gas. Two component gas mixtures were made with methane or ethene and nitrogen. The gas mixtures were stored in gas bottles previously evacuated. Once evacuated the bottle was filled by a certain amount of nitrogen and the pressure measured. The second gas component would then be added and the total pressure measured a second time. The concentration of either gas could then be calculated based on their partial pressure and the total absolute pressure inside the bottle. To validate this method, comparison tests were made between custom made low concentration mixtures and Scotty's calibration mixtures. The comparison tests revealed that the custom mixture concentrations were within ±3% of the predicted concentrations.

Table 2.6. Species, retention time and gas chromatograph analyzer

Species	Retention Time (in minutes)	Analyzer	Species	Retention Time (in minutes)	Analyzer
H_2	3.1	TCD	C_3H_6	21.0	FID
CH_4	3.9	TCD/FID	C_3H_8	21.8	FID
O_2	6.6	TCD	C_4H_8	23.3	FID
CO_2	7.7	TCD	C_4H_{10}	25.4	FID
N_2	8.7	TCD	C_5H_{10}	28.1	FID
C_2H_4	13.4	TCD/FID	C_5H_{12}	29.5	FID
C_2H_2	14.6	FID	C_6H_{12}	34.6	FID
C_2H_6	15.7	FID	C_6H_{14}	36.6	FID
CO	18.4	TCD	C_6H_6	39.6	FID

2.5. Soot Sampling

Soot samples were taken simultaneously with the CO and CO_2 overall measurements. Soot collected on filters allowed a quantitative measurement of smoke emissions. Soot samples were also collected on microscope grids and observed under a Transmission Electron Microscope (TEM). Other soot samples were sent to a professional laboratory (Sunset Laboratory, Oregon) to measure organic and elemental content of soot samples.

2.5.1. Soot emissions

A diagram of the soot sampling system was previously shown as part of the gas sampling system in Figure 2.5. The smoke was collected through a 15.9mm OD stainless tube 360mm long and a 47mm diameter filter holder. Pre-weighted filter were used to collect soot samples. A vacuum pump forced a flow through the filter and a critical orifice controlled the flow. The smoke sampling tube provided cooling of the gases and prevented deterioration of the polytetrafluoethylene (PTFE) coated filter. The collection efficiency for the glass fiber filter (Pallflex T60A20) is 60% to 70% for 0.035µm diameter and at least 93% for particles with diameters of 0.3µm and larger according to Liu et al. (1983). The nominal flow through the filter of $153cm^3/s$ was calibrated each day with a dry meter. Pressure gauges were used to monitor the vacuum pressure and the pressure drop across the filter. The maximum pressure drop cross the filter was 1.3kPa (50" of water) during collection and this corresponds to about 15mg of smoke on the filter. Smoke collection required about five minutes after which the filter was removed and replaced with another pre-weighed filter. Filter weighings were repeatable to ±0.02mg using a microbalance with a 0.01mg sensitivity.

Soot was visibly depositing on the surface of the chimney and inside the sampling probe during the measurements. An estimate was made of the amount of smoke deposited on the tube wall relative to the amount collected on the filter. The smoke deposited on the wall was removed using a plunger device. Repeat measurements gave smoke

Table 2.7. Scotty calibration mixture number and composition

Mixture	Content ±2% (balance N_2 unless specified otherwise)
216	C_2H_2 1.00%, C_2H_6 1.00%, C_2H_4 1.00%, CH_4 1.00%, CO_2 1.00%, CO 1.00%
218	CH_4 1.00%, CO 1.00%, CO_2 1.00%, H_2 1.00%, O_2 1.00%
220	CH_4 0.010%, C_2H_6 0.010%, C_3H_8 0.010%, C_4H_{10} 0.010%, C_5H_{12} 0.010%, C_6H_{14} 0.010%
222	C_2H_4 0.010%, C_3H_6 0.010%, C_4H_8 0.010%, C_5H_{10} 0.010%, C_6H_{12} 0.010%
234	O_2 4.98%, CH_4 3.97%, N_2 4.99%, H_2 4.02%, CO_2 5.05%, CO 5.02% balance He
237	CH_4 4.51%, O_2 7.01%, CO_2 15.0%, CO 7.00%

depositions of 12% and 14%. These measurements were done at a relatively high gas temperature of 170°C and are expected to be an upper bound.

2.5.2. Transmission Electron Microscope

To obtain a qualitative understanding of the structure of soot aggregates, samples of soot produced by the ethene flame at different equivalence ratios were studied under an electronic microscope. A Phillips 420T transmission electron microscope was used at a voltage of 100kV with a 60 000 magnification. The diameter of the primary particles was then measured using the magnification factor of the microscope. Only particles which were in focus were chosen to prevent larger out of focus images artificially increasing the mean diameter of the primary particles.

2.5.3. Organic and Elemental Soot Content

The organic and elemental content of the soot samples were determined using a thermal-optical method described by Johnson et al. (1981) and summarized here. The analysis was performed by a professional laboratory (Sunset Laboratory, Oregon) which specializes in this type of measurement. The soot samples were collected on filters supplied by Sunset Laboratory using the same procedure as described in Section 2.5.1. The sampling time was established based on the sampling time of soot samples collected for soot emissions.

The carbon analyzer consists of three parts: an oven, a laser reflectance system and an electronic control system. The organic carbon is oxidized and then vaporized through a two-step (two temperature) procedure. During the first step, organic carbon is oxidized and vaporized at a temperature of 350°C by a carrier gas composed of 2% O_2 and 98% He. During the second step, the carrier gas is replaced by pure He and the temperature is increased to 600°C. The volatilized organic carbon is oxidized by a bed of granular MnO_2 to CO_2. The oxidized organic carbon (CO_2) is then reduced to CH_4 in a methanator and measured by a flame ionization detector. This two-step procedure minimizes pyrolytic conversion of organic to elemental carbon. The remaining carbon comes from elemental carbon originally on the filter, pyrolyzed carbon from the organic oxidation and vaporization steps and other types of carbon. Once the organic carbon is oxidized, the carrier gas is replaced by the 2%O_2-98%He mixture and the elemental carbon is oxidized at three different temperatures (400, 500 and 600°C) resulting in a slow oxidation process. The oxidized carbon is again converted to CH_4 and analyzed through the FID analyzer. During the oxidation of the elemental carbon, the reflectance of a He-Ne laser beam off the carbon containing filter is monitored. The amount of carbon oxidation required to return the filter to its original reflectance is measured and used to correct the organic content measurement for pyrolytic conversion of organic to elemental carbon. The authors note that the correction for pyrolytic conversion of organic to elemental cannot be neglected. The electronic system handles all the gas flow switching, the temperature programming, the FID signal integration and the data storage. The results of this analysis will be reported in the next section.

2.6. Temperature Profiles

The temperature profiles were obtained using an uncoated platinum/platinum rhodium thermocouple (bead diameter 0.25mm). For the temperature measurements the thermocouple was mounted vertically on a translation

stage and positioned, using two stepper motors, relative to the fixed burner. The stepper motors were controlled through an analog/digital (A/D) board by an IBM compatible computer. The controlling program was design to position the thermocouple, take 100 voltage readings and then move the thermocouple to a non-sooting area of the flame where soot built up on the thermocouple could be burned off. If the temperature measurements were made below the top of the under-ventilated laminar diffusion flame, the thermocouple needed only to be retracted radially. If the measurements were done above the flame, the thermocouple was first lowered and then moved radially to a non sooting region of the flame. After 100 readings were taken and the soot was burned off from the thermocouple bead, the thermocouple would be moved to the next position and another set of measurements taken. The maximum, the minimum and the average of the 100 measurements were displayed, printed and stored on disk. Since soot accumulating on the thermocouple bead reduced the temperature reading, only the maximum temperature for each different position was noted. At each position though, the variation between the maximum and minimum temperature measurement was not more than 10K.

To limit heat loss from the thermocouple, the thermocouple wires were inserted in a ceramic insulator. During the first series of measurements, it was noted that the temperature reading depended on the distance between the thermocouple bead and the insulator. The wires were therefore drawn from the insulator until no temperature variation was noted. Figure 2.11 shows the typical arrangement of the thermocouple during a temperature measurement. The thermocouple wires were connected to an Electronic Ice Point before input to the A/D board.

As explained above a ceramic insulator was used to limit heat loss from the thermocouple. Unfortunately this insulator could not prevent all heat loss from the thermocouple bead and corrections for radiation loss had to be estimated. Since the bead is in steady state, the heat loss through radiation equals the heat gained from the convection of the hot gases. For estimating radiation losses the thermocouple bead was assumed spherical (0.25mm diameter) and its emissivity equal to platinum (0.18). The wall temperature was estimated at each height by extrapolating the temperature measurements out to the quartz tube. To estimate the convective heat gain, the convective heat transfer coefficient of the hot gases to the bead was determined from the Nusselt number. The Nusselt number is a function of the Reynolds number and the Prandtl number and therefore depends on the bead geometry, the velocity and the properties of the hot gases. As explained before the bead geometry was assumed spherical and the thermal conductivity, the density and the viscosity of the gases were based on the thermophysical properties of nitrogen. The velocity was approximated from continuity and the average temperature at a particular height, and since the Nusselt number is relatively insensitive to velocity, this assumption is not critical. The final temperatures were all computed using a computer program.

Although conductive losses were neglected at first, it soon became obvious that the thermocouple configuration used for the temperature measurements in this study induced large conductive losses. This is due to large temperature gradients around the thermocouple bead and to a large wire section area compared to the thermocouple bead surface. Because of this, at higher temperatures (were the temperature gradient is most significant) the conductive losses could be as high as four to seven times the radiation losses. Thus, the temperature measurements should not be taken as quantitative in nature. However, general trends associated with the structure of these under-ventilated laminar diffusion flames are valid.

Electronic Ice Point

Thermocouple Holder

Ceramic Insulator

Quartz Tube

Flame Front
(Under-Ventilated)

Thermocouple Bead

Burner
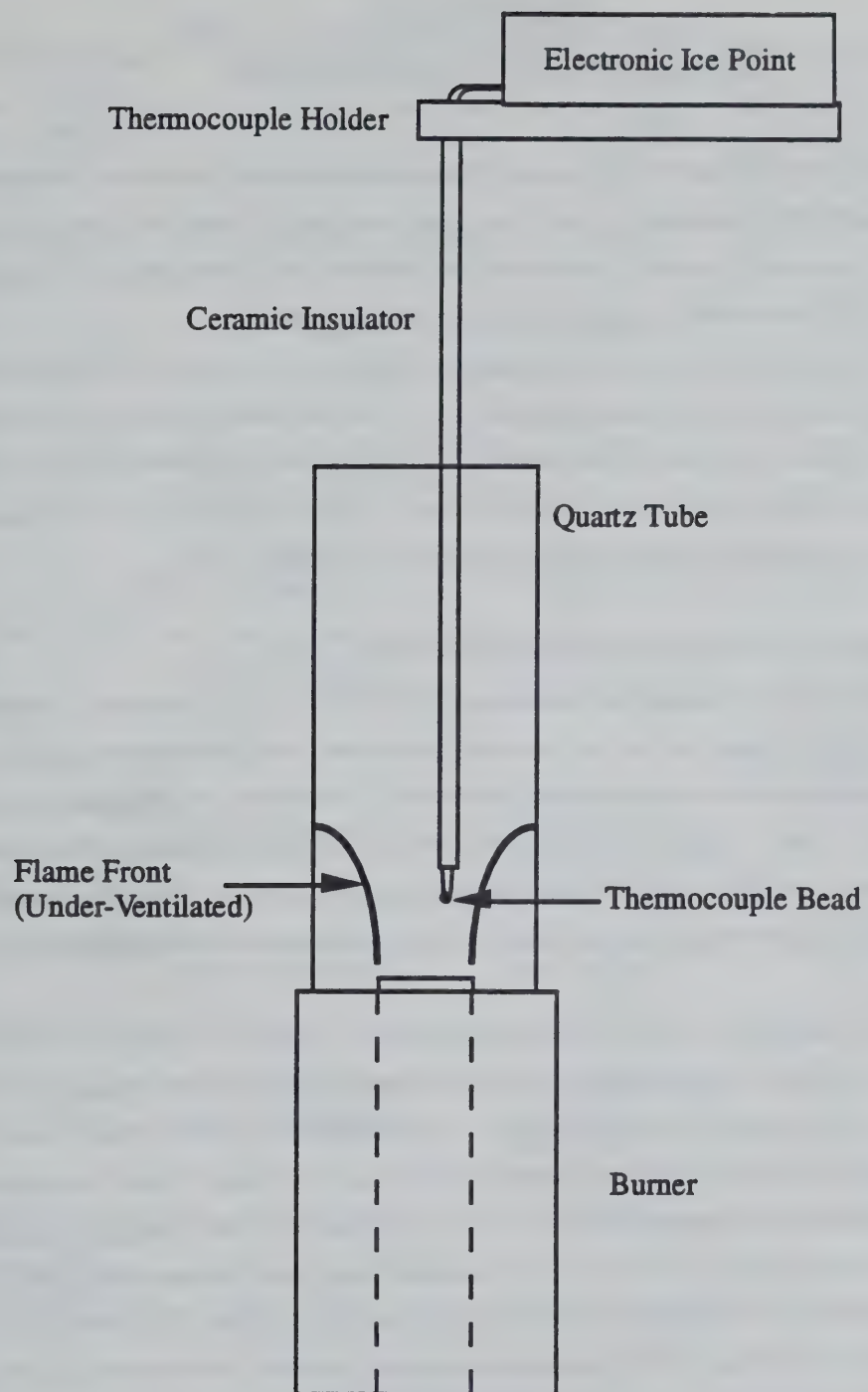
Figure 2.11. Schematic diagram of the thermocouple assembly

83

CHAPTER 3
RESULTS AND DISCUSSION

In the following chapter the results from the study of a series of under-ventilated laminar diffusion flame will be presented. Specifically measurements of the CO and smoke emissions as a function of global equivalence ratio will be described along with the results of studies done using methanol and toluene additives. Finally the results of detailed sampling measurements obtained in the flame will be described.

The entire set of data obtained in this work is contained in Appendices A, B and C. The figures shown below are based on the data obtained using the Horiba model VIA-150 and the Beckman model 864 NDIR analyzers for CO and CO_2 measurements respectively and the Hewlett-Packard gas chromatograph described in the previous chapter. Measurements were done on a dry basis with nitrogen used for dilution except for the concentrations measured using the gas chromatograph in which case the diluent gas was helium.

3.1. Flame Stability and Flame Heights Measurements

The first task in this study of under-ventilated laminar diffusion flames was to determine the appropriate conditions for obtaining stable flames. Fuel and air flows were chosen based on the global equivalence ratio, and the fuel and air tubes were picked so that a stable flame could be obtained. The different possible combinations of air and fuel tubes are listed in Table 3.1 along with a description of the resulting flame appearance. Note that in Table 3.1 the air flow rate is varied to achieve the desired variation in global equivalence ratio. Therefore, the air flow rate for specific flame stability characteristics can be determined from the tabulated fuel flow rate and global equivalence ratio, Φ.

Barr (1953) described most of the instabilities presented in Table 3.1 but more needs to be said about the specific flame behavior in terms of the present work. The over-ventilated flames were stable or acceptable diffusion flames except for two cases: 1) high air velocities (22mm I.D. air tube) caused the methane $20cm^3$/s flame to lift and eventually blow off and 2) high air velocities also produced a nonsmoking over-ventilated ethene flame under fuel flow conditions which exceeded the smoke point. Thus, a flame which would have been expected to be a smoking flame displayed non-smoking behavior. For the under-ventilated cases three types of instability were observed. The oscillating flame (Osc.), or Barr's (1953) lambent flame, had a periodic sideways motion. The pulsating flame (Pul.), which would correspond to Barr's (1953) rich tilted flame, would periodically change height, sometimes even drop below the outlet of the fuel tube. The curved flame (Cur.) which did not vary in time, but instead of extending straight upward, the flame plume would snake up the chimney.

The effect of global equivalence ratio on flame shape and size for the methane and ethene flames was evaluated photographically and is shown in Figure 3.1. As previously described in Chapter 2, global equivalence ratio is defined by the amount of air and fuel supplied to the burner. The general relationship for the equivalence ratio Φ is given by

$$\Phi = \frac{A/F_{Stoi}}{A/F} ,$$

84

Table 3.1. a) Flame Conditions for Methane Flames

Burner	Glass Tube CH_4 Flow	22mm I.D.	29mm I.D.	35mm I.D.
9.6mm O.D.	$10cm^3/s$	Stable	$\Phi = 4$, Small Osc.	$\Phi = 1$, Small Osc. $\Phi = 1.5$, Small Osc., Pul $\Phi = 2.52$, Osc., $\Phi = 4$, Osc., Pul.
9.6mm O.D.	$20cm^3/s$	$\Phi = 1$, Flame starts separating $\Phi = 0.72$, Flame blows off	Stable	$\Phi = 1.52$, Small Osc., $\Phi = 2.52$, Osc., $\Phi = 4$, Osc.
12.7mm O.D.	$10cm^3/s$	Stable	Stable	$\Phi = 1$, Cur. $\Phi = 1.5$, Osc., Pul., $\Phi = 2.52$, Osc., Pul., $\Phi = 4$, Pul.
12.7mm O.D.	$20cm^3/s$	$\Phi = 1$, Flame starts separating $\Phi = 0.72$, Flame blows off	Stable	$\Phi = 4$, Osc.

Table 3.1. b) Flame Conditions for Ethene Flames

Burner	Glass Tube C_2H_4 Flow	22mm I.D.	29mm I.D.	35mm I.D.
9.6mm O.D.	$6.4cm^3/s$	Stable $\Phi=0.5$, Nonsmoking	Stable	$\Phi = 0.5$, Osc. $\Phi = 1$, Osc., Cur. $\Phi = 1.5$, Osc., Cur. $\Phi = 2.5$, Osc., Pul., Cur. $\Phi = 4$, Osc., Pul., Cur.
9.6mm O.D.	$3.2cm^3/s$	Stable $\Phi=0.5$, Nonsmoking	$\Phi = 1$, Cur. $\Phi = 1.5$, Osc., Pul., Cur. $\Phi = 2.5$, Osc., Pul., Cur. $\Phi = 4$, Osc., Pul.	$\Phi = 0.5$, Osc. $\Phi = 1$, Osc. $\Phi = 1.5$, Osc., Cur. $\Phi = 2.5$, Osc., Pul., Cur. $\Phi = 4$, Flame out.
12.7mm O.D.	$6.4cm^3/s$	Stable $\Phi=0.5$, Nonsmoking	$\Phi = 1.5$, Cur. $\Phi = 2.5$, Cur. $\Phi = 4$, Pul.	$\Phi = 0.5$, Osc. $\Phi = 1$, Osc. $\Phi = 1.5$, Osc. $\Phi = 2.5$, Osc. $\Phi = 4$, Pul.
12.7mm O.D.	$3.2cm^3/s$	Stable $\Phi=0.5$, Nonsmoking	$\Phi = 0.5$, Nonsmoking $\Phi = 1$, Cur. $\Phi = 1.5$, Osc. $\Phi = 2.5$, Pul. $\Phi = 4$, Pul.	$\Phi = 0.5$, Osc. $\Phi = 1$, Osc. $\Phi = 1.5$, Osc., Pul. $\Phi = 2.5$, Pul. $\Phi = 4$, Pul.

Osc.: Oscillating Flame
Pul.: Pulsating Flame
Cur.: Curved Flame
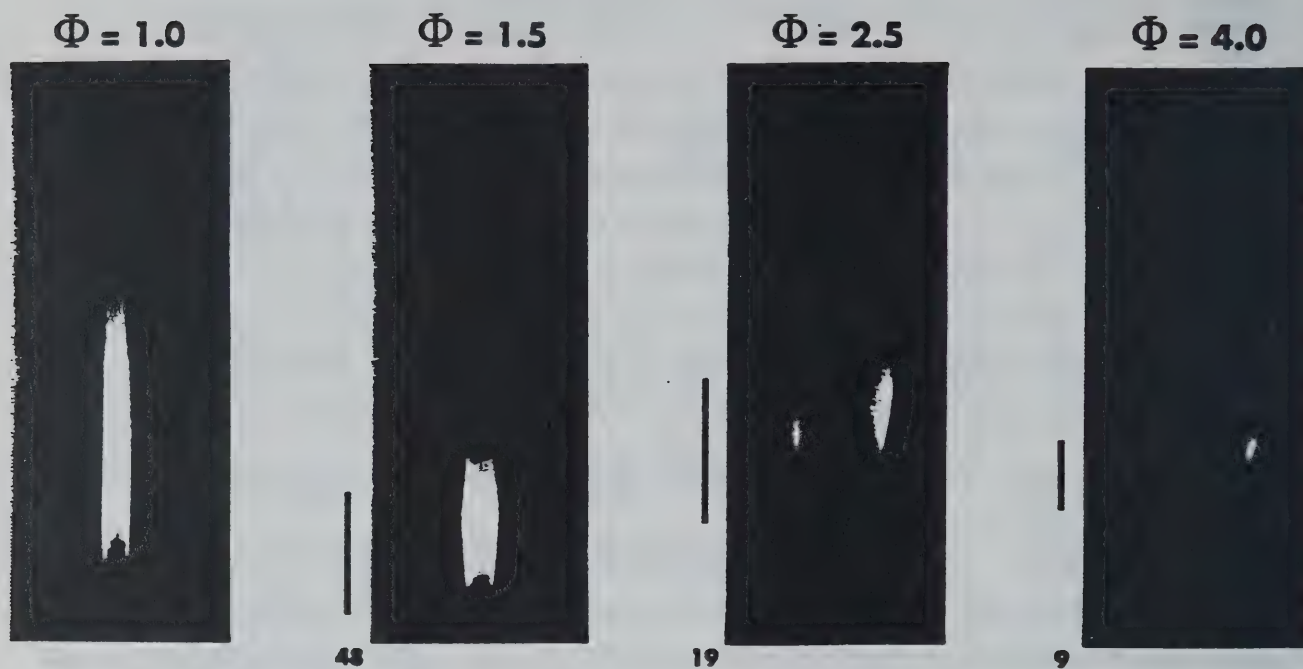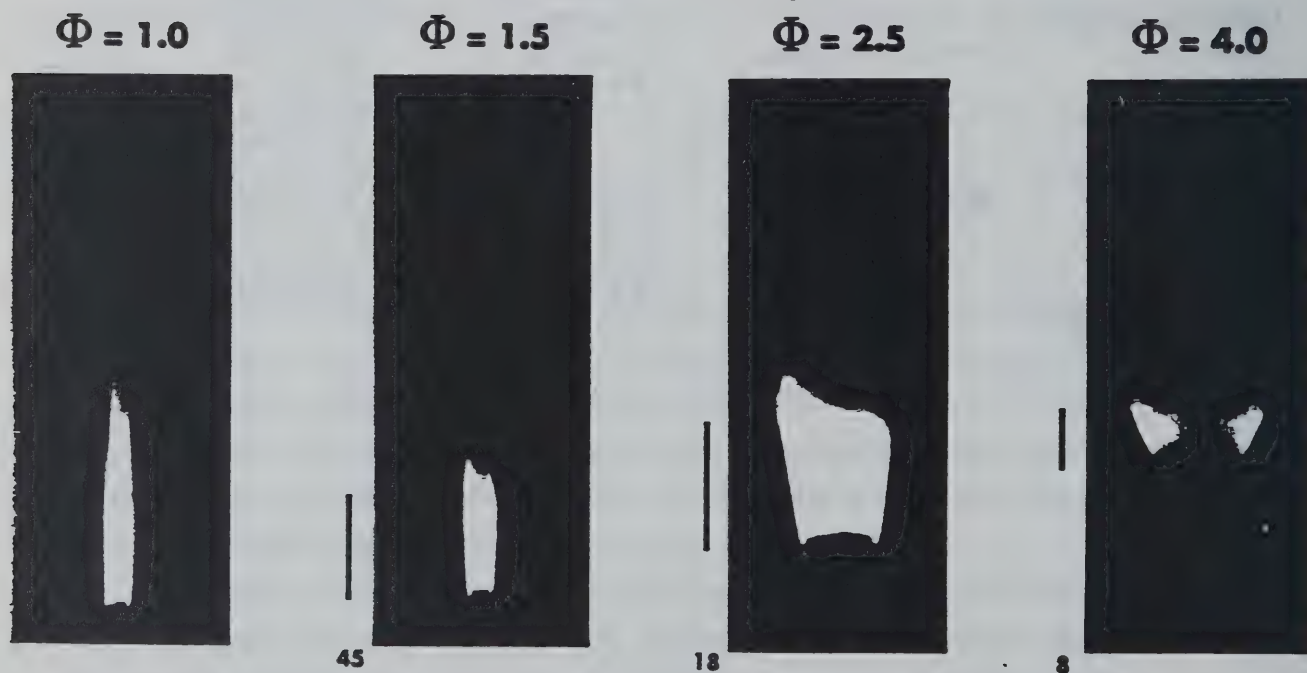
Figure 3.1 Height and structure of laminar diffusion flames for methane and ethene at different global equivalence ratios. Φ. The solid lines adjacent to pictures for Φ > 1 represent the predicted flame height in millimeters from the Burke and Schumann theory.

where A/FS_{toi} is the stoichiometric air and fuel flow rate ratio and A and F are the actual air and fuel flow rates. The pictures shown in Figure 3.1 clearly indicate the change in flame structure as the equivalence ratio increases from 1 to 4. The flames shorten and widen as the equivalence ratio increases. For $\Phi = 4$ the flame front is clearly curving toward the outer tube, though such a curvature is not clearly evident at $\Phi = 1.52$. This may signify the quenching of the outward flame zone by the quartz chimney wall. When looking at the flame pictures one has to keep in mind that the flame height is not determined by the incandescent soot particles but by the actual reaction zone. In the case of under-ventilated flames it is especially difficult to determine the flame height simply by visual observations. The reaction zone cannot extend out to the quartz tube because of quenching and therefore the flame height appears somewhat shorter. One indication of the flame height is the necking of the flame which could be due to the flame extending almost to the wall and to the upward convection of radiating particles. If this is the case, the necking of the flame would offer a reference point for the measure of the flame height which has been used to compare to theoretical predictions.

Next to the flame pictures appear the predicted flame heights in millimeters along with a solid bar which represents this height. These predicted flame heights were calculated using the Burke and Schumann theory (Burke and Schumann 1928). The diffusion coefficient used for the calculations was $0.60 cm^2/s$ which Roper et al. (1977) found best fit their data, rather than $0.492 cm^2/s$ which Burke and Schumann (1928) used in their work. Since the Burke and Schumann theory assumed equal air and fuel velocities some adjustment had to be made to account for the different gas velocities in the present study at different equivalence ratios. In the present study the fuel volumetric flow rate was maintained constant for different equivalence ratios. Using the actual fuel diameter to calculate the fuel velocity, an effective diameter was then calculated for the outer air passage based on the actual air flow rate such that the air and fuel velocities would be equal. The effective air tube diameter was then used in the flame height calculations. Burke and Schumann (1928) in their discussion of the effect of varying the size of the tubes inferred that the height of a cylindrical flame is not affected by the tube dimensions as long as the air and fuel flow rates are kept the same. This fact was bourne out in their studies.

The predicted flame height is greater than the blue zone but less than the bright luminous part of the flame. The decrease in flame height with increasing Φ is qualitatively predicted by the Burke and Schumann theory. The flame shapes are similar for methane and ethene flames but much more luminous radiation is emitted from the ethene flame. At an equivalence ratio equal to 1 the theory predicts a flame of infinite length and, thus, no predicted height is shown on Figure 3.1 for this condition.

3.2. Gas and Soot Concentration Measurements

Gas concentration measurements were obtained for two distinctly different flame sampling conditions. Global measurements of CO and CO_2 from samples taken at the outlet of the chimney were obtained for different global equivalence ratio flames and point sampling measurements were made in which a wider range of species were determined at different heights inside a flame of global equivalence ratio of 4. Both sampling methods were described in the preceding chapter. Soot measurements were done only for the global equivalence ratio studies and were always obtained at the outlet of the chimney. Point sampling measurements were analyzed using a gas chromatograph and

global measurements were done mainly with NDIR analyzers, although some comparison measurements were done using the gas chromatograph and found to agree with the NDIR results.

3.2.1. Global Measurements of CO and Smoke Concentration

All the results presented are reported on a dry basis with nitrogen used as diluent in the combustion products (see Chapter 2). Some of the data is reported in terms of a yield (ε) on a mass basis. The CO yield, ε_{CO}, is equal to the mass of CO produced per unit mass of fuel entering the burner. The procedure for determining the yield is outlined below. First the volume flow rate of CO, F_{CO}, is computed from the measured volume concentration of CO (in percent), X_{CO}, and the total volumetric flow rate through the dilution tube, F_T, corrected to ambient conditions,

$$F_{CO} = \frac{X_{CO}F_T}{100}. \tag{3.1}$$

Next the density of CO, ρ_{CO}, is obtained from the ideal gas law as

$$\rho_{CO} = \frac{M_{CO}P_A}{RT_A}, \tag{3.2}$$

where M_{CO} is the molecular weight of CO and the subscript A refers to ambient conditions. From Equations 3.1 and 3.2, the total mass flow rate of CO, $\dot{m}_{CO}$, is obtained as

$$\dot{m}_{CO} = \frac{X_{CO}F_T}{100}\frac{M_{CO}P_A}{RT_A}. \tag{3.3}$$

To compute the yield of CO the mass flow rate of fuel is also needed, which is obtained from the volumetric flow rate of the fuel, F_F, and its density, ρ_F. Using an expression similar to Equation 3.2 for computing the density, the following expression is obtained for the mass flow rate of fuel:

$$\dot{m}_F = F_F\frac{M_FP_A}{RT_A}. \tag{3.4}$$

The yield of CO, ε_{CO}, is obtained from Equations 3.3 and 3.4 as the ratio of the mass flow rate of CO to the mass flow rate of fuel,

$$\varepsilon_{CO} = \frac{\dot{m}_{CO}}{\dot{m}_F} = \frac{X_{CO}F_TM_{CO}}{100F_FM_F}. \tag{3.5}$$

The above expression requires that the fuel and combustion products are at, or are corrected to, the same temperature and pressure.

In Equation 3.5 the total volumetric flow rate F_T was approximated as the sum of the volumetric flow rates of N_2, fuel and air. This is a good approximation since the volumetric flow rate of N_2 accounts for at least 94% of the inlet flow rate for both the methane flame at a flow rate of $10\text{cm}^3/\text{s}$ and the ethene flame at a flow rate of $6.4\text{cm}^3/\text{s}$ for all values of Φ measured for a typical dilution flow rate of N_2 of $590\text{cm}^3/\text{s}$. Furthermore, for both methane and ethene, the sum of the number of moles of CO_2 and H_2O produced by complete combustion is equal to the sum of the number of fuel and oxygen moles. For $\Phi \leq 1$ complete combustion is a good approximation. For $\Phi > 1$ there is a significant amount of CO and possibly H_2 produced in addition to H_2O and CO_2; however as Φ increases, an increasingly large percentage of the inlet flow is N_2. For $\Phi = 1.5$, 97% of the inlet flow is N_2 for the two fuel flow rates given above. The production of smoke will result in a reduction in the outlet gas flow rate;

However, even if 10% of the fuel carbon becomes smoke for ethene, which is greater than any value measured, the reduction in the volumetric flow rate is only 0.1% for $\Phi = 1$.

So we see that for $\Phi > 1$, the above flow rate approximation is valid to within about 3%. One other factor plays a role for Φ in the range 0.5-1.0; that is, the fact that the water produced by the combustion, is removed by the wet and dry ice traps. Assuming complete combustion and assuming all the water is removed by the cold traps, the total flow rate is reduced by 2.9% for the methane diffusion flame with a fuel flow rate of $10 \text{cm}^3/\text{s}$ and 1.9% for the ethene diffusion flame with a fuel flow rate of $6.4 \text{cm}^3/\text{s}$. Therefore, F_T approximated as the sum of the N_2, air, and fuel flow rate is estimated valid to within 3%.

The smoke yield had to be calculated in a slightly different manner than the CO yield. The smoke yield, ε_S, was determined by multiplying the mass flow rate of smoke collected on a filter ($\dot{m}_S$), by a dilution factor (f_D) and dividing by the fuel mass flow rate:

$$\varepsilon_S = \frac{\dot{m}_S \, f_D}{F_F \rho_F}, \tag{3.6}$$

where F_F is the fuel volumetric flow rate and ρ_F the density of the fuel. The dilution factor (f_D) was defined as the ratio of the total volumetric flow rate and the volumetric flow rate through the filter.

Typical results for the methane diffusion flame with a fuel flow rate of $10 \text{cm}^3/\text{s}$ and the ethene diffusion flame with a fuel flow rate of $6.4 \text{cm}^3/\text{s}$ are given in Table 3.2. The repeat CO yield measurements for $\Phi > 1.52$ agree within 2%; the large difference at $\Phi = 1.0$ results from the great sensitivity of yield to Φ near $\Phi = 1$.

An estimate of the accuracy of the method for computing gaseous yields can be made by comparing measured CO_2 yield for $\Phi = 0.5$ with the predicted CO_2 yield for complete combustion for methane and ethene. For over-ventilated burning the major carbon containing product of combustion is CO_2. For methane at $\Phi = 0.5$, the measured yields are about 4% greater than the predicted value of 2.75, while for ethene the measured values are about 2% less than the predicted value of 3.14. From the CO_2 analog of Equation 3.5 the overall uncertainty is estimated to be ±6%, by combining the uncertainties associated with volume fraction and flow rate measurements. Thus, the methane and ethene results are within the expected uncertainty range. For ethene, 2% or 3% of the fuel carbon is emitted as smoke particulate at $\Phi = 0.5$ so perfect agreement with the predicted value of 3.14 is not expected. In Table 3.2 a carbon balance is included as the ratio of the mass outflow of carbon based on CO_2, CO and smoke to mass inflow of carbon in the fuel. The repeatability of the CO yield measurements is ±3% over the range $1.15 < \Phi < 4$ (see Table 3.2). Combining in quadrature the repeatability uncertainty with the systematic uncertainties in the CO gas analyzer, ±2%, and the flow uncertainty, ±3%, leads to a combined uncertainty of ±5% of the measured CO yield. At $\Phi = 0.5$, the uncertainty is on the order of ±50% because of the CO concentration is so low as to approach the instrument noise.

The measured smoke yields are an underestimate by 20% to 25% because of the estimated 13% wall deposition and a nominal 10% penetration of particles larger than $0.3 \mu m$. The estimated repeatability of the smoke yield results, ±8%, is more variable than for the CO yield, because one additional flow rate (smoke sampling flow) is needed and because of the variability associated with particle deposition and penetration.

With the definitions given above in mind, a discussion of the results obtained from global concentration measurements as a function of global equivalence ratio will be presented. Figures 3.2, 3.3 and 3.4 show the CO and

Table 3.2. Results for burner configuration 1 for methane and ethene

Methane: 10 cm³/s; Dilution: 590 cm³/s of N_2

Results for CO and CO_2 Measurements

Φ	air flow cm³/s	total flow cm³/s	X_{CO} vol. %	X_{CO2} vol. %	smoke mg	ε_{CO} gCO/gCH4	ε_{CO2} gCO2/gCH4	ε_s gC/gCH4	carbon balance
0.50	190	790	0.001	1.32	-	0.001	2.87	-	1.04
0.57	166	766	0.001	1.36	-	0.001	2.87	-	1.04
0.66	144	744	0.001	1.40	-	0.001	2.87	-	1.04
0.76	126	726	0.001	1.44	-	0.001	2.86	-	1.04
0.87	109	709	0.001	1.48	-	0.001	2.88	-	1.05
1.00	95.2	695	0.013	1.47	-	0.016	2.80	-	1.03
1.15	82.8	683	0.245	1.14	-	0.293	2.14	-	0.95
1.32	72.2	672	0.311	0.93	-	0.366	1.72	-	0.83
1.52	62.8	663	0.308	0.78	-	0.357	1.42	-	0.72
1.74	54.7	655	0.284	0.69	-	0.325	1.23	-	0.63
2.00	47.7	648	0.258	0.60	-	0.292	1.07	-	0.56
2.52	37.8	638	0.203	0.49	-	0.227	0.85	-	0.44
3.18	30.0	630	0.156	0.40	-	0.172	0.69	-	0.35
4.00	23.8	624	0.105	0.33	-	0.115	0.56	-	0.27

Results for CO, CO_2 and Smoke Measurements

Φ	air flow cm³/s	total flow cm³/s	X_{CO} vol. %	X_{CO2} vol. %	smoke mg	ε_{CO} gCO/gCH4	ε_{CO2} gCO2/gCH4	ε_s^a gC/gCH4	carbon balance
0.50	190	790	0.0	1.30	0.0	0.0	2.82	0.0	1.03
1.00	95.2	695	0.055	1.38	4.29	0.067	2.64	0.010	1.01
1.52	62.8	663	0.305	0.76	4.68	0.354	1.38	0.009	0.72
2.52	37.8	638	0.205	0.46	0.79	0.229	0.81	0.0013	0.43
4.00	23.8	624	0.102	0.31	0.0	0.111	0.52	0.0	0.25

a Sampling conditions correspond to laboratory temperature and pressure conditions: T=23°C and P=731.7mmHg at a sample probe flow rate of 152cm³/s

Ethene: 6.4 cm³/s; Dilution: 590 cm³/s of N_2

Results for CO and CO_2 Measurements

Φ	air flow cm³/s	total flow cm³/s	X_{CO} vol. %	X_{CO2} vol. %	smoke mg	ε_{CO} gCO/gC₂H₄	ε_{CO2} gCO₂/gC₂H₄	ε_s gC/gC₂H₄	carbon balance
0.50	183	779	0.002	1.60	-	0.002	3.07	-	0.98
0.57	159	755	0.002	1.66	-	0.002	3.07	-	0.98
0.66	139	735	0.002	1.69	-	0.002	3.05	-	0.97
0.76	121	717	0.003	1.72	-	0.003	3.03	-	0.96
0.87	105	701	0.005	1.74	-	0.006	3.00	-	0.96
1.00	91.3	688	0.015	1.75	-	0.016	2.96	-	0.95
1.15	79.5	676	0.209	1.50	-	0.221	2.49	-	0.90
1.32	69.2	666	0.369	1.22	-	0.384	2.00	-	0.83
1.52	60.3	657	0.448	1.00	-	0.459	1.62	-	0.74
1.74	52.5	649	0.459	0.84	-	0.465	1.34	-	0.66
2.00	45.7	642	0.434	0.72	-	0.435	1.13	-	0.58
2.52	36.3	633	0.363	0.56	-	0.359	0.87	-	0.46
3.18	28.8	625	0.280	0.46	-	0.273	0.71	-	0.36
4.00	22.8	619	0.180	0.37	-	0.174	0.56	-	0.27

Results for CO, CO_2 and Smoke Measurements

Φ	air flow cm³/s	total flow cm³/s	X_{CO} vol. %	X_{CO2} vol. %	smoke mg	ε_{CO} gCO/gC₂H₄	ε_{CO2} gCO₂/gC₂H₄	ε_s^b gC/gC₂H₄	carbon balance
0.50	183	779	0.002	1.59	7.03	0.002	3.05	0.028	0.99
1.00	91.3	688	0.032	1.69	14.70	0.034	2.85	0.051	0.96
1.52	60.3	657	0.446	0.98	13.70	0.457	1.58	0.044	0.76
2.52	36.3	633	0.358	0.54	5.95	0.354	0.84	0.019	0.45
4.00	22.8	619	0.177	0.35	1.99	0.171	0.53	0.0037	0.26

[b] Sampling conditions correspond to laboratory temperature and pressure conditions; T=23°C and P=736.4mmHg at a sample probe flow rate of 155cm³/s
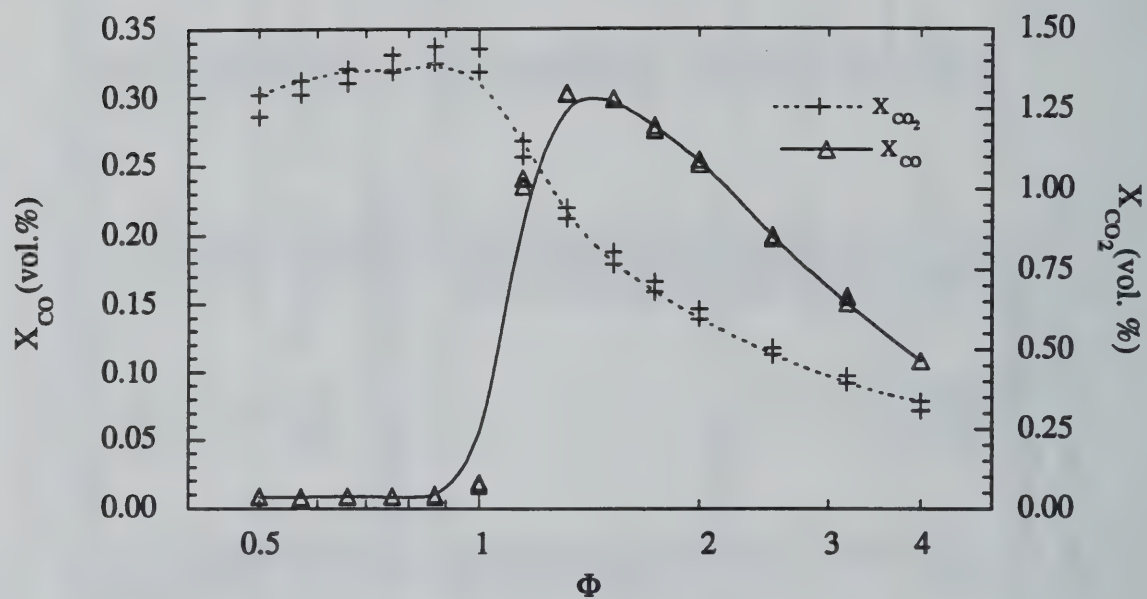
Figure 3.2. Volume concentration in percent of CO and CO_2 as a function of global equivalence ratio, Φ, from the methane diffusion flame with a fuel flow rate of 10 cm^3/s for burner configuration 1.
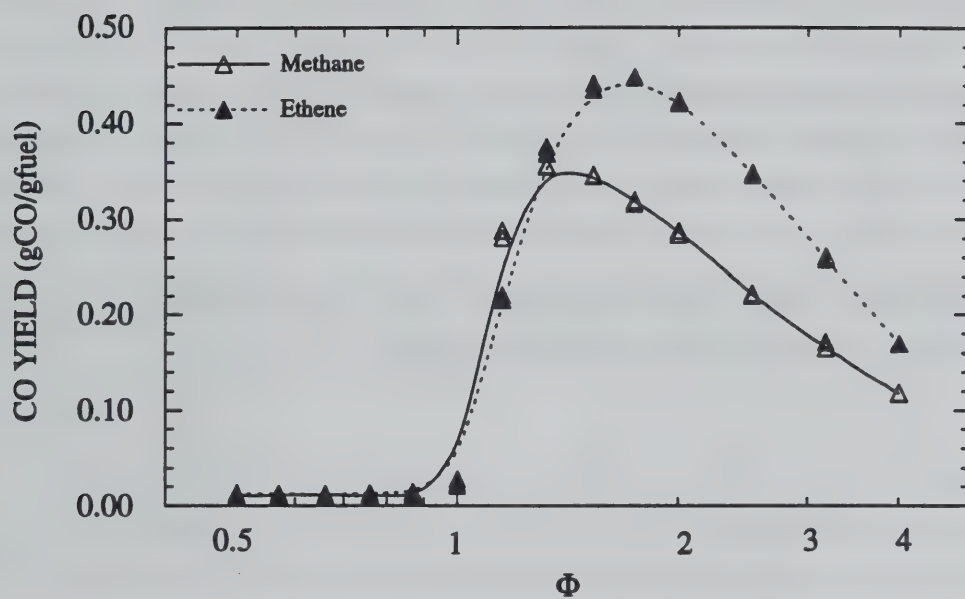
Figure 3.3. CO yield as a function of global equivalence ratio, Φ, from the methane diffusion flame with a fuel flow rate of 10 cm^3/s and ethene with a fuel flow rate of 6.4 cm^3/s for burner configuration 1.
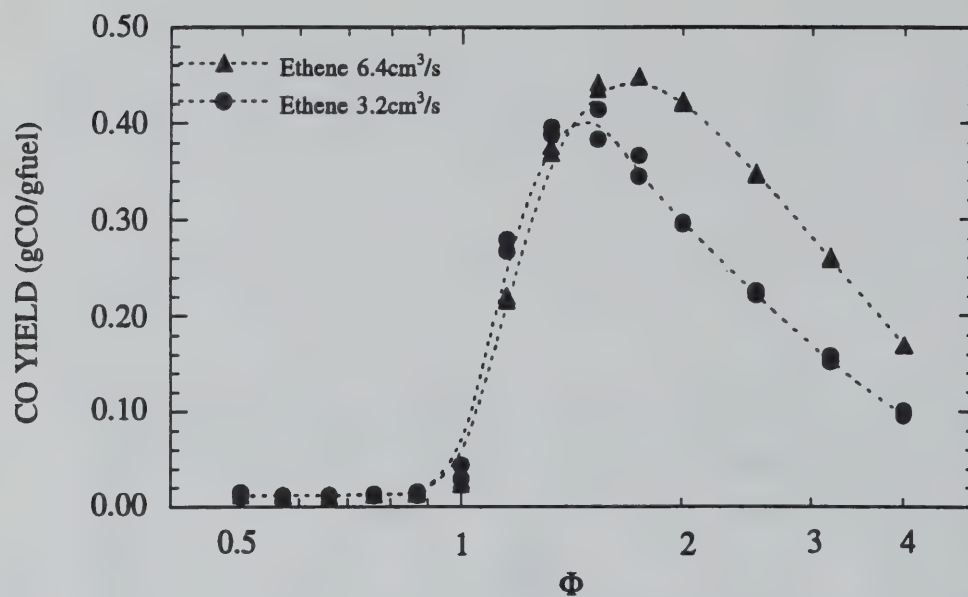
Figure 3.4. CO yield as a function of global equivalence ratio, Φ, from the ethene diffusion flame with fuel flow rates of 6.4 cm^3/s and 3.2cm^3/s for burner configuration 1.

CO_2 volume concentration and yields as a fur ·ion of the global equivalence ratio, Φ. One striking characteristic of Figures 3.2, 3.3 and 3.4 is the sudden increase in CO production when the global equivalence ratio reaches a value of 1. At this point insufficient oxygen is available for the complete oxidation of CO and since the oxidation reaction of CO to CO_2 is relatively slow compared to the oxidation of the fuel to form CO, the fuel is oxidized to CO but the CO remains unoxidized. This behavior is observed for both the methane and ethene flames. Although not shown in the data plotted in these figures, results were less repeatable at $\Phi = 1$ because of the great sensitivity of CO yield to Φ near $\Phi = 1$. In Figure 3.2 the reduction of both CO and CO_2 production indicates a lower combustion efficiency when $\Phi > 1$. Figure 3.3 shows that an under-ventilated ethene flame produces more CO per gram of fuel than a methane flame and that the CO production peaks at a higher Φ than in the methane flame. A higher fuel flow rate, as shown in Figure 3.4 for ethene, seems to promote formation of CO and also shift the CO yield peak to higher Φ. The same trend was observed with methane when the flow rate was increased to $20 cm^3/s$. Figure 3.5 shows the CO and the smoke yield for an ethene diffusion flame with a fuel flow rate of 6.4 cm^3/s as a function of the global equivalence ratio. Ethene, which is known as a strongly sooting flame, produces smoke even at a global equivalence ratio of 0.5. Almost no CO is produced until Φ reaches a value of 1, but the smoke yield increases from $\Phi = 0.5$ to 1.0. No direct relationship between CO and smoke formation similar to the ones reported by McCaffrey and Harkleroad (1988) and Fisher and Grosshandler (1988) in their work on over-ventilated pool fires and Köylü et al. (1991) in their work on over-ventilated turbulent diffusion flames seems to be valid. As noted by Köylü et al. (1991), the reason why no variation of CO concentration was observed for $\Phi < 1$ might be because of the lower resolution of the CO concentration measurements, in the case of the present work, due to high nitrogen dilution.

In Figure 3.6 (notice the change in scale for the smoke yields), the smoke yield from an ethene flame is compared to a methane flame, the latter is known to be a low sooting fuel and is observed to produce little soot below $\Phi = 1$. The peak smoke yield of methane and ethene differ by about a factor of five but the peak CO yield differ by only 20%. When Figures 3.6 and 3.3 are compared, it is found that an under-ventilated (fuel rich, $\Phi > 1$) ethene diffusion flame produces more CO and more smoke than a methane diffusion flame at the same equivalence ratio. This results contradicts the findings of Beyler (1986) on over-ventilated pool fires and Puri and Santoro (1991) on over-ventilated laminar diffusion flames. These workers found that in fuel rich regions (local equivalence ratio, ϕ, > 1) as soot concentration increased, CO concentration decreased. The specific reason for the reversal of the trends in the CO and soot concentrations between under- and over-ventilated diffusion flames is not clear from the present global studies and further study is warranted. The differences in the flame structure between the ventilation conditions may be the basis for the observed differences. As the global equivalence ratio increases above 2, the smoke yield drops and is almost 0 at $\Phi = 4$ for both methane and ethene. The reduction in soot formation at high global equivalence ratio is probably due to lower temperatures in the inception soot particle zone. Although ethene is normally considered to be a strongly sooting fuel, two interesting results are shown in Figure 3.7 and 3.8. Figure 3.7 shows that no smoke is produced by an ethene flame at $\Phi = 0.5$ with a flow rate of 3.2cm^3/s in the same burner configuration as the smoking flame with a flow rate of 6.4cm^3/s. This result is consistent with the reported smoke point fuel flow rate of 4.3cm^3/s for ethene (Schug et al. 1980) since the fuel flow rates studied here lie well below or above the reported smoke point fuel flow rate. Thus the 3.2cm^3/s ethene flame should be non-smoking while
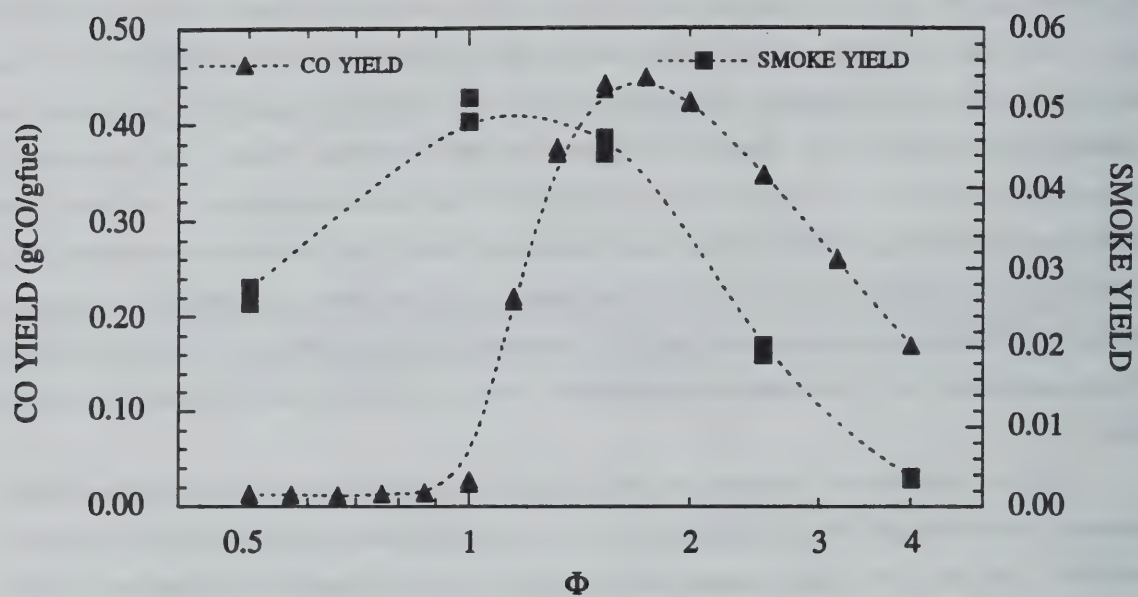
Figure 3.5. CO and smoke yield as a function of global equivalence ratio, Φ, for the ethene diffusion flame with a fuel flow rate of 6.4 cm^3/s for burner configuration 1.
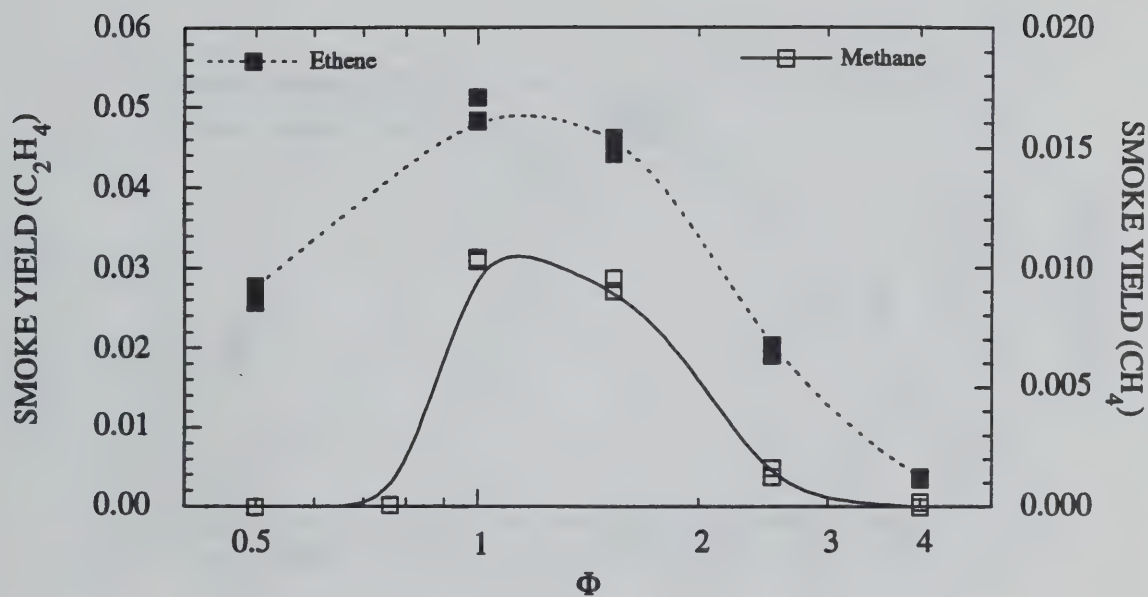
Figure 3.6. Smoke yield as a function of global equivalence ratio, Φ, for the methane diffusion flame with a fuel flow rate of $10 cm^3/s$ and ethene diffusion flame with a fuel flow rate of $6.4 cm^3/s$ for burner configuration 1.
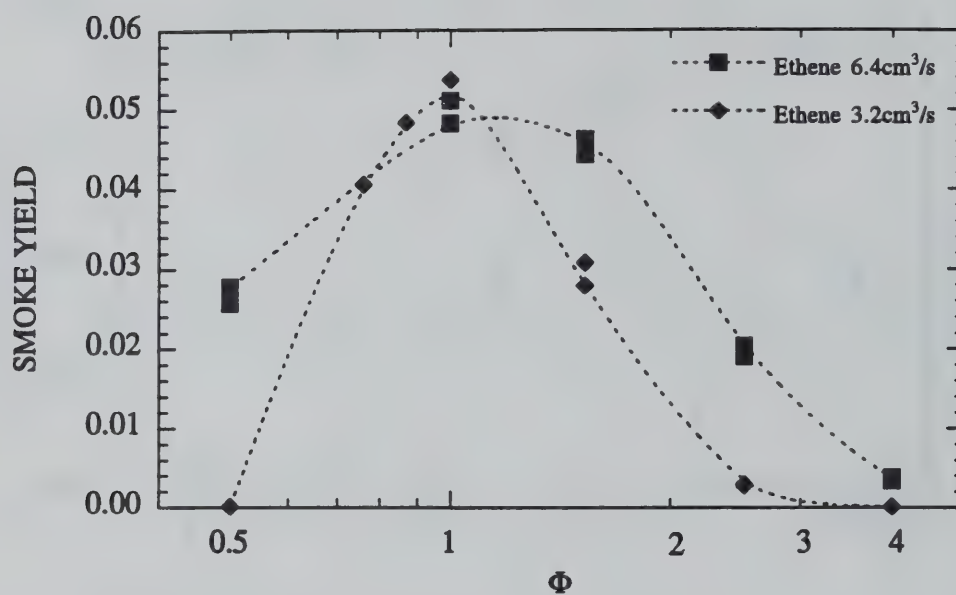
Figure 3.7. Smoke yield as a function of global equivalence ratio, Φ, for the ethene diffusion flame with fuel flow rates of 6.4cm^3/s and 3.2cm^3/s for burner configuration 1.
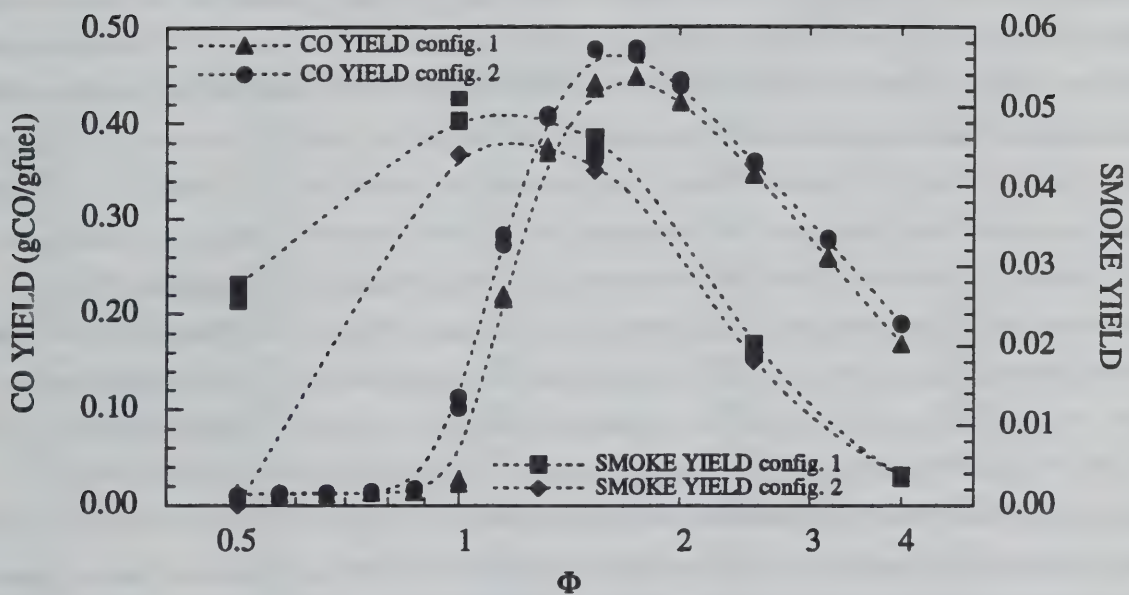
Figure 3.8. CO and smoke yields as a function of global equivalence ratio, Φ, for the ethene diffusion flame with a fuel flow rate of 6.4cm^3/s for burner configurations 1 and 2.

6.4cm^3/s flame should exhibit smoking characteristics. In Figure 3.8 the CO and smoke yields are plotted for two different burner configurations for flames burning ethene with the same fuel flow rate of 6.4cm^3/s. An interesting feature of this plot is the drop of the smoke yield when $\Phi < 1$, and essentially no smoke is produced at $\Phi = 0.5$ in burner configuration 2 which is distinctly different from the observations for burner configuration 2. From Figure 3.8, one can see that a reduction in soot formation results in a slight increase of CO formation.

The major effect in changing from burner configuration 1 to burner configuration 2 is to increase the exit velocity of the air stream by a factor of 1.91. The specific reason for the observed change in the smoking conditions of the flame is not known at the present time. Since this effect was observed at over-ventilated conditions, it was deemed to be outside the scope of the present research effort which is focused on under-ventilated conditions. None the less, this is an interesting feature given the importance of smoke point tests in the development of an understanding of soot formation processes.

When some of the fuel, in a methane or ethene under-ventilated flame at a constant carbon flow rate, is replaced by methanol or toluene, the amount of carbon converted to CO with respect to CO_2 varies, as do the sooting properties of the flame. Figures 3.9 and 3.10 show the effects on the CO to CO_2 volume concentration ratio of methanol and toluene addition to the methane and ethene diffusion flames. The specific fuel flow rate conditions for these mixture flames are given in Table 3.3. Figures 3.11 and 3.12 show similar plots for the yield of CO and CO_2 in these same flames. No complementary quantitative data was taken on the soot yield. However, visually soot formation was greatly reduced in the methanol additive flame while soot significantly increased in the toluene case. This is consistent with the reported sooting tendencies of these fuels (Glassman, 1987, pp. 366). Thus, in both the methane and ethene diffusion flames, toluene reduced CO formation and increased soot formation, while methanol had the opposite effect and increased CO formation but reduced soot formation. Comparison of Figure 3.9 with Figure 3.11 shows that for the methane mixture flames, methanol increases the CO yield and the ratio of the CO and CO_2 volume concentrations, while toluene decreases both of these quantities. The effect on the ratio of the CO and CO_2 volume concentrations is observed to be more produced for methanol in the methane mixture case than for toluene. The largest effects are observed over a global equivalence ratio range between $1 < \Phi < 2$.

Figures 3.10 and 3.12 show similar results for methanol and toluene addition to the ethene laminar diffusion flames. In general the same trends are observed as described above for methane diffusion flame. The CO and CO_2 volume concentration ratio and CO yield decrease with increasing soot concentration. However, the changes in the CO yield are much smaller for methanol addition in the ethene flame than in the methane flame. The differences observed between the methanol additive flames is likely due to the difference in the balance between OH radical attack on soot particles and CO in the two flames. Since methanol includes OH as part of its fuel structure, higher levels of OH may occur in the flames to which methanol is added. The relative reactivity of OH to soot particles and CO will therefore be influenced by the local OH concentration and temperature which could differ widely in the two flames. The reduction in soot formation and increase in CO formation in the under-ventilated mixture flames differs from the trend observed previously (see Figure 3.3 and 3.6) in which CO concentration was seen to increase with increasing soot concentration. These latter results are similar to the work of Beyler (1986) and Puri

Table 3.3. Air flow rates (in cm^3/s) for gas and liquid mixtures as a function of equivalence ratio.

Φ	Methane 12.8cm^3/s		Ethene 6.4cm^3/s	
	20% Methanol	20% Toluene	20% Methanol	20% Toluene
0.50	231.4	226.3	182.8	177.5
0.57	203.0	198.5	160.3	155.7
0.66	175.3	171.5	138.5	134.5
0.76	152.3	148.9	120.3	116.8
0.87	133.0	130.1	105.0	102.0
1.00	115.7	113.2	91.4	88.8
1.15	100.6	98.4	79.5	77.2
1.32	87.7	85.7	69.2	67.2
1.52	76.1	74.5	60.1	58.4
1.74	66.5	65.0	52.5	51.0
2.00	57.9	56.6	45.7	44.4
2.52	45.9	44.9	36.3	35.2
3.18	36.4	35.6	28.7	27.9
4.00	28.9	28.3	22.8	22.2

Figure 3.9. CO and CO$_2$ volume concentration ratio as a function of global equivalence ratio, Φ, for methane and methane mixture diffusion flames burning additions of methanol or toluene (see Table 3.3 for flow conditions).
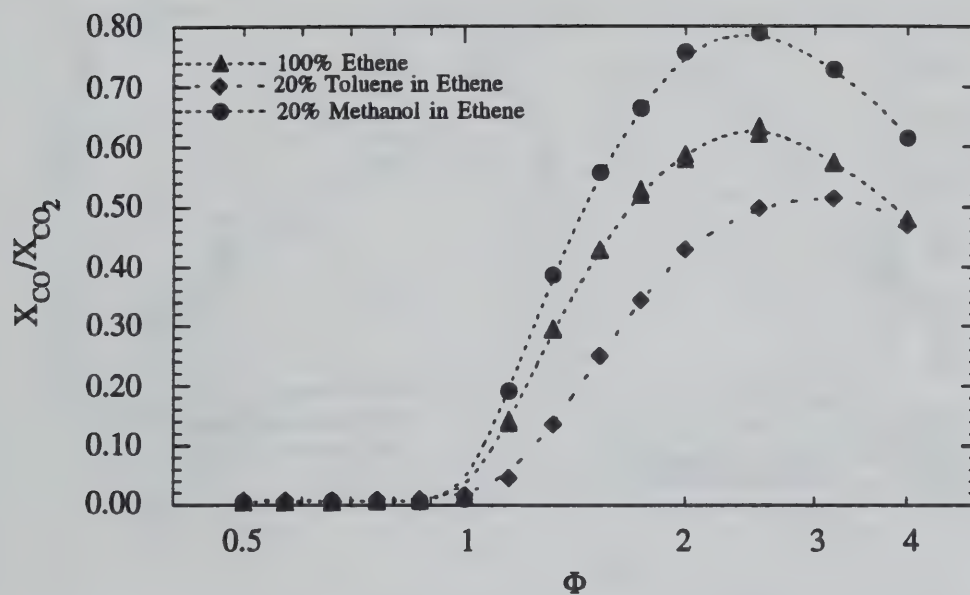
Figure 3.10. CO and CO_2 volume concentration ratio as a function of global equivalence ratio, Φ, for ethene and ethene mixture diffusion flames burning additions of methanol or toluene (see Table 3.3 for flow conditions).
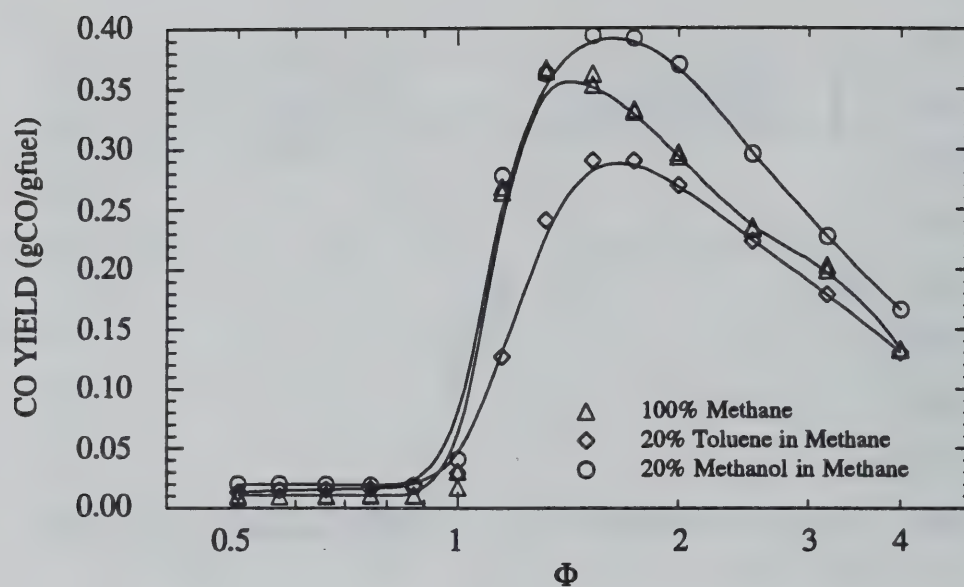
Figure 3.11. CO yield as a function of global equivalence ratio, Φ, for methane and methane mixture diffusion flames burning additions of methanol or toluene (see Table 3.3 for flow conditions).
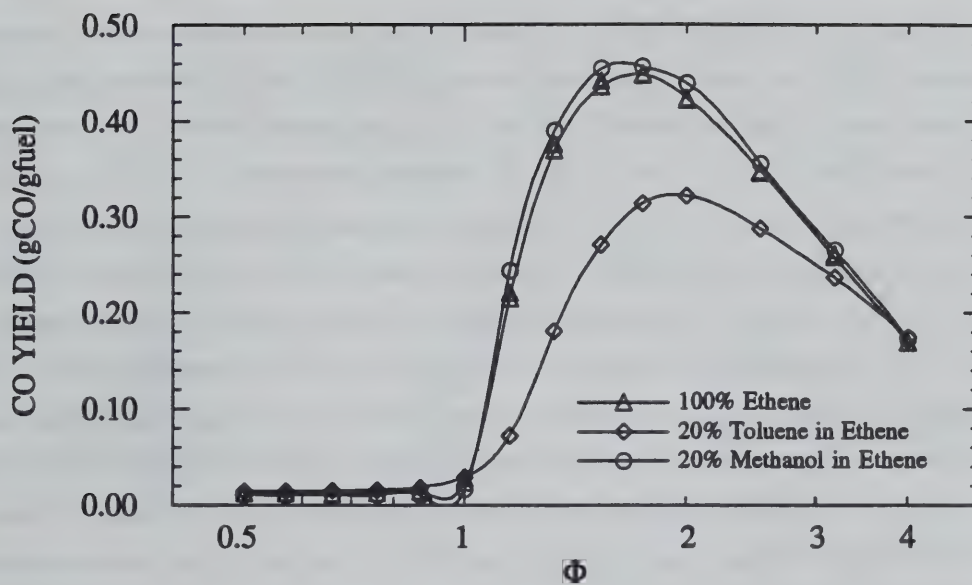
Figure 3.12. CO yield as a function of global equivalence ratio, Φ, for ethene and ethene mixture diffusion flames burning additions of methanol or toluene (see Table 3.3 for flow conditions).

and Santoro (1991) with regard to the relative trends in CO and soot concentration. Very little CO was measured when $\Phi < 1$ and there does not seem to be a relationship between CO formation and soot formation in the over-ventilated mixture flames.

Measurements of species concentration as a function of equivalence ratio have been made in other diffusion flame experiments and can be compared to the present results. In Figure 3.13, the present results for the ratio of CO and CO_2 volume concentrations are compared with the measurements of Mitchell et al. (1980), for over-ventilated laminar methane/air diffusion flames and Puri (1992) for under-ventilated laminar methane/air diffusion flames. In the studies of Mitchell et al. (1980) and Puri (1992), the equivalence ratio was determined locally in the flame based on point sampling probe measurements. Thus, the results shown in Figure 3.13 compare measurements of local CO and CO_2 concentrations with global measurements undertaken in the present study. The CO and CO_2 concentration ratio assesses changes in flame chemistry as the global equivalence ratio is varied since CO and CO_2 are the major combustion products containing carbon. Clearly all three sets of data show the same qualitative trends as the equivalence ratio (global, Φ, or local, ϕ) is varied. The under- and over-ventilated diffusion flames show nearly identical trends based on local measurements with X_{CO}/X_{CO_2} first showing an increase at a local equivalence ratio of 0.8. The local measurements in Figure 3.13 indicate a relative constant value of X_{CO}/X_{CO_2} when $\Phi >$ 1.5. The global equivalence ratio studies conducted in the present work show similar general trends to those observed for the local measurements described above. However the increase in X_{CO}/X_{CO_2} occurs at a slightly richer equivalence ratio near a value of 1. The global equivalence ratio studies also show a slight decrease in X_{CO}/X_{CO_2} for $\Phi > 3.0$. These differences likely reflect the fact that the global measurements represent some average over the local equivalence ratio value in the flame. Thus, even for rich global equivalence ratios, there are some locations in the flame which have lean or stoichiometric conditions (lowering X_{CO}/X_{CO_2}) while for lean conditions complete conversion of CO to CO_2 will occur (leaving X_{CO}/X_{CO_2} unchanged between the global and local equivalence ratio representations). Based on this view, the results for the global equivalence ratio studies are quite consistent with the local equivalence results.

Studies have also been conducted on the emission of CO using large unsteady buoyant diffusion flames (Toner et al. 1987; Morehart et al. 1990). In these studies the flame products issued into a large hood where species measurements were made. In these experiments, the height of the collection hood relative to the burner controlled the air entrainment into the flame. The results of the studies by Toner et al. (1987) and Morehart et al. (1990) for X_{CO}/X_{CO_2} are shown in Figure 3.14 along with the global equivalence ratio results obtained as part of the present study. The results from Toner et al. (1987) and Morehart et al. (1990) do not show a sudden increase in CO formation at $\Phi = 1$ but rather a gradual increase when $\Phi > 0.5$ which continue to increase nearly linearly into the fuel rich region ($\Phi \le 3$).

The difference in these results in terms of the behavior for X_{CO}/X_{CO_2} with variations in the global equivalence ratio is quite striking and points to the importance of local mixing conditions on the emission of CO from fires. The studies of Toner et al. (1987) and Morehart et al. (1990) involved longer residence times and different temperature conditions than employed in the present under-ventilated laminar diffusion flame studies. Thus, to understand these more complicated fire situations, the results of our more basic studies need to be integrated with appropriate mixing and chemistry models which account for these other features.
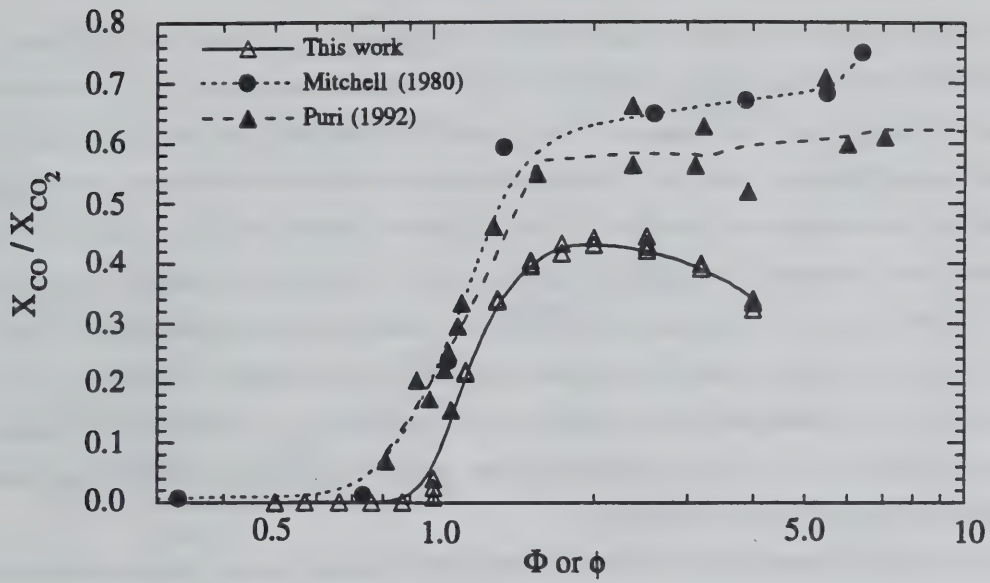
Figure 3.13. Comparison of local X_{CO}/X_{CO_2} versus local equivalence ratio, ϕ, for under- and over-ventilated laminar methane/air diffusion flames and global X_{CO}/X_{CO_2} versus global equivalence ratio, Φ. The under-ventilated laminar diffusion flame results were taken from Puri (1992) while the over-ventilated studies are those of Mitchell et al. (1980).

3.2.2. Point Measurements of Species Concentration in Under-Ventilated Laminar Diffusion Flames.

Local concentration measurements were obtained using two types of quartz microprobes as described in the Chapter 2. Concentration profiles of the species contained in a methane and ethene under-ventilated laminar diffusion flame at a global equivalence ratio of 4 were obtained at three different heights in the flame. These heights were determined based on the local equivalence ratio at the center line to allow comparisons between the different flames. The local equivalence ratio is defined as the ratio of the stoichiometric number of oxygen atoms needed to react with all the carbon and hydrogen atoms to form CO_2 and H_2O, to the available number of oxygen atoms. For example if methane and ethene are the only hydrocarbons locally present in a combustion process under consideration, the expression for the local equivalence ratio would be

$$\text{Local } \Phi = \frac{H_2 + 2CO_2 + 4CH_4 + 2CO + 6C_2H_4 + H_2O}{2CO_2 + 2O_2 + CO + H_2O} , \tag{3.7}$$

where the species are given in wet volumetric concentrations. In the present experiments the species concentrations were measured with a gas chromatograph on a dry basis with H_2O calculated based on a H atom balance and included in the concentration calculations of each species. In the particular gas chromatograph configuration used in this work, H_2 was neglected because it could not be calibrated due to its similar thermal conductivity with the helium carrier gas, its small concentration and the fact that H_2 would appear as a double peak on the integrator of the FID analyzer. Other species measured by the gas chromatograph and their coefficients in Equation 3.7 are shown in the Table 3.4. One should note that a much more extensive group of hydrocarbon species are included in Table 3.4 since in these rich under-ventilated flames many hydrocarbons form from the parent methane or ethene fuel. These species must be included in the expression for the local equivalence ratio since they occur in significant concentrations. The expression given in Equation 3.7, which includes only methane and ethene, is for a simplified case and is used to simply illustrate the local equivalence ratio concept.

Detailed species measurements were obtained for two under-ventilated laminar diffusion flames with a global equivalence ratio of 4. A methane and an ethene diffusion flame were studied. For the methane flame the fuel flow rate was 10 cm^3/s with a corresponding air flow rate of 23.8cm^3/s while for the ethene case, the fuel was supplied at a flow rate of 6.4 cm^3/s and air at a flow rate of 22.8cm^3/s. For each flame, burner configuration 1 was used (see Table 2.1). Since the size and shape for these two flames were quite different (see Figure 3.1), it was decided to profile the flames at the centerline positions which displayed similar local equivalence ratios. Unfortunately this proved to be difficult in the ethene flame because of sampling complications. It was impossible to sample the ethene diffusion flame with the smaller orifice quartz probe (referred to as "quartz microprobe") above a height of 2.5mm due to soot particle clogging of the probe. On the other hand measurements done below 14mm with the Electromagnetic Sonic Probe (referred to as "EMS probe") would perturb the flame seriously. By careful selection of the appropriate probe and sample locations some measurements were obtained for both flames and are shown in Figure 3.15. Figure 3.15 indicates that each of the flames display similar trends in terms of the variation of the local equivalence ratio, ϕ, with increasing height. In addition to the ethene and methane flames described above, measurements for an under-ventilated methane flame previously studied by Puri (1992), which had a fuel flow rate of 21 cm^3/s, are shown. This higher methane flow rate case shows the effect of fuel flow rate on the axial profile of the local equivalence ratio, ϕ. As expected as the fuel flow rate increases the axial profile for ϕ shifts to higher
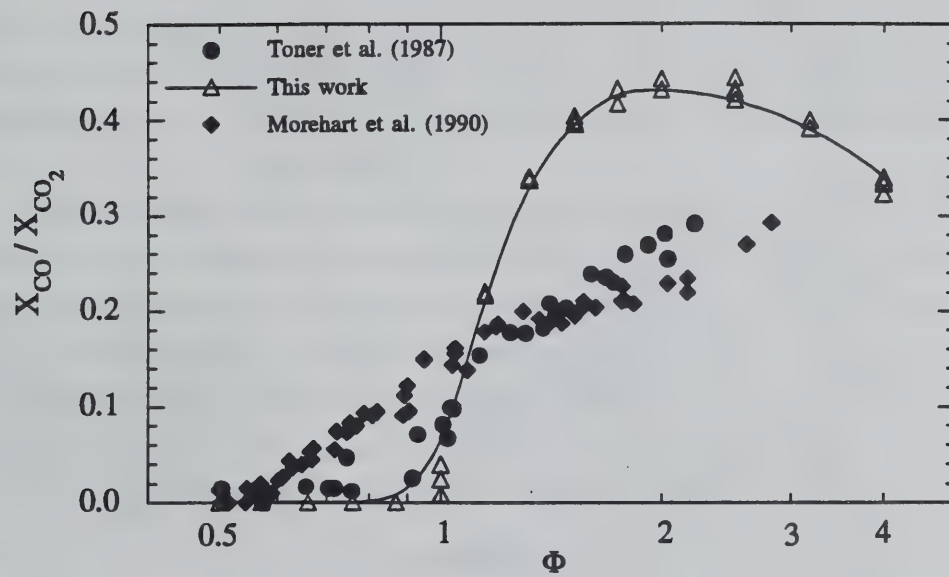
Figure 3.14. Comparison of XCO/XCO2 versus global equivalence ratio, F, for the present under-ventilated laminar diffusion flames and the turbulent natural gas flames studied by Toner et al. (1987) and Morehart (1990).
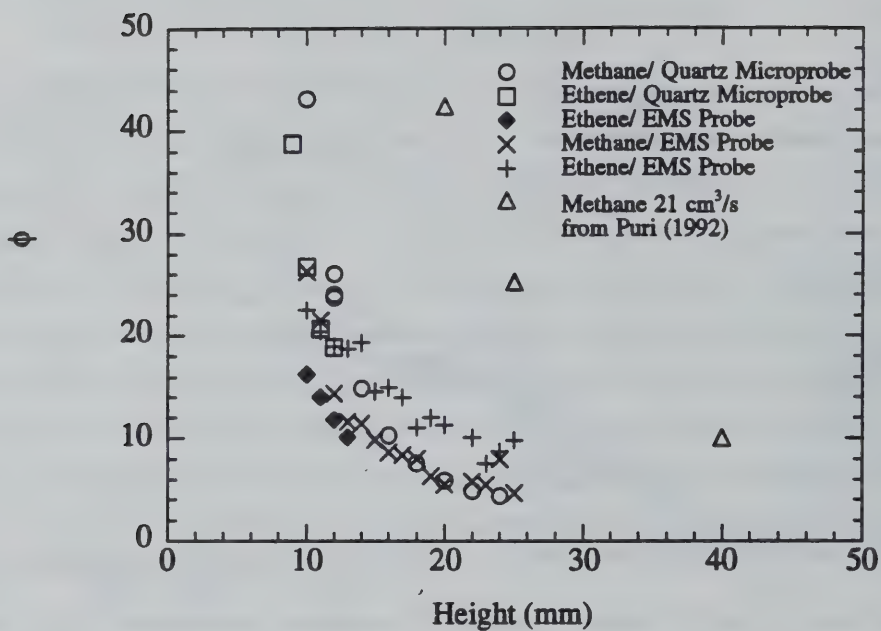
Figure 3.15. Local equivalence ratio as a function of height along the center line in a methane and an ethene under-ventilated laminar diffusion flame of a global equivalence ratio of 4 for both probes used in this study.

locations. Results taken with the two different probes, in general, show similar results. This is particularly true for the methane flame with a flow rate of 10 cm^3/s. Reproducibility of the ethene flame is not as good and this led to some difficulties in comparing the concentration profiles at similar centerline values of ϕ.

In the end, two heights were chosen for comparison based on the centerline equivalence ratio and a third height was chosen arbitrarily and corresponded to a location where concentration profiles could be easily obtained. The two sets of heights chosen for comparison based the centerline value of ϕ correspond to: 1) a height of 3.5mm ($\phi = 1590$) in the methane flame and 2.5mm ($\phi = 1703$) in the ethene flame and a height of 16mm ($\phi = 13$) in the methane flame and 21mm ($\phi = 4$) in the ethene flame. Finally, measurements were also taken at a height of 10mm ($\phi = 25$) in the methane flame and at 1.5 mm ($\phi = 3061$) in the ethene flame. Although the conditions achieved at these center line locations can be argued to be similar, they also reflect the difficulty in obtaining reproducible concentration measurements in these under-ventilated diffusion flames. Thus, comparisons between the results in the two flames must keep these limitations in mind. None the less, the trends observed in the present study are viewed to be representation of under-ventilated flames in general. Additional quantitative comparisons should be pursued in future work.

The concentration profiles obtained for the methane and ethene flames, in terms of mole fraction, are shown in Figures 3.16 and 3.17. The concentration profiles at the heights of 3.5mm and 2.5mm for the methane and ethene flames respectively (Figure 3.16 (top) and 3.17 (middle)) show that the reaction zone, as indicated by the respective coincident minimum in the fuel and oxygen concentrations, occurs at a radial location of 7mm. Both of these measurements heights (as well as the 1.5mm position in the ethene flame shown in Figure 3.17 (top)) display concentration profiles similar to those observed in over-ventilated flames at similar axial positions. In particular, note that the CO profile achieves a local maximum just to the fuel rich side of the reaction zone as is typically observed in over-ventilated flames (Mitchell et al., 1980). A similar profile shape will be observed for the temperature field at this location (see Section 3.5). Both flames are observed to have small amounts of oxygen on the fuel rich side of the diffusion flame at these lower heights. This is likely due to oxygen diffusing into the flame near the exit of the burner where the flame front is quenched by the presence of the fuel tube.

At higher locations in the flame, the species concentration profiles are quite different from those describe above. At the 16mm location in the methane flame and the 21mm location in the ethene flame, the concentration

Table 3.4. Coefficients of Different Species Measured for the Determination of the Local Equivalence Ratio (ϕ).

Name	Formula	Coefficient	Name	Formula	Coefficient
Ethane	C_2H_6	7	Acetylene	C_2H_2	5
Propane	C_3H_8	10	Propene	C_3H_6	9
Butane	C_4H_{10}	13	Butene	C_4H_8	12
Pentane	C_5H_{12}	16	Pentene	C_5H_{10}	15
Hexane	C_6H_{14}	19	Hexene	C_6H_{12}	18

profiles are considerably more uniform across the entire flame. Since these positions likely lie above the location where the flame has reached the wall (or been quenched by the wall), no distinct reaction zone is observed as was the case for the lower positions. Fairly large concentrations of fuel remain as would be expected for these under-ventilated conditions. The continued presence of oxygen is somewhat surprising, but may reflect the temperature conditions presence in these flames (see Section 3.5). The concentration profiles observed at these higher locations differ greatly from those observed in over-ventilated flames at similar heights and reflect the unique structure of under-ventilated laminar diffusion flames.

Figures 3.18 and 3.19 show the fuel and CO molar fractions as a function of local equivalence ratio in the methane and ethene under-ventilated flames($\Phi = 4$) at the measurement heights specified above. In both flames the fuel and CO fractions are strongly dependent on the local equivalence ratio. Both species increase rapidly as the equivalence ratio (ϕ) exceeds 1. However the CO mole fraction is observed to decrease towards 0 for $\phi \gg 1$. This strong dependence on local equivalence ratio can be explained by the rapid reaction rates of characteristic fuel oxidation to form CO. At the temperatures found in the flame, fuel and oxidizer react quickly to form CO, however, CO oxidation, on the other hand, is comparatively slow. The oxidation of CO to form CO_2 depends on the presence of radicals formed by reacting O_2 molecules, typically OH and O, which are in low concentrations in fuel rich regions. The unoxidized CO is therefore able to diffuse throughout the rich side of the flame where little O_2 is found to form radicals.

It would be expected that CO should be found in greater amounts at lower heights in an under-ventilated laminar diffusion flame since this is where it is produced, and then diffuses throughout the flame. Figure 3.18 supports this argument for the methane flame where a larger CO peak mole fraction of 0.03 is found at a ϕ between 1 and 2 at a height of 3.5mm which then decreases to a CO mole fraction of 0.025 at a height of 10mm and finally at a height of 16mm to approximately 0.02 throughout the flame. A similar trend is observed for the ethene flame where the CO peak mole fraction measured at the 1.5mm and 2.5mm are approximately 0.042 as compared to 0.035 at the 21mm height. There are two additional points to note regarding the ethene diffusion flame results. First, the peak CO mole fractions occur at slightly larger local equivalence ratios as compared to the methane flame. A similar trend with respect to the CO yield as a function of global equivalence ratio was observed between the two fuels. Second, the CO mole fraction does increase slightly between the 1.5mm and the 2.5mm heights which likely indicates that the peak CO may increase slightly until the flame height is exceeded (see Figure 3.1). More axial locations would need to be measured to further resolve this point.

In Figures 3.20 and 3.21 global measurements and point measurements in the flame of the ratio of CO and CO_2 mole fractions are compared as was previously done in Figure 3.13 and 3.14, comparing the results of other workers with the present study. The overall shape of the global and local measurements are similar except for the presence of a decrease in X_{CO}/X_{CO2} global measurements. This decrease occurred at $\Phi = 2$ for the methane diffusion flame and $\Phi = 2.5$ for the ethene diffusion flame. The local measurements of X_{CO}/X_{CO2} do not show this decrease but indicate an increase in CO concentration with respect to CO_2 as measurements are taken closer to the centerline where ϕ, the local equivalence ratio, tends to infinity. These results can be compared to those presented in Figure 3.13 which compared results from other workers. The X_{CO}/X_{CO2} ratio presented in
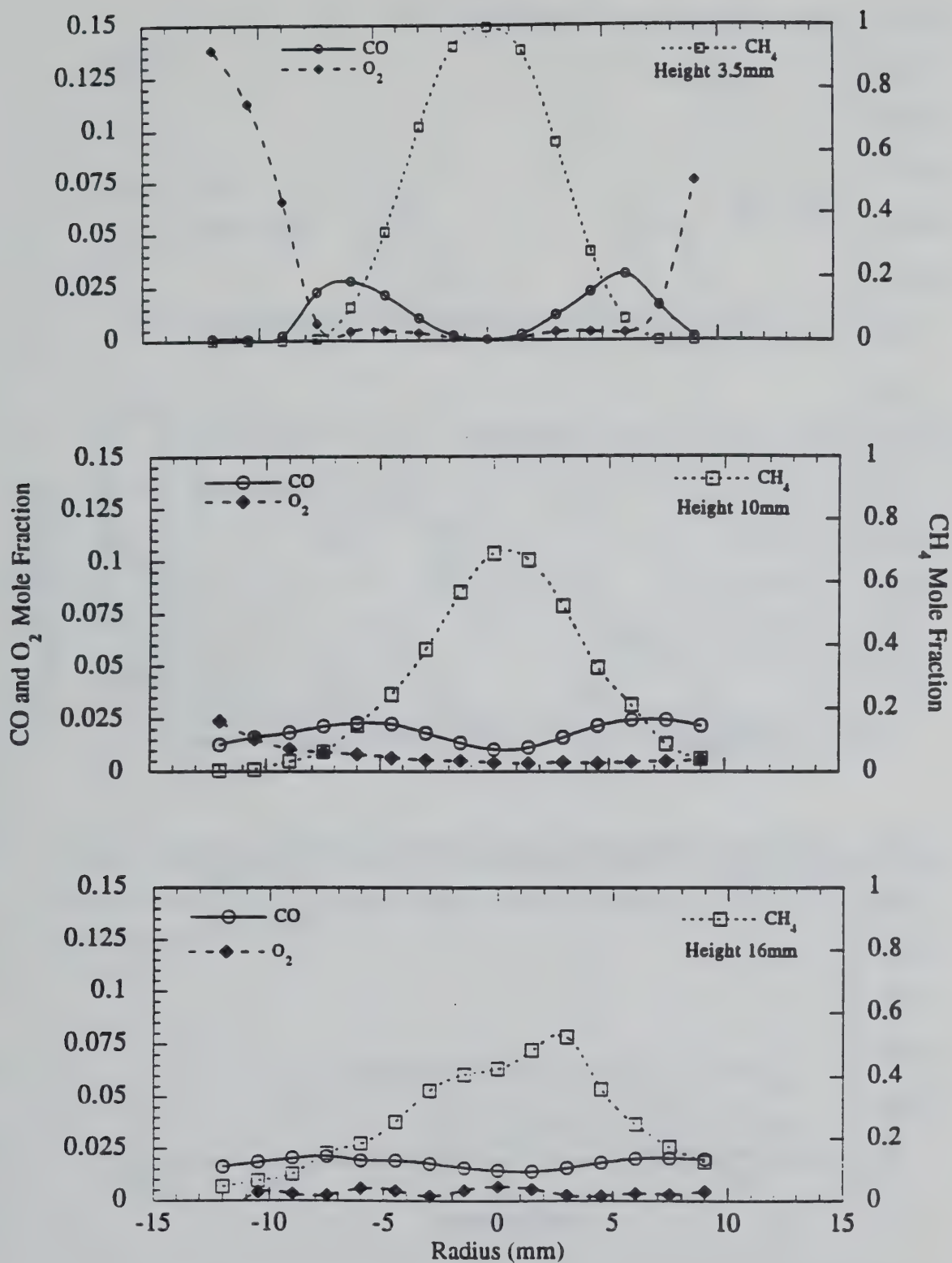
Figure 3.16. CO, O_2 and CH_4 mole fraction radial profiles in a methane under-ventilated laminar diffusion flame with a fuel flow rate of $10cm^3/s$ at three different heights: 3.5mm (top), 10mm (center) and 16mm (bottom).
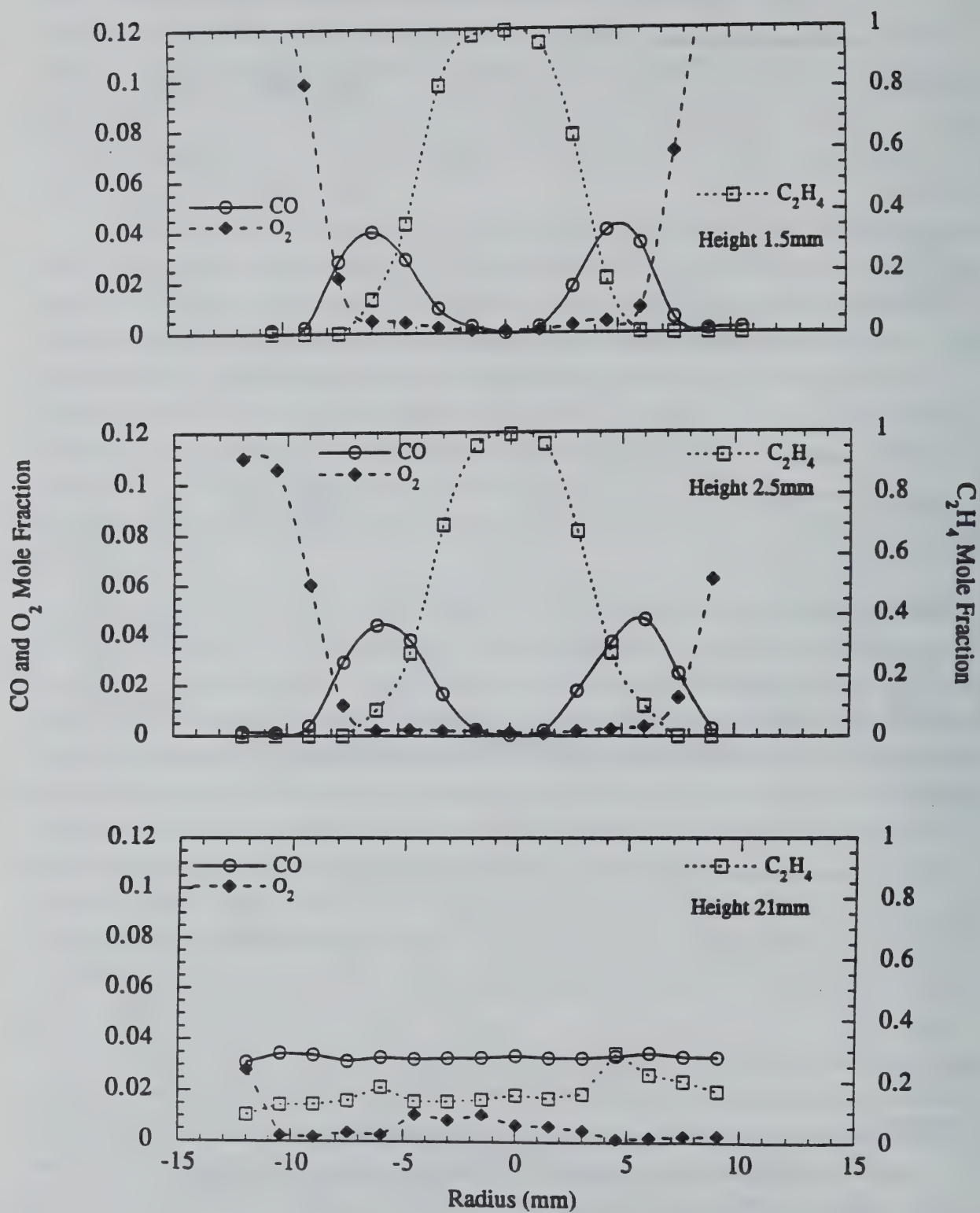
Figure 3.17. CO, O_2 and C_2H_4 mole fraction radial profiles in an ethene under-ventilated laminar diffusion flame with a fuel flow rate of 6.4cm^3/s at three different heights: 2.5mm (top), 11mm (center) and 21mm (bottom).
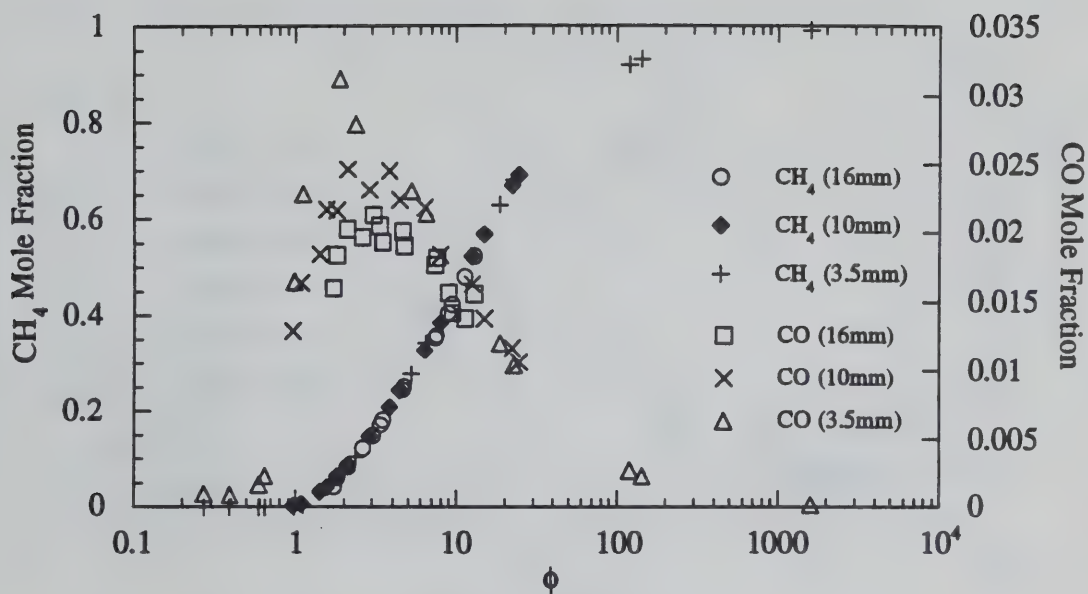
Figure 3.18. Mole fraction of CH4 and CO versus local equivalence ratio, ϕ, for selected axial locations (3.5mm, 10mm, 16mm) in the methane diffusion flame with a fuel flow rate of $10cm^3/s$ at a global equivalence ratio, Φ, of 4..
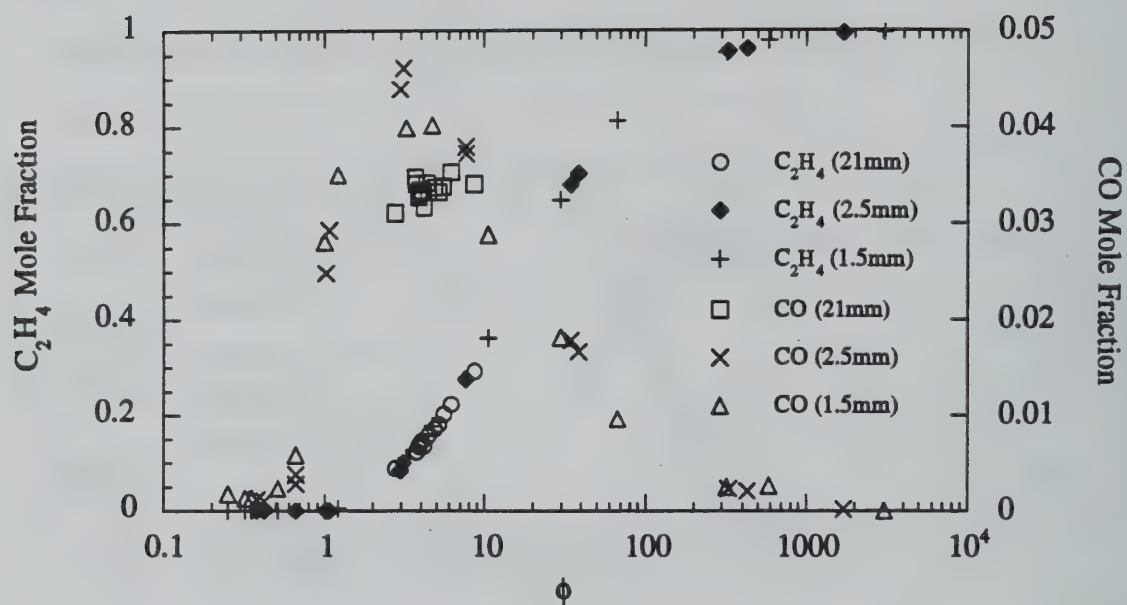
Figure 3.19. Mole fraction of C_2H_4 and CO versus local equivalence ratio, ϕ, for selected axial locations (1.5mm, 2.5mm, 21mm) in the ethene diffusion flame with a fuel flow rate of 6.4cm^3/s at a global equivalence ratio, Φ, of 4..
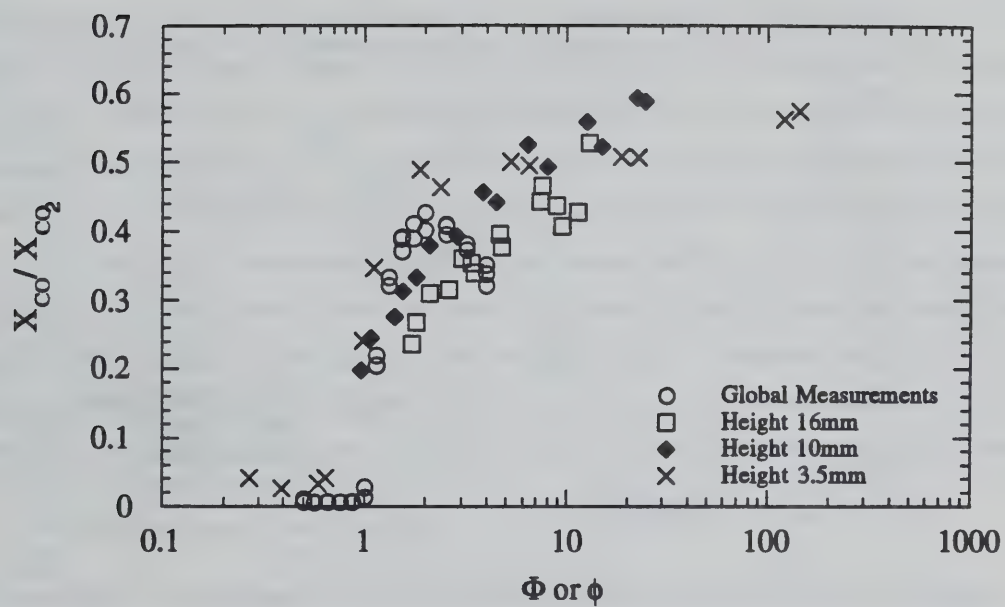
Figure 3.20. Local and global X_{CO}/X_{CO_2} as a function of local (ϕ) or global (Φ) equivalence ratio in a methane diffusion flame with a fuel flow rate of $10cm^3$/s. Local measurements of X_{CO}/X_{CO_2} ratio are shown for three different heights.
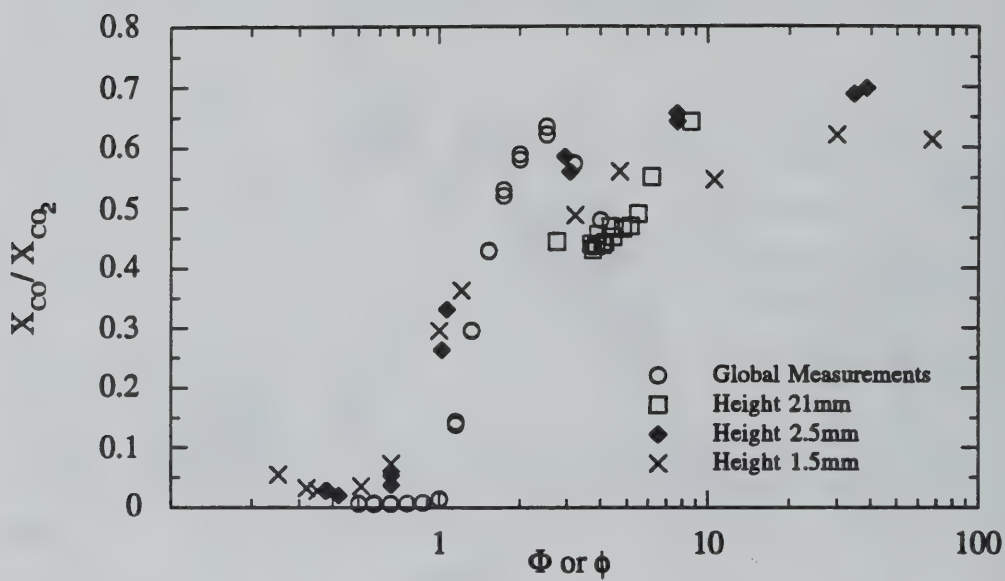
Figure 3.21. Local and global X_{CO}/X_{CO2} ratio as a function of local (ϕ) or global (Φ) equivalence ratio in an ethene diffusion flame with a fuel flow rate of 6.4cm^3/s. Local measurements of X_{CO}/X_{CO2} ratio are shown for three different heights.

Figure 3.20 tends toward the value of 0.6 for large ϕ, similar to the results of Puri (1992) taken for an under-ventilated methane flame. Over-ventilated methane diffusion flame (Mitchell et al. 1980) appears to produce locally more CO, resulting in a X_{CO}/X_{CO2} ratio of 0.7.

It is difficult to argue that there are any significant trends with respect to concentration measurements shown in Figures 3.20 and 3.21. One can observe a slight decrease in the X_{CO}/X_{CO2} ratio of the highest measurement locations (16mm and 21mm respectively for the methane and ethene flames) which would be consistent with the argument that longer reactions times are required to convert CO to CO_2 as compared with its production from the fuel oxidation process. Note that both the methane and the ethene diffusion flames had a global equivalence ratio of 4 which correspond to the largest global equivalence ratio studied. The global X_{CO}/X_{CO2} ratio value was approximately 0.34 and 0.46 respectively for the methane and ethene flames at $\Phi = 4$. As the measurement height increases the local values of X_{CO}/X_{CO2} ratio appear to be slowly approaching the global values.

Figure 3.22 shows the molar fraction of CO, O_2, C_2H_4 and C_2H_2 in a methane flame. The acetylene, C_2H_2, mole fraction peak is just inside of the reaction zone located where the oxygen and fuel concentration tend to zero. The fuel rich zone is where soot is observed to form. Comparing Figure 3.22 with the results for the ethene diffusion flame presented in Figure 3.23 and 3.24 shows that the concentration of C_2H_2 in the ethene flame at approximately the same height is seven times greater. Since the ethene produces a sootier flame than methane, the higher concentration of acetylene lower in the ethene flame is consistent with the hypothesis that acetylene is related to soot particle growth. The larger differences in the acetylene mole fraction as compared to the CO mole fraction in the methane and ethene diffusion flames is striking. The CO mole fractions in the two flames differ by less than a factor of two at the locations shown in Figures 3.22, 3.23 and 3.24, but the C_2H_2 are about a factor of seven greater.

3.3. Temperature Measurements in Under-Ventilated Laminar Diffusion Flames

Temperature profiles have been obtained in methane and ethene under-ventilated diffusion flames under conditions identical to those employed for the in-flame concentration measurements. The flame conditions selected correspond to a global equivalence ratio of 4. For the methane under-ventilated diffusion flame, the fuel and air flow rates were $10 cm^3/s$ and $23.8 cm^3/s$, respectively. In the case of the ethene flame, the fuel and air flow rates were $6.4 cm^3/s$ and $22.8 cm^3/s$, respectively. The calculated adiabatic flame temperature for these flames is 944 K for the methane flame and 1279 K for the ethene flame corresponding to an equivalence ratio of 4. Radial profiles of the temperature field were obtained as a function of axial location above the fuel tube exit.

Temperature measurements were obtained using uncoated Pt-Pt/Rh thermocouples which were rapidly inserted into the flame to minimize soot deposition (see Section 2.6). Soot deposited on the thermocouple bead during the measurements was removed by placing the thermocouple bead near the flame front where the soot was rapidly oxidized. Figures 3.25 and 3.26 show plots of the measured temperatures as a function of the measurement location (displacement) for several axial locations for both the methane (Figure 3.25) and the ethene (Figure 3.26) under-ventilated diffusion flames. The displacement distance is simply the position relative to the edge of the measurement field where data was first obtained. It can be converted to radial position by selecting the origin of the radial coordinate based on flame symmetry considerations. These data have been corrected for radiation effects, but
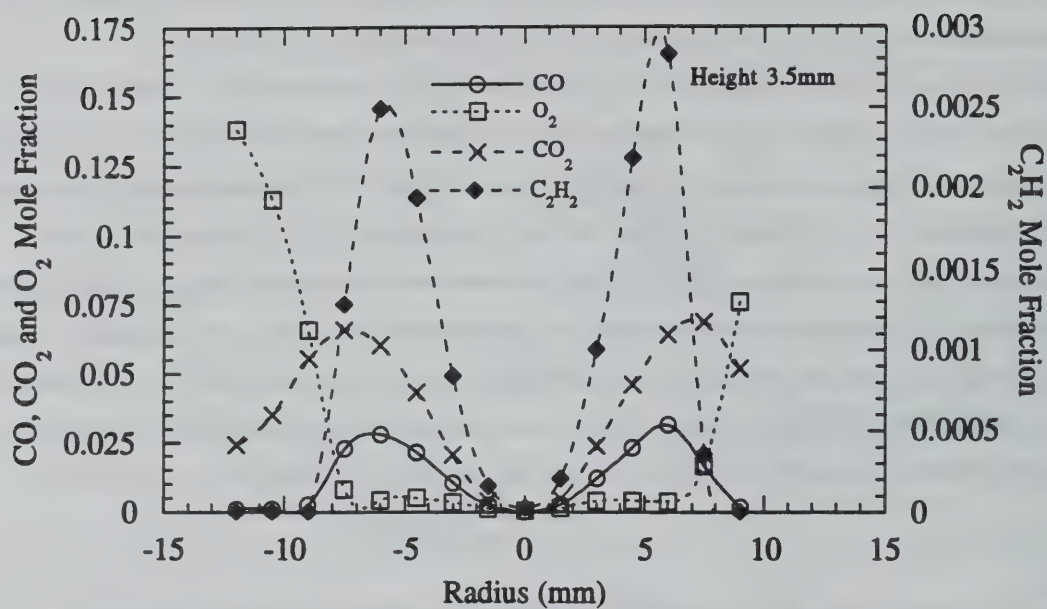
Figure 3.22. Mole fraction of CO, CO_2, C_2H_2 and O_2 in a methane diffusion flame with a fuel

flow rate of $10 cm^3$/s and $\Phi = 4$ at a height of 3.5mm.
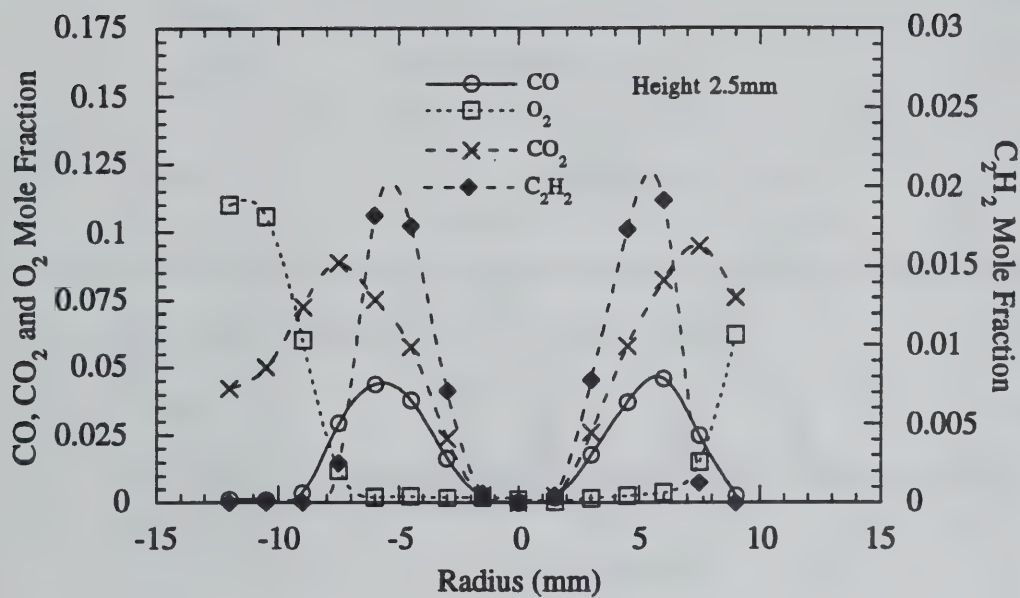
Figure 3.23. Mole fraction of CO, CO_2, C_2H_2 and O_2 in an ethene diffusion flame with a fuel flow rate of $6.4cm^3/s$ and $\Phi = 4$ at a height of 2.5mm.
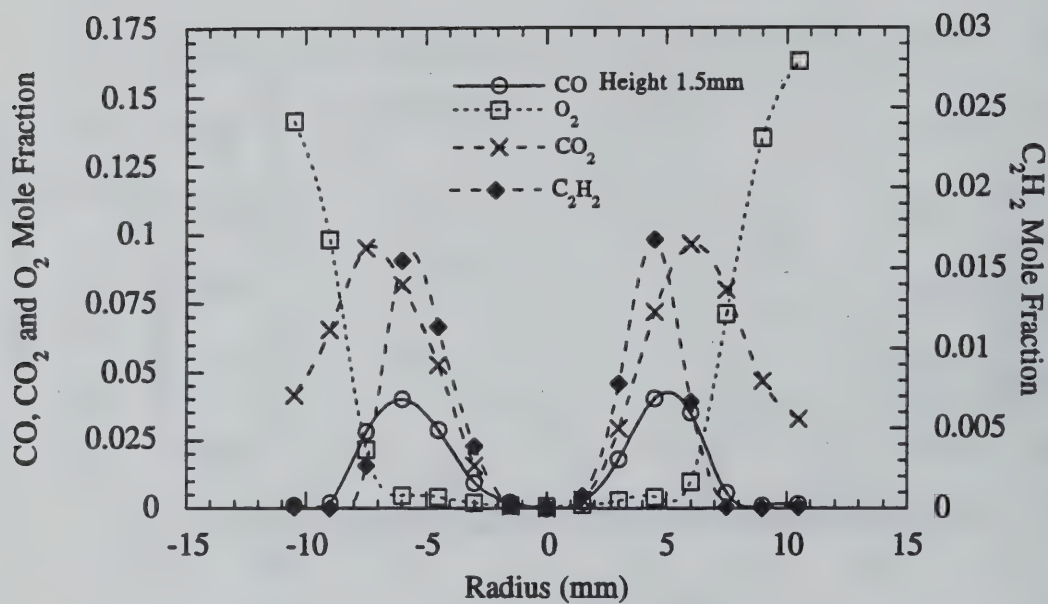
Figure 3.24. Mole fraction of CO, CO_2, C_2H_2 and O_2 in an ethene diffusion flame with a fuel flow rate of 6.4cm^3/s and $\Phi = 4$ at a height of 1.5mm.
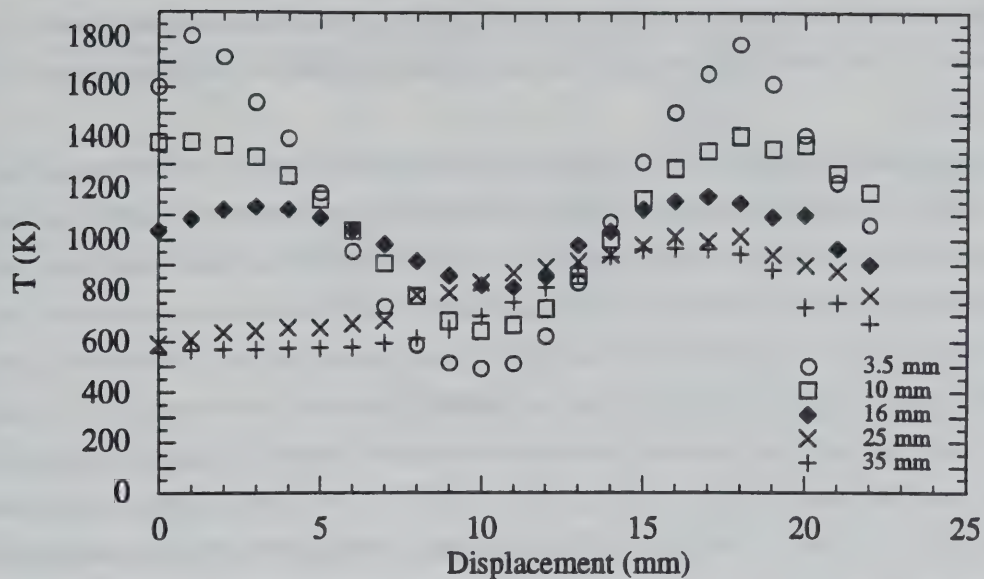
Figure 3.25. Radial temperature measurements in a methane laminar diffusion flame with a fuel flow rate of 10cm^3/s and a global equivalence ratio of 4 at selected heights.
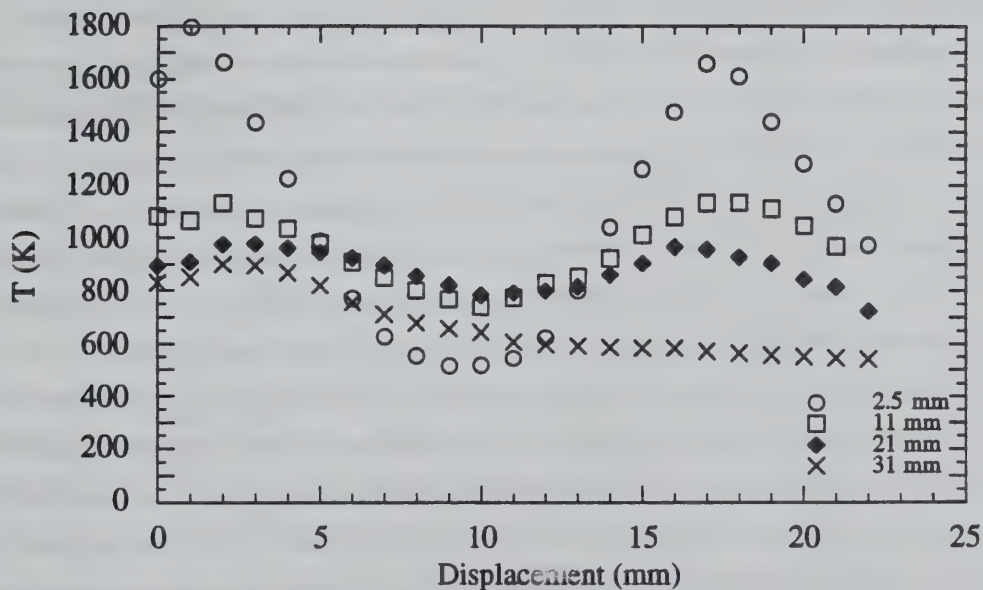
Figure 3.26. Radial temperature measurements in an ethene laminar diffusion flame with a fuel flow rate of 6.4cm^3/s and a global equivalence ratio of 4 for selected heights.

have not been centered relative to the axis of symmetry of the profiles. The measurements generally show good symmetry for the lower axial locations (heights lower than 25mm), while showing some deviation from symmetry at the higher locations. This trend reflects the difficulty in achieving stable under-ventilated flames as well as the higher sensitivity of this flame to the presence of intrusive probes as compared to the situation observed for over-ventilated flames.

The general trends for the evolution of the temperature field in the two under-ventilated flames are similar. At the lowest axial positions a maximum of about 1800K in the temperature field is observed near the edges of the measurement field. This maximum temperature decreases rapidly with increasing height in the flame and the profile broadens towards the interior of the flame. At the highest axial locations measured, a flat, although non-symmetric, profile is achieved which varies between 600K and 900K. The evolution of this temperature field is quite different from that observed in over-ventilated flames. For over-ventilated conditions, a similar profile to that observed for the under-ventilated flame would be observed at the lowest axial location. However, the annular structure of the temperature profile is maintained over a much larger axial extent for the over-ventilated flame with a smaller decrease in the maximum temperature as a function of height in the flame. Additionally, for the over-ventilated case, the annular structure also broadens with height, but eventually achieves a maximum along the centerline of the flame. Thus, the temperature results indicate that a quite different flame structure results for under-ventilated flame conditions as one would expect. It should be noted that the adiabatic flame temperatures for a global equivalence ratio of 4 for the methane and ethene flames are 944K and 1279K, respectively. Comparisons with the measured temperature data show that we should expect relatively low temperatures in these flames which is reflected in the data taken at the higher axial locations in the methane (height of 35mm) and the ethene flame (height of 31mm). However, even at these positions, the measured temperatures are lower than the calculated adiabatic values which indicates that energy lost from the flame due to radiation and conduction through the burner wall is significant.

The variation in the measured temperature as a function of radial position for the lowest axial positions (3.5mm for methane and 2.5mm for ethene) reflects the classic diffusion mixing control nature of these flames similar to over-ventilated flames. The maximum in the temperature field should occur near the region where the local equivalence, ϕ, is 1. As one moves higher in the flame, the depletion of oxygen due to combustion reduces the availability of oxidizer and the local equivalence ratio will eventually exceed 1 everywhere in the flame.

These observations are further illustrated in Figures 3.27 and 3.28 which show plots of the temperature and local equivalence ratio profiles for the methane and ethene diffusion flames respectively. The local equivalence ratios were determined based on the in-flame concentration measurements describe in Section 3.2.2. As pointed out above, the highest temperatures at the lowest axial positions correspond to the region where $\phi = 1$. This location occurs at a radial position between 7mm and 9mm from the centerline of the flame in close agreement with the observation that the fuel and oxygen concentrations approach zero at this same location (see Section 3.2.2). It should also be noted that at the lowest heights, 3.5mm in the methane diffusion flame and 2.5mm in the ethene diffusion flame, that local equivalence ratios less than 1 are observed near the edges of the flame. However, at the higher heights ϕ is always equal to or greater than 1 in agreement with the overall under-ventilated nature of these flames. As was pointed out previously in discussing the in-flame concentration measurements, at the higher locations concentration
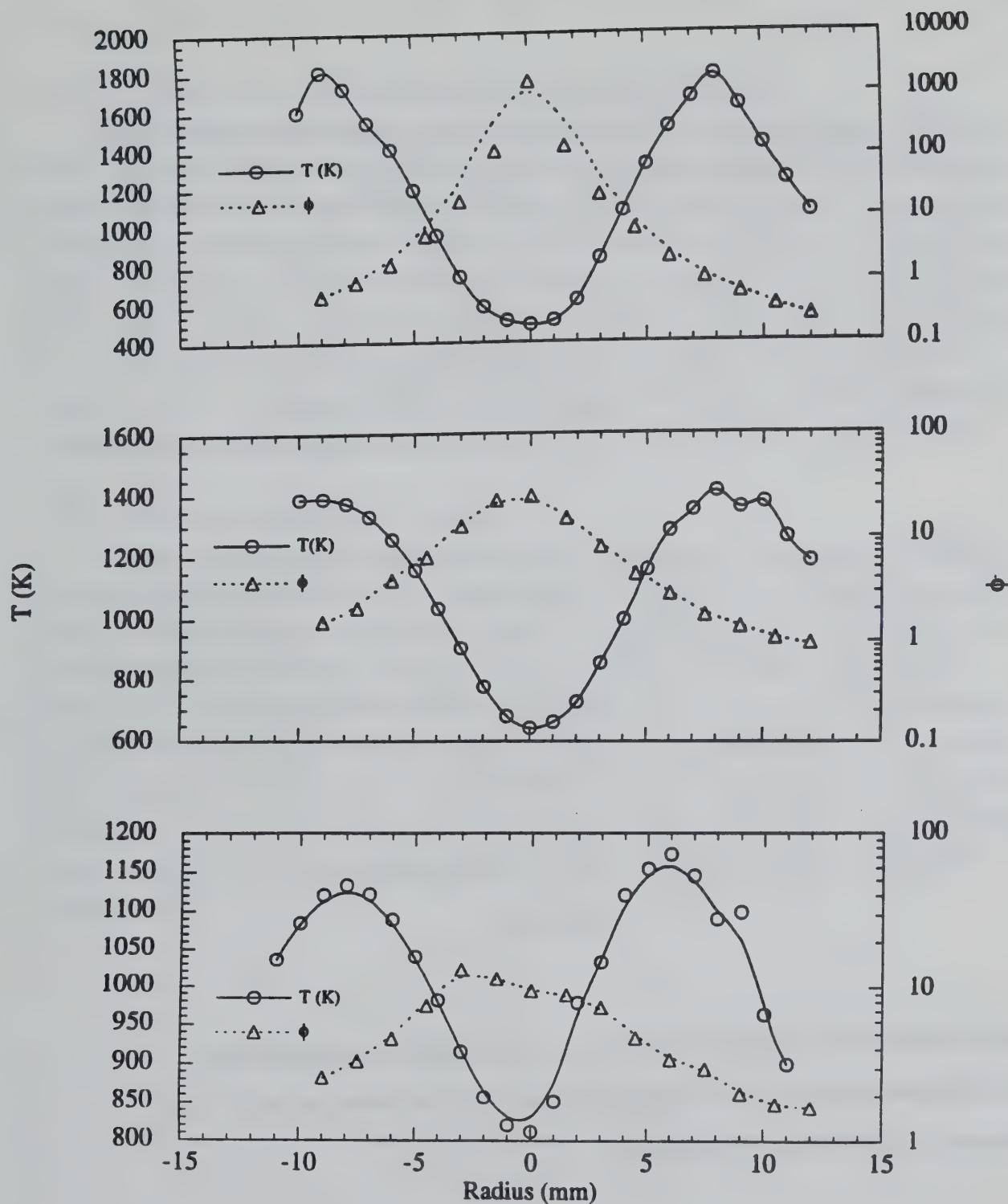
Figure 3.27. Radial temperature combined with local equivalence ratio profile measurements from in-flame concentration measurements for a methane diffusion flame with a fuel flow rate of $10cm^3/s$ at three different heights: 3.5mm (top), 10mm (center) and 16mm (bottom).
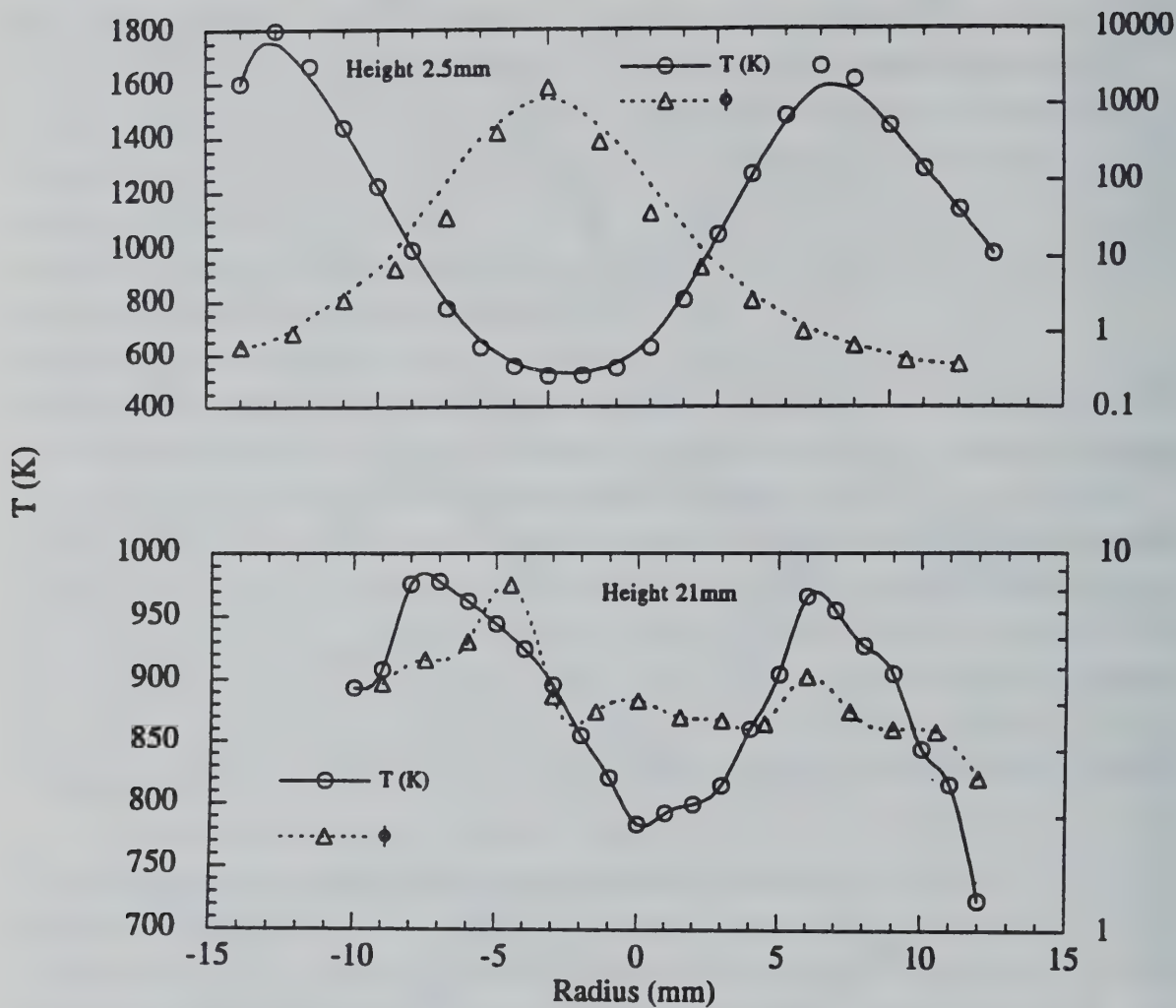
Figure 3.28. Radial temperature combined with local equivalence ratio profile measurements from in-flame concentration measurements for an ethene diffusion flame with a fuel flow rate of 6.4cm^3/s at two different heights: 2.5mm (top) and 21mm (bottom).

gradients and consequently the variatio᠎ ᠎n the local equivalence ratio decreases. Thus at these higher position᠎ the average of the local equivalence across the flame should approach the global equivalence ratio of 4. This appears to be the trend exhibited in Figures 3.27 and 3.28.

3.4. Transmission Electron Microscopy of Collected Soot Particles

During the soot sampling studies it was noticed that the soot collected at high equivalence ratios (e.g., $\Phi = 4$) had a lighter color than soot samples collected at lower equivalence ratios (e.g., $\Phi = 1$). In fact, for the methane diffusion flame at $\Phi = 4$ the filter had a yellowish appearance. To investigate the potential for changes in the soot structure at these conditions, soot particles were collected on Transmission Electron Microscopy (TEM) grids. Soot samples were taken for an ethene diffusion flame at $\Phi = 1$ and $\Phi = 4$ at the top of the burner. Figure 3.29 show the resulting TEM pictures for these two conditions. While in both cases the smoke has an agglomerated structure, $\Phi = 4$ the agglomerate is agglutinated indicating the presence of a liquid-like component. This liquid-like substance is not present for the $\Phi = 1$ conditions. Several different TEM images were analyzed and, even if the overall size of the soot particles varied, the same liquid-like substance appeared to cover the particles at $\Phi = 4$.

3.5. Organic and Elemental Soot Content

As Φ increases not only does the structure of the soot particles change but their composition also change. The organic and elemental carbon content of soot particles is shown in Table 3.5. The elemental carbon refers to carbon atoms which are not bonded to any hydrogen atoms (i.e. graphitic in nature) while the organic carbon atoms refers to carbon atoms bonded to one or more hydrogen atoms. The method for determining the elemental and organic content of the soot was described in Chapter 2. Previous studies on crude oil, lumber, heptane, polyurethane and asphalt shingles in over-ventilated fires have shown that at most 25% of the carbon found in soot samples was organic (Mulholland et al. 1989; Benner et al. 1990; Dod et al. 1989). At higher equivalence ratios the results below show that the organic carbon content can be as high as 80% in methane and 50% in ethene. Thus, the very chemical nature of the soot formed in these under-ventilated diffusion flames is quite different for that observed for over-ventilated conditions.
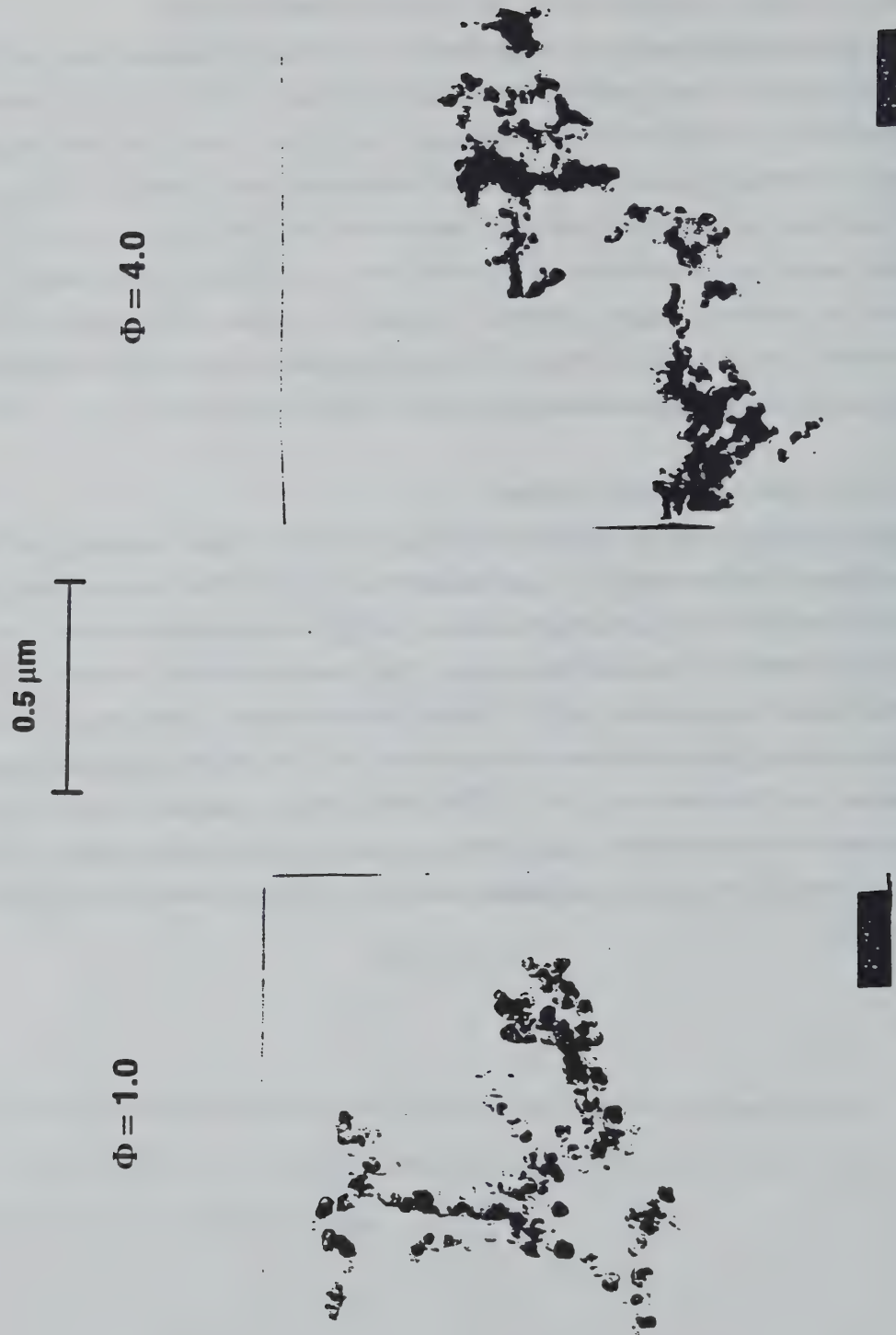
Figure 3.29 TEM pictures of soot particles collected from an ethene flame with a fuel flow rate of 6.4cm^3/s.

Table 3.5. Organic and Elemental Carbon Analysis

			Methane 10cm^3/s		
Φ	Organic Carbon $\mu g/cm^2$	Organic Carbon Error	Elemental Carbon $\mu g/cm^2$	Elemental Carbon Error	$\dfrac{\text{Organic}}{\text{Elemental}}$
1	1.0	0.2	21	1	0.05
2	8.4	0.5	4.9	0.3	1.7
4	3.4	0.3	0.4	0.1	8.5
4	5.2	0.4	1.0	0.2	5.2

			Ethene 6.4cm^3/s		
Φ	Organic Carbon $\mu g/cm^2$	Organic Carbon Error	Elemental Carbon $\mu g/cm^2$	Elemental Carbon Error	$\dfrac{\text{Organic}}{\text{Elemental}}$
0.5	0.7	0.1	19	1	0.04
1	1.3	0.2	27	1	0.5
2	7.2	0.5	15	0.9	0.48
4	7.0	0.5	6.2	0.4	1.13

CHAPTER 4
CONCLUSION

An experimental investigation of the generation of CO and smoke for under-ventilated laminar diffusion flames has revealed both strong similarities and differences with studies considering over-ventilated conditions. In particular, the proportionality between smoke yield and CO yield observed for the post-flame (over-fire) region of over-ventilated flames for a wide range of fuels is not found to be valid for the under-ventilated case. In fact, the soot observed in the under-ventilated flames is observed to vary considerably in terms of the chemical structure from that typically observed in over-ventilated flames. The highly organic nature of the soot implies that the structure of the soot may be more similar to early agglutinated soot particles recently observed in diffusion flames than to the more aged aggregates typical of the post-flame region for over-ventilated flames.

Comparisons in terms of the ratio of CO and CO_2 as a function of global equivalence ratio in the post-flame region of the under-ventilated flames show a similar behavior to that previously observed for in-flame measurements for both over-ventilated and under-ventilated diffusion flames which examined the dependence of this ratio on local equivalence ratio conditions. There appears to be a rough scaling between the global and the local equivalence ratio results for the formation of CO and CO_2 which suggests that the global equivalence ratio represent behavior averaged over the local equivalence ratios occurring in the flame. This suggests that for the in-flame fuel-rich region, the chemical environment excluding soot is correlated with equivalence ratio in a similar way for both an over-ventilated flame and an under-ventilated flame. The low production of CO in the post-flame region of over-ventilated flames is simply a result of the oxidation of CO to CO_2 in the upper region of these flames.

Studies involving different fuels also show results specific to under-ventilated conditions. For a more sooting fuel such as ethene as compared to methane, as soot formation increased CO yield was also observed to increase. This is just the opposite effect observed for over-ventilated laminar diffusion flames studied by Puri and Santoro (1992). However, when additive fuels containing oxygenated species (methanol) or aromatic structures (toluene) were added to either the methane or ethene flames for under-ventilated conditions the behavior showed increased (decreased) soot formation resulted in decreased (increased) CO yield in agreement with over-ventilated flame studies. This behavior is argued to be due to the competition for OH between CO and soot particles. For the flames studied here, the balance between this competition can favor either CO or soot particles depending on the local temperature and concentration conditions. Unfortunately the present studies were not of sufficient detail to resolve these competitive channels quantitatively. Thus, the above explanation for the observed behavior of the CO and soot particle yield remains to be tested in future studies.

Finally, the present studies illustrate the utility of the study of under-ventilated flame environments where product yields and trends can be quite different from over-ventilated conditions. These studies should have significance for combustion phenomena in which under-ventilated conditions are typical, such as in fires.

REFERENCES

Barr, J. (1949). Combustion in Vitiated Atmospheres II- Some Preliminary Studies of Diffusion Flames, Fuel, 28(9), pp. 200.

Barr, J. (1953). Diffusion Flames, *Fourth Symposium (International) on Combustion*, The Combustion Institute, pp. 765.

Benner, B.A., Bryner, N.P., Wise, S.A., Mulholland, G.W., Lao, R.C. and Fingas, M.F. (1990). Polycyclic Aromatic Hydrocarbon Emissions from the Combustion of Crude Oil on Water, *Environmental Science and Technology*, **24(9)**, pp. 1418.

Beyler, C.L. (1986) Major Species Production by Solid Fuels in a Two-Layer Compartment Fire Environment, *Proceedings of the First International Symposium on Fire Safety Science*, pp. 431.

Burke, S.P. and Schumann, T.E.W. (1928). Diffusion Flames, *Industrial and Engineering Chemistry*, **20(10)**, pp. 998.

Dod, R.L., Brown, N.J., Mowrer, F.W., Novakov, T. and Williamson, R.B. (1989). Smoke Emission Factors from Medium-Scale Fires: Part 2, *Aerosol Science and Technology*, **10**, pp. 20.

Fenimore, C.P. and Jones, G.W. (1967). Oxidation of Soot by Hydroxyl Radicals, *The Journal of Physical Chemistry*, **71(3)**, pp. 593.

Fisher, S.J. and Grosshandler, W.L. (1988). Radiance, Soot, and Temperature Interactions in Turbulent Alcohol Fires, *Twenty-Second Symposium (International) on Combustion*, The Combustion Institute, pp. 1241.

Frenklach, M., Clary, D.W., Gardiner, W.C. and Stein, S.E.(1984). Detailed Kinetic Modeling of Soot Formation in Shock-Tube Pyrolysis of Acetylene, *Twentieth Symposium (International) on Combustion*, The Combustion Institute, pp. 887.

Friedman, R. (1986). Some Unresolved Fire Chemistry Problems, *Proceedings of the First International Symposium on Fire Safety Science*, pp. 349.

Glassman, I. (1987). *Combustion*, Academic Press, Inc.

Glassman, I. (1988). Soot Formation in Combustion Processes, *Twenty-Second Symposium (International) on Combustion*, The Combustion Institute, pp. 295.

Gomez, A., Littman, M.G. and Glassman, I. (1987). Comparative Study of Soot Formation on the Centerline of Axisymmetric Laminar Diffusion Flames: Fuel and Temperature Effects, *Combustion and Flame*, **70**, pp. 225.

Gomez, A., Sidebotham, G. and Glassman, I. (1984). Sooting Behavior in Temperature-Controlled Laminar Diffusion Flames, *Combustion and Flame*, **58**, pp. 45.

Harris, S.J. and Weiner, A.M. (1984). Some Constraints on Soot Particle Inception in Premixed Ethylene Flames, *Twentieth Symposium (International) on Combustion*, The Combustion Institute, pp. 969.

Harris, S.J. and Weiner, A.M. (1983). Surface Growth of Soot Particles in Premixed Ethylene/Air Flames, *Combustion Science and Technology*, **31**, pp. 155.

Haynes, B.S. and Wagner, H.GG. (1981). Soot Formation, *Progress in Energy and Combustion Science*, **7**, pp. 229.

Johnson, R.L., Shah, J.J., Cary, R.A. and Huntzicker, J.J. (1981). An Automated Thermal-Optical Method for the Analysis of Carbonaceous Aerosol, *Atmospheric Aeorosol: Source/Air Quality Relationships*, ACS Symposium Series 167, American Chemical Society, Washington D.C.

Jones, J.M. and Rosenfeld, J.L.J. (1972) A Model for Sooting in Diffusion Flames, *Combustion and Flame*, **19**, pp. 427.

Kent, J.H. and Honnery, D.R. (1991). Soot Formation Rates in Diffusion Flames- A Unifying Trend, *Combustion Science and Technology*, **75**, pp. 167.

Kent, J.H. and Wagner, H.GG. (1984). Why do Diffusion Flames Emit Smoke?, *Combustion Science and Technology*, **41**, pp. 245.

Köylü, Ü.Ö., Sivathanu, Y.R. and Faeth, G.M. (1991). Carbon Monoxide and Soot Emissions from Buoyant Turbulent Diffusion Flames, *Proceedings of the Third International Symposium on Fire Safety Science*, pp. 625.

Lomax, S. and Simmons, R.F. (1986). The Formation of Carbon Monoxide from Diffusion Flames, *Proceedings of the First International Symposium on Fire Safety Science*, pp. 441.

McCaffrey, B.J. and Harkleroad, M. (1988). Combustion Efficiency, Radiation, CO and Soot Yield from a Variety of Gaseous, Liquid, and Solid Fueled Buoyant Diffusion Flames, *Twenty-Second Symposium (International) on Combustion*, The Combustion Institute, pp. 1251.

Megaridis, C.M. and Dobbins, R.A. (1990). Morphological Description of Flame-Generated Materials, *Combustion Science and Technology*, **71**, pp. 95.

Mitchell, R.E. (1975). Nitrogen Oxide Formation in Laminar Methane-Air Diffusion Flames, Ph D. Thesis, Massachusetts Institute of Technology.

Mitchell, R.E., Sarofim, A.F. and Clomburg, L.A. (1980). Experimental and Numerical Investigation of Confined Laminar Diffusion Flames, *Combustion and Flame*, **37**, pp. 227.

Morehart, J.H., Zukoski, E.E. and Kubota, T. (1990). Species Produced in Fires Burning in Two- Layered and Homogeneous Vitiated Environments, *National Institute of Standards and Technology - Grants Contract Research Report 90-585*, Gaithersburg, MD.

Mulholland, G.W., Henzel, V. and Babrauskas, V. (1989). The Effect of Scale on Smoke Emission, *Proceedings of the Second International Symposium on Fire Safety Science*, pp. 347.

Palmer, H.B. and Cullis, C.C. (1965). The Formation of Carbon from Gases, *Chemistry and Physics of Carbon Volume 1*, Marcel Dekker Inc., New-York.

Puri, R. (1992). The Interaction of Soot Particles with Carbon Monoxide in Laminar Diffusion Flames, Ph. D. Thesis, The Pensylvania University.

Puri, R., Richardson, T.F., Santoro, R.J. and Dobbins, R.A. (1993). Aerosol Dynamic Processes of Soot Aggregates in a Laminar Ethene Diffusion Flame, *Combustion and Flame*, **92**, pp. 320.

Puri, R. and Santoro, R.J. (1991). The Role of Soot Particle Formation on the Production of Carbon Monoxide in Fires, *Proceedings of the Third International Symposium on Fire Safety Science*, pp. 595.

Purser, D.A., "The Effects of Fire Products on Escape Capability in Primates and Human Fire Victims", *Proceedings of the First International Symposium on Fire Safety Science*, pp. 1101.

Reid, R.C., Prausnitz, J.M. and Poling, B.E. (1987). *The Properties of Gases and Liquids 4th Edition*, McGraw-Hill.

Roper, F.G. (1977). The Prediction of Laminar Jet Diffusion Flame Sizes: Part I. Theoritical Model, *Combustion and Flame*, **29**, pp. 219.

Roper, F.G. and Smith, C. (1979). Soot Escape from Laminar Air-Starved Hydrocarbon Flames, *Combustion and Flame*, **36**, pp. 125.

Roper, F.G., Smith, C. and Cunningham, A.C. (1977). The Prediction of Laminar Jet Diffusion Flame Sizes: Part II. Experimental Verification, *Combustion and Flame*, **29**, pp. 227.

Santoro, R.J., Yeh, T.T., Horvath, J.J. and Semerjian, H.G. (1987). The Transport and Growth of Soot Particles in Laminar Diffusion Flames, *Combustion Science and Technology*, **53**, pp. 89.

Savage, L.D. (1962). The Enclosed Laminar Diffusion Flame, *Combustion and Flame*, **6**, pp. 77.

Schoenung, S.M. and Hanson, R.K. (1981). CO and Temperature Measurements in a Flat Flame by Laser Absorption Spectroscopy and Probe Techniques, *Combustion Science and Technology*, **24**, pp. 227.

Schug, K.P., Manheimer-Timnat, Y., Yaccarino, P. and Glassman, I. (1980). Sooting Behavior of Gaseous Hydrocarbon Diffusion Flames and the Influence of Additives, *Combustion Science and Technology*, **22**, pp. 235.

Sidebotham, G.W. and Glassman, I. (1992). Flame Temperature, Fuel Structure, and Fuel Concentration Effects on Soot Formation in Inverse Diffusion Flames, *Combustion and Flame*, **90**, pp. 269.

Toner, S.J., Zukoski, E.E. and Kubota, T. (1987). Entrainment, Chemistry, and Structure of Fire Plumes, *National Bureau of Standards - Grants Contract Research Report 87-528*, Gaithersburg, MD.

Wagner, H. GG. (1978). Soot Formation in Combustion, *Seventeeth Symposium (International) on Combustion*, The Combustion Institute, pp. 3.

Walker, J. (1979). Flames in which Air is Introduced into a Flammable Gas rather than vice versa, *Scientific American*, **Nov.**, pp. 192.

Wu, K.-T. and Essenhigh, R.H. (1984). Mapping and Structure of Inverse Diffusion Flames of Methane, *Twentieth Symposium (International) on Combustion*, The Combustion Institute, pp. 1925.

Yetter, R.A., Dryer, F.L. and Rabitz, H. (1985). Some Interpretive Aspects of Elementary Sensitivity Gradients in Combustion Kinetics Modeling, *Combustion and Flame*, **59**, pp. 107.

Zukoski, E.E., Morehart, J.H., Kubota, T. and Toner, S.J. (1991). Species Production and Heat Release Rates in Two-Layered Natural Gas Fires, *Combustion and Flame*, **83**, pp. 325.

APPENDIX A
DATA FROM GOBAL MEASUREMENTS

As explained in Section 2.4.1.2 a discrepency was noted during this study between the results of the Horiba NDIR analyzers model PIR-2000 and the gas chromatograph. After further investigation using the SRM Gas Mixtures it was found that the CO_2 concentration measurements were slightly low. The CO_2 results shown in this appendix, taken from 02/15/92 to 05/20/92 inclusively, were corrected by a factor of 1.0554. The CO_2 results taken after 05/20/92 were obtained using a different CO_2 analyzer (Beckman NDIR model 864) and did not require to be corrected.

For every set of data the fuel and fuel flow rate (in some cases two fuels for fuel mixtures) are indicated along with the dilution flow rate, the size of the brass fuel tube, the air quartz tube and the date when the measurements were made. The CO yield is given in grams of CO per gram of fuel and the smoke yield is given in grams of smoke collected on the filter per grams of fuel.

Methane 10cm^3/s, N$_2$ dilution 472cm^3/s
12.7mm O.D. Fuel Tube 35mm I.D. Air Tube (02/15/92)

Φ	CO (%)	CO$_2$ (%)	Smoke (g)	CO Yield	Smoke Yield
0.50	0.001	1.54	-	0.001	-
1.00	0.103	1.60	-	0.104	-
1.00	0.086	1.61	-	0.087	-
2.00	0.293	0.69	-	0.272	-
4.00	0.131	0.33	-	0.116	-

Methane 21cm^3/s, N$_2$ dilution 708cm^3/s
12.7mm O.D. Fuel Tube 35mm I.D. Air Tube (02/15/92)

Φ	CO (%)	CO$_2$ (%)	Smoke (g)	CO Yield	Smoke Yield
0.72	0.003	2.21	-	0.003	-
1.00	0.145	2.12	-	0.112	-
2.00	0.431	0.91	-	0.298	-
4.00	0.237	0.44	-	0.154	-

Methane $10cm^3/s$, N_2 dilution $472cm^3/s$
12.7mm O.D. Fuel Tube 22mm I.D. Air Tube (02/15/92)

Φ	CO (%)	CO_2 (%)	Smoke (g)	CO Yield	Smoke Yield
0.50	0.002	1.54	-	0.002	-
1.00	0.168	1.56	-	0.170	-
2.00	0.329	0.69	-	0.305	-
4.00	0.148	0.33	-	0.131	-

Methane $21cm^3/s$, N_2 dilution $708cm^3/s$
12.7mm O.D. Fuel Tube 22mm I.D. Air Tube (02/15/92)

Φ	CO (%)	CO_2 (%)	Smoke (g)	CO Yield	Smoke Yield
1.00	0.215	2.05	-	0.166	-
2.00	0.466	0.88	-	0.322	-
4.00	0.250	0.44	-	0.162	-

Methane $10cm^3/s$, N_2 dilution $472cm^3/s$
9.6mm O.D. Fuel Tube 22mm I.D. Air Tube (02/15/92)

Φ	CO (%)	CO_2 (%)	Smoke (g)	CO Yield	Smoke Yield
0.50	0.001	1.54	-	0.001	-
1.00	0.085	1.70	-	0.086	-
2.00	0.328	0.68	-	0.304	-
4.00	0.145	0.33	-	0.128	-

Methane $21cm^3/s$, N_2 dilution $708cm^3/s$
9.6mm O.D. Fuel Tube 22mm I.D. Air Tube (02/15/92)

Φ	CO (%)	CO_2 (%)	Smoke (g)	CO Yield	Smoke Yield
1.00	0.081	2.21	-	0.063	-
2.00	0.473	0.88	-	0.327	-
4.00	0.250	0.45	-	0.162	-

Methane $10cm^3/s$, N_2 dilution $472cm^3/s$
9.6mm O.D. Fuel Tube 35mm I.D. Air Tube (02/15/92)

Φ	CO (%)	CO_2 (%)	Smoke (g)	CO Yield	Smoke Yield
0.50	0.001	1.52	-	0.001	-
1.00	0.039	1.70	-	0.039	-
1.00	0.050	1.69	-	0.051	-
2.00	0.297	0.69	-	0.275	-
4.00	0.133	0.32	-	0.178	-

Methane 21cm^3/s, N$_2$ dilution 708cm^3/s
9.6mm O.D. Fuel Tube 35mm I.D. Air Tube (02/15/92)

Φ	CO (%)	CO$_2$ (%)	Smoke (g)	CO Yield	Smoke Yield
0.72	0.003	2.14	-	0.003	-
1.00	0.094	2.14	-	0.073	-
2.00	0.434	0.89	-	0.300	-
4.00	0.238	0.44	-	0.154	-

Methane 10cm^3/s, N$_2$ dilution 472cm^3/s
9.6mm O.D. Fuel Tube 35mm I.D. Air Tube (02/29/92)

Φ	CO (%)	CO$_2$ (%)	Smoke (g)	CO Yield	Smoke Yield
0.50	0.002	1.53	-	0.002	-
1.00	0.030	1.73	-	0.030	-
2.00	0.298	0.73	-	0.276	-
4.00	0.123	0.31	-	0.109	-

Methane 21cm^3/s, N$_2$ dilution 708cm^3/s
9.6mm O.D. Fuel Tube 35mm I.D. Air Tube (02/29/92)

Φ	CO (%)	CO$_2$ (%)	Smoke (g)	CO Yield	Smoke Yield
0.72	0.003	2.17	-	0.003	-
1.00	0.091	2.22	-	0.070	-
2.00	0.430	0.92	-	0.297	-
4.00	0.240	0.47	-	0.156	-

Methane 10cm^3/s, N$_2$ dilution 472cm^3/s
12.7mm O.D. Fuel Tube 22mm I.D. Air Tube (02/29/92)

Φ	CO (%)	CO$_2$ (%)	Smoke (g)	CO Yield	Smoke Yield
0.50	0.002	1.53	-	0.002	-
1.00	0.140	1.64	-	0.141	-
2.00	0.315	0.72	-	0.292	-
4.00	0.150	0.35	-	0.133	-

Methane 21cm^3/s, N$_2$ dilution 708cm^3/s
12.7mm O.D. Fuel Tube 22mm I.D. Air Tube (02/15/92)

Φ	CO (%)	CO$_2$ (%)	Smoke (g)	CO Yield	Smoke Yield
1.00	0.228	2.15	-	0.176	-
2.00	0.459	0.93	-	0.317	-
4.00	0.250	0.46	-	0.162	-

Methane 10cm^3/s, N$_2$ dilution 472cm^3/s
12.7mm O.D. Fuel Tube 29mm I.D. Air Tube (03/13/92)

Φ	CO (%)	CO$_2$ (%)	Smoke (g)	CO Yield	Smoke Yield
0.50	0.002	1.51	-	0.002	-
0.57	0.004	1.61	-	0.005	-
0.66	0.002	1.64	-	0.002	-
0.76	0.004	1.72	-	0.004	-
0.87	0.01	1.75	-	0.010	-
1.00	0.1	1.65	-	0.101	-
1.15	0.251	1.38	-	0.248	-
1.32	0.344	1.16	-	0.334	-
1.52	0.351	0.95	-	0.335	-
1.74	0.333	0.81	-	0.313	-
2.00	0.303	0.74	-	0.281	-
2.52	0.235	0.58	-	0.214	-
3.18	0.179	0.47	-	0.160	-
4.00	0.125	0.38	-	0.111	-

Methane 10cm^3/s, N$_2$ dilution 590cm^3/s
9.6mm O.D. Fuel Tube 22mm I.D. Air Tube (03/21/92)

Φ	CO (%)	CO$_2$ (%)	Smoke (g)	CO Yield	Smoke Yield
0.50	0.001	1.26	1.00E-5	0.001	2.71E-5
1.00	0.081	1.34	2.87E-3	0.099	6.52E-3
1.52	0.320	0.73	2.68E-3	0.371	6.10E-3
2.52	0.210	0.44	4.40E-4	0.234	9.63E-4
4.00	0.118	0.27	1.00E-4	0.129	2.14E-4

Methane 10cm^3/s, N$_2$ dilution 590cm^3/s
9.6mm O.D. Fuel Tube 29mm I.D. Air Tube (04/11/92)

Φ	CO (%)	CO$_2$ (%)	Smoke (g)	CO Yield	Smoke Yield
0.50	0.000	1.30	0	0.000	0
1.00	0.055	1.38	4.29E-3	0.067	1.04E-2
1.52	0.305	0.76	4.68E-3	0.354	9.02E-3
2.52	0.205	0.46	7.90E-4	0.229	1.26E-3
4.00	0.102	0.31	0	0.111	0

Methane 10cm^3/s, N$_2$ dilution 590cm^3/s
9.6mm O.D. Fuel Tube 29mm I.D. Air Tube (04/18/92)

Φ	CO (%)	CO$_2$ (%)	Smoke (g)	CO Yield	Smoke Yield
0.50	0.001	1.30	-	0.001	-
1.00	0.055	1.39	-	0.067	-
1.52	0.304	0.77	-	0.352	-
2.52	0.205	0.46	-	0.229	-
4.00	0.103	0.31	-	0.112	-

Methane 20cm^3/s, N$_2$ dilution 590cm^3/s

9.6mm O.D. Fuel Tube 29mm I.D. Air Tube (04/18/92)

Φ	CO (%)	CO$_2$ (%)	Smoke (g)	CO Yield	Smoke Yield
0.72	0.002	2.40	-	0.002	-
1.00	0.165	2.43	-	0.116	-
1.52	0.577	1.46	-	0.371	-
2.52	0.430	0.88	-	0.258	-
4.00	0.275	0.57	-	0.158	-

Methane 10cm^3/s, N$_2$ dilution 590cm^3/s

12.7mm O.D. Fuel Tube 22mm I.D. Air Tube (04/23/92)

Φ	CO (%)	CO$_2$ (%)	Smoke (g)	CO Yield	Smoke Yield
0.50	0.001	1.30	-	0.001	-
1.00	0.079	1.37	-	0.096	-
1.52	0.325	0.77	-	0.377	-
2.52	0.215	0.46	-	0.240	-
4.00	0.122	0.32	-	0.133	-

Methane 20cm^3/s, N$_2$ dilution 590cm^3/s

12.7mm O.D. Fuel Tube 22mm I.D. Air Tube (02/15/92)

Φ	CO (%)	CO$_2$ (%)	Smoke (g)	CO Yield	Smoke Yield
1.00	0.257	2.35	-	0.180	-
1.52	0.629	1.44	-	0.405	-
2.52	0.466	0.85	-	0.279	-
4.00	0.300	0.54	-	0.173	-

Methane 10cm^3/s, N$_2$ dilution 590cm^3/s

9.6mm O.D. Fuel Tube 29mm I.D. Air Tube (04/30/92)

Φ	CO (%)	CO$_2$ (%)	Smoke (g)	CO Yield	Smoke Yield
0.50	0.001	1.34	-	0.001	-
1.00	0.010	1.49	-	0.012	-
1.52	0.307	0.80	-	0.356	-
2.52	0.204	0.50	-	0.228	-
4.00	0.105	0.33	-	0.115	-

Methane 20cm^3/s, N$_2$ dilution 590cm^3/s
9.6mm O.D. Fuel Tube 29mm I.D. Air Tube (04/30/92)

Φ	CO (%)	CO$_2$ (%)	Smoke (g)	CO Yield	Smoke Yield
0.72	0.003	2.45	-	0.002	-
1.00	0.063	2.62	-	0.044	-
1.52	0.598	1.51	-	0.385	-
2.52	0.432	0.93	-	0.259	-
4.00	0.276	0.61		0.159	-

Methane 10cm^3/s, N$_2$ dilution 590cm^3/s
12.7mm O.D. Fuel Tube 22mm I.D. Air Tube (04/30/92)

Φ	CO (%)	CO$_2$ (%)	Smoke (g)	CO Yield	Smoke Yield
0.50	0.002	1.31	-	0.003	-
1.00	0.069	1.39	-	0.084	-
1.52	0.322	0.77	-	0.373	-
2.52	0.216	0.47	-	0.241	-
4.00	0.120	0.32	-	0.131	-

Methane 20cm^3/s, N$_2$ dilution 590cm^3/s
12.7mm O.D. Fuel Tube 22mm I.D. Air Tube (04/30/92)

Φ	CO (%)	CO$_2$ (%)	Smoke (g)	CO Yield	Smoke Yield
1.00	0.243	2.37	-	0.170	-
1.52	0.626	1.45	-	0.403	-
2.52	0.466	0.87	-	0.279	-
4.00	0.300	0.57	-	0.173	-

Methane 10cm^3/s, N$_2$ dilution 590cm^3/s
9.6mm O.D. Fuel Tube 29mm I.D. Air Tube (05/20/92)

Φ	CO (%)	CO$_2$ (%)	Smoke (g)	CO Yield	Smoke Yield
0.76	0.001	1.42	2.00E-5	0.001	4.73E-5
1.00	0.035	1.42	3.63E-3	0.043	1.03E-2
1.52	0.307	0.78	4.41E-3	0.356	9.54E-3
2.52	0.204	0.47	7.70E-4	0.228	1.60E-3
4.00	0.105	0.32	9.00E-5	0.115	1.83E-4

Methane 10cm^3/s, N$_2$ dilution 590cm^3/s

9.6mm O.D. Fuel Tube 22mm I.D. Air Tube (05/20/92)

Φ	CO (%)	CO$_2$ (%)	Smoke (g)	CO Yield	Smoke Yield
0.50	0.001	1.42	0	0.001	0
1.00	0.089	1.36	2.73E-3	0.108	7.74E-3
1.52	0.307	0.78	2.83E-3	0.356	6.12E-3
2.52	0.213	0.46	6.40E-4	0.238	1.33E-3
4.00	0.120	0.31	5.00E-5	0.131	1.02E-4

Methane 10cm^3/s, N$_2$ dilution 590cm^3/s

9.6mm O.D. Fuel Tube 29mm I.D. Air Tube (06/17/92)

Φ	CO (%)	CO$_2$ (%)	Smoke (g)	CO Yield	Smoke Yield
0.50	0.001	1.32	-	0.001	-
0.57	0.001	1.36	-	0.001	-
0.66	0.001	1.40	-	0.001	-
0.76	0.001	1.44	-	0.001	-
0.87	0.001	1.48	-	0.001	-
1.00	0.013	1.47	-	0.016	-
1.15	0.245	1.14	-	0.293	-
1.32	0.311	0.93	-	0.366	-
1.52	0.308	0.78	-	0.357	-
1.74	0.284	0.69	-	0.325	-
2.00	0.258	0.60	-	0.292	-
2.52	0.203	0.49	-	0.226	-
3.18	0.156	0.40	-	0.172	-
4.00	0.105	0.33	-	0.115	-

Methane 10cm^3/s, N$_2$ dilution 590cm^3/s

9.6mm O.D. Fuel Tube 29mm I.D. Air Tube (06/18/92)

Φ	CO (%)	CO$_2$ (%)	Smoke (g)	CO Yield	Smoke Yield
0.50	0.001	1.30	-	0.001	-
0.57	0.001	1.35	-	0.001	-
0.66	0.001	1.38	-	0.001	-
0.76	0.001	1.42	-	0.001	-
0.87	0.001	1.46	-	0.001	-
1.00	0.013	1.45	-	0.016	-
1.15	0.247	1.13	-	0.295	-
1.32	0.314	0.93	-	0.369	-
1.52	0.309	0.78	-	0.358	-
1.74	0.290	0.68	-	0.332	-
2.00	0.260	0.59	-	0.295	-
2.52	0.202	0.47	-	0.225	-
3.18	0.155	0.39	-	0.171	-
4.00	0.107	0.32	-	0.117	-

Methane 10cm^3/s, N$_2$ dilution 590cm^3/s
12.7mm O.D. Fuel Tube 29mm I.D. Air Tube (06/18/92)

Φ	CO (%)	CO$_2$ (%)	Smoke (g)	CO Yield	Smoke Yield
0.50	0.001	1.29	-	0.001	-
0.57	0.000	1.35	-	0.000	-
0.66	0.000	1.38	-	0.000	-
0.76	0.001	1.41	-	0.001	-
0.87	0.001	1.47	-	0.001	-
1.00	0.017	1.45	-	0.021	-
1.15	0.244	1.13	-	0.291	-
1.32	0.309	0.93	-	0.363	-
1.52	0.309	0.78	-	0.358	-
1.74	0.286	0.68	-	0.328	-
2.00	0.258	0.60	-	0.292	-
2.52	0.201	0.47	-	0.224	-
3.18	0.153	0.39	-	0.169	-
4.00	0.105	0.32	-	0.115	-

Ethene 6.4cm^3/s, N$_2$ dilution 472cm^3/s
12.7mm O.D. Fuel Tube 22mm I.D. Air Tube (02/15/92)

Φ	CO (%)	CO$_2$ (%)	Smoke (g)	CO Yield	Smoke Yield
0.50	0.002	1.76	-	0.002	-
1.00	0.090	1.87	-	0.080	-
2.00	0.545	0.76	-	0.446	-
4.00	0.231	0.37	-	0.181	-

Ethene 2.3cm^3/s, N$_2$ dilution 472cm^3/s
12.7mm O.D. Fuel Tube 22mm I.D. Air Tube (02/15/92)

Φ	CO (%)	CO$_2$ (%)	Smoke (g)	CO Yield	Smoke Yield
0.50	0.001	0.69	-	0.002	-
1.00	0.028	0.65	-	0.062	-
2.00	0.119	0.27	-	0.254	-
4.00	0.090	0.21	-	0.063	-

Ethene 6.4cm^3/s, N$_2$ dilution 472cm^3/s
9.6mm O.D. Fuel Tube 35mm I.D. Air Tube (02/15/92)

Φ	CO (%)	CO$_2$ (%)	Smoke (g)	CO Yield	Smoke Yield
0.50	0.004	2.96	-	0.004	-
1.00	0.060	3.40	-	0.053	-
2.00	0.637	1.12	-	0.522	-
4.00	0.220	0.46	-	0.172	-

Ethene 2.3cm^3/s, N$_2$ dilution 472cm^3/s

9.6mm O.D. Fuel Tube 35mm I.D. Air Tube (02/15/92)

Φ	CO (%)	CO$_2$ (%)	Smoke (g)	CO Yield	Smoke Yield
0.50	0.001	1.17	-	0.002	-
1.00	0.036	1.03	-	0.079	-
2.00	0.223	0.49	-	0.476	-
4.00	0.099	0.15	-	0.208	-

Ethene 6.4cm^3/s, N$_2$ dilution 472cm^3/s

9.6mm O.D. Fuel Tube 35mm I.D. Air Tube (02/29/92)

Φ	CO (%)	CO$_2$ (%)	Smoke (g)	CO Yield	Smoke Yield
0.50	0.003	1.82	-	0.003	-
1.00	0.043	2.03	-	0.038	-
2.00	0.512	0.84	-	0.419	-
4.00	0.190	0.41	-	0.149	-

Ethene 2.3cm^3/s, N$_2$ dilution 472cm^3/s

9.6mm O.D. Fuel Tube 35mm I.D. Air Tube (02/29/92)

Φ	CO (%)	CO$_2$ (%)	Smoke (g)	CO Yield	Smoke Yield
0.50	0.001	0.83	-	0.002	-
1.00	0.035	0.78	-	0.077	-
2.00	0.153	0.31	-	0.326	-
4.00	0.089	0.12	-	0.187	-

Ethene 6.4cm^3/s, N$_2$ dilution 472cm^3/s

12.7mm O.D. Fuel Tube 22mm I.D. Air Tube (02/29/92)

Φ	CO (%)	CO$_2$ (%)	Smoke (g)	CO Yield	Smoke Yield
0.50	0.003	2.37	-	0.003	-
1.00	0.151	2.23	-	0.134	-
2.00	0.566	0.92	-	0.464	-
4.00	0.264	0.43	-	0.207	-

Ethene 2.3cm^3/s, N$_2$ dilution 472cm^3/s

12.7mm O.D. Fuel Tube 22mm I.D. Air Tube (02/29/92)

Φ	CO (%)	CO$_2$ (%)	Smoke (g)	CO Yield	Smoke Yield
0.50	0.002	0.92	-	0.005	-
1.00	0.061	0.89	-	0.135	-
2.00	0.159	0.39	-	0.339	-
4.00	0.081	0.18	-	0.170	-

Ethene 6.4cm^3/s, N$_2$ dilution 472cm^3/s
12.7mm O.D. Fuel Tube 22mm I.D. Air Tube (02/29/92)

Φ	CO (%)	CO$_2$ (%)	Smoke (g)	CO Yield	Smoke Yield
0.50	0.003	2.09	-	0.003	-
1.00	0.142	2.12	-	0.126	-
2.00	0.569	0.91	-	0.466	-
4.00	0.255	0.42	-	0.200	-

Ethene 2.3cm^3/s, N$_2$ dilution 472cm^3/s
12.7mm O.D. Fuel Tube 22mm I.D. Air Tube (02/29/92)

Φ	CO (%)	CO$_2$ (%)	Smoke (g)	CO Yield	Smoke Yield
0.50	0.002	0.87	-	0.005	-
1.00	0.055	0.81	-	0.121	-
2.00	0.145	0.35	-	0.309	-
4.00	0.067	0.14	-	0.141	-

Ethene 6.4cm^3/s, N$_2$ dilution 472cm^3/s
12.7mm O.D. Fuel Tube 29mm I.D. Air Tube (03/13/92)

Φ	CO (%)	CO$_2$ (%)	Smoke (g)	CO Yield	Smoke Yield
0.50	0.006	1.93	-	0.006	-
0.57	0.006	2.14	-	0.006	-
0.66	0.006	2.04	-	0.006	-
0.76	0.006	2.07	-	0.006	-
0.87	0.010	2.13	-	0.009	-
1.00	0.081	2.13	-	0.072	-
1.15	0.265	1.92	-	0.231	-
1.32	0.406	1.51	-	0.347	-
1.52	0.534	1.31	-	0.450	-
1.74	0.554	1.07	-	0.460	-
2.00	0.513	0.88	-	0.420	-
2.52	0.430	0.68	-	0.346	-
3.18	0.340	0.59	-	0.269	-
4.00	0.209	0.45	-	0.134	-

Ethene 6.4cm^3/s, N$_2$ dilution 590cm^3/s
9.6mm O.D. Fuel Tube 22mm I.D. Air Tube (03/21/92)

Φ	CO (%)	CO$_2$ (%)	Smoke (g)	CO Yield	Smoke Yield
0.50	0.002	1.69	1.00E-5	0.002	2.39E-5
1.00	0.070	1.71	1.25E-2	0.075	4.40E-2
1.52	0.520	0.96	1.92E-2	0.533	4.30E-2
2.52	0.405	0.54	9.30E-3	0.400	1.81E-2
4.00	0.206	0.34	1.96E-3	0.199	3.72E-3

Ethene 6.4cm^3/s, N$_2$ dilution 590cm^3/s
9.6mm O.D. Fuel Tube 29mm I.D. Air Tube (04/11/92)

Φ	CO (%)	CO$_2$ (%)	Smoke (g)	CO Yield	Smoke Yield
0.50	0.002	1.59	6.40E-3	0.002	2.57E-2
1.00	0.026	1.71	1.36E-2	0.028	4.83E-2
1.52	0.453	0.97	1.36E-2	0.465	4.62E-2
2.52	0.363	0.54	6.22E-3	0.359	2.03E-2
4.00	0.180	0.36	1.79E-3	0.174	3.43E-3

Ethene 6.4cm^3/s, N$_2$ dilution 590cm^3/s
9.6mm O.D. Fuel Tube 29mm I.D. Air Tube (04/18/92)

Φ	CO (%)	CO$_2$ (%)	Smoke (g)	CO Yield	Smoke Yield
0.50	0.002	1.59	-	0.002	-
1.00	0.050	1.70	-	0.054	-
1.52	0.441	0.98	-	0.452	-
2.52	0.361	0.54	-	0.357	-
4.00	0.178	0.35	-	0.172	-

Ethene 3.2cm^3/s, N$_2$ dilution 590cm^3/s
9.6mm O.D. Fuel Tube 29mm I.D. Air Tube (04/18/92)

Φ	CO (%)	CO$_2$ (%)	Smoke (g)	CO Yield	Smoke Yield
0.50	0.000	0.95	-	0.000	-
1.00	0.017	0.93	-	0.034	-
1.52	0.197	0.52	-	0.384	-
2.52	0.114	0.32	-	0.218	-
4.00	0.045	0.21	-	0.085	-

Ethene 3.2cm^3/s, N$_2$ dilution 590cm^3/s
12.7mm O.D. Fuel Tube 22mm I.D. Air Tube (04/23/92)

Φ	CO (%)	CO$_2$ (%)	Smoke (g)	CO Yield	Smoke Yield
0.50	0.001	0.95	-	0.002	-
1.00	0.065	0.85	-	0.130	-
1.52	0.219	0.50	-	0.426	-
2.52	0.139	0.30	-	0.265	-
4.00	0.075	0.19	-	0.142	-

Ethene 6.4cm^3/s, N$_2$ dilution 590cm^3/s
12.7mm O.D. Fuel Tube 22mm I.D. Air Tube (04/23/92)

Φ	CO (%)	CO$_2$ (%)	Smoke (g)	CO Yield	Smoke Yield
0.50	0.002	1.68	-	0.002	-
1.00	0.118	1.60	-	0.127	-
1.52	0.455	0.98	-	0.467	-
2.52	0.373	0.54	-	0.369	-
4.00	0.197	0.34	-	0.191	-

Ethene 6.4cm^3/s, N$_2$ dilution 590cm^3/s
9.6mm O.D. Fuel Tube 29mm I.D. Air Tube (04/23/92)

Φ	CO (%)	CO$_2$ (%)	Smoke (g)	CO Yield	Smoke Yield
0.50	0.002	1.59	7.03E-3	0.002	2.77E-2
1.00	0.032	1.69	1.47E-2	0.034	5.12E-2
1.52	0.446	0.98	1.37E-2	0.457	4.43E-2
2.52	0.358	0.54	5.95E-3	0.354	1.90E-2
4.00	0.177	0.35	1.99E-3	0.171	3.73E-3

Ethene 3.2cm^3/s, N$_2$ dilution 590cm^3/s
9.6mm O.D. Fuel Tube 29mm I.D. Air Tube (04/23/92)

Φ	CO (%)	CO$_2$ (%)	Smoke (g)	CO Yield	Smoke Yield
0.50	0.001	0.95	3.00E-5	0.002	1.24E-4
0.87	0.003	0.92	7.42E-3	0.006	4.84E-2
1.00	0.011	0.92	8.33E-3	0.022	5.37E-2
1.52	0.204	0.52	4.43E-3	0.397	2.79E-2
2.52	0.114	0.32	7.60E-4	0.218	2.82E-3
4.00	0.040	0.20	2.00E-5	0.076	7.33E-5

Ethene 3.2cm^3/s, N$_2$ dilution 590cm^3/s
9.6mm O.D. Fuel Tube 29mm I.D. Air Tube (04/30/92)

Φ	CO (%)	CO$_2$ (%)	Smoke (g)	CO Yield	Smoke Yield
0.50	0.001	1.00	-	0.002	-
1.00	0.015	0.98	-	0.030	-
1.52	0.207	0.57	-	0.403	-
2.52	0.115	0.36	-	0.220	-
4.00	0.041	0.26	-	0.077	-

Ethene 3.2cm^3/s, N$_2$ dilution 590cm^3/s
12.7mm O.D. Fuel Tube 22mm I.D. Air Tube (04/30/92)

Φ	CO (%)	CO$_2$ (%)	Smoke (g)	CO Yield	Smoke Yield
0.50	0.001	0.95	-	0.002	-
1.00	0.053	0.88	-	0.106	-
1.52	0.231	0.50	-	0.450	-
2.52	0.138	0.30	-	0.264	-
4.00	0.074	0.19	-	0.140	-

Ethene 6.4cm^3/s, N$_2$ dilution 590cm^3/s
12.7mm O.D. Fuel Tube 22mm I.D. Air Tube (04/30/92)

Φ	CO (%)	CO$_2$ (%)	Smoke (g)	CO Yield	Smoke Yield
0.50	0.002	1.68	-	0.002	-
1.00	0.078	1.67	-	0.084	-
1.52	0.487	0.97	-	0.499	-
2.52	0.384	0.54	-	0.379	-
4.00	0.200	0.35	-	0.193	-

Ethene 3.2cm^3/s, N$_2$ dilution 590cm^3/s
9.6mm O.D. Fuel Tube 29mm I.D. Air Tube (05/20/92)

Φ	CO (%)	CO$_2$ (%)	Smoke (g)	CO Yield	Smoke Yield
0.76	0.002	0.95	8.54E-3	0.004	4.06E-2
1.00	0.013	0.93	1.10E-2	0.026	5.10E-2
1.52	0.219	0.51	8.48E-3	0.426	3.08E-2
2.52	0.116	0.32	8.30E-4	0.222	2.96E-3
4.00	0.054	0.22	4.00E-5	0.102	1.41E-4

Ethene 6.4cm^3/s, N$_2$ dilution 590cm^3/s
9.6mm O.D. Fuel Tube 22mm I.D. Air Tube (05/20/92)

Φ	CO (%)	CO$_2$ (%)	Smoke (g)	CO Yield	Smoke Yield
0.50	0.000	1.67	2.00E-5	0.000	4.54E-5
1.00	0.071	1.67	1.32E-2	0.076	4.41E-2
1.52	0.488	0.96	1.32E-2	0.500	4.20E-2
2.52	0.387	0.54	7.93E-3	0.382	1.83E-2
4.00	0.199	0.34	2.11E-3	0.192	3.81E-3

Ethene 3.2cm^3/s, N$_2$ dilution 590cm^3/s

9.6mm O.D. Fuel Tube 29mm I.D. Air Tube (06/17/92)

Φ	CO (%)	CO$_2$ (%)	Smoke (g)	CO Yield	Smoke Yield
0.50	0.000	0.98	-	0.000	-
0.57	0.001	0.98	-	0.002	-
0.66	0.001	0.96	-	0.002	-
0.76	0.001	0.96	-	0.002	-
0.87	0.002	0.96	-	0.004	-
1.00	0.019	0.94	-	0.038	-
1.15	0.149	0.76	-	0.295	-
1.32	0.211	0.60	-	0.414	-
1.52	0.207	0.53	-	0.403	-
1.74	0.185	0.45	-	0.358	-
2.00	0.154	0.39	-	0.296	-
2.52	0.118	0.33	-	0.225	-
3.18	0.078	0.27	-	0.148	-
4.00	0.050	0.22	-	0.094	-

Ethene 6.4cm^3/s, N$_2$ dilution 590cm^3/s

9.6mm O.D. Fuel Tube 29mm I.D. Air Tube (06/17/92)

Φ	CO (%)	CO$_2$ (%)	Smoke (g)	CO Yield	Smoke Yield
0.50	0.002	1.60	-	0.002	-
0.57	0.002	1.66	-	0.002	-
0.66	0.002	1.69	-	0.002	-
0.76	0.003	1.72	-	0.003	-
0.87	0.005	1.74	-	0.006	-
1.00	0.015	1.75	-	0.016	-
1.15	0.209	1.50	-	0.221	-
1.32	0.369	1.22	-	0.384	-
1.52	0.448	1.00	-	0.459	-
1.74	0.459	0.84	-	0.465	-
2.00	0.434	0.72	-	0.435	-
2.52	0.363	0.56	-	0.359	-
3.18	0.280	0.46	-	0.273	-
4.00	0.180	0.37	-	0.174	-

Ethene 3.2cm^3/s, N$_2$ dilution 590cm^3/s

9.6mm O.D. Fuel Tube 29mm I.D. Air Tube (06/18/92)

Φ	CO (%)	CO$_2$ (%)	Smoke (g)	CO Yield	Smoke Yield
0.50	0.001	0.96	-	0.002	-
0.57	0.001	0.97	-	0.002	-
0.66	0.001	0.95	-	0.002	-
0.76	0.002	0.95	-	0.004	-
0.87	0.003	0.95	-	0.006	-
1.00	0.022	0.93	-	0.044	-
1.15	0.151	0.75	-	0.299	-
1.32	0.211	0.58	-	0.414	-
1.52	0.218	0.51	-	0.424	-
1.74	0.189	0.44	-	0.366	-
2.00	0.153	0.38	-	0.294	-
2.52	0.120	0.32	-	0.229	-
3.18	0.079	0.26	-	0.150	-
4.00	0.054	0.21	-	0.102	-

Ethene 6.4cm^3/s, N$_2$ dilution 590cm^3/s

9.6mm O.D. Fuel Tube 29mm I.D. Air Tube (06/18/92)

Φ	CO (%)	CO$_2$ (%)	Smoke (g)	CO Yield	Smoke Yield
0.50	0.003	1.59	-	0.004	-
0.57	0.002	1.65	-	0.002	-
0.66	0.003	1.68	-	0.003	-
0.76	0.003	1.71	-	0.003	-
0.87	0.005	1.73	-	0.006	-
1.00	0.018	1.75	-	0.019	-
1.15	0.214	1.50	-	0.226	-
1.32	0.377	1.21	-	0.392	-
1.52	0.455	0.98	-	0.467	-
1.74	0.467	0.83	-	0.473	-
2.00	0.441	0.71	-	0.442	-
2.52	0.369	0.55	-	0.365	-
3.18	0.283	0.44	-	0.276	-
4.00	0.180	0.36	-	0.174	-

Ethene 6.4cm^3/s, N$_2$ dilution 590cm^3/s
12.7mm O.D. Fuel Tube 29mm I.D. Air Tube (06/18/92)

Φ	CO (%)	CO$_2$ (%)	Smoke (g)	CO Yield	Smoke Yield
0.50	0.002	1.60	-	0.002	-
0.57	0.002	1.64	-	0.002	-
0.66	0.002	1.67	-	0.002	-
0.76	0.003	1.70	-	0.003	-
0.87	0.006	1.71	-	0.007	-
1.00	0.040	1.71	-	0.043	-
1.15	0.212	1.48	-	0.224	-
1.32	0.362	1.23	-	0.376	-
1.52	0.454	0.98	-	0.466	-
1.74	0.459	0.83	-	0.465	-
2.00	0.444	0.71	-	0.445	-
2.52	0.365	0.55	-	0.361	-
3.18	0.271	0.45	-	0.265	-
4.00	0.174	0.36	-	0.168	-

Methane 12.8cm^3/s, N$_2$ dilution 590cm^3/s
9.6mm O.D. Fuel Tube 29mm I.D. Air Tube (03/17/93)

Φ	CO (%)	CO$_2$ (%)	Smoke (g)	CO Yield	Smoke Yield
0.50	0.012	1.60	-	0.014	-
1.00	0.060	1.77	-	0.059	-
1.52	0.391	1.01	-	0.366	-
2.52	0.278	0.63	-	0.248	-
4.00	0.164	0.42	-	0.142	-

Methane 10cm^3/s, N$_2$ dilution 590cm^3/s
9.6mm O.D. Fuel Tube 29mm I.D. Air Tube (03/17/93)

Φ	CO (%)	CO$_2$ (%)	Smoke (g)	CO Yield	Smoke Yield
0.50	0.013	1.33	-	0.018	-
1.00	0.040	1.45	-	0.49	-
1.52	0.313	0.80	-	0.363	-
2.52	0.208	0.51	-	0.232	-
4.00	0.116	0.34	-	0.127	-

Methane 10.2cm^3/s + Methanol 2.56cm^3/s, N_2 dilution 590cm^3/s
9.6mm O.D. Fuel Tube 29mm I.D. Air Tube (03/17/93)

Φ	CO (%)	CO_2 (%)	Smoke (g)	CO Yield	Smoke Yield
0.50	0.021	1.55	-	0.020	-
0.57	0.022	1.61	-	0.020	-
0.66	0.022	1.68	-	0.020	-
0.76	0.022	1.70	-	0.019	-
0.87	0.022	1.78	-	0.018	-
1.00	0.050	1.78	-	0.041	-
1.15	0.346	1.42	-	0.277	-
1.32	0.460	1.17	-	0.362	-
1.52	0.510	0.98	-	0.394	-
1.74	0.514	0.86	-	0.392	-
2.00	0.491	0.76	-	0.369	-
2.52	0.400	0.61	-	0.296	-
3.18	0.312	0.50	-	0.227	-
4.00	0.231	0.41	-	0.166	-

Ethene 5.77cm^3/s + Methanol 1.28cm^3/s, N_2 dilution 590cm^3/s
9.6mm O.D. Fuel Tube 29mm I.D. Air Tube (03/19/93)

Φ	CO (%)	CO_2 (%)	Smoke (g)	CO Yield	Smoke Yield
0.50	0.010	1.71	-	0.011	-
0.57	0.011	1.78	-	0.012	-
0.66	0.013	1.78	-	0.013	-
0.76	0.013	1.79	-	0.013	-
0.87	0.014	1.79	-	0.014	-
1.00	0.039	1.80	-	0.037	-
1.15	0.290	1.47	-	0.271	-
1.32	0.442	1.21	-	0.407	-
1.52	0.512	1.00	-	0.465	-
1.74	0.520	0.85	-	0.467	-
2.00	0.499	0.73	-	0.443	-
2.52	0.411	0.57	-	0.360	-
3.18	0.317	0.47	-	0.274	-
4.00	0.208	0.37	-	0.178	-

Ethene 6.4cm^3/s, N_2 dilution 590cm^3/s
9.6mm O.D. Fuel Tube 29mm I.D. Air Tube (03/19/93)

Φ	CO (%)	CO_2 (%)	Smoke (g)	CO Yield	Smoke Yield
0.50	0.012	1.61	-	0.015	-
1.00	0.030	1.74	-	0.037	-
1.52	0.440	1.02	-	0.454	-
2.52	0.350	0.58	-	0.348	-
4.00	0.180	0.37	-	0.175	-

Ethene 6.4cm^3/s, N$_2$ dilution 590cm^3/s

9.6mm O.D. Fuel Tube 29mm I.D. Air Tube (03/25/93)

Φ	CO (%)	CO$_2$ (%)	Smoke (g)	CO Yield	Smoke Yield
0.50	0.011	1.58	-	0.013	-
0.76	0.012	1.69	-	0.013	-
1.00	0.027	1.74	-	0.029	-
1.15	0.192	1.52	-	0.203	-
1.32	0.350	1.25	-	0.364	-
1.52	0.429	1.02	-	0.440	-
1.74	0.442	0.87	-	0.448	-
2.00	0.419	0.74	-	0.420	-
2.52	0.353	0.57	-	0.349	-
3.18	0.275	0.47	-	0.269	-
4.00	0.180	0.37	-	0.174	-

Ethene 6.4cm^3/s, N$_2$ dilution 590cm^3/s

9.6mm O.D. Fuel Tube 29mm I.D. Air Tube (03/25/93)

Fuel temperature of 71°C at outlet of fuel tube

Φ	CO (%)	CO$_2$ (%)	Smoke (g)	CO Yield	Smoke Yield
0.50	0.012	1.76	-	0.015	-
0.76	0.013	1.82	-	0.015	-
1.00	0.028	1.87	-	0.030	-
1.15	0.208	1.57	-	0.220	-
1.32	0.362	1.33	-	0.376	-
1.52	0.441	1.05	-	0.452	-
1.74	0.448	0.93	-	0.454	-
2.00	0.426	0.78	-	0.427	-
2.52	0.359	0.59	-	0.355	-
3.18	0.278	0.47	-	0.271	-
4.00	0.182	0.39	-	0.176	-

Ethene 5.12cm^3/s + Methanol 2.56cm^3/s, N_2 dilution 590cm^3/s

9.6mm O.D. Fuel Tube 29mm I.D. Air Tube (03/19/93)

Φ	CO (%)	CO_2 (%)	Smoke (g)	CO Yield	Smoke Yield
0.50	0.011	1.69	-	0.011	-
0.57	0.011	1.74	-	0.010	-
0.66	0.012	1.78	-	0.011	-
0.76	0.012	1.82	-	0.011	-
0.87	0.012	1.81	-	0.011	-
1.00	0.019	1.81	-	0.016	-
1.15	0.290	1.51	-	0.244	-
1.32	0.470	1.22	-	0.389	-
1.52	0.556	1.00	-	0.454	-
1.74	0.565	0.85	-	0.456	-
2.00	0.549	0.73	-	0.439	-
2.52	0.451	0.57	-	0.355	-
3.18	0.340	0.47	-	0.265	-
4.00	0.224	0.37	-	0.173	-

Ethene 3.2cm^3/s, N_2 dilution 590cm^3/s

9.6mm O.D. Fuel Tube 29mm I.D. Air Tube (04/01/93)

Φ	CO (%)	CO_2 (%)	Smoke (g)	CO Yield	Smoke Yield
0.50	0.007	0.97	-	0.015	-
0.57	0.005	0.97	-	0.011	-
0.66	0.006	0.94	-	0.012	-
0.76	0.007	0.92	-	0.014	-
0.87	0.006	0.93	-	0.012	-
1.00	0.015	0.92	-	0.030	-
1.15	0.141	0.75	-	0.279	-
1.32	0.198	0.59	-	0.388	-
1.52	0.213	0.51	-	0.415	-
1.74	0.178	0.45	-	0.344	-
2.00	0.154	0.37	-	0.296	-
2.52	0.116	0.32	-	0.222	-
3.18	0.080	0.26	-	0.152	-
4.00	0.053	0.21	-	0.100	-

Ethene 3.2cm^3/s, N$_2$ dilution 590cm^3/s

9.6mm O.D. Fuel Tube 29mm I.D. Air Tube (04/02/93)

Φ	CO (%)	CO$_2$ (%)	Smoke (g)	CO Yield	Smoke Yield
0.50	0.005	0.97	-	0.011	-
0.57	0.006	0.98	-	0.013	-
0.66	0.006	0.97	-	0.012	-
0.76	0.006	0.96	-	0.012	-
0.87	0.008	0.95	-	0.016	-
1.00	0.022	0.94	-	0.044	-
1.15	0.135	0.78	-	0.267	-
1.32	0.202	0.62	-	0.396	-
1.52	0.197	0.54	-	0.383	-
1.74	0.189	0.45	-	0.366	-
2.00	0.153	0.39	-	0.294	-
2.52	0.118	0.33	-	0.225	-
3.18	0.083	0.27	-	0.158	-
4.00	0.051	0.22	-	0.096	-

Ethene 6.4cm^3/s, N$_2$ dilution 590cm^3/s

9.6mm O.D. Fuel Tube 22mm I.D. Air Tube (04/02/93)

Φ	CO (%)	CO$_2$ (%)	Smoke (g)	CO Yield	Smoke Yield
0.50	0.008	1.67	-	0.010	-
0.57	0.010	1.72	-	0.012	-
0.66	0.011	1.74	-	0.013	-
0.76	0.011	1.72	-	0.012	-
0.87	0.016	1.71	-	0.018	-
1.00	0.095	1.64	-	0.102	-
1.15	0.259	1.42	-	0.273	-
1.32	0.393	1.20	-	0.409	-
1.52	0.465	0.97	-	0.477	-
1.74	0.464	0.84	-	0.470	-
2.00	0.437	0.72	-	0.438	-
2.52	0.362	0.56	-	0.358	-
3.18	0.284	0.45	-	0.277	-
4.00	0.197	0.35	-	0.191	-

Ethene 6.4cm^3/s, N$_2$ dilution 590cm^3/s

9.6mm O.D. Fuel Tube 22mm I.D. Air Tube (04/02/93)

Φ	CO (%)	CO$_2$ (%)	Smoke (g)	CO Yield	Smoke Yield
0.50	0.009	1.67	-	0.011	-
0.57	0.011	1.72	-	0.013	-
0.66	0.012	1.74	-	0.014	-
0.76	0.013	1.74	-	0.015	-
0.87	0.015	1.73	-	0.016	-
1.00	0.105	1.65	-	0.113	-
1.15	0.268	1.44	-	0.283	-
1.32	0.390	1.20	-	0.405	-
1.52	0.464	0.98	-	0.476	-
1.74	0.471	0.84	-	0.477	-
2.00	0.443	0.72	-	0.444	-
2.52	0.364	0.56	-	0.360	-
3.18	0.286	0.45	-	0.279	-
4.00	0.196	0.35	-	0.190	-

Methane 10.2cm^3/s + Toluene 0.37cm^3/s, N$_2$ dilution 590cm^3/s

9.6mm O.D. Fuel Tube 29mm I.D. Air Tube (04/05/93)

Φ	CO (%)	CO$_2$ (%)	Smoke (g)	CO Yield	Smoke Yield
0.50	0.011	1.43	-	0.013	-
0.57	0.013	1.47	-	0.015	-
0.66	0.014	1.50	-	0.015	-
0.76	0.015	1.51	-	0.016	-
0.87	0.018	1.53	-	0.019	-
1.00	0.029	1.54	-	0.029	-
1.15	0.128	1.41	-	0.127	-
1.32	0.247	1.16	-	0.240	-
1.52	0.303	0.97	-	0.290	-
1.74	0.307	0.84	-	0.290	-
2.00	0.289	0.73	-	0.269	-
2.52	0.244	0.59	-	0.223	-
3.18	0.198	0.48	-	0.179	-
4.00	0.146	0.39	-	0.130	-

Ethene 5.12cm^3/s + Toluene 0.37cm^3/s, N$_2$ dilution 590cm^3/s

9.6mm O.D. Fuel Tube 29mm I.D. Air Tube (04/05/93)

Φ	CO (%)	CO$_2$ (%)	Smoke (g)	CO Yield	Smoke Yield
0.50	0.012	1.37	-	0.015	-
0.57	0.012	1.39	-	0.014	-
0.66	0.013	1.43	-	0.015	-
0.76	0.014	1.46	-	0.016	-
0.87	0.017	1.50	-	0.019	-
1.00	0.027	1.52	-	0.029	-
1.15	0.068	1.46	-	0.072	-
1.32	0.172	1.27	-	0.180	-
1.52	0.262	1.05	-	0.271	-
1.74	0.307	0.89	-	0.314	-
2.00	0.318	0.74	-	0.322	-
2.52	0.288	0.58	-	0.287	-
3.18	0.240	0.47	-	0.237	-
4.00	0.178	0.38	-	0.174	-

APPENDIX B

GAS CHROMATOGRAPH MEASUREMENTS

Methane laminar diffusion flame with a fuel flow rate of $10 cm^3/s$ at $\Phi = 4$ and at a height of 16mm. Gas sampled using EMS probe.

r(mm)	O_2(%)	CO_2(%)	N_2(%)	CO(%)	CH_4(%)	C_2H_4(%)	C_2H_2(%)	C_2H_6(%)
-12.0	2.206	8.661	88.800	2.046	5.564	0.068	0.166	0.025
-10.0	1.517	8.817	84.138	2.362	8.010	0.077	0.224	0.023
-9.0	1.358	8.329	80.660	2.582	10.734	0.089	0.272	0.026
-7.5	1.240	7.627	75.309	2.747	19.469	0.105	0.317	0.030
-6.0	1.653	7.461	74.396	2.535	23.964	0.095	0.260	0.031
-4.5	1.410	6.559	66.736	2.470	32.587	0.098	0.263	0.032
-3.0	0.968	5.174	58.560	2.293	45.703	0.094	0.262	0.029
-1.5	1.262	4.563	53.249	1.987	51.519	0.082	0.208	0.028
0.0	1.448	4.353	50.857	1.776	52.882	0.073	0.171	0.025
1.5	1.185	3.905	43.696	1.671	58.111	0.068	0.159	0.023
3.0	0.752	3.478	38.278	1.838	61.861	0.071	0.198	0.024
4.5	0.971	5.053	58.080	2.350	46.505	0.097	0.279	0.030
6.0	1.227	6.491	66.021	2.566	31.310	0.102	0.286	0.032
7.5	1.256	7.452	73.244	2.629	22.120	0.098	0.290	0.029
9.0	1.499	8.056	78.293	2.549	15.970	0.089	0.252	0.028

Methane laminar diffusion flame with a fuel flow rate of $10 cm^3/s$ at $\Phi = 4$ and at a height of 10mm. Gas sampled using EMS probe.

r(mm)	O_2(%)	CO_2(%)	N_2(%)	CO(%)	CH_4(%)	C_2H_4(%)	C_2H_2(%)	C_2H_6(%)
-12.0	4.160	8.310	92.346	1.648	0.504	0.027	0.068	0.016
-10.0	3.043	8.453	89.684	2.068	1.030	0.045	0.130	0.025
-9.0	2.411	8.466	85.985	2.339	4.197	0.075	0.192	0.031
-7.5	2.122	8.098	81.065	2.696	8.047	0.085	0.232	0.029
-6.0	1.907	7.378	72.451	2.894	18.542	0.090	0.256	0.029
-4.5	1.586	6.321	63.598	2.798	30.455	0.098	0.290	0.031
-3.0	1.328	4.657	52.981	2.302	48.268	0.089	0.256	0.029
-1.5	1.001	3.026	33.564	1.578	65.033	0.062	0.164	0.020
0.0	0.743	1.933	22.544	1.135	74.009	0.046	0.107	0.014
1.5	0.725	2.116	24.299	1.258	72.591	0.049	0.125	0.015
3.0	0.988	3.443	37.815	1.920	61.551	0.075	0.215	0.025
4.5	1.215	5.202	57.465	2.732	41.114	0.100	0.318	0.032
6.0	1.336	6.447	63.751	2.944	25.152	0.092	0.280	0.031
7.5	1.377	7.094	67.495	2.695	9.714	0.080	0.238	0.028
9.0	1.335	6.833	65.079	2.138	4.212	0.067	0.190	0.024

Methane laminar diffusion flame with a fuel flow rate of $10 \text{cm}^3/\text{s}$ at $\Phi = 4$ and at a height of 3.5mm. Gas sampled using quartz microprobe.

r(mm)	O_2(%)	CO_2(%)	N_2(%)	CO(%)	CH_4(%)	C_2H_4(%)	C_2H_2(%)	C_2H_6(%)
-12.0	15.665	2.561	82.539	0.103	0.045	0.000	0.000	0.000
-10.0	12.584	3.603	79.401	0.088	0.011	0.000	0.000	0.000
-9.0	6.147	4.558	61.843	0.188	0.000	0.000	0.000	0.000
-7.5	1.249	5.002	53.663	1.731	0.360	0.031	0.098	0.030
-6.0	0.745	3.930	39.393	1.824	6.905	0.072	0.163	0.030
-4.5	0.763	3.262	33.314	1.620	25.856	0.069	0.147	0.031
-3.0	0.536	1.803	18.849	0.918	59.756	0.040	0.074	0.018
-1.5	0.167	0.374	4.238	0.213	87.065	0.012	0.015	0.003
0.0	0.036	0.028	0.519	0.023	105.522	0.006	0.003	0.000
1.5	0.217	0.511	5.739	0.287	98.880	0.015	0.022	0.004
3.0	0.761	2.606	27.632	1.320	69.470	0.057	0.111	0.026
4.5	1.156	5.316	56.839	2.664	32.201	0.108	0.253	0.049
6.0	1.134	6.573	63.578	3.214	7.000	0.114	0.291	0.051
7.5	2.093	5.735	59.992	1.385	0.094	0.005	0.030	0.002
9.0	7.112	4.342	63.374	0.146	0.004	0.000	0.000	0.000

Ethene laminar diffusion flame with a fuel flow rate of $6.4 \text{cm}^3/\text{s}$ at $\Phi = 4$ and at a height of 21mm. Gas sampled using EMS probe.

r(mm)	O_2(%)	CO_2(%)	N_2(%)	CO(%)	CH_4(%)	C_2H_4(%)	C_2H_2(%)	C_2H_6(%)
-12.0	4.423	8.606	79.865	3.825	0.227	10.980	1.567	0.021
-10.0	1.219	9.949	76.370	4.367	0.210	15.448	2.148	0.010
-9.0	1.096	9.505	72.983	4.086	0.195	14.952	2.022	0.010
-7.5	0.954	6.199	53.585	2.740	0.136	11.760	1.327	0.008
-6.0	0.640	4.731	37.978	2.218	0.108	12.112	1.120	0.006
-4.5	2.114	8.692	70.577	3.832	0.193	15.674	1.814	0.014
-3.0	1.871	8.990	71.439	3.916	0.441	15.955	1.811	0.013
-1.5	2.090	8.515	69.537	3.887	0.181	16.394	1.785	0.014
0.0	1.529	8.230	65.963	3.850	0.226	17.681	1.860	0.015
1.5	1.538	8.774	67.978	3.852	0.219	16.838	1.804	0.011
3.0	1.279	8.093	64.209	3.656	0.158	17.636	1.730	0.012
4.5	0.698	5.184	48.008	3.318	0.150	28.515	1.749	0.016
6.0	0.600	4.669	38.794	2.570	0.120	16.257	1.342	0.009
7.5	0.453	3.447	27.461	1.686	0.077	10.090	0.831	0.016
9.0	0.525	3.979	31.600	1.850	0.167	9.398	0.887	0.000

Ethene laminar diffusion flame with a fuel flow rate of 6.4cm³/s at $\Phi = 4$ and at a height of 2.5mm. Gas sampled using quartz microprobe.

r(mm)	O_2(%)	CO_2(%)	N_2(%)	CO(%)	CH_4(%)	C_2H_4(%)	C_2H_2(%)	C_2H_6(%)
-12.0	8.785	3.112	58.332	0.089	0.002	0.004	0.002	0.000
-10.0	11.866	5.154	80.642	0.098	0.000	0.000	0.000	0.000
-9.0	5.172	5.400	57.814	0.281	0.000	0.000	0.000	0.000
-7.5	1.530	6.526	54.296	2.157	0.007	0.020	0.186	0.001
-6.0	0.810	6.324	53.075	3.692	0.093	7.115	1.531	0.003
-4.5	0.847	5.944	50.477	3.895	0.126	28.239	1.803	0.013
-3.0	0.357	1.961	16.391	1.371	0.045	57.902	0.582	0.022
-1.5	0.153	0.179	1.841	0.148	0.006	60.307	0.039	0.019
0.0	0.133	0.013	0.342	0.016	0.004	83.909	0.000	0.026
1.5	0.098	0.207	2.228	0.180	0.008	81.246	0.046	0.026
3.0	0.359	2.070	17.064	1.419	0.047	54.256	0.623	0.019
4.5	0.972	6.579	55.646	4.224	0.140	31.291	1.959	0.016
6.0	1.228	9.244	66.699	5.179	0.141	11.286	2.149	0.005
7.5	2.785	11.018	85.264	2.892	0.005	0.070	0.150	0.000
9.0	7.967	8.466	86.193	0.317	0.000	0.005	0.003	0.000

Ethene laminar diffusion flame with a fuel flow rate of 6.4cm³/s at $\Phi = 4$ and at a height of 1.5mm. Gas sampled using quartz microprobe.

r(mm)	O_2(%)	CO_2(%)	N_2(%)	CO(%)	CH_4(%)	C_2H_4(%)	C_2H_2(%)	C_2H_6(%)
-12.0	15.408	4.253	78.293	0.129	0.004	0.025	0.009	0.006
-10.0	11.284	6.898	79.559	0.241	0.000	0.004	0.000	0.000
-9.0	3.283	10.380	78.081	3.059	0.010	0.047	0.297	0.002
-7.5	1.449	9.775	72.020	4.764	0.130	13.191	1.856	0.011
-6.0	1.069	5.909	49.876	3.229	0.103	40.436	1.276	0.020
-4.5	0.375	1.591	12.812	0.970	0.032	82.415	0.400	0.025
-3.0	0.123	0.094	1.249	0.260	0.005	97.349	0.017	0.028
-1.5	0.104	0.009	0.425	0.000	0.004	98.877		0.027
0.0	0.169	0.331	3.174	0.245	0.009	94.673	0.075	0.026
1.5	0.593	2.992	24.199	1.847	0.061	66.236	0.794	0.023
3.0	1.275	8.317	64.090	4.657	0.142	20.528	1.949	0.013
4.5	1.762	9.388	68.227	3.412	0.033	0.471	0.651	0.007
6.0	8.506	8.489	79.576	0.612	0.001	0.018	0.008	0.000
7.5	14.939	4.820	78.677	0.134	0.001	0.007	0.002	0.000
9.0	17.444	3.324	76.961	0.184	0.002	0.032	0.008	0.000

APPENDIX C
TEMPERATURE MEASUREMENTS

The temperature measurements shown in this table are not corrected for radiation or conduction losses. All temperature measurements are shown as a function of relative displacement. All temperatures are in K.

Methane laminar diffusion flame with a fuel flow rate of $10 \text{cm}^3/\text{s}$ at $\Phi = 4$

Displacement (mm)	Height (mm)				
	3.5	10	16	25	35
0	1530.4	1343.0	1021.5	588.37	556.13
1	1703.7	1345.2	1067.2	606.08	563.66
2	1631.4	1330.7	110..5	633.67	567.00
3	1480.1	1292.8	1112.6	640.43	566.67
4	1357.1	1226.4	1102.0	652.79	571.83
5	1162.7	1137.0	1071.5	652.96	573.49
6	944.91	1021.5	1026.4	669.57	577.97
7	737.49	899.47	971.58	681.80	593.14
8	587.22	774.44	908.82	779.99	612.93
9	514.18	680.06	852.14	787.39	647.98
10	491.03	641.88	816.64	827.61	696.84
11	512.62	661.91	807.94	863.89	750.73
12	619.10	725.77	847.16	885.76	806.41
13	825.93	852.59	968.53	906.15	859.98
14	1054.4	989.37	1019.8	932.43	924.93
15	1275.1	1138.5	1101.2	968.53	950.17
16	1446.6	1251.5	1131.9	1001.6	957.47
17	1578.0	1311.8	1149.3	982.73	953.24
18	1676.3	1365.3	1123.9	1002.2	933.76
19	1544.2	1318.3	1073.3	933.32	874.40
20	1367.4	1334.0	1081.8	892.03	732.34
21	1199.5	1233.9	954.85	870.35	748.40
22	1044.4	1163.8	894.41	777.37	669.89

Ethene laminar diffusion flame with a fuel flow rate of 6.4cm^3/s at $\Phi = 4$

Displacement (mm)	Height (mm)			
	2.5	11	21	31
0	1528.7	1065.1	886.36	825.48
1	1695.5	1048.1	900.21	845.95
2	1582.9	1110.6	965.19	892.47
3	1386.0	1056.8	967.08	887.11
4	1195.3	1020.8	952.07	862.54
5	978.10	969.11	934.93	814.35
6	769.96	901.10	915.78	752.44
7	625.91	843.53	888.75	708.98
8	553.61	797.22	849.42	677.20
9	515.92	764.08	816.34	655.04
10	518.68	736.09	780.46	642.52
11	545.68	770.27	789.08	605.59
12	622.67	823.35	796.14	596.26
13	795.84	848.67	810.84	591.34
14	1025.9	916.07	854.41	586.07
15	1230.1	998.88	897.09	582.77
16	1421.4	1062.2	955.87	583.26
17	1578.5	1111.7	945.78	572.49
18	1537.6	1113.0	918.73	565.33
19	1388.8	1092.6	897.83	557.64
20	1248.3	1033.0	839.44	551.92
21	1110.1	958.35	811.61	546.70
22	963.01		722.01	541.62

U.S. DEPARTMENT OF COMMERCE
NATIONAL INSTITUTE OF STANDARDS AND TECHNOLOGY

	(ERB USE ONLY)	
ERB CONTROL NUMBER		DIVISION

MANUSCRIPT REVIEW AND APPROVAL

PUBLICATION REPORT NUMBER	CATEGORY CODE
NIST-GCR-94-661	

INSTRUCTIONS: ATTACH ORIGINAL OF THIS FORM TO ONE (1) COPY OF MANUSCRIPT AND SEND TO:
THE SECRETARY, APPROPRIATE EDITORIAL REVIEW BOARD.

PUBLICATION DATE	NUMBER PRINTED PAGES
November 1994	

TITLE AND SUBTITLE (CITE IN FULL)

Fundamental Mechanisms for CO and Soot Formation

CONTRACT OR GRANT NUMBER	TYPE OF REPORT AND/OR PERIOD COVERED
60NANBOD1035	Final Report, June, 1994

AUTHOR(S) (LAST NAME, FIRST INITIAL, SECOND INITIAL)

Santoro, R. J.
Pennsylvania State University
University Park, PA 16802-2320

PERFORMING ORGANIZATION (CHECK (X) ONE BOX)

[ ] NIST/GAITHERSBURG
[ ] NIST/BOULDER
[ ] JILA/BOULDER

LABORATORY AND DIVISION NAMES (FIRST NIST AUTHOR ONLY)

SPONSORING ORGANIZATION NAME AND COMPLETE ADDRESS (STREET, CITY, STATE, ZIP)

U.S. Department of Commerce
National Institute of Standards and Technology
Gaithersburg, MD 20899

RECOMMENDED FOR NIST PUBLICATION

[ ] JOURNAL OF RESEARCH (NIST JRES)	[ ] MONOGRAPH (NIST MN)		[ ] LETTER CIRCULAR
[ ] J. PHYS. & CHEM. REF. DATA (JPCRD)	[ ] NATL. STD. REF. DATA SERIES (NIST NSRDS)		[ ] BUILDING SCIENCE SERIES
[ ] HANDBOOK (NIST HB)	[ ] FEDERAL INF. PROCESS. STDS. (NIST FIPS)		[ ] PRODUCT STANDARDS
[ ] SPECIAL PUBLICATION (NIST SP)	[ ] LIST OF PUBLICATIONS (NIST LP)	[X]	OTHER NIST-GCR
[ ] TECHNICAL NOTE (NIST TN)	[ ] NIST INTERAGENCY/INTERNAL REPORT (NISTIR)		

RECOMMENDED FOR NON-NIST PUBLICATION (CITE FULLY) [ ] U.S. [ ] FOREIGN

PUBLISHING MEDIUM
[X] PAPER [ ] CD-ROM
[ ] DISKETTE (SPECIFY)
[ ] OTHER (SPECIFY)

SUPPLEMENTARY NOTES

ABSTRACT (A 1500-CHARACTER OR LESS FACTUAL SUMMARY OF MOST SIGNIFICANT INFORMATION. IF DOCUMENT INCLUDES A SIGNIFICANT BIBLIOGRAPHY OR LITERATURE SURVEY, CITE IT HERE. SPELL OUT ACRONYMS ON FIRST REFERENCE.) (CONTINUE ON SEPARATE PAGE, IF NECESSARY.)

Studies investigating the oxidation of soot and carbon monoxide (CO) have been conducted in a series of laminar diffusion flames. Both overventilated and undervenilated conditions have been examined. For the overventilated studies, the production and destruction of CO has been found to be influenced by the amount of soot present in the flame. Measurements of the hydroxyl radical (OH•) have demonstrated that soot can compete for OH• when undergoing oxidation and, thus, impede the oxidation of CO to CO_2. Absolute concentration measurements for OH• have shown that superequilibrium values of OH• are achieved in the upper region of these diffusion flames. In these situations, equilibrium estimates for OH• are in error, underestimating the OH• concentration significantly. However, as soot concentration increases to a point where soot is emitted from the flame, rapid reactions between soot particle and OH• result in concentration levels close to equilibrium values. These results clearly demonstrate that soot particles are far from passive species in flames and can directly affect the chemical pathways involved in the oxidation process through radiative effects on temperature and soot particle reactivity effects on radical concentrations.   (continued)

KEY WORDS (MAXIMUM 9 KEY WORDS; 28 CHARACTERS AND SPACES EACH; ALPHABETICAL ORDER; CAPITALIZE ONLY PROPER NAMES)

carbon monoxide; diffusion flames; fire research; oxidation; soot

AVAILABILITY

[X] UNLIMITED   [ ] FOR OFFICIAL DISTRIBUTION. DO NOT RELEASE TO NTIS.
[ ] ORDER FROM SUPERINTENDENT OF DOCUMENTS, U.S. GPO, WASHINGTON, D.C. 20402
[X] ORDER FROM NTIS, SPRINGFIELD, VA 22161

NOTE TO AUTHOR(S) IF YOU DO NOT WISH THIS MANUSCRIPT ANNOUNCED BEFORE PUBLICATION, PLEASE CHECK HERE. [ ]

ELECTRONIC FORM

Title: Fundamental Mechanisms for CO and Soot Formation
Author: Santoro, R.J.
No.: GCR-94-661

Abstract (continued)

The CO and smoke yields were observed for underventilated laminar diffusion flames burning methane and ethene for global equivalence ratio Φ over the range 0.5 to 4.0. A Burke-Schumann type burner with fuel in the center tube and air in the annular region was used. The peak CO yields for methane and ethene, 0.37 and 0.47 respectively, are at least a factor of 100 greater than for overventilated burning. The ratio of CO/CO_2 versus Φ for the methane flame is compared with local measurements of this ratio for both overventilated and underventilated laminar diffusion flames and with the results for turbulent natural gas flames quenched in an upper layer. The peak smoke yields for methane at a flow rate of 10 cm^3/s and for ethene at a fuel flow rate of 6.4 cm^3/s are 0.01 and 0.05, respectively, compared to yields of 0. and 0.028 for the overventilated case. The proportionality between smoke yield and CO yield observed for overventilated burning for a wide range of fuels is found not to be valid for the underventilated case. The chemical makeup and structure of the smoke produced at high equivalence ratio is qualitatively different from smoke produced under overventilated conditions; the smoke is mainly organic rather than graphitic and it has an agglutinated structure rather than an agglomerate structure with distinct primary spheres usually observed in overventilated burning.